MAGNETIC RESONANCE PERFUSION IMAGING AND DOUBLE QUANTUM COHERENCE TRANSFER MAGNETIC RESONANCE SPECTROSCOPY

BY

HAO LEI

A Thesis
Submitted to the Faculty of Graduate Studies
in Partial Fulfillment of the Requirements
for the Degree of

DOCTOR OF PHILOSOPHY

Department of Chemistry
University of Manitoba
Winnipeg, Manitoba, Canada

August 1999

THE UNIVERSITY OF MANITOBA

FACULTY OF GRADUATE STUDIES

*****

COPYRIGHT PERMISSION PAGE

Magnetic Resonance Perfusion Imaging and Double Quantum Coherence Transfer Magnetic Resonance Spectroscopy

BY

Hao Lei

A Thesis/Practicum submitted to the Faculty of Graduate Studies of The University of Manitoba in partial fulfillment of the requirements of the degree of Doctor of Philosophy

ACKNOWLEDGEMENTS

First of all, I want to express my most sincere gratitude to my supervisor, Dr. J. Peeling, without whose constant guidance, encouragement and support, this thesis would be impossible. Jim is not only a great mentor but also like a father and a close friend to me. The most important things I learned from him, I think, are what is scientific research really about, what virtues it takes to make a good scientist, and what is a great personality.

Secondly, I would like to thank Dr. R. Buist, the system manager of the magnetic resonance (MR) lab. When I first came to the lab, I virtually knew nothing about MR. It was Richard's patient hand-by-hand training in the first three years of this program that helped me become familiar with the operations of the spectrometer and the basics of MR. Discussion with Richard is always a pleasure for me, especially when philosophy is the topic.

My thanks also go to M. Campbell for his appreciated help with animal preparation. Mark has also been a big help with my English as this thesis was written. I am grateful to the members of my advisory committee, Drs. M. Del Bigio, J. O'Neil and F. Hruska for their stimulating suggestions and comments on my research projects and for their time and patience in writing reference letters for me. Dr. K. Malisza is thanked for allowing me to use a table from her paper as Table 5.1 of this thesis. J. Dowden is thanked for helping me with the focal ischemia experiments described in chapter 4. The Faculty of Graduate Studies of The University of Manitoba is acknowledged for providing financial support for me for two years.

Finally, I want to take this opportunity to thank my grandparents, my parents and my sister for their emotional support. Particularly, I want to thank my maternal grandparents who brought me up and constantly encouraged me to go down the road of science since I was just a little kid who could barely read and write. This thesis, I think, is the best way to say thank you to them. Unfortunately, my grandma, who passed away 9 years ago, can no longer hear me say that, but I think she would be delighted if she could.

ABSTRACT

The thesis is composed of two parts. Magnetic resonance (MR) perfusion imaging using continuous arterial spin tagging (CAST) and double quantum (DQ) coherence transfer MR spectroscopy (MRS) are the main themes respectively. Part one first discusses the importance of cerebral blood flow (CBF) measurements for both clinical management and experimental investigation of neurological diseases such as ischemic stroke. This is followed by a review of the commonly used methods for measuring CBF. MR perfusion imaging using CAST is then discussed, starting with derivation of a general equation for CBF calculation. A comprehensive examination of all the factors affecting absolute CBF quantification and an error propagation analysis to estimate the signal-to-noise ratio of the perfusion images (SNR_{perfu}) obtained with this technique are then given. A strategy to optimize SNR_{perfu} in one-coil CAST perfusion imaging is proposed and demonstrated experimentally. Improved SNR_{perfu} enables higher temporal resolution for perfusion measurements, as is demonstrated experimentally with an acetazolamide stimulation test. With the MR perfusion imaging technique developed, the effects of anesthetics on CBF in rats were investigated. CBF in rats after transient focal cerebral ischemia was also measured. A delayed hyperemia in brain regions sustaining ischemic injuries was observed.

DQ coherence transfer or DQ filtering (DQF) is a common spectral editing technique used in *in vivo* proton MRS to suppress water/lipid signals and to eliminate spectral overlapping. Part two of the thesis involves developing new DQF techniques and improving existing DQF techniques with the objective of making them more useful for practical applications. A

localized DQF sequence for *in vivo* observation of taurine was developed and optimized. This may be useful as a tool in investigating the pathophysiology of taurine-related disorders. Because the conventional DQF sequences recover spectra of only one metabolite at a time, a stimulated-echo enhanced selective DQ coherence transfer sequence and a DQ double-editing sequence were developed, both of which are capable of observing more than one metabolite simultaneously. Finally, spatial localization using two-dimensional longitudinal Hadamard encoding was combined with a conventional DQF sequence to acquire multiple-voxel localized and lactate edited spectra *in vivo*.

LIST OF FIGURES

LIST OF TABLES

LIST OF ABBREVIATIONS

1D: one dimensional

2D: two dimensional

2τ: double quantum coherence creation period

α: degree of spin labeling

ACE: acquiring combined echo

ACQ: acquisition

ANOVA: analysis of variance

AST: arterial spin tagging

ATP: adenosine triphosphate

B_1: strength of radiofrequency pulse

BBB: blood brain barrier

BIR: B_1-insensitive rotation

BOLD: blood oxygenation level dependent

C_a: arterial concentration of the tracer

CAST: continuous arterial spin tagging

CBF: cerebral blood flow

CBV: cerebral blood volume

Cho: Choline

CMR_{glu}: cerebral glucose metabolic rate

$CMRO_2$: cerebral oxygen metabolic rate

CO: cardiac output

COSY: J-correlated spectroscopy

Cr: creatine

CSI: chemical shift imaging

CT: computed tomography

C_t: concentration of the tracer in tissue

C_v: venous concentration of the tracer

DANTE: delays alternating with nutations for tailored excitation

ΔB_0: inhomogeneity of the main magnetic field

DIGGER: discrete isolation from gradient-governed elimination of resonances

DORI: direct off-resonance irradiation

DQ: double quantum

DQC: double quantum coherences

DQF: double quantum filtering

DRESS: depth resolved surface coil spectroscopy

$\Delta\upsilon$: chemical shift difference in Hz

$\Delta\omega$: chemical shift difference in rads·s^{-1}

off-resonance frequency

E: extraction fraction for water

EPI: echo planar imaging

EPISTAR: echo-planar-imaging with signal targeting with alternating radiofrequency

EST: extraslice spin tagging

f: perfusion rate in ml·g^{-1}·min^{-1}

ϕ: phase of radiofrequency pulse

F: perfusion rate in ml·min^{-1}

FAIR: flow sensitive alternating inversion recovery

FID: free induction decay

FLASH: fast low angle shot

FOV: field of view

FRIVOL: frequency interval selective volume localization

G: strength of magnetic field gradient

γ: gyromagnetic ratio

GABA: γ-aminobutyric acid

G_I: gradient strength for arterial spin tagging

Glx: glutamate/glutamine

He: helium

Ino: *myo*-inositol

ISIS: image selected *in vivo* spectroscopy

J: scalar coupling constant

k_{for}: forward magnetization transfer rate constant

k_{rev}: reverse magnetization transfer rate constant

Λ: strong coupling frequency

λ: brain:blood partition coefficient

Lac: lactate

LDF: laser Doppler flowmetry

L-NAME: N^G-nitro-L-arginine methylester

LOCUS: localization of affected spins

M_a: longitudinal magnetization of water spins in arterial blood

M_a^0: equilibrium value of M_a

M_b: longitudinal magnetization of water spins in brain tissue

M_b^0: equilibrium value of M_b

M_m: longitudinal magnetization of macromolecule spins in brain tissue

M_m^0: equilibrium value of M_m

MCA: middle cerebral artery

MQ: multiple quantum

MQC: multiple quantum coherences

MR: magnetic resonance

MRI: magnetic resonance imaging

MRS: magnetic resonance spectroscopy

MT: magnetization transfer

MTT: mean transit time

M_v: longitudinal magnetization of water spins in venous blood

N: number of microspheres

noise level

NAA: N-acetylaspartate

NDP: nucleotide diphosphate

NMR: nuclear magnetic resonance

N_2O: nitrous oxide

NO: nitric oxide

NOS: nitric oxide synthase

OEF: oxygen extraction fraction

p: order of coherence

P: vector representing a coherence transfer pathway

PAST: pulsed arterial spin tagging

PCr: phosphocreatine

PDE: phosphodiesters

PET: positron emission tomography

P_i: inorganic phosphate

PICORE: control for offset-resonance effects

PME: phosphomonoesters

PRESS: point resolved spectroscopy

θ: flip angle of radiofrequency pulse

QUIPSS: quantitative imaging of perfusion using a single subtraction

r: position coordinate

R: rate at which longitudinal magnetization is lost due to off-resonance irradiation

rCBF: regional cerebral blood flow

RF: radiofrequency

RFS: rotating frame spectroscopy

SD: standard deviations

SEE: double spin echo

SI: spectroscopic imaging

SNR: signal-to-noise ratio

SNR_{image}: signal-to-noise ratio of proton weighted images

SNR_{perfu}: signal-to-noise ratio of perfusion images

SNRT: signal-to-noise ratio per unit time

SPACE: spatial and chemical shift encoded excitation

SPARS: spatially resolved spectroscopy

SPECT: single photon emission tomography

SQ: single quantum

SQC: single quantum coherences

SSAP: solvent suppression adiabatic pulses

STE: stimulated echo

STEAM: stimulated echo acquisition mode

T1: longitudinal relaxation time

t_1: double quantum coherence evolution period

τ_1: first part of double quantum coherence detection period

$T1_a$: T1 of water spins in arterial blood

$T1_b$: T1 of brain tissue water

$T1_m$: T1 of brain macromolecule spins

$T1_o$: observed T1 for brain tissue water

τ_2: second part of double quantum coherence detection period

T2: transverse relaxation time

$T2^*$: transverse relaxation time in the presence of B_0 inhomogeneity

$T2_a$: T2 of water spins in arterial blood

$T2_b$: T2 of water spins in brain tissue

$T2_m$: T2 of macromolecule spins in brain tissue

Tau: taurine

TCA: tricarboxylic acid

TE: echo time

TI: inversion recovery time

TM: mixing time

TMR: topical magnetic resonance

TQC: triple quantum coherences

TR: repetition time

V: laminar velocity of arterial blood in the carotid arteries

V_d: volume of tracer distribution

VEST: volume excitation using stimulated echo

VOI: volume of interest

VOSINER: volume of interest by selective inversion, excitation and refocusing

VOSING: volume selective spectral editing

VOSY: volume selective spectroscopy

VSE: volume selective excitation

VSR: volume selective refocusing

W: weight of the brain

weighting coefficients

ω: chemical shift

Doppler frequency

Xe: xenon

ZQC: zero quantum coherences

TABLE OF CONTENTS

Prologue

In the last two decades, the technology of magnetic resonance (MR) and its applications in biomedicine have developed in a way that few would have expected. Biomedical MR, including magnetic resonance imaging (MRI) and *in vivo* magnetic resonance spectroscopy (MRS), not only has become an essential tool in many areas of basic research, but also provides a powerful diagnostic technique used clinically. Driven by more and more demanding applications, the technical development of biomedical MR is still progressing rapidly. In 1963, E. M. Packard, one of the early pioneers in nuclear magnetic resonance (NMR), commented on the fast growth in high resolution MRS at the time (1), and said: "*Chemists got the point very quickly, thanked the physicists and took over.*" It seems to me that the growth currently experienced by biomedical MR is exactly the same as that experienced by high resolution MRS three decades ago, and thus I think it is appropriate to paraphrase Packard's words and say: Physiologists and radiologists got the point very quickly, thanked the physicists and chemists and took over. The remaining question is who will come the next. "*Maybe, the bankers*", joked R. V. Pound, another early pioneer in NMR, during the inaugural Paul Lauterbur Lecture which he gave in 1997 at the 5th annual conference of the International Society of Magnetic Resonance for Medicine (ISMRM).

The earliest MR-related observations can be traced back to the turn of the century when it was found that each line in the ultraviolet spectrum of a substance splits into two wavelengths in the presence of an external magnetic field. This "mysterious" splitting remained unexplained until 1924 when W. Pauli realized that it was caused by the

interactions between the electrons and the separated energy states of the nucleus induced by the presence of the external magnetic field (2). Pauli then suggested that the nucleus must have magnetic properties. Using an apparatus devised by themselves, O. Stern and W. Gerlach carried out a series of experiments in the 1930s, which are now referred as the classic Stern-Gerlach experiments (3), and demonstrated that both the proton and the neutron have a magnetic moment, indeed, just as Pauli predicted. The next step in understanding the magnetic properties of the nucleus was made by I. I. Rabi who designed a resonance experiment in which a beam of nuclei was deflected by a magnetic field oscillating at a radiofrequency (RF) and the amount of the deflection was used to measure the magnetic moment of the nucleus precisely (4,5). Although Rabi did not establish the concept of *magnetic resonance* that we are familiar with today, his experiment did establish the basis for the discovery of NMR in 1946 by F. Bloch and E. M. Purcell (6-9). For their achievements, Rabi was awarded a Nobel prize in 1944, and Bloch and Purcell were awarded a Nobel prize in 1952.

In the early stages, MR signals were observed using the conventional absorption method (i.e. the continuous-wave method) which was not only insensitive but also extremely slow in data acquisition, and the application of MR at the time was limited to studying simple nuclear physics such as spin diffusion and relaxation. However, everything started to change at the beginning of 1950s, thanks to two breakthroughs. The first was the accidental discovery of the free induction decay (FID), a form of MR signal in the time domain, and the spin echo by E. L. Hahn when he tried to perform a simple inversion-recovery experiment and observe the MR signals on an oscilloscope (10,11). Hahn's discovery together with the Fourier

Transformation (FT) theory that was introduced later revolutionized the way MR signals were observed and eventually led to the development of modern MR technology. The second breakthrough was the discovery of the chemical shift and the scalar spin coupling (12-15). With these discoveries, high resolution MRS started to attract interest from chemists since its usefulness in analytical chemistry and in determining the chemical structures of unknown compounds was now becoming obvious. The triumph of high resolution MRS came in the 1970s when two-dimensional MRS techniques were developed and shown to be capable of determining the structures of molecules as complex as proteins (16).

MR was introduced to the field of biomedicine in the mid 1960s. Early experiments included using MRS to analyze the structures of proteins, the conformation of enzymes and the metabolic pathways in living cells. In 1971, R. Damadian first observed different relaxation characteristics of water in normal tissue and in cancerous tissue, and suggested the potential of MR in clinical medicine (17). The breakthrough which created the entire field of biomedical MR came in 1973 when Paul Lauterbur proposed a MR imaging method which he called zeugmatography (18). The first MR image of experimental animals was obtained at the University of Aberdeen, Scotland in 1974 (19), only one year after Lauterbur's original paper was published. Using a line scan method, the first MR images of a human abdomen were obtained in 1978 (20). Significant improvement in the quality of MR images came at the beginning of the 1980s when the spin warp technique and FT theory were introduced to acquire and reconstruct MR images (21). With improved image quality, MRI passed preliminary clinical trials in 1983 and started to make its appearance as a novel diagnostic tool in clinics (21).

What makes MR so attractive in biomedicine is its noninvasiveness so that imaging and spectroscopy can be performed without perturbing or harming the sample itself. Clinically, noninvasiveness is the an essential requirement for a diagnostic technique. In basic research, the noninvasiveness of MR makes it possible to obtain metabolic and structural information on intact biological tissue. Such information is usually lost if invasive techniques are used. Another attractive feature of MR is its versatility and flexibility. Different MR techniques can be used to obtain different information about the tissue in a single experiment. For example, MRI with different contrast mechanisms can be used to measure different properties of the tissue, ranging from microscopic water movement to macroscopic blood flow.

After a half century of research, the fundamental basics of MR are very well established. However, this could be bad news rather than good news to latecomers in science such as myself because making discoveries like the ones made in the earlier days is now highly unlikely, although one can never say impossible. However, this does not mean there is nothing important left for us to discover and there is also no need to be pessimistic. Maybe we can never supersede or even match the splendid achievements made by earlier scientists in pure science, *the search for knowledge for its own sake*. What we can do is applied science — refining and applying the brilliant discoveries made previously and making them beneficial to our world and our lives at large. The field of MR in biomedicine belongs to applied science rather than pure science which I would prefer if I had been born one hundred years ago.

The main objective of the work described in this thesis is to improve existing MRI and MRS techniques and to develop new MRI and MRS techniques with potential applications in biomedicine. The thesis is composed of ten chapters, with the first nine constituting the body text and the last one serving as an overall summary. Among these, chapters one to four describe the development, experimental implementation and applications of a MR perfusion imaging technique for measuring cerebral blood flow, while the development of several *in vivo* proton MRS techniques is described in chapters five to nine. The background and rationale for each study are given when it is described individually in the different chapters.

References

1. E. Rogers, E. M. Packard and J. N. Shoolery, The Origins of NMR Spectroscopy, Varian Associates, Palo Alto, 1963.

2. W. Pauli, Zur Frage der theoretischen Deutung der Satelliten einiger Spektrallinien und ihrer Beeinflussung durch magnetische Felder, *Naturwiss* **12**, 741, (1924).

3. J. S. Townsend, A Modern Approach to Quantum Mechanics, McGraw-Hill Inc., New York 1992; Chapter 1, Stern-Gerlach Experiments. p. 1-23.

4. J. M. B. Kellogg, I. I. Rabi and N. F. Ramsey Jr., An electrical quadrupole moment of the deuteron: The radiofrequency spectra of HD and D_2 molecules in a magnetic field, *Phys. Rev.* **57**, 677, (1940).

5. I. I. Rabi, S. Millman, P. Kusch and J. R. Zacharias, The molecular beam resonance method for measuring nuclear magnetic moments: The magnetic moments of $_3Li^6$, $_3Li^7$ and $_9F^{19}$, *Phys. Rev.* **55**, 526, (1939).

6. F. Bloch, Nuclear induction, *Phys. Rev.* **70**, 460, (1946).

7. F. Bloch, W. W. Hansen and M. Packard, Nuclear induction, *Phys. Rev.* **69**, 127, (1946).

8. F. Bloch, W. W. Hansen and M. Packard, The nuclear induction experiment, *Phys. Rev.* **70**, 474, (1946).

9. E. M. Purcell, H. C. Torrey and R. V. Pound, Resonance absorption by nuclear magnetic moments in a solid, *Phys. Rev.* **69**, 37, (1946).

10. E. L. Hahn, Nuclear induction due to free Larmor precession, *Phys. Rev.* **77**, 297, (1950).

11. E. L. Hahn, Spin echoes, *Phys. Rev.* **80**, 580, (1950).

12. W. G. Proctor and F. C. Yu, The dependence of a nuclear magnetic resonance frequency upon chemical compound, *Phys. Rev.* **77**, 717, (1950).

13. W. C. Dickson, Dependence of the F^{19} nuclear magnetic resonance position on chemical compound, *Phys. Rev.* **77**, 736, (1950).

14. H. S. Gutowsky and C. J. Hoffman, Chemical shifts in the magnetic resonance of F^{19}, *Phys. Rev.* **80**, 110, (1950).

15. W. G. Proctor and F. C. Yu, On the nuclear magnetic moments of several stable isotopes, *Phys. Rev.* **81** , 20, (1951).

16. R. R. Ernst, G. Bodenhausen and A. Wokaun, Principles of Nuclear Magnetic Resonance in One or Two Dimensions, Oxford University Press, London, 1987.

17. R. Damadian, Tumor detection by nuclear magnetic resonance, *Science* **171**, 1151, (1971).

18. P. C. Lauturber, Image formation by induced local interactions: Examples employing nuclear magnetic resonance, *Nature* **242**, 190, (1973).

19. J. Mallard, J. M. Hutchison, W. Edelstein, R. Ling and M. Foster, Imaging by nuclear magnetic resonance and its bio-medical implications, *J. Biomed. Eng.* **1**, 153, (1979).

20. P. Mansfield, I. L. Pykett and P. G. Morris, Human whole body line-scan imaging by NMR, *Br. J. Radiol.* **51**, 921, (1978).

21. P. G. Morris, Nuclear Magnetic Resonance Imaging in Medicine and Biology, Oxford University Press, New York, 1986.

Chapter 1. Brain and Cerebral Blood Flow

The brain is the organ with the most active energy metabolism in the body. In normal humans, the brain, which represents only about 2% of the body weight, receives 15% of the cardiac output and accounts for about 20% of the total body baseline oxygen consumption (1). Under resting conditions, the cerebral oxygen metabolic rate ($CMRO_2$) in man is about 3.5 $ml \cdot g^{-1} \cdot min^{-1}$ (2). Unlike other organs, which usually exhibit considerable flexibility in using different substrates for their energy metabolism, normal brain uses glucose almost exclusively (2). The cerebral glucose utilization rate (CMR_{glu}) in man under normal conditions is about 0.3 $\mu mol \cdot g^{-1} \cdot min^{-1}$. CMR_{glu} values in some experimental animal species are even higher (2). However, despite the vast demand for oxygen and glucose, the storage of both substances in the brain is negligible. Therefore, an uninterrupted delivery and regional distribution of oxygen and glucose to the brain tissue by cerebral blood flow (CBF) are of critical importance in maintaining the brain's functional and structural integrity. Disturbances in normal CBF, even though transient, can have long lasting and far reaching consequences on the brain, ranging from mildly impaired brain function to complete brain infarction. Altered CBF may play a role in many neurological diseases. In particular, it is the primary pathogenesis of ischemic stroke in which global or regional cerebral blood flow (rCBF) is reduced or totally abolished due to narrowed or occluded cerebral blood vessels. In investigating, diagnosing and managing CBF-related diseases, the ability to measure global and regional CBF is, therefore, of clear importance. Particularly, in the studies of clinical and experimental stroke, CBF measurements have been used mainly in three ways.

1) Measurement of CBF in investigating the pathophysiology of ischemic stroke

In normal brain, resting CBF is tightly coupled with tissue metabolism (2). During cerebral ischemia, CBF is reduced and the supply of oxygen and glucose to the brain becomes insufficient for normal metabolism. Consequently, cerebral energy metabolism is impaired and energy-consuming processes in the brain are affected adversely in a sequential manner. Functional activities are suppressed first, followed by alteration or suppression of normal metabolic activities. This in turn triggers a cascade of neurochemical events that affect the brain's cellular integrity and will potentially cause brain damage. Each particular event induced by cerebral ischemia happens only when CBF is reduced below a certain level which is called the *ischemic threshold* for that event (3). Defining the ischemic threshold for each ischemic event is of obvious importance in investigating the mechanisms of pathophysiology for ischemic stroke. Guided by quantitative CBF measurements, ischemic thresholds for a wide range of functional, metabolic, neurochemical and histological events have been determined in the past using graded cerebral ischemia models (3-6). The results of those studies have greatly improved our understanding of the disease.

In addition to the absolute CBF, the duration of ischemia is another parameter of interest in defining the severity and predicting the outcome of an ischemic stroke. In a cat model of focal ischemia, 30 minutes of ischemia produced no or only minor brain damage while severe cerebral infarction was evident in cats undergoing 60 or 120 minutes ischemia (7). The duration of ischemia also plays a role in defining the ischemic thresholds. For example, the blood flow thresholds for some ischemic events have been shown to become higher when the duration of ischemia is prolonged (8-11). Accurate determination of the duration of

ischemia is not trivial, and in many cases may require continuous and quantitative measurements of rCBF. This is especially true in studies of animal models of transient focal ischemia. In these models, restoration of rCBF after reperfusion is not homogeneous. The ischemic core often recovers much more slowly than the peripheral areas of the ischemic zone so that ischemia is effectively longer in the ischemic core. Distinguishing such a difference in the duration of ischemia between the ischemic core and the periphery of the ischemic zone relies on the ability to measure rCBF continuously and quantitatively.

2) Measurement of CBF in diagnosing and predicting stroke

Clinically, there are two main objectives in the acute diagnosis of stroke (12). First, it is important to distinguish ischemic stroke from hemorrhagic stroke before a specific therapy such as thrombolysis is administrated. Both computed tomography (CT) and magnetic resonance imaging (MRI) can be used to do so although the sensitivity of CT in detecting intracerebral hemorrhage is reported to be higher (13,14). The use of MRI to distinguish ischemic and hemorrhagic stroke relies on multimodal MRI, including magnetic resonance (MR) perfusion imaging which measures rCBF quantitatively (14). Immediately after the onset of an ischemic stroke, CBF is severely reduced or completely abolished in the brain region supplied by the occluded artery. On the CBF images, the brain region with decreased rCBF appears as a well-defined area of hypointensity which indicates an ongoing ischemic stroke. Perfusion imaging can also be used to identify ischemic events, whether due to vascular occlusion, brain swelling, arterial/venous malformation etc. Another objective in the acute diagnosis of stroke is to estimate the extent of brain damage caused by the stroke. In this context, CBF imaging is useful in determining the volume of ischemic brain tissue which

is at risk of evolving into brain infarction. In addition, quantitative measurements of rCBF after stroke may also be helpful in assessing the reversibility of the brain damage and in predicting the outcome of the stroke (15-18) although its value for such prognosis remains to be fully defined (19). In the diagnosis of subarachnoid hemorrhage, CBF measurement is useful in tracking the course of vasospasm when combined with other techniques (20).

Identifying groups of patients with high risk of stroke is important for preventing the occurrence of this disease. Many factors increase the risk of stroke, such as carotid stenosis, hypertension, heart diseases, diabetes, cigarette smoking and alcohol consumption (21). Patients with severe carotid stenosis (>70%) are among those with the highest risk of ischemic stroke. Although having no clear correlation with the degree of carotid stenosis, cerebral hemodynamics in this group of patients is likely impaired. It has been hypothesized that impaired cerebral hemodynamics can be used as a predictor for subsequent stroke in these patients (22,23). Although earlier data from a small number of patients did not support this hypothesis (24-26), more recent studies showed that stroke in this group of patients can be predicted using a so-called cerebral vasomotor reactivity test (i.e. an acetazolamide stimulation test) (27-31), in which CBF is measured before and after intravenous injection of acetazolamide, a carbonic anhydrase inhibitor which increases the tissue CO_2 level and in turn increases CBF globally without altering the tissue metabolic rate significantly (32). The information about cerebral vasomotor reactivity is obtained by comparing CBF values measured before and after the acetazolamide injection. Stroke occurrences were found significantly higher in both symptomatic and asymptomatic patients with impaired cerebral vasomotor reactivity (28-30,33). Both qualitative and quantitative CBF measuring techniques

have been used in the past in the acetazolamide stimulation test. However, it is shown in a recent study that only results from quantitative CBF measurement can serve as a robust predictor of the subsequent stroke occurrence while predictions made from qualitative measurements are much less reliable (27).

3) Measurement of CBF in prognosis and treatment evaluation for ischemic stroke

CBF measurements might also be useful in the prognosis and treatment evaluation for ischemic stroke. When focal ischemia occurs, the entire ischemic zone can be divided into two parts, the *ischemic core* and the so-called *ischemic penumbra.* Within the ischemic core, blood flow decreases below the ischemic threshold that is required to maintain the structural integrity of the brain cells and consequently the functional and metabolic activities of the brain tissue are completely suppressed in this region. Unless normal CBF is restored within 30 minutes or so, viability of the brain cells will be lost and the brain damage caused by ischemia will become irreversible. The ischemic penumbra can be defined in several ways. Hossmann recently suggested that ischemic penumbra is "a region of constrained blood supply in which energy metabolism is preserved" (6), a definition challenged immediately by Ginsberg and Pulsinelli who consider the ischemic penumbra as a region of "electrophysiological silence" and "besieged by intermittent bioenergetic compromise" (34). In general, the ischemic penumbra can be simply viewed as a region within which the brain tissue at risk can be rescued if proper therapeutic interventions are applied.

The ischemic penumbra lasts for several hours after ischemia in animal models (35), and perhaps even longer in humans (36). The concept of an ischemic penumbra is important for

both experimental investigation and the clinical management of ischemic stroke (37) because it not only provides a target for potential therapeutic treatments of cerebral ischemia but also can be used to evaluate the efficacy of such treatments. The ischemic penumbra has first to be identified or, in most cases, to be visualized after an ischemic stroke before it can be used to guide and evaluate any potential treatments. To differentiate the ischemic penumbra from the ischemic core and the normal brain tissue and to visualize its existence, regional CBF and regional energy metabolism profiles of the brain tissue have to be determined simultaneously. In experimental focal ischemia, this has been done successfully using autoradiography (i.e. measuring CBF) in conjunction with the ATP-induced bioluminescence technique (i.e. assessing tissue energy metabolism) (9,38). However, these techniques are invasive so that they can not be used clinically. There is a family of noninvasive tomographic techniques, including magnetic resonance (MR) perfusion imaging, available now to measure rCBF quantitatively in both humans and experimental animals. The problem that remains in visualizing the ischemic penumbra noninvasively is to find a noninvasive way to image the energy metabolism status of the brain tissue. ^{31}P chemical shift imaging (39-42), diffusion-weighted MR imaging (11,43-45) and quantitative T2 imaging (46) have shown some potential. However, some technical problems remain to be solved before they can be used routinely. Currently, identification and visualization of the ischemic penumbra are attracting more and more research interest and hopefully significant progress will be made in the near future.

References

1. E. V. Golanov and D. J. Reis (K. M. A. Welch, L. R. Caplan, D. J. Reis, B. K. Siesjo and B. Weir, Eds). Primer on cerebrovascular diseases, Academic Press, London, 1997; Chapter 9, Oxygen and cerebral blood flow. p. 58-60.

2. B. K. Siesjo, Brain energy metabolism, John Wiley & Sons Ltd., New York, 1978.

3. W. D. Heiss, Flow thresholds of functional and morphological damage of brain tissue, *Stroke* **14**, 329, (1983).

4. W. Paschen, G. Mies and K. A. Hossmann, Threshold relationship between cerebral blood flow, glucose utilization, and energy metabolites during development of stroke in gerbils, *Exp. Neurol.* **117**, 325, (1992).

5. W. D. Heiss, Experimental evidence of ischemic thresholds and functional recovery, *Stroke* **23**, 1668, (1992).

6. K. A. Hossmann, Viability thresholds and the penumbra of focal ischemia, *Ann. Neurol.* **36**, 557, (1994).

7. W. D. Heiss, R. Graf, J. Lottgen, K. Ohta, T. Fujita, R. Wagner, M. Grond and K. Weinhard, Repeat positron emission tomographic studies in transient middle cerebral artery occlusion in cats: residual perfusion and efficacy of postischemic reperfusion, *J. Cereb. Blood Flow Metab.* **17**, 388, (1997).

8. W. D. Heiss and G. Rosner, Functional recovery of cortical neurons as related to degree and duration of ischemia, *Ann. Neurol.* **14**, 294, (1983).

9. G. Mies, S. Ishimaru, Y. Xie, K. Seo and K. A. Hossmann, Ischemic thresholds of cerebral protein synthesis and energy state following middle cerebral artery occlusion in rat, *J. Cereb. Blood Flow Metab.* **11**, 753, (1991).

10. K. Matsumoto, R. Graf, G. Rosner, J. Taguchi and W. D. Heiss, Elevation of neuroactive substances in the cortex of cats during prolonged focal ischemia, *J. Cereb. Blood Flow Metab.* **13**, 586, (1993).

11. K. Kohno, B. M. Hoehn, G. Mies, T. Back and K. A. Hossmann, Relationship between diffusion-weighted MR images, cerebral blood flow, and energy state in experimental brain infarction, *Magn. Reson. Imaging* **13**, 73, (1995).

12. L. C. McHenry Jr., Cerebral Circulation and Stroke, Warren H. Green Inc., St. Louise, 1978.

13. J. P. Broderick, H. P. Adams Jr., W. Barsan, W. Feinberg, E. Feldmann, J. Grotta, C. Kase, D. Krieger, M. Mayberg, B. Tilley, J. M. Zabramski and M. Zuccarello, Guidelines for the management of spontaneous intracerebral hemorrhage: A statement for health care professionals from a special writing group of the Stroke Council, American Heart Association, *Stroke* **30**, 905, (1999).

14. P. D. Schellinger, O. Jansen, J. B. Fiebach, W. Hacke and K. Sartor, A standardized MRI stroke protocol: comparison with CT in hyperacute intracerebral hemorrhage, *Stroke* **30**, 765, (1999).

15. M. Doran and G. M. Bydder, Magnetic resonance: perfusion and diffusion imaging, *Neuroradiology* **32**, 392, (1990).

16. M. D. King, N. van Bruggen, A. L. Busza, J. Houseman, S. R. Williams and D. G. Gadian, Perfusion and diffusion MR imaging, *Magn. Reson. Med.* **24**, 288, (1992).

17. K. A. Hossmann and M. Hoehn Berlage, Diffusion and perfusion MR imaging of cerebral ischemia, *Cerebrovasc. Brain Metab. Rev.* **7**, 187, (1995).

18. P. Jezzard, Advances in perfusion MR imaging, *Radiology* **208**, 296, (1998).

19. W. J. Powers and J. Zivin, Magnetic resonance imaging in acute stroke: not ready for prime time, *Neurology* **50**, 842, (1998).

20. G. Rordorf, W. J. Koroshetz, W. A. Copen, G. Gonzalez, K. Yamada, P. W. Schaefer, L. H. Schwamm, C. S. Ogilvy and A. G. Sorensen, Diffusion- and perfusion-weighted imaging in vasospasm after subarachnoid hemorrhage, *Stroke* **30**, 599, (1999).

21. P. A. Wolf, J. L. Cobb and R. B. D'Agostino (H. J. M. Barnett, B. M. Stein, J. P. Mohr, and F. M. Yatsu Eds). Stroke: Pathophysiology, Diagnosis, and Management, Churchill Livingstone Ltd., New York, 1992; Chapter 1, Epidemiology of stroke. p. 3-27.

22. W. J. Powers, Cerebral hemodynamics in ischemic cerebrovascular disease, *Ann. Neurol.* **29**, 231, (1991).

23. W. J. Powers, Hemodynamics and metabolism in ischemic cerebrovascular disease, *Neurol. Clin.* **10**, 31, (1992).

24. W. J. Powers, J. Grubb-RL and M. E. Raichle, Clinical results of extracranial-intracranial bypass surgery in patients with hemodynamic cerebrovascular disease, *J. Neurosurg.* **70**, 61, (1989).

25. W. J. Powers, L. W. Tempel and J. Grubb-RL, Influence of cerebral hemodynamics on stroke risk: one-year follow-up of 30 medically treated patients, *Ann. Neurol.* **25**, 325, (1989).

26. R. L. Levine, H. L. Lagreze, J. A. Dobkin, J. M. Hanson, M. R. Satter, B. R. Rowe and R. J. Nickles, Cerebral vasocapacitance and TIAs, *Neurology* **39**, 25, (1989).

27. H. Yonas, R. R. Pindzola, C. C. Meltzer and H. Sasser, Qualitative versus quantitative assessment of cerebrovascular reserves, *Neurosurgery* **42**, 1005, (1998).

28. A. Y. Gur, I. Bova and N. M. Bornstein, Is impaired cerebral vasomotor reactivity a predictive factor of stroke in asymptomatic patients, *Stroke* **27**, 2188, (1996).

29. M. W. Webster, M. S. Makaroun, D. L. Steed, H. A. Smith, D. W. Johnson and H. Yonas, Compromised cerebral blood flow reactivity is a predictor of stroke in patients with symptomatic carotid artery occlusive disease, *J. Vasc. Surg.* **21**, 338, (1995).

30. H. Yonas, H. A. Smith, S. R. Durham, S. L. Pentheny and D. W. Johnson, Increased stroke risk predicted by compromised cerebral blood flow reactivity, *J. Neurosurg.* **79**, 483, (1993).

31. R. W. Tarr, D. W. Johnson, M. Rutigliano, S. T. Hecht, S. Pentheny, C. A. Jungreis, J. A. Horton and H. Yonas, Use of acetazolamide-challenge xenon CT in the assessment of cerebral blood flow dynamics in patients with arteriovenous malformations, *Am. J. Neuroradiol.* **11**, 441, (1990).

32. S. Vorstrup, L. Henriksen and O. B. Paulson, Effect of acetazolamide on cerebral blood flow and cerebral metabolic rate for oxygen, *J. Clin. Invest.* **74**, 1634, (1984).

33. F. Vernieri, P. Pasqualetti, F. Passarelli, P. M. Rossini and M. Silvestrini, Outcome of Carotid Artery Occlusion Is Predicted by Cerebrovascular Reactivity, *Stroke* **30**, 593, (1999).

34. M. D. Ginsberg and W. A. Pulsinelli, The ischemic penumbra, injury thresholds, and the therapeutic window for acute stroke, *Ann. Neurol.* **36**, 553, (1994).

35. H. Memezawa, M. L. Smith and B. K. Siesjo, Penumbral tissues salvaged by reperfusion following middle cerebral artery occlusion in rats, *Stroke* **23**, 552, (1992).

36. P. Pantano, F. Caramia, L. Bozzao, C. Dieler and R. von Kummer, Delayed increase in infarct volume after cerebral ischemia: correlations with thrombolytic treatment and clinical outcome, *Stroke* **30**, 502, (1999).

37. A. M. Kaufmann, A. D. Firlik, M. B. Fukui, L. R. Wechsler, C. A. Jungries and H. Yonas, Ischemic core and penumbra in human stroke, *Stroke* **30**, 93, (1999).

38. K. A. Hossmann, G. Mies, W. Paschen, L. Csiba, W. Bodsch, J. R. Rapin, M. Le Poncin Lafitte and K. Takahashi, Multiparametric imaging of blood flow and metabolism after middle cerebral artery occlusion in cats, *J. Cereb. Blood Flow Metab.* **5**, 97, (1985).

39. M. Sasahira, K. Uchimura, K. Yatsushiro, T. Fujimoto and T. Asakura, Early detection of cerebral infarction by ^{31}P spectroscopic imaging, *Neuroradiology* **32**, 43, (1990).

40. L. H. Chang, Y. Cohen, P. R. Weinstein, L. Chileuitt and T. L. James, Interleaved ^{1}H and ^{31}P spectroscopic imaging for studying regional brain injury, *Magn. Reson. Imaging* **9**, 223, (1991).

41. J. W. Hugg, G. B. Matson, D. B. Twieg, A. A. Maudsley, M. D. Sappey and M. W. Weiner, Phosphorus-31 MR spectroscopic imaging (MRSI) of normal and pathological human brains, *Magn. Reson. Imaging* **10**, 227, (1992).

42. R. S. Lara, G. B. Matson, J. W. Hugg, A. A. Maudsley and M. W. Weiner, Quantitation of in vivo phosphorus metabolites in human brain with magnetic resonance spectroscopic imaging (MRSI), *Magn. Reson. Imaging* **11**, 273, (1993).

43. B. M. Hoehn, Diffusion-weighted NMR imaging: application to experimental focal cerebral ischemia, *NMR. Biomed.* **8**, 345, (1995).

44. J. Rother, A. J. de-Crespigny, H. D'Arceuil, K. Iwai and M. E. Moseley, Recovery of apparent diffusion coefficient after ischemia-induced spreading depression relates to cerebral perfusion gradient, *Stroke* **27**, 980, (1996).

45. A. R. Pierce, E. H. Lo, J. B. Mandeville, R. G. Gonzalez, B. R. Rosen and G. L. Wolf, MRI measurements of water diffusion and cerebral perfusion: their relationship in a rat model of focal cerebral ischemia, *J. Cereb. Blood Flow Metab.* **17**, 183, (1997).

46. O. H. Grohn, J. A. Lukkarinen, J. M. Oja, P. C. van-Zijl, J. A. Ulatowski, R. J. Traystman and R. A. Kauppinen, Noninvasive detection of cerebral hypoperfusion and reversible ischemia from reductions in the magnetic resonance imaging relaxation time T2, *J. Cereb. Blood Flow Metab.* **18**, 911, (1998).

Chapter 2. An Overview of Methods for Measuring Cerebral Blood Flow

Introduction

Since Kety and Schmidt's pioneering work in the 1940s (1,2), considerable research effort has been made to develop methods which can be used to measure cerebral blood flow (CBF). From the earliest methods using nitrous oxide gas to the most recent magnetic resonance (MR) perfusion imaging methods, many CBF measuring methods have been developed and the application of these methods in both basic research and the clinical setting has proven beneficial. Although different CBF measuring methods have different characteristics, the underlying principles they share are similar. To measure CBF, a tracer is introduced into the vascular system of the subject undergoing CBF measurements. Upon administration, the tracer is carried by the blood and perfuses the brain tissue with kinetics dependent on CBF. By observing the build-up and/or clearance of the tracer in the brain tissue as a function of time and modeling the kinetic processes mathematically, CBF can be determined .

In this chapter, a historic overview of the commonly used methods for measuring CBF is given. Theoretical principles and typical technical procedures for each of the methods are described. The advantages and disadvantages associated with each method are also discussed.

Fick's Principle

In 1870, Adolph Fick, a German physiologist, first described a method to measure cardiac output in intact animal and human. The basis for this method, now called Fick's principle, is simply an application of the law of conservation of mass. For a substance which is consumed by the brain, Fick's principle states that the amount of the substance delivered to the brain per unit time (Δt) by arterial blood ($Q_a/\Delta t$) must be equal to the sum of the amount leaving the brain through venous blood ($Q_v/\Delta t$), the amount consumed by the brain ($Q_c/\Delta t$) and the amount accumulated in the brain ($Q_t/\Delta t$).

$$\frac{Q_a}{\Delta t} = \frac{Q_v}{\Delta t} + \frac{Q_c}{\Delta t} + \frac{Q_t}{\Delta t} \qquad [2.1]$$

Kety and Schmidt's Theory to Measure Global Cerebral Blood Flow

Fick's principle was originally used to calculate cardiac output in humans. It was Kety and his co-workers who adapted this principle and used it in the pioneering work of measuring global CBF in the 1940s (1,2). Suppose a non-metabolizable tracer is introduced into the circulatory system by either inhalation or intravenous injection. Since the tracer is non-metabolizable, Q_c in Eq. [2.1] is zero and the differential form of Eq. [2.1] can then be written as

$$\frac{dQ_t(t)}{dt} = \frac{dQ_a(t)}{dt} - \frac{dQ_v(t)}{dt} \qquad [2.2]$$

Since $Q_t(t)=W\times C_t(t)$, $Q_a(t)= F\times C_a(t)$ and $Q_v(t)= F\times C_v(t)$, Eq. [2.2] can also be written as

$$\frac{dC_t(t)}{dt}=\frac{F}{W}[C_a(t)-C_v(t)]=f[C_a(t)-C_v(t)] \qquad [2.3]$$

where $C_t(t)$ is the tracer concentration (in grams per gram of brain tissue) in brain tissue (including its own blood) at time t, $C_a(t)$ and $C_v(t)$ are the tracer concentrations in the arterial and venous blood (in grams per milliliter of blood) at time t, respectively. W is the weight (in grams) of the brain, F is the flow rate (in $ml\cdot min^{-1}$) and f is the CBF (in $ml\cdot g^{-1}\cdot min^{-1}$).

Providing that f remains constant during the period of observation, integrating Eq. [2.3] and solving for f gives

$$f=\frac{C_t(t_2)-C_t(t_1)}{\int_{t_1}^{t_2}[C_a(t)-C_v(t)]dt} \qquad [2.4]$$

where t_1 and t_2 are the starting and the end time points of observation.

Two different strategies based on Eq. [2.4] can be used to measure global CBF.

1) Saturation Method: In this method, tracer is administered with no pre-existing presence in either the brain or the blood. During the period of time (T) in which the tracer is administered, both the arterial and venous blood are sampled regularly for analysis. The tracer concentration in the brain tissue is measured at the end of tracer administration. Under such circumstance, Eq. [2.4] can be written as

$$f = \frac{C_t(T)}{\int_0^T [C_a(t) - C_v(t)]dt} \quad . \qquad [2.5]$$

If T is kept long enough (usually 10 minutes), an equilibrium will be reached between brain tissue and venous blood so that $C_t(T)$ is given by

$$C_t(T) = \lambda C_v(T) \qquad [2.6]$$

where λ is the brain:blood partition coefficient of the tracer and can be determined separately. Substituting Eq. [2.6] into Eq. [2.5] gives

$$f = \frac{1}{\lambda} \times \frac{C_v(T)}{\int_0^T [C_a(t) - C_v(t)]dt} . \qquad [2.7]$$

Using nitrous oxide (N_2O) gas as a tracer, Kety and Schmidt determined global CBF in humans with Eq. [2.7] (1,2). Based on the same principle, Lassen et al later employed krypton-85 (^{85}Kr) as a tracer and measured global CBF in humans (3).

2) Desaturation Method: In this method, the brain tissue is first saturated with the tracer using a long period of inhalation or infusion before the actual CBF measurements. Then the inhalation or infusion is stopped and the desaturation process of the tracer from brain tissue is monitored by continuously recording the tracer concentration in both the arterial and venous blood. In this case, an equilibrium between brain tissue and venous blood is maintained throughout the entire desaturation process and Eq. [2.4] can be written as

$$f = \frac{\lambda[C_v(t_2) - C_v(t_1)]}{\int_{t_1}^{t_2} [C_a(t) - C_v(t)]dt} \quad . \qquad [2.8]$$

Equation [2.8] was first used by McHenry to measure global CBF in humans (4,5). Compared with the original saturation method, the desaturation method has higher sensitivity and is less sensitive to technical errors such as a leaky mask when the tracer is administered by inhalation.

Both the saturation and desaturation methods measure mean CBF over the entire brain or a large portion of the brain, depending on where the venous blood is sampled. Normally, these methods determine CBF in the part of brain tissue which delivers blood to the sampling vein. As pointed out by Kety and Schmidt, almost any substance that passes through the blood-brain-barrier (BBB) with sufficient speed can be used as the tracer in these methods and it is not required that the tracer be freely-diffusible (2). However, the tracer used in these methods must not be absorbed by either the brain tissue or the cerebrospinal fluid (CSF), otherwise a systematic error will be introduced. Difficulties with the saturation and desaturation methods also include their requirement for intensive surgical preparation (i.e. catheterizing major arteries and veins) and their susceptibility to systematic error induced by contamination of venous blood sample with extracerebral blood.

Kety and Schmidt's Theory to Measure Regional Cerebral Blood Flow

Equation [2.3] can be extended to measure regional CBF (rCBF) (6,7),

$$\frac{dC_{t,r}(t)}{dt} = f_r[C_a(t) - C_{v,r}(t)] \qquad [2.9]$$

where the variables with the subscript r refer to their regional values.

Because regional venous blood samples are usually not readily obtained, Eq. [2.9] can not be integrated directly as is done for Eq. [2.3]. However, if the tracer used is freely diffusible, or in other words, an equilibrium between brain tissue and venous blood is reached instantaneously, Eq. [2.10] holds.

$$C_{v,r}(t) = \frac{1}{\lambda_r} C_{t,r}(t) \qquad [2.10]$$

Substituting Eq. [2.10] into Eq. [2.9] and solving for $C_{t,r}(t)$ gives

$$C_{t,r}(T) = f_r \times \int_0^T C_a(t) \times \exp\left[-\frac{f_r}{\lambda_r}(T-t)\right] dt . \qquad [2.11]$$

Equation [2.9] can also be solved for the special case when the initial (t=0) tissue concentration of the tracer is $C_{t,r}(0)$ and the arterial concentration of the tracer is zero ($C_a(t) \equiv 0$), giving

$$C_{t,r}(t) = C_{t,r}(0) \times \exp[-\frac{f_r}{\lambda_r} t] \ . \qquad [2.12]$$

Equations [2.11] and [2.12] represent two different strategies to determine rCBF. With the first strategy, rCBF can be derived by solving Eq. [2.11] numerically, provided the regional tracer concentration in the tissue at a given moment following the onset of the tracer administration $C_{t,r}(T)$, the history of the arterial concentration of the tracer $C_a(t)$, and the regional brain:blood partition coefficient λ_r of the tracer are known. In most cases, a global value of λ for the entire brain, instead of λ_r, is used to calculate rCBF values due to the technical difficulties in measuring λ_r. In fact, Eq. [2.11] is the

theoretical basis for many commonly used rCBF measuring methods, such as autoradiography and almost all the tomographic methods including single photon emission tomography (SPECT), x-ray computed tomography (CT) and positron emission tomography (PET). In some cases, Eq. [2.12] provides a simpler way to calculate rCBF since it requires repeated measurements of the tracer concentrations in the brain tissue only and no blood sampling is necessary. Equation [2.12] predicts that, if $C_a \equiv 0$, the regional tracer concentration in the brain tissue decreases exponentially with time, and the rate constant of such a decrease is directly proportional to rCBF. In order to use this method, C_a must equal zero during the entire course of measurement. In practice this requirement is met by introducing the tracer in a bolus so that C_a of the tracer is negligible after its first pass through the brain tissue provided there is no significant recirculation. This method was first introduced by Lassen et al who used ^{85}Kr as the tracer and recorded its concentration changes in the brain tissue using an external gamma detector after a bolus injection (8-10). Following this work, other tracers, including gamma-emitting xenon gas (^{i33}Xe), hydrogen gas (H_2) and deuterium oxide (D_2O), were soon developed to measure rCBF using the same or similar principles.

Hydrogen Clearance Method

Considering the technical difficulties in recording regional ^{85}Kr concentration changes with an external gamma detector, Aukland et al (11) modified Lassen's method to measure blood flow and first reported the hydrogen clearance method in 1964. The hydrogen clearance method measures rCBF using H_2 as the tracer and an intracerebral

platinum electrode as a detector to monitor local H_2 concentration changes in the brain tissue. With this method, H_2 is administered by inhalation or infusion (H_2 saturated saline), followed by continuously monitoring its desaturation from the brain tissue (12-14). Because the clearance rate of H_2 through the lungs is high, the arterial concentration of H_2 is negligible so that Eq. [2.12] can be used to calculate CBF values in this method. The hydrogen clearance method measures rCBF at the site where the platinum electrode is implanted. If the brain region of interest is homogeneous with only one compartment, Eq. [2.12] can be used directly to derive rCBF in that region. However, if multiple compartments with different flow rates exist, the clearance curve of hydrogen gas from the region will not be single exponential. In this case, a compartment analysis based on Eq. [2.12] is needed to obtain flow rates from different cerebral compartments (8-10). The hydrogen clearance method allows quantitative and repeated rCBF measurements with relatively simple technical procedures. However, it requires brain penetration to implant the hydrogen electrode(s) and it does not allow simultaneous measurements of rCBF in multiple brain regions unless multiple electrodes are used.

Similar to the hydrogen clearance method, the helium (He) clearance method measures the desaturation process of helium gas from the brain tissue using mass spectrometry (15). Although such a method permits simultaneous monitoring of oxygen and carbon dioxide tensions at the site of CBF measurement, it is not as popular as the hydrogen clearance method because of its technical complexity.

Autoradiography

The technique of autoradiography was first developed by Landau et al in 1955 to measure rCBF in cats, using an inert radioactive gas tracer ^{131}I-labeled trifluoroiodomethane ([^{131}I]CF_3I) (16). Because of the long half-life of the isotope ^{131}I and the technical inconvenience in performing autoradiographic procedures for detecting gas tracers, the use of [^{131}I]CF_3I in autoradiography was soon abandoned and better tracers were sought (17-20). The most successful tracer so far is [^{14}C]iodoantipyrine which is injectable and diffuses nearly freely through the BBB (18). With this method, [^{14}C]iodoantipyrine is infused intravenously. Simultaneously, the arterial blood is sampled with a high temporal resolution in order to record $C_a(t)$ dynamically. Toward the end of the infusion (time point T), the animal is decapitated and the brain is rapidly removed and sliced, followed by a quantitative autoradiographic assay to determine the regional radioactivity. For the autoradiographic assay, brain slices together with a set of calibrated reference standards are exposed to an x-ray film. Then the exposed film is developed. Using the calibrated standards, a calibration curve relating the optical density of the film to the concentration of the radioactive tracer can be determined for each film by densitometric measurement. From the calibration curve, $C_{t,r}(T)$ can be determined by measuring the optical densities of the film in the regions representing various brain structures. With known $C_a(t)$ and $C_{t,r}(T)$, rCBF values can then be obtained by solving Eq. [2.11].

Among the existing methods to measure rCBF, the autoradiography method provides the highest spatial resolution. With this method, rCBF can be measured accurately in an anatomical structure with a size as small as a fraction of 1 mm^3 (21). Provided that the tracer concentrations are determined accurately, CBF values obtained from this method are accurate and reliable, and autoradiography has been widely accepted as the "gold standard" in measuring rCBF in animal experiments. One major disadvantage of autoradiography is that it requires sacrifice of the animal so that CBF can only be measured once on an animal.

Radioactive Microsphere Method

The method of using radioactive microspheres to measure organ blood flow was developed in the 1960s and has been used as a common technique to measure rCBF in experimental animals (22). In this method, radionuclide-labeled microspheres are injected directly into the heart (usually left atrium) or into a major artery supplying the tissue of interest. Upon injection, the microspheres distribute evenly in the blood and are carried by the blood to perfuse the tissue of interest. The size of the microspheres is carefully chosen (usually 15 μm diameter) so that they are trapped in the microvasculature (small arterioles and capillaries) of the tissue during their first pass (22,23). By assuming complete mixing of the microspheres and the blood, the number of the microspheres trapped in the tissue of interest is proportional to the blood flow through it. In case of the brain, CBF can be calculated using a indicator fractionation principle (22) which can be expressed mathematically by either Eq. [2.13] or Eq. [2.14],

$$f_r = \frac{F_r}{W} = \frac{1}{W} \times \frac{CO \times N_r}{N_{total}} \quad [2.13]$$

$$f_r = \frac{F_r}{W} = \frac{1}{W} \times \frac{F_{ref} \times N_r}{N_{ref}} \quad [2.14]$$

where f_r, F_r and W have their usual meanings, CO is the cardiac output in $ml \cdot min^{-1}$, F_{ref} is the flow rate in $ml \cdot min^{-1}$ of a reference "organ", N_r is the number of microspheres detected in a given brain region, N_{total} is the total number of microspheres injected and N_{ref} is the number of microspheres detected in the reference "organ". The number of the microspheres is usually counted by analyzing the radioactivity of the tissue/blood samples.

Using Eq. [2.13] to calculate blood flow requires independent measurement of the cardiac output and therefore it is difficult to implement in practice. Currently, methods based on Eq. [2.14] are the most commonly used. To be able to use Eq. [2.14] to calculate f_r, a reference "organ" with known blood flow is required, as is usually produced artificially by withdrawing blood from a catheterized artery into a syringe with a fixed withdrawal rate (24). The withdrawal procedure is conducted simultaneously with the injection and lasts for 1-5 minutes until all the microspheres have been cleared from the circulation.

Because the microspheres are non-metabolizable, a "frozen" picture of rCBF at the instant of injection is recorded permanently upon the entrapment of microspheres in the microvasculature. This feature makes the radioactive microsphere method extremely useful under some circumstances. Because the picture of blood flow is "frozen", it is not necessary to sacrifice the animal immediately after the injection in order to retrieve the

blood flow data. Instead, this can be done several days or even months later. Injection of microspheres labeled with different radio-nuclides allows rCBF to be measured repeatedly at sequential time points in the same animal as long as the total number of microspheres injected does not exceed a limit, below which partial occlusion of the microvasculature by injected microspheres will not disturb the normal hemodynamics and the normal physiological state of the brain tissue (24,25). There are two major limitations with the radioactive microsphere method. First, like autoradiography, it is invasive and requires sacrifice of the animal at the end of the experiments in order to count the number of the microspheres trapped in the brain tissue. Second, under certain circumstances, it requires the insertion of an intracardiac catheter to inject microspheres, an invasive procedure which can potentially cause significant disturbance in the systematic hemodynamics and affect rCBF measurements.

Laser-Doppler Flowmetry

Laser-Doppler flowmetry (LDF) was introduced by Stern in 1975 to measure microcirculatory blood flow (26), and has been constantly refined and used extensively to monitor blood flow in various organs. The principles of LDF to measure blood flow are based on the well-known Doppler effect. When a sound wave with a given frequency is reflected back by a moving object, a frequency shift for the reflected wave relative to the incidental frequency results and the size of the frequency shift (Doppler frequency) depends on the velocity of the moving object. When an infrared laser beam illuminates a small volume of biological tissue, the backscattered light consists of light with the

incident frequency which has been scattered by stationary tissue and Doppler-frequency-shifted light which has been scattered by moving red blood cells. The frequency shift for the latter depends on the relative velocity of the moving red blood cells and the stationary tissue. The intensity of the frequency-shifted light is related to the total number of the red blood cells in the region of interest. At a photomultiplier detector, the unshifted light and frequency-shifted light interfere with each other and produce an interference pattern (i.e. Doppler spectrum), from which a flow-related parameter called the Doppler flow index (F) can be derived

$$F = \sqrt{\int_0^\infty \omega^2 P(\omega) d\omega} \qquad [2.15]$$

where ω is the Doppler frequency and $P(\omega)$ is the power spectrum of the Doppler signals as a function of the Doppler frequency. F is commonly used as an indirect measurement for blood flow. However, with certain calibration factors, it can potentially be converted into absolute blood flow values in traditional units (i.e. $ml \cdot g^{-1} \cdot min^{-1}$) (27-29).

LDF allows instantaneous, continuous and noninvasive (to the target tissue itself) blood flow measurements (30). LDF is easy to use and has a much lower cost than any of the tomography methods. There are also some disadvantages associated with this method. First, the capability of LDF to measure absolute blood flow has not been demonstrated adequately. Second, when it is applied to measure CBF, a craniotomy is required in order to place the Laser-Doppler probe in proximity to the brain so that the method becomes invasive. Finally, a Laser-Doppler probe can only measure microcirculatory blood flow from one region of interest with a volume of approximately 1 mm^3 so that simultaneous

regional measurements by LDF are not possible unless multiple probes (and multiple craniotomies) are used (21).

Tomographic Methods to Measure Regional CBF

Since the introduction of autoradiography to measure rCBF, much effort has been made to develop noninvasive forms of this method so that they can be used on humans. In the last two decades, such effort has paid off. With technical advances made in modern tomography such as positron emission tomography (PET), single photon emission computed tomography (SPECT), x-ray computed tomography (CT), and magnetic resonance imaging (MRI), noninvasive methods to measure rCBF have now become available and are widely used clinically and in research. In this section, PET, SPECT and CT methods to measure rCBF are discussed. rCBF measurements with MRI will be discussed separately.

PET

The technique of PET was developed in the mid 1970s and its clinical utilization did not begin until the late 1980s (31). With PET, positron emitting isotopes are chemically integrated into radiopharmaceuticals which serve as tracers. The commonly used positron emitting isotopes include oxygen-15 (^{15}O), carbon-11 (^{11}C), nitrogen-13 (^{13}N), fluorine-18 (^{18}F) and rubidium-82 (^{82}Rb). For CBF measurement, the most popular PET tracers

are $C^{15}O_2$ (32,33), $^{15}O_2$ (33-35), $H_2{}^{15}O$ (36-40) and [^{11}C]-butanol (38). Although different tracers are used, all PET methods for rCBF measurement share similar technical procedures. To measure rCBF, injectable tracers are administered by intravenous bolus injection or continuous infusion and gaseous tracers are administered by either a single or continuous inhalation. This is followed by measuring regional radioactivity of the tracers in the brain and the arterial input functions, which together can be used to derive rCBF values using kinetic models developed specifically for the particular method used. For example, in 1983, Herscovitch and Raichle proposed the use of $H_2{}^{15}O$ as a tracer to measure rCBF with PET (36,37). In their method, a bolus of $H_2{}^{15}O$ was injected intravenously, followed by acquisition of a PET scan and the arterial input function. With this method, it may appear that, as with autoradiography, rCBF values can be calculated by solving Eq. [2.11] numerically. However, it was pointed out by the authors that, unlike autoradiography, PET does not have enough temporal resolution to measure regional tissue concentrations (radioactivity) of the tracer instantaneously so that accurate determination of $C_{t,r}(T)$ in Eq. [2.11] is difficult. To solve this problem, Herscovitch and Raichle derived Eq. [2.16] to calculate rCBF (36),

$$C_{t,r} = m f_r \times \int_{T_s}^{T_e} \int_0^T C_a(t) \times \exp\left[-\left(\frac{m f_r}{\lambda} + \alpha\right)(T - t)\right] dt \qquad [2.16]$$

where T is the time period during which the tracer is administered, T_s and T_e are the starting and the end time points of the PET scan, $C_{t,r}$ is the regional tissue concentration (radioactivity) of the tracer recorded by the PET scan during the time period from T_s to T_e, m is a constant between 0 and 1 that denotes the extent to which diffusion equilibrium is achieved between blood and brain tissue during passage of the tracer from the arterial end to the venous end of the capillaries, and α is the physical decay constant of the tracer.

Because of the short half lives of the positron emitting isotopes (ranging from seconds to minutes), PET allows repeated measurements of rCBF. With different tracers, PET is capable of mapping regional CBF, cerebral blood volume (CBV), oxygen extraction fraction (OEF), $CMRO_2$ and CMR_{glu} simultaneously with absolute quantification and high accuracy, making it currently the most powerful tool in studying cerebral function (41-43). The main limitation of using PET to study cerebral function is the high monetary cost of both the instrument and the tracers, and consequently its limited accessibility.

SPECT

SPECT emerged during the 1950s and 1960s and was soon applied to study cerebral function (31). The usefulness of SPECT for measurement and tomographic imaging of CBF was first explored by Lassen et al in the late 1970s (44). To measure CBF, SPECT uses tracers which are labeled with isotopes that emit single photon radiation, most typically in the form of gamma rays. Isotopes commonly used for SPECT CBF measurements include xenon-133 (^{133}Xe), iodine-123 (^{123}I) and technetium-99m (^{99m}Tc).

Using ^{133}Xe gas as the tracer, SPECT can be used to measure rCBF quantitatively (45,46). In this method, ^{133}Xe is administered by 1.0-1.5 minutes of inhalation. During the inhalation as well as for several minutes following the inhalation, SPECT scans are repeated at short time intervals (usually 1 minute). Simultaneously, the arterial input function of ^{133}Xe is estimated from the end-tidal ^{133}Xe concentrations in the lung, which

are recorded continuously using a collimated NaI detector. Using an algorithm developed by Celsis et al (47), which is simply a modification of Eq. [2.11], quantitative CBF images can be calculated from the raw SPECT images and the arterial input function. ^{133}Xe SPECT can be used in the same subject repeatedly because of the short retention time of ^{133}Xe gas in the body (usually 10-15 minutes). This, on the other hand, restricts the time available for SPECT scans so that the spatial resolution of this method is often limited compared to that seen in SPECT using ^{123}I or ^{99m}Tc labeled tracers (see below). The clinical use of ^{133}Xe SPECT to measure rCBF is limited except that it is sometimes used as a standard to calibrate qualitative SPECT methods to measure rCBF (48,49).

^{99m}Tc and ^{123}I labeled tracers are usually large lipophilic chelates such as ^{99m}Tc labeled hexamethylpropyleneamine oxime (HMPAO) (50-52) or ethyl cysteinate dimer (ECD) (53,54) and [^{123}I]iodoamphetamine (IMP) (55-56). Upon administration, such tracers pass through the BBB and are rapidly converted to their hydrophilic forms in brain tissue. The hydrophilic forms of the tracers become trapped inside the brain with a retention time up to 24 hours, thus forming a "frozen picture" of CBF before and just after the injection. Technically, such tracers behave like the radioactive microspheres discussed before and are usually referred as "chemical microspheres". Due to the complicated tracer kinetics, absolute quantification of rCBF with this method is difficult. Instead, perfusion indexes are used for flow assessment, and relative rCBF is usually measured using Lassen's algorithm (57),

$$\frac{F}{F_{ref}} = 100 \times \frac{\alpha_{ref} \times N/N_{ref}}{1 + \alpha_{ref} - N/N_{ref}} \qquad [2.17]$$

where F, F_{ref}, N, N_{ref}, and α_{ref} are rCBF, reference CBF, regional SPECT count, reference SPECT count and conversion/clearance ratio of the tracer in the reference region, respectively. CBF in the cerebellum or an averaged CBF value over the entire brain is usually used as a reference in this method. If absolute quantification of rCBF is desired, F_{ref}, and α_{ref} have to be determined independently.

Because the CBF pictures are "frozen", the time available for SPECT scans is not limited so that CBF images can be obtained with high spatial resolution and signal-to-noise ratio (SNR) with this method. However, also owing to the long retention time of the tracers, this method does not allow repeated rCBF measurements. ^{123}I labeled tracers were among the first used tracers in SPECT to measure rCBF. These have been replaced by ^{99m}Tc labeled tracers due to the long half time of ^{123}I and therefore the high radiation dose delivered to patients. In spite of its shortcomings such as chemical instability and slow blood clearance, ^{99m}Tc-HMPAO has been one of the most widely used tracers for measuring rCBF with SPECT. Recently, a new ^{99m}Tc labeled SPECT tracer, ^{99m}Tc-ECD, was developed for rCBF measurement. ^{99m}Tc-ECD is chemically stable and has higher blood clearance rate than ^{99m}Tc-HMPAO and the potential to measure rCBF quantitatively (52,53,58). The most attractive feature of using SPECT to measure rCBF is its high performance/cost ratio. Although being less quantifiable and of lower spatial resolution than PET, SPECT provides estimates of relative rCBF and rCBV with much less cost in both the instrument and the tracers. The reason that SPECT tracers are cheaper than PET tracers is because isotopes used in SPECT (^{99m}Tc and ^{123}I) usually have long half times and do not require on-site production.

CT

Xenon-enhanced CT was first used by Drayer et al to measure rCBF in 1978 (59). With technical advances made in the last two decades, this method has become one of the most commonly used methods to measure rCBF clinically. Unlike SPECT, in which the gamma-emitting isotope of xenon, $^{133}_{54}Xe$, is used, xenon enhanced CT uses the stable isotope $^{132}_{54}Xe$. Xenon is a freely-diffusible tracer and highly lipid soluble. Xenon is also a CT contrast enhancement agent whose use in CT was first suggested by Foley et al (60). When an x-ray beam passes through the body, its intensity is attenuated by an amount that is dependent on the characteristics of the tissue in its path. When xenon is present, the attenuation increases in proportion to the concentration of xenon in the tissue, providing a theoretical basis to measure tissue Xe concentrations by CT.

To measure rCBF, xenon gas (usually 33%) is administered by inhalation, usually for a duration of 4.5 minutes in clinics (61). During and after inhalation, the kinetics of xenon build-up/clearance in the tissue are measured by dynamic CT scans. Simultaneously, the arterial input function of xenon is recorded by measuring the time course of end-tidal xenon concentration in the expired gas with a thermoconductivity analyzer. With an algorithm modified from Eq. [2.11], rCBF values can then be derived from the CT images and the arterial input function.

Stable xenon-enhanced CT measures rCBF with full quantification and high spatial resolution coupled to anatomical CT images. Because of the rapid clearance of xenon

from the body (15-20 minutes), this method can be used repeatedly, allowing dynamic observation of rCBF. With most methods of measuring rCBF, direct determination of the regional brain:blood partition coefficient (λ_r) is difficult so that a global value of λ is usually assumed to calculate rCBF. By making such an assumption, significant calculation errors may be introduced, especially in physiologically perturbed brain tissue in which λ will most likely be different from that in normal tissue. With stable xenon-enhanced CT, λ_r can actually be measured directly with simultaneous measurements of xenon concentrations in tissue and blood so that there is no need to assume a global λ value and therefore no error will be introduced (62). The major concerns about the Xe-enhanced CT method are the high radiation dose from the CT scanner and the pharmacologic effect of xenon gas itself (61). Xe gas affects sensorium in many individuals and may cause agitation. When used at high concentrations (>71%), xenon induces anesthesia, affecting baseline CBF, and may cause apnea in some cases (61).

MR Methods Using Freely Diffusible Tracers

Being non-invasive, both magnetic resonance imaging (MRI) and spectroscopy (MRS) have been employed to measure global and regional CBF using freely diffusible MR sensitive tracers, such as deuterium oxide (D_2O), oxygen-17 gas ($^{17}O_2$), oxygen-17 water ($H_2{}^{17}O$), and fluorine-19 (^{19}F) based compounds (i.e. halothane, Freon-22 and Freon-23) (63,64). As with other CBF measuring methods, the MR methods also involve three steps, namely tracer administration, tracer detection and kinetics modeling.

Administration of D_2O, $^{17}O_2$ or $H_2{}^{17}O$ is usually done in bolus by either inhalation or injection while ^{19}F based tracers are usually introduced by prolonged inhalation. After tracer administration, MRS or MRI is used to monitor the build-up/clearance of tracer in the brain tissue, simultaneously with the sampling of the arterial input functions. Depending on the MR techniques used for tracer detection, either global or regional CBF can be measured. With non-localized MRS, global CBF is measured. With localized MRS or MRI, rCBF is obtained. The kinetic models used to calculate CBF differ from tracer to tracer, depending on the properties of the tracer itself and how it is administered. For example, when Freon-23 is used as the tracer, the kinetics of its clearance from saturated brain tissue after a long period of inhalation is typically observed and a mathematical model analogous to Eq. [2.11] is used to calculate CBF values (65-67). However, when D_2O is used as the tracer, it is usually administered by bolus injection and its first pass through the brain tissue is observed (68-71), as is done in the hydrogen clearance method. However, unlike hydrogen gas, the retention time of D_2O in the blood is long and significant recirculation occurs so that the requirement of $C_a(t)\equiv 0$ is not valid and Eq. [2.12] can not be used directly to calculate CBF. To solve this problem, Kim et al (72) developed an algorithm specifically for D_2O based on a two-compartments in series model.

The MR methods using freely diffusible MR sensitive tracers provide a way to measure global and regional CBF non-invasively and without hazardous radiation. However, two limitations exist. First, CBF measurements with these methods can potentially be complicated by the pharmacologic effects of some of the tracers used (i.e. D_2O and

halothane). Second, the spatial resolution with which CBF can be measured in these methods is generally limited because of the intrinsic insensitivity of MR detection. Besides the exogenous tracers mentioned above, endogenous MR-sensitive tracers such as water can also be used to measure CBF. This will be discussed in detail in the next chapter.

MR Perfusion Imaging Using First Pass Bolus Tracking

As discussed previously, freely diffusible tracers are used in most methods of measuring CBF. Other types of tracers, such as vascular tracers, are also available for CBF measurement. Vascular tracers, as implied by the name, remain in the intravascular space during their passage through the brain as long as the BBB is intact. Kety and Schmidt's theory is inapplicable to vascular tracers. Instead, a tracer dilution principle and a central volume principle must be used for this type of tracer.

Central Volume Principle

In a closed system like the brain, the flow rate of a tracer (F, in $ml \cdot min^{-1}$) can be written

$$F = \frac{V_d}{MTT} \qquad [2.18]$$

where V_d is the volume of the distribution of the tracer, MTT is the mean vascular transit time of the tracer. Equation [2.18], validated by Robertson et al (73), does not require that

the tracer is freely diffusible. Dividing both sides of Eq. [2.18] by the weight of the brain (W) gives

$$f = \frac{F}{W} = \frac{V_d / W}{MTT}. \qquad [2.19]$$

When a vascular tracer passes through the brain, it distributes in the intravascular space only so that V_d equals the total volume of blood in brain (V_b) and

$$\frac{V_d}{W} = \frac{V_b}{W} = CBV \qquad [2.20]$$

where CBV is the cerebral blood volume which defines the volume of blood per unit weight of brain tissue. Combining Eqs. [2.19] and [2.20] gives

$$f = \frac{CBV}{MTT}. \qquad [2.21]$$

Tracer Dilution Principle

For a tracer that passes through the brain, CBV can be calculated from the integrated tracer concentration-time courses (74):

$$CBV = \frac{\int_0^\infty C_t(t)dt}{\int_0^\infty C_b(t)dt}. \qquad [2.22]$$

Provided there is no recirculation, the tracer dilution principle also states that MTT is the ratio of the first and zeroth moment of the function $C_t(t)$,

$$MTT = \frac{\int_0^\infty tC_t(t)dt}{\int_0^\infty C_t(t)dt}. \qquad [2.23]$$

MR Perfusion Imaging With First Pass Bolus Tracking

Contrast agents for MRI enhance the contrast of MR images, improving their sensitivity in detecting tissue undergoing physiological perturbations. Most MR contrast agents are paramagnetic chelates of lanthanides which contain unpaired electrons, such as Gd-DTPA and Dy-DTPA (gadolinium/dysprosium diethylene triaminepentaacetic acid) (75). Depending on the mechanisms with which they affect MR contrast, contrast agents can be divided into relaxivity contrast agents and susceptibility contrast agents. Relaxivity contrast agents reduce both the transverse relaxation time T2 and the longitudinal relaxation times T1 of the tissue through the dipolar interactions between the unpaired electrons and the proton nuclear spins. Normally, the reduction in T1 is much greater than that in T2. By altering local susceptibility, the presence of susceptibility contrast agents in tissue increases the diversity of local magnetic fields and decreases $T2^*$ of the tissue. For both relaxivity and susceptibility contrast agents, it has been shown both experimentally (75,76) and theoretically (77,78) that there is an essentially linear relationship between the concentration of the contrast agent in tissue and the change in the relaxation rate, so that

$$\Delta R1 = \Delta\frac{1}{T1} = \left(\frac{1}{T1_{pre}} - \frac{1}{T1_{post}}\right) = k_1 \times C_{rc} \qquad [2.24]$$

$$\Delta R2^* = \Delta\frac{1}{T2^*} = \left(\frac{1}{T2^*_{pre}} - \frac{1}{T2^*_{post}}\right) = k_2 \times C_{sc} \qquad [2.25]$$

where R1 and $R2^*$ are the relaxation rates corresponding to T1 and $T2^*$, $T1_{pre}$ and $T1_{post}$ are the T1 values before and after the injection of relaxivity contrast agent, $T2^*_{pre}$ and

$T2^*_{post}$ are the $T2^*$ values before and after the injection of susceptibility contrast agent, C_{rc} and C_{sc} are the concentrations of the relaxivity and susceptibility contrast agents in the tissue, and k_1 and k_2 are proportionality constants.

The BBB is not permeable to commonly-used MR contrast agents such as Gd-DTPA and Dy-DTPA so that they can be used as vascular tracers to measure cerebral hemodynamics (79,80). The use of MR contrast agents to measure CBF was first reported by Belliveau et al in 1990 (81). In Belliveau's experiments, a bolus of susceptibility contrast agent Dy-DTPA was injected into the external jugular vein of canines and the first pass of Dy-DTPA through the brain was monitored dynamically by rapid gradient-echo MR imaging which produced one $T2^*$ weighted image every second. Although remaining in the intravascular space, the presence of Dy-DTPA reduced $T2^*$ of the brain tissue by altering the local susceptibility, and this was manifested as reduced intensities on the $T2^*$ weighted images. Using Eq. [2.25], the regional tissue concentration of Dy-DTPA at a given moment t after injection can be written as

$$C_{t,r}(t) = \frac{1}{TE \times k} \ln \frac{S_r(t)}{S_{0,r}} \qquad [2.26]$$

where TE is the echo time of the imaging sequence used, $S_r(t)$ is the regional intensity of the $T2^*$ weighted image at time t after Dy-DTPA injection, $S_{0,r}$ is the regional intensity of the $T2^*$ weighted image before Dy-DTPA injection and k is a proportionality constant which depends on the properties of the brain tissue, the imaging sequence used and the field strength at which the experiments are carried out.

By combining Eqs. [2.22] and [2.26], regional CBV (rCBV) can be calculated as

$$\mathrm{rCBV} = \frac{1}{\mathrm{TE} \times k} \frac{\int_0^\infty \ln[S_r(t)/S_{0,r}]dt}{\int_0^\infty C_b(t)dt}. \qquad [2.27]$$

When regional values are measured, the integrated blood tracer concentration $C_b(t)$ can be lumped together with TE and k into a lumped constant K so that

$$\mathrm{rCBV} = K \int_0^\infty \ln\left[\frac{S_r(t)}{S_{0,r}}\right] dt \qquad [2.28]$$

where,

$$K = \frac{1}{\mathrm{TE} \times k \times \int_0^\infty C_b(t)dt}.$$

In analogy to Eq. [2.27], the regional mean vascular transit time (rMTT) can be written

$$\mathrm{rMTT} = \frac{\int_0^\infty t \times \ln[S_r(t)/S_{0,r}]dt}{\int_0^\infty \ln[S_r(t)/S_{0,r}]dt}. \qquad [2.29]$$

By combining Eqs. [2.21], [2.27] and [2.29], rCBF can be expressed as

$$f_r = K \frac{\left[\int_0^\infty \ln[S_r(t)/S_{0,r}]dt\right]^2}{\int_0^\infty t \times \ln[S_r(t)/S_{0,r}]dt}. \qquad [2.30]$$

Equation [2.30] forms the theoretical basis to calculate CBF with the first pass bolus tracking method. For quantification of rCBF and rCBV, the proportionality constant K must be known. Otherwise the first pass bolus tracking method provides only relative rCBF and rCBV values. In principle, K can be determined either for each measurement, which would not be feasible to achieve, or by correlating data obtained from this method

to other independent measurements to provide semi-quantitative results (79,81). Recently, progress has been made in obtaining truly quantitative rCBF and rCBV values with this method (82).

The first pass bolus tracking method allows rCBF and rCBV to be measured simultaneously (79,80). Despite the fact that it only provides semi-quantitative data, it is to date the most widely used MR method of measuring cerebral hemodynamics. Technically, the method is very easy to implement, to use and to standardize, which partially contributes to its popularity. The speed of MR imaging determines the SNR and the spatial resolution of the CBF measurements with this method. Currently, first pass bolus tracking experiments are often done using echo-planar-imaging (EPI), with which $T2^*$ weighted images can be acquired within 100 ms. The time resolution of CBF measurements using first pass bolus tracking is limited by the slow clearance rate of MR contrast agents from the body (i.e. about 30-60 min for Gd-DPTA) so that it is not possible to monitor dynamic CBF/CBV changes with this method.

References

1. S. S. Kety and C. F. Schmidt, The determination of cerebral blood flow in man by the use of nitrous oxide in low concentrations, *Am. J. Physiol.* **143**, 53, (1945).

2. S. S. Kety and C. F. Schmidt, The nitrous oxide method for the quantitative determination of cerebral blood flow in man: theory, procedure and normal values, *J. Clin. Invest.* **27**, 478, (1948).

3. N. A. Lassen and O. Munck, The cerebral blood flow in man determined by the use of radioactive krypton, *Acta Physiol. Scand.* **33**, 30, (1955).

4. L. C. McHenry Jr., Determination of cerebral blood flow by a krypton-85 desaturation method, *Nature* **200**, 1297, (1963).

5. L. C. McHenry Jr., Quantitative cerebral blood flow determination: application of a krypton-85 desaturation technique in man, *Neurology* **14**, 785, (1964).

6. S. S. Kety, Theory and applications of exchange of inert gas at lungs and tissue, *Pharmacol. Rev.* **3**, 1, (1951).

7. S. S. Kety (H. D. Bruner Ed). Methods in Medical Research, The Year Book Publishers Inc., Chicago, 1960; Chapter I, Blood-tissue exchange methods. Theory of blood-tissue exchange and its application to measurement of blood flow. p. 223-227.

8. D. H. Ingvar and N. A. Lassen, Regional blood flow of the cerebral cortex determined by Krypton^{85}, *Acta Physiol. Scand.* **54**, 325, (1962).

9. N. A. Lassen, K. Hoedt-Rasmussen, S. C. Sorensen, E. Skinhoj, S. Cronquist, B. Bodforss and D. H. Ingvar, Regional cerebral blood flow in man determined by radioactive Krypton^{85}, *Neurology (Minneap.)* **13**, 719, (1963).

10. N. A. Lassen and D. H. Ingvar, Blood flow of the cerebral cortex determined by radioactive krypton^{85}, *Experientia (Basel)* **17**, 42, (1961).

11. K. Aukland, B. Bower and R. Berliner, Measurement of local blood flow with hydrogen gas, *Circ. Res.* **14**, 164, (1964).

12. R. B. Morawetz, U. DeGirolami, R. G. Ojemann, F. W. Marcoux and R. M. Crowell, Cerebral blood flow determined by hydrogen clearance during middle cerebral artery occlusion in unanesthetized monkeys, *Stroke* **9**, 143, (1978).

13. E. Pasztor, L. Symon, N. W. Dorsch and N. M. Branston, The hydrogen clearance method in assessment of blood flow in cortex, white matter and deep nuclei of baboons, *Stroke* **4**, 556, (1973).

14. J. L. Haining, M. D. Turner and R. M. Pantall, Measurement of local cerebral blood flow in the unanesthetized rat using a hydrogen clearance method, *Circ. Res.* **23**, 313, (1968).

15. J. Seylaz, E. Pinard, P. Meric and J. L. Correze, Local cerebral PO_2, PCO_2, and blood flow measurements by mass spectrometry, *Am. J. Physiol.* **245**, H513, (1983).

16. W. M. Landau, W. H. Freygang Jr. , L. P. Rowland, L. Sokoloff and S. S. Kety, The local circulation of the living brain: values in the unanesthetized and anesthetized cat, *Trans. Amer. Neurol. Assoc.* **80**, 125, (1955).

17. M. Reivich, J. Jehle, L. Sokoloff and S. S. Kety, Measurement of regional cerebral blood flow with antipyrine-^{14}C in awake cats, *J. Appl. Physiol.* **27**, 296, (1969).

18. O. Sakurada, C. Kennedy, J. Jehle, J. D. Brown, G. L. Carbin and L. Sokoloff, Measurement of local cerebral blood flow with iodo [^{14}C] antipyrine, *Am. J. Physiol.* **234**, H59, (1978).

19. J. R. Rapin, M. Le-Poncin-Lafitte, D. Duterte, R. Rips, E. Morier and N. A. Lassen, Iodoamphetamine as a new tracer for local cerebral blood flow in the rat: comparison with isopropyliodoamphetamine, *J. Cereb. Blood Flow Metab.* **4**, 270, (1984).

20. T. M. Jay, G. Lucignani, A. M. Crane, J. Jehle and L. Sokoloff, Measurement of local cerebral blood flow with [^{14}C]iodoantipyrine in the mouse, *J. Cereb. Blood Flow Metab.* **8**, 121, (1988).

21. C. Iadecola (K. M. A. Welch, L. R. Caplan, D. J. Reis, B. K. Siesjo and B. Weir, Eds). Primer on cerebrovascular diseases, Academic Press, London, 1997; Chapter 9, Principle and methods for measurement of cerebral blood flow: experimental methods. p. 34-37.

22. M. A. Heymann, B. D. Payne, J. I. Hoffman and A. M. Rudolph, Blood flow measurements with radionuclide-labeled particles, *Prog. Cardiovasc. Dis.* **20**, 55, (1977).

23. M. L. Marcus, D. D. Heistad, J. C. Ehrhardt and F. M. Abboud, Total and regional cerebral blood flow measurement with 7-, 10-, 15-, 25-, and 50-mum microspheres, *J. Appl. Physiol.* **40**, 501, (1976).

24. K. A. Stanek, T. L. Smith, W. R. Murphy and T. G. Coleman, Hemodynamic disturbances in the rat as a function of the number of microspheres injected, *Am. J. Physiol.* **245**, H920, (1983).

25. M. Nakai, K. Tamaki, J. Yamamoto, A. Shimouchi and M. Maeda, A minimally invasive technique for multiple measurement of regional blood flow of the rat brain using radiolabeled microspheres, *Brain Res.* **507**, 168, (1990).

26. M. D. Stern, In vivo evaluation of microcirculation by coherent light scattering, *Nature* **254**, 56, (1975).

27. A. D. Feld, J. D. Fondacaro, G. A. Holloway Jr. and E. D. Jacobson, Measurement of mucosal blood flow in the canine intestine with laser doppler velocimetry, *Life Sci.* **31**, 1509, (1982).

28. I. Rundquist, Q. R. Smith, M. E. Michel, P. Ask, P. A. Oberg and S. I. Rapoport, Sciatic nerve blood flow measured by laser Doppler flowmetry and [14C]iodoantipyrine, *Am. J. Physiol.* **248**, H311, (1985).

29. H. Ahn, J. Lindhagen, G. E. Nilsson, E. G. Salerud, M. Jodal and O. Lundgren, Evaluation of laser Doppler flowmetry in the assessment of intestinal blood flow in cat, *Gastroenterology* **88**, 951, (1985).

30. U. Dirnagl, B. Kaplan, M. Jacewicz and W. Pulsinelli, Continuous measurement of cerebral cortical blood flow by laser-Doppler flowmetry in a rat stroke model, *J. Cereb. Blood Flow Metab.* **9**, 589, (1989).

31. J. Mazziotta, M. Cohen and A. Toga (K. M. A. Welch, L. R. Caplan, D. J. Reis, B. K. Siesjo and B. Weir, Eds). Primer on cerebrovascular diseases, Academic Press, London, 1997; Chapter 10, The measurement of cerebral blood flow and metabolism in human subject. p. 38-41.

32. P. Herscovitch and M. E. Raichle, Effect of tissue heterogeneity on the measurement of cerebral blood flow with the equilibrium $C^{15}O_2$ inhalation technique, *J. Cereb. Blood Flow Metab.* **3**, 407, (1983).

33. R. Subramanyam, N. M. Alpert, B. Hoop, G. L. Brownell and J. M. Taveras, A model for regional cerebral oxygen distribution during continuous inhalation of $^{15}O_2$, $C^{15}O$, and $C^{15}O_2$, *J. Nucl. Med.* **19**, 48, (1978).

34. R. S. Frackowiak, G. L. Lenzi, T. Jones and J. D. Heather, Quantitative measurement of regional cerebral blood flow and oxygen metabolism in man using ^{15}O and positron emission tomography: theory, procedure, and normal values, *J. Comput. Assist. Tomogr.* **4**, 727, (1980).

35. T. O. Videen, J. S. Perlmutter, P. Herscovitch and M. E. Raichle, Brain blood volume, flow, and oxygen utilization measured with ^{15}O radiotracers and positron emission tomography: revised metabolic computations, *J. Cereb. Blood Flow Metab.* **7**, 513, (1987).

36. P. Herscovitch, J. Markham and M. E. Raichle, Brain blood flow measured with intravenous $H_2(^{15})O$. I. Theory and error analysis, *J. Nucl. Med.* **24**, 782, (1983).

37. M. E. Raichle, W. R. Martin, P. Herscovitch, M. A. Mintun and J. Markham, Brain blood flow measured with intravenous $H_2(^{15})O$. II. Implementation and validation, *J. Nucl. Med.* **24**, 790, (1983).

38. P. Herscovitch, M. E. Raichle, M. R. Kilbourn and M. J. Welch, Positron emission tomographic measurement of cerebral blood flow and permeability-surface area product of water using [^{15}O]water and [^{11}C]butanol, *J. Cereb. Blood Flow Metab.* **7**, 527, (1987).

39. P. T. Fox, M. A. Mintun, M. E. Raichle and P. Herscovitch, A noninvasive approach to quantitative functional brain mapping with $H_2(^{15})O$ and positron emission tomography, *J. Cereb. Blood Flow Metab.* **4**, 329, (1984).

40. S. C. Huang, R. E. Carson, E. J. Hoffman, J. Carson, N. MacDonald, J. R. Barrio and M. E. Phelps, Quantitative measurement of local cerebral blood flow in humans by positron computed tomography and ^{15}O-water, *J. Cereb. Blood Flow Metab.* **3**, 141, (1983).

41. G. L. Lenzi, T. Jones and R. S. Frackowiak, Positron emission tomography: state of the art in neurology, *Prog. Nucl. Med.* **7**, 118, (1981).

42. J. C. Baron, R. S. Frackowiak, K. Herholz, T. Jones, A. A. Lammertsma, B. Mazoyer and K. Wienhard, Use of PET methods for measurement of cerebral energy metabolism and hemodynamics in cerebrovascular disease, *J. Cereb. Blood Flow Metab.* **9**, 723, (1989).

43. K. Broich, A. Alavi and M. Kushner, Positron emission tomography in cerebrovascular disorders, *Semin. Nucl. Med.* **22**, 224, (1992).

44. N. A. Lassen, E. Sveinsdottir, I. Kanno, E. M. Stokely and P. Rommer, A fast moving, single photon emission tomography for regional cerebral blood flow studies in man, *J. Comput. Assist. Tomogr.* **2**, 661, (1978).

45. I. Kanno and N. A. Lassen, Two methods for calculating regional cerebral blood flow from emission computed tomography of inert gas concentrations, *J. Comput. Assist. Tomogr.* **3**, 71, (1979).

46. N. A. Lassen, L. Henriksen and O. Paulson, Regional cerebral blood flow in stroke by ^{133}Xenon inhalation and emission tomography, *Stroke* **12**, 284, (1981).

47. P. Celsis, T. Goldman, L. Henriksen and N. A. Lassen, A method for calculating regional cerebral blood flow from emission computed tomography of inert gas concentrations, *J. Comput. Assist. Tomogr.* **5**, 641, (1981)

48. D. Huglo, M. Rousseaux, D. Leys, P. Fialdes and M. Steinling, Regional cerebral blood flow imaging: a quantitative comparison of ^{99m}Tc-bicisate with ^{133}Xe using single photon emission computed tomography, *J. Cereb. Blood Flow Metab.* **14 Suppl 1**, S76, (1994).

49. A. R. Andersen, H. H. Friberg, J. F. Schmidt and S. G. Hasselbalch, Quantitative measurements of cerebral blood flow using SPECT and [99mTc]-d,l-HM-PAO compared to xenon-133, *J. Cereb. Blood Flow Metab.* **8**, S69, (1988).

50. R. D. Neirinckx, L. R. Canning, I. M. Piper, D. P. Nowotnik, R. D. Pickett, R. A. Holmes, W. A. Volkert, A. M. Forster, P. S. Weisner, J. A. Marriott and a. et, Technetium-99m d,l-HM-PAO: a new radiopharmaceutical for SPECT imaging of regional cerebral blood perfusion, *J. Nucl. Med.* **28**, 191, (1987).

51. H. Matsuda, H. Oba, H. Seki, S. Higashi, H. Sumiya, S. Tsuji, H. Terada, K. Imai, K. Shiba, H. Mori and a. et, Determination of flow and rate constants in a kinetic model of [^{99m}Tc]-hexamethyl-propylene amine oxime in the human brain, *J. Cereb. Blood Flow Metab.* **8**, S61, (1988).

52. N. A. Lassen and R. G. Blasberg, Technetium-99m-d,l-HM-PAO, the development of a new class of 99mTc-labeled tracers: an overview, *J. Cereb. Blood Flow Metab.* **8**, S1, (1988).

53. J. Leveille, G. Demonceau, M. De-Roo, P. Rigo, R. Taillefer, R. A. Morgan, D. Kupranick and R. C. Walovitch, Characterization of technetium-99m-L,L-ECD for brain perfusion imaging, Part 2: Biodistribution and brain imaging in humans, *J. Nucl. Med.* **30**, 1902, (1989).

54. J. H. Greenberg and N. A. Lassen, Characterization of ^{99m}Tc-bicisate as an agent for the measurement of cerebral blood flow with SPECT, *J. Cereb. Blood Flow Metab.* **14 Suppl 1**, S1, (1994).

55. H. Matsuda, S. Higashi, S. Tsuji, H. Seki, H. Sumiya, H. Fujii, H. Oba, H. Terada, K. Imai, N. Tonami and a. et, A new noninvasive quantitative assessment of cerebral blood flow using N-isopropyl-(iodine 123)p-iodoamphetamine, *Am. J. Physiol. Imaging* **2**, 49, (1987).

56. G. Takeshita, H. Maeda, K. Nakane, H. Toyama, E. Sakakibara, S. Komai, A. Takeuchi, S. Koga, M. Ono and T. Nakagawa, Quantitative measurement of regional cerebral blood flow using N-isopropyl-(iodine-123)p-iodoamphetamine and single-photon emission computed tomography, *J. Nucl. Med.* **33**, 1741, (1992).

57. N. A. Lassen, A. R. Andersen, L. Friberg and O. B. Paulson, The retention of [^{99m}Tc]-d,l-HM-PAO in the human brain after intracarotid bolus injection: a kinetic analysis, *J. Cereb. Blood Flow Metab.* **8**, S13, (1988).

58. R. Takeuchi, H. Matsuda, Y. Yonekura, H. Sakahara and J. Konishi, Noninvasive quantitative measurements of regional cerebral blood flow using technetium-99m-L,L-ECD SPECT activated with acetazolamide: quantification analysis by equal-

volume-split ^{99m}Tc-ECD consecutive SPECT method, *J. Cereb. Blood Flow Metab.* **17**, 1020, (1997).

59. B. P. Drayer, S. K. Wolfson, O. M. Reinmuth, M. Dujovny, M. Boehnke and E. E. Cook, Xenon enhanced CT for analysis of cerebral integrity, perfusion, and blood flow, *Stroke* **9**, 123, (1978).

60. W. D. Foley, V. M. Haughton, J. Schmidt and C. R. Wilson, Xenon contrast enhancement in computed body tomography, *Radiology* **129**, 219, (1978).

61. H. Yonas, R. P. Pindzola and D. W. Johnson, Xenon/computed tomography cerebral blood flow and its use in clinical management, *Neurosurg. Clin. N. Am.* **7**, 605, (1996).

62. F. Kelcz, S. K. Hilal, P. Hartwell and P. M. Joseph, Computed tomographic measurement of the xenon brain-blood partition coefficient and implications for regional cerebral blood flow: a preliminary report, *Radiology* **127**, 385, (1978).

63. S. G. Kim and J. J. Ackerman, Quantification of regional blood flow by monitoring of exogenous tracer via nuclear magnetic resonance spectroscopy, *Magn. Reson. Med.* **14**, 266, (1990).

64. J. J. Neil, The use of freely diffusible, NMR-detectable tracers for measuring organ perfusion, *Concepts Magn. Reson.* **3**, 1, (1991).

65. J. R. Ewing, C. A. Branch, S. C. Fagan, J. A. Helpern, R. T. Simkins, S. M. Butt and K. M. Welch, Fluorocarbon-23 measure of cat cerebral blood flow by nuclear magnetic resonance, *Stroke* **21**, 100, (1990).

66. D. Barranco, L. N. Sutton, S. Florin, J. Greenberg, T. Sinnwell, L. Ligeti and A. C. McLaughlin, Use of ^{19}F NMR spectroscopy for measurement of cerebral blood flow: a comparative study using microspheres, *J. Cereb. Blood Flow Metab.* **9**, 886, (1989).

67. J. A. Detre, C. J. Eskey and A. P. Koretsky, Measurement of cerebral blood flow in rat brain by ^{19}F-NMR detection of trifluoromethane washout, *Magn. Reson. Med.* **15**, 45, (1990).

68. C. S. Ewy, J. J. Ackerman and R. S. Balaban, Deuterium NMR cerebral imaging in situ, *Magn. Reson. Med.* **8**, 35, (1988).

69. J. A. Detre, V. H. Subramanian, M. D. Mitchell, D. S. Smith, A. Kobayashi, A. Zaman and J. S. Leigh Jr., Measurement of regional cerebral blood flow in cat brain using intracarotid ^2H_2O and ^2H NMR imaging, *Magn. Reson. Med.* **14**, 389, (1990).

70. J. J. Ackerman, C. S. Ewy, N. N. Becker and R. A. Shalwitz, Deuterium nuclear magnetic resonance measurements of blood flow and tissue perfusion employing ^2H_2O as a freely diffusible tracer, *Proc. Natl. Acad. Sci. U. S. A.* **84**, 4099, (1987).

71. J. J. Ackerman, C. S. Ewy, S. G. Kim and R. A. Shalwitz, Deuterium magnetic resonance in vivo: the measurement of blood flow and tissue perfusion, *Ann. N. Y. Acad. Sci.* **508**, 89, (1987).

72. S. G. Kim and J. J. Ackerman, Multicompartment analysis of blood flow and tissue perfusion employing D_2O as a freely diffusible tracer: a novel deuterium NMR technique demonstrated via application with murine RIF-1 tumors, *Magn. Reson. Med.* **8**, 410, (1988).

73. G. W. Robertson, K. B. Larson and E. E. Speath, The interpretation of mean transit time measurements for multiphase tissue systems, *J. Theor. Biol.* **39**, 447, (1973).

74. F. A. Gibbs, H. Maxwell and E. L. Gibbs, Volume flow of blood through the human brain, *Arch. Neurol. Psychiat.* **57**, 137, (1947).

75. M. E. Moseley, Z. Vexler, H. S. Asgari, J. Mintorovitch, N. Derugin, S. Rocklage and J. Kucharczyk, Comparison of Gd- and Dy-chelates for T2 contrast-enhanced imaging, *Magn. Reson. Med.* **22**, 259, (1991).

76. A. Villringer, B. R. Rosen, J. W. Belliveau, J. L. Ackerman, R. B. Lauffer, R. B. Buxton, Y. S. Chao, V. J. Wedeen and T. J. Brady, Dynamic imaging with lanthanide chelates in normal brain: contrast due to magnetic susceptibility effects, *Magn. Reson. Med.* **6**, 164, (1988).

77. C. R. Fisel, J. L. Ackerman, R. B. Buxton, L. Garrido, J. W. Belliveau, B. R. Rosen and T. J. Brady, MR contrast due to microscopically heterogeneous magnetic susceptibility: numerical simulations and applications to cerebral physiology, *Magn. Reson. Med.* **17**, 336, (1991).

78. S. Majumdar and J. C. Gore, Studies of diffusion in random fields produced by variations in susceptibility, *J. Magn. Reson.* **78**, 41, (1988).

79. B. R. Rosen, J. W. Belliveau, J. M. Vevea and T. J. Brady, Perfusion imaging with NMR contrast agents, *Magn. Reson. Med.* **14**, 249, (1990).

80. B. R. Rosen, J. W. Belliveau, B. R. Buchbinder, R. C. McKinstry, L. M. Porkka, D. N. Kennedy, M. S. Neuder, C. R. Fisel, H. J. Aronen and K. K. Kwong, Contrast agents and cerebral hemodynamics, *Magn. Reson. Med.* **19**, 285, (1991).

81. J. W. Belliveau, B. R. Rosen, H. L. Kantor, R. R. Rzedzian, D. N. Kennedy, R. C. McKinstry, J. M. Vevea, M. S. Cohen, I. L. Pykett and T. J. Brady, Functional cerebral imaging by susceptibility-contrast NMR, *Magn. Reson. Med.* **14**, 538, (1990).

82. L. Ostergaard, D. F. Smith, P. Vestergaard Poulsen, S. B. Hansen, A. D. Gee, A. Gjedde and C. Gyldensted, Absolute cerebral blood flow and blood volume measured by magnetic resonance imaging bolus tracking: comparison with positron emission tomography values, *J. Cereb. Blood Flow Metab.* **18**, 425, (1998).

Chapter 3. Magnetic Resonance Perfusion Imaging Using Arterial Spin Tagging

Introduction

As discussed in the previous chapter, cerebral blood flow (CBF) is usually measured by observing and mathematically modeling the wash-in and/or wash-out kinetics of an exogenously administered tracer during its passage through the brain. The use of exogenous tracers is often associated with some disadvantages. First, most of the exogenous CBF tracers are either radioactive or toxic when applied at high concentrations, and thus are potentially hazardous to the subject undergoing CBF measurement. Second, the pharmacologic effects of some tracers, such as xenon gas, will potentially alter the resting physiological state of the brain and complicate the results of the CBF measurement. Finally, the temporal resolution of CBF measurements with methods using exogenous tracers is often limited by the clearance rate of the tracers from the body so that observation of dynamic CBF changes is difficult. It is therefore advantageous to measure CBF using endogenous tracers.

Magnetic resonance imaging (MRI) is an excellent imaging modality to map regional CBF (rCBF) because it is totally noninvasive and it allows high spatial resolution. Early methods of mapping rCBF with MRI include the use of deuterium (1,2), oxygen-17 (^{17}O) (3-6), fluorine-19 (^{19}F) (6-10), and proton (^{1}H) MRI with first pass bolus tracking (11-15). Spatial resolution of the CBF maps (or perfusion images) that can be obtained with

deuterium, ^{17}O or ^{19}F MRI is usually low because of either the intrinsic MR insensitivity or the low natural abundance of these nuclei. Using MR contrast agents as tracers, ^{1}H MRI using first pass bolus tracking is capable of measuring rCBF with higher spatial resolution. However, this method does not allow quantitative CBF measurement, as pointed out in the previous chapter, and is subject to the general disadvantages associated with the use of exogenous tracers.

Using magnetically labeled water molecules in the arterial blood as an endogenous tracer, Detre et al in 1992 proposed a method for rCBF mapping with ^{1}H MRI known as MR perfusion imaging using arterial spin tagging (AST) (16,17). The word "perfusion" has the same meaning as the word "CBF" in the context of this thesis, and they will be used interchangeably in this thesis. In the AST method, ^{1}H spins from water molecules in the arterial blood are first "tagged" by magnetization saturation or adiabatic inversion. Tagged arterial blood then perfuses the brain tissue and reduces its longitudinal magnetization by an amount that is dependent on CBF. With MR proton density imaging, such a reduction can be determined through measuring the longitudinal magnetization of the brain tissue with and without (control experiment) AST, and then used to calculate CBF with appropriate mathematical modeling. Although some technical problems remain to be solved, this method is capable of measuring rCBF noninvasively, with full quantification and potentially high spatial and temporal resolution (18). It is thus superior to the methods for rCBF measurement discussed previously (19).

Depending on the AST strategy, the methods of MR perfusion imaging using AST can be divided into methods of MR perfusion imaging using continuous AST (CAST) and methods of MR perfusion imaging using pulsed AST (PAST). By applying a long radiofrequency (RF) pulse (typically in the order of seconds) along with a spin-tagging magnetic field gradient, CAST labels arterial blood in the carotid arteries. One problem associated with CAST is the safety concern due to its high energy power deposition on the subject undergoing CBF measurement. Consequently, these methods so far are used primarily for rCBF measurements in animals (17,20-25), although their usefulness in human subjects has also been demonstrated (26-28). MR perfusion imaging using CAST has also been used to measure blood flow in rat heart (29), kidney (30) and ovary (31). In the methods using PAST, a relatively short RF pulse (typically of the order of several milliseconds) along with a slice-selective gradient is used to tag the longitudinal magnetization of the arterial blood in a brain slab proximal with respect to the direction of blood flow to the brain slice of interest. Compared to the methods using CAST, the methods using PAST are less quantifiable, but have technical characteristics that make them more suitable for human studies (32). As a result, these methods have been used primarily in mapping rCBF in human brain (33-38). The usefulness of these methods in measuring CBF in rat brain has also been demonstrated, but with only limited success (39). Despite their differences, the signal-to-noise ratios per unit time (SNRT) for CBF measurement with the two categories of perfusion imaging methods are the same (40).

In this chapter of the thesis, the theoretical principles and technique characteristic of perfusion imaging using PAST and CAST are both discussed, with emphasis on the

latter. For perfusion imaging using CAST, a comprehensive examination of all the factors that are known to affect absolute CBF quantification is also given, followed by an error propagation analysis to estimate the signal-to-noise ratio (SNR) of the perfusion measurement using this method. A strategy to optimize the SNR of the measurement with perfusion imaging using one-coil CAST is proposed and demonstrated with experiments on normal rat brain. This is followed by a discussion regarding the temporal resolution of this method for perfusion measurements. At the end of the chapter, some recent developments in MR perfusion imaging methods using AST are discussed.

Arterial Spin Tagging

The water proton spins in the arterial blood can be tagged magnetically by either saturation or inversion and the degree of spin tagging (α) can be defined as (18)

$$\alpha = -\frac{M_a - M_a^0}{2M_a^0} \qquad [3.1]$$

where M_a is the longitudinal magnetization of water protons in the arterial blood and M_a^0 is the equilibrium value of M_a. α has a value between 0 and 1. When the water proton spins in the arterial blood are completely saturated, M_a=0 and thus α=0.5. When the water proton spins in the arterial blood are completely inverted, M_a= -M_a^0 and thus α=1.0.

In the methods using PAST, a saturation pulse followed by a dephasing gradient or an adiabatic inversion pulse is used for spin-tagging, and it is usually applied along with a slice-selective gradient to saturate or invert arterial blood inside a brain slab that is posterior

to the imaging slice. With CAST, arterial blood in the carotid arteries are either saturated by continuous irradiation (16) or inverted with an adiabatic-fast-passage inversion scheme (17,18).

By applying continuous low-power RF irradiation in the presence of a magnetic field gradient, the longitudinal magnetization of the blood water spins in the carotid arteries can be inverted if the power of the RF irradiation (B_1) and the gradient strength (G_l) applied meet the adiabatic-fast-passage requirements (17,41,42),

$$\frac{1}{T1_a}, \frac{1}{T2_a} << \frac{1}{B_1} G_l V << \gamma B_1 \qquad [3.2]$$

where γ is the gyromagnetic ratio of the ^1H nucleus, $T1_a$, $T2_a$ are the longitudinal and transverse relaxation times of water molecules in the arterial blood and V is the laminar flow rate of blood in the carotid arteries.

Figure 3.1 is a numerical simulation of the inversion process of an ensemble of flowing ^1H spins undergoing adiabatic-fast-passage inversion. Simulation was done using a finite rotation matrix algorithm, with B_1=100 mG, G_l=1 G/cm and V=10 cm/s. T1 and T2 of the flowing water protons were assumed to be 1.89 s and 80 ms (typical values for arterial blood at 7 T) respectively. In Fig. 3.1, the normalized longitudinal magnetization of the flowing spins (M_z) is plotted as a function of time, where time zero corresponds to the time point when the flowing spins pass through the inversion plane. Before passing through the inversion plane, M_z remains at its equilibrium value (M_z=1.0) until the spins reach the proximity of the inversion plane. As the spins pass through the inversion plane, M_z is inverted adiabaticly. M_z reaches a maximal negative value shortly after the spins pass

through the inversion plane, and then starts to return to its equilibrium value through T1 relaxation. In this particular case, the maximal degree of inversion (M_z=-0.659) is obtained at t=330 ms and corresponds to an α value of 0.83. Perfect inversion is not obtained because the adiabatic-fast-passage requirements are not satisfied perfectly by using the assumed parameters (12.5<<100.0<<428.8).

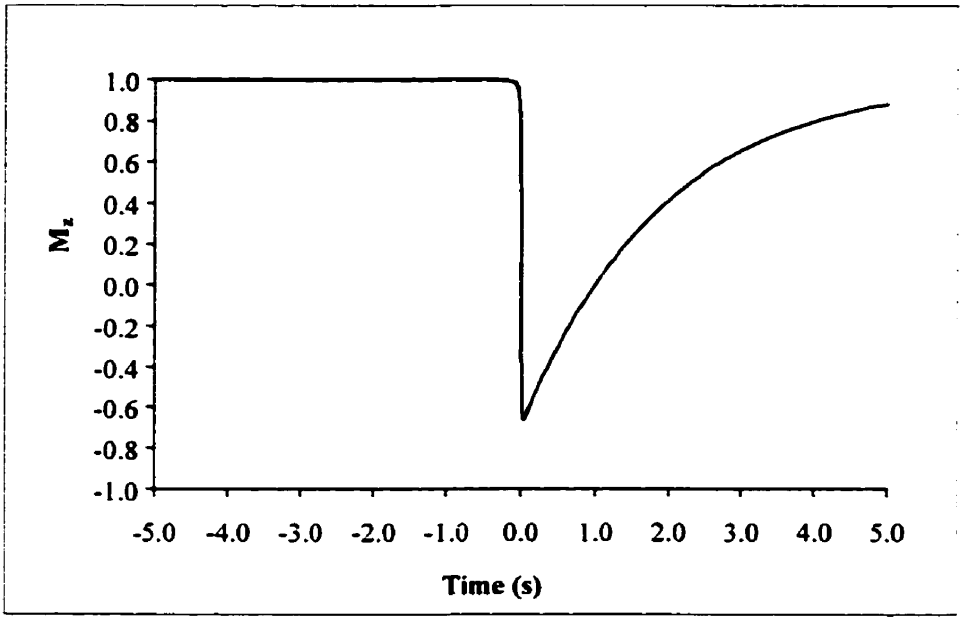

Figure 3.1 Simulated time course of the longitudinal magnetization of an ensemble of ^{1}H spins undergoing adiabatic inversion calculated using a finite rotation matrix algorithm.

MR Perfusion Imaging Using Pulsed Arterial Spin Tagging

This method of AST was first reported by Kwong et al (43), and has subsequently undergone a number of variations, including echo planar imaging with signal targeting with alternating radiofrequency (EPISTAR) (33), perfusion imaging with flow-sensitive alternating inversion recovery (FAIR) (34,35,39), proximal inversion with a control for

offset-resonance effects (PICORE) (36), quantitative imaging of perfusion using a single subtraction (QUIPSS and QUIPSS II) (36,37,44) and extraslice spin tagging MR perfusion imaging (EST) (38). The basic principles for perfusion measurement underlying all these methods are the same, and they differ from each other in how the control experiments are conducted and in their sensitivity to blood flow from the distal side of the imaging slice(s) to the image slice(s). In this thesis, the FAIR method will be used as an example to discuss the theoretical aspects and the technical characteristics of perfusion imaging using PAST.

With the FAIR method (34,35,39), two inversion recovery experiments are performed in an interleaved manner, one with a slice selective inversion (acting as the control experiment and hereafter referred as the SS experiment) and the other with a non-slice-selective inversion (hereafter referred as the NS experiment). Proton density weighted images are acquired with a delay (TI) after the inversion pulse. Subtraction of the images obtained in those two experiments gives a perfusion-weighted image.

In an inversion-recovery experiment, the modified Bloch equation for the longitudinal magnetization of brain tissue water (M_b) in the presence of blood flow is:

$$\frac{dM_b(t)}{dt} = \frac{M_b^0 - M_b(t)}{T1_b} + fM_a(t) - fM_v(t) \qquad [3.3]$$

where M_b^0 is the equilibrium value of M_b, $T1_b$ is the spin-lattice relaxation time of brain tissue water in the absence of perfusion, f is the perfusion rate and M_v is the longitudinal magnetization of water protons in the venous blood.

If water is assumed to be a freely diffusible tracer so that there is an instantaneous equilibrium among brain tissue water, arterial water and venous water, M_a in the absence of spin tagging (M_a^0) and M_v can be written

$$M_a^0 = \frac{f}{\lambda} M_b^0 \qquad [3.4]$$

$$M_v(t) = \frac{f}{\lambda} M_b(t) \qquad [3.5]$$

where λ is the brain:blood partition coefficient of water.

In the SS experiment, spins are inverted only in the imaging plane so that it is always "fresh" blood that perfuses the imaging slice when t>0 and,

$$M_a(t) = M_a^0 = \frac{f}{\lambda} M_b^0 . \qquad [3.6]$$

Substituting Eqs. [3.5] and [3.6] into Eq. [3.3] and with the boundary condition,

$$M_b(0) = (1 - 2\alpha) M_b^0 \qquad [3.7]$$

the equation can be solved to give

$$M_b(t) = M_b^0 \left(1 - 2\alpha \exp\left[-\left(\frac{1}{T1_b} + \frac{f}{\lambda} \right) t \right] \right). \qquad [3.8]$$

In the NS experiment, spins in the whole head or sometimes in the whole body are inverted. Therefore, inverted blood, which relaxes during TI, perfuses the imaging slice when t>0 so that

$$M_a(t) = \begin{cases} [1 - 2\alpha \exp(-t/T1_a)]M_a^0 = [1 - 2\alpha \exp(-t/T1_a)]\dfrac{f}{\lambda}M_b^0 & t < \Delta t \\ M_a^0 = \dfrac{f}{\lambda}M_b^0 & t > \Delta t \end{cases} \quad [3.9]$$

where Δt is the time for the "fresh" blood to reach the imaging slice. When $t<\Delta t$, substituting Eqs. [3.5] and [3.9] into Eq. [3.3] and solving with the boundary condition described in Eq. [3.7] gives

$$M_b(t) = M_b^0\left(1 - 2\alpha C \exp\left[-\frac{t}{T1_a}\right] - 2\alpha(1-C)\exp\left[-\left(\frac{1}{T1_b} + \frac{f}{\lambda}\right)t\right]\right) \quad [3.10]$$

where

$$C = \frac{\dfrac{f}{\lambda}}{\dfrac{1}{T1_b} + \dfrac{f}{\lambda} - \dfrac{1}{T1_a}}.$$

The difference in M_b between the SS and NS experiments at the time point TI then is

$$\Delta M_b(TI) = 2\alpha C\left(\exp\left[-\left(\frac{1}{T1_b} + \frac{f}{\lambda}\right)TI\right] - \exp\left[-\frac{TI}{T1_a}\right]\right)M_b^0 \quad . \quad [3.11]$$

In principle, f can be calculated by combining Eqs. [3.8] and [3.11] provided that $T1_b$, $T1_a$ and λ are known. Since f appears in the exponential terms, obtaining an analytical solution for f from Eqs. [3.8] and [3.11] is difficult. Semi-quantitative perfusion determination in a FAIR experiment can be carried out by comparing the experimental ΔM value to a ΔM .vs f calibration curve constructed with given $T1_b$, $T1_a$, λ and TI values (32,34,39,40). As a result, perfusion imaging methods using PAST such as FAIR are often used to measure relative, not quantitative, perfusion or dynamic perfusion changes.

In order for a FAIR experiment to work, two requirements for the selection of the TI value have to be met. First, TI has to be close to both $T1_b$ and $T1_a$ in order to obtain optimal sensitivity for the perfusion measurement. Secondly, TI cannot be longer than Δt, otherwise in the NS experiment, fresh spins will flow into the imaging slice before TI so that the optimal sensitivity will never be obtained. For human studies at low field strength, it is possible to choose a TI value which satisfies both the requirements. For example, at 1.5 T, typical T1 values for human brain are 0.9 s for grey matter, 0.5 s for white matter and 1.2 s for arterial blood (32). If a whole-head coil is used, the non-slice-selective inversion in the NS experiment will invert the proton spins in the whole head including those in the blood in the carotid arteries so that Δt is somewhere between 1.2 and 2.0 s. The requirements can then be essentially satisfied by using a TI value around 1.4 s. However, this is not the case in many animal studies which are usually conducted at a high field strength. For example, at 7 T, T1 for rat brain is about 1.7 s, so that TI should be around 1.7 s. However, unless a whole-body coil for spin inversion is used, Δt is much shorter than $T1_b$ in a rat (i.e. about 200 ms if a head coil is used), making the second requirement ($T1<\Delta t$) hard to meet. Considering the difficulties in absolute perfusion quantification and in achieving optimal detection sensitivity, it has been concluded that perfusion imaging methods using PAST are not suitable for perfusion measurement in experimental animals at high field strength (39).

Two-compartment Model of Magnetization Transfer

Based on their mobility, two groups of protons exist in biological tissue (45). The first group is the protons in bulk water with relatively unrestricted motion, giving a narrow resonance in the MR frequency domain and hereafter called ^1H_f. The second group is the protons (^1H_m) in moieties with restricted motion such as those in proteins and cell membranes. These protons usually have a broad resonance in the MR frequency domain. The spins of the protons in the two groups are in constant exchange via dipole-dipole interaction, chemical exchange and diffusion.

When an off-resonance RF pulse is applied to biological tissue, it reduces the proton density signal intensity of ^1H_f not only through the direct off-resonance irradiation (DORI) effect but also through the so-called magnetization transfer (MT) effect (45,46). The MT effect is produced by saturation of the ^1H_m protons by the DORI effect of the RF pulse and the exchange of these protons with the ^1H_f protons. Since two proton compartments are involved, the model used here to describe the MT effect is usually referred as the two-compartment MT model, and a schematic representation of this model is shown in Fig. 3.2. The MT effect in biological tissue has also been described using more complicated models with different numbers of proton compartments assumed, including a two-compartment with a dipolar reservoir model (47), a three-compartment model (48) and a four-compartment model (49). However, the two-compartment MT model seems to be adequate in most cases (47,49) and its use is therefore justified because of its simplicity.

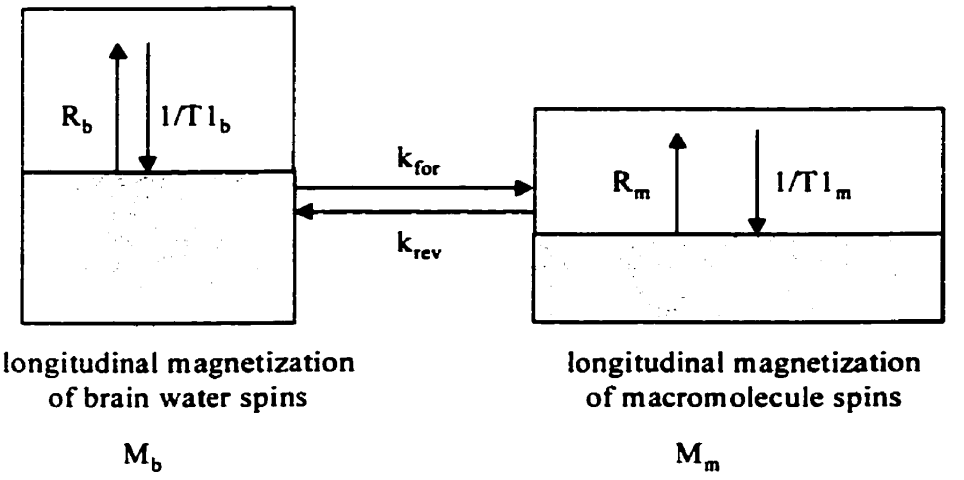

Figure 3.2 A two-compartment model of magnetization transfer in brain.

MR Perfusion Imaging Using Continuous Arterial Spin Tagging

When an RF pulse is applied at the carotid arteries along with a magnetic field gradient, it not only tags the water spins in the arterial blood, but also introduces MT and DORI effects in the imaging brain slice, reducing the longitudinal magnetization of brain tissue water in that slice (18). Using a two-compartment exchange model for MT and including the effects of perfusion and off-resonance irradiation, the modified Bloch equations for the longitudinal magnetization of brain tissue water (M_b) and macromolecule spins (M_m) in a CAST experiment are:

$$\frac{dM_b(t)}{dt} = \frac{M_b^0 - M_b(t)}{T1_b} - k_{for}M_b(t) + k_{rev}M_m(t) + fM_a(t) - fM_v(t) - R_bM_b(t) \qquad [3.12]$$

$$\frac{dM_m(t)}{dt} = \frac{M_m^0 - M_m(t)}{T1_m} + k_{for}M_b(t) - k_{rev}M_m(t) - R_mM_m(t) \qquad [3.13]$$

where M^0 is the equilibrium value of M, T1 is the spin-lattice relaxation time in the absence of perfusion and cross-relaxation, R is the rate at which longitudinal magnetization is lost

due to the DORI effect, subscripts b and m refer to brain water and macromolecule spins, k_{for} and k_{rev} are the forward and reverse rate constants for magnetization transfer .

If water is assumed to be a freely-diffusible tracer so that there is an instantaneous equilibrium among brain tissue water, arterial water and venous water, M_a and M_v can then be written (18)

$$M_a(t) = -(2\alpha - 1)\frac{f}{\lambda}M_b^0 \qquad [3.14]$$

$$M_v(t) = \frac{f}{\lambda}M_b(t) \qquad [3.15]$$

Substituting Eqs. [3.14] and [3.15] into Eq. [3.12],

$$\frac{dM_b(t)}{dt} = \frac{M_b^0 - M_b(t)}{T1_b} - k_{for}M_b(t) + k_{rev}M_m(t) - (2\alpha - 1)\frac{f}{\lambda}M_b^0 - \frac{f}{\lambda}M_b(t) - R_bM_b(t) \qquad [3.16]$$

With the boundary conditions

$$M_b(0) = M_b^0$$

$$M_m(0) = M_m^\circ = \frac{k_{for} \times M_b^0}{k_{rev}}$$

$$\left.\frac{dM_b}{dt}\right|_{t=0} = -\left(\frac{2\alpha f}{\lambda} + R_b\right)M_b^0 = -F \times M_b^0,$$

solving Eqs. [3.13] and [3.16] gives

$$M_b(t) = M_b^{ss} + C_b^1 \exp\left[-\frac{t}{T1_{app1}}\right] + C_b^2 \exp\left[-\frac{t}{T1_{app2}}\right] \qquad [3.17]$$

$$M_m(t) = M_m^{ss} + C_m^1 \exp\left[-\frac{t}{T1_{app1}}\right] + C_m^2 \exp\left[-\frac{t}{T1_{app2}}\right] \qquad [3.18]$$

where, M_b^{ss} and M_b^{ss} are the steady state values of M_b and M_m, $T1_{app1}$ and $T1_{app2}$ are the apparent longitudinal relaxation times and C_b^1, C_b^2, C_m^1 and C_m^2 are coefficients.

$$M_b^{ss} = \frac{\left[\frac{k_{for}}{T1_m} + \left(\frac{1}{T1_m} + k_{rev} + R_m\right)\left(\frac{1}{T1_b} - (2\alpha - 1)\frac{f}{\lambda}\right)\right]M_b^0}{\frac{1}{T_{app}}\left(\frac{1}{T1_m} + k_{rev} + R_m\right) - k_{for}k_{rev}} \quad [3.19]$$

$$M_m^{ss} = \frac{\left[\left(\frac{1}{T1_b} - (2\alpha - 1)\frac{f}{\lambda}\right)k_{rev} - \left(\frac{1}{T1_b} + k_{for} + \frac{f}{\lambda} + R_b\right)\frac{1}{T1_m}\right]M_m^0}{\frac{1}{T1_{app}}\left(\frac{1}{T1_m} + k_{rev} + R_m\right) - k_{for}k_{rev}} \quad [3.20]$$

$$\frac{1}{T1_{app1}} = \lambda_1 = \frac{1}{2}\left\{\frac{1}{T1_{app}} + \left(\frac{1}{T1_m} + k_{rev} + R_m\right) + \sqrt{\left[\left(\frac{1}{T1_m} + k_{rev} + R_m\right) - \frac{1}{T1_{app}}\right]^2 + 4k_{for}k_{rev}}\right\} \quad [3.21]$$

$$\frac{1}{T1_{app2}} = \lambda_2 = \frac{1}{2}\left\{\frac{1}{T1_{app}} + \left(\frac{1}{T1_m} + k_{rev} + R_m\right) - \sqrt{\left[\left(\frac{1}{T1_m} + k_{rev} + R_m\right) - \frac{1}{T1_{app}}\right]^2 + 4k_{for}k_{rev}}\right\} \quad [3.22]$$

$$\frac{1}{T1_{app}} = \frac{1}{T1_b} + \frac{f}{\lambda} + k_{for} + R_b \quad [3.23]$$

$$C_b^1 = \frac{F - (1 - M_b^{ss}) \times \lambda_2}{\lambda_1 - \lambda_2} \quad [3.24]$$

$$C_b^2 = \frac{(1 - M_b^{ss}) \times \lambda_1 - F}{\lambda_1 - \lambda_2} \quad [3.25]$$

To measure f, M_b^{ss} is measured with (M_b^{inv}) and without (α=0; M_b^{con}) spin tagging and f can be calculated from M_b^{inv} and M_b^{con},

$$f = \lambda\left(\frac{1}{T1_b} + \delta\right)\left(\frac{M_b^{con} - M_b^{inv}}{M_b^{inv} + (2\alpha - 1)M_b^{con}}\right). \quad [3.26]$$

or, rearranging,

$$f = \lambda\left(\frac{1}{T1_o} + \delta\right)\left(\frac{M_b^{con} - M_b^{inv}}{2\alpha M_b^{con}}\right) \qquad [3.27]$$

where

$$\delta = \frac{k_{for}}{1 + k_{rev}T1_m + R_m T1_m} \qquad [3.28]$$

and

$$\frac{1}{T1_o} = \frac{1}{T1_b} + \frac{f}{\lambda}. \qquad [3.29]$$

Note that R_b does not appear in Eq. [3.27], so that direct irradiation of brain water spins does not affect *f*. However, R_m remains in the expression, so that quantification of perfusion depends on the rate at which macromolecule spins are saturated by the spin-tagging pulse.

One-Coil and Two-Coil Continuous Arterial Spin Tagging

In the conventional CAST experiment, a single RF coil is used both to tag the arterial spins and to obtain the MR image (16-18,26,27). As a result, the proton density signal intensity of the imaging slice is reduced not only by in-flowing arterial blood carrying tagged spins but also by the MT and the DORI effects of the spin-tagging pulse. Although the MT/DORI effects do not affect the perfusion quantification directly as long as they are accounted for by performing a control experiment, the presence of these effects does reduce the intensity of the proton density images by up to 70% (24), decreasing SNR and thus the accuracy of the perfusion measurement. Furthermore, in the presence of the spin-tagging gradient, the MT/DORI effect is not homogeneous along the axis perpendicular to the

imaging slice, so that different imaging slices experience different amounts of MT/DORI effects and require different control experiments, making multiple-slice perfusion imaging difficult. This problem can be solved to some extent by performing the control experiment with an amplitude-modulated RF pulse which produces the same amount of MT/DORI effects as the spin-tagging pulse for all the brain slices so that one control is sufficient for all brain slices (50). Although this method is capable of multiple-slice perfusion imaging, two problems remain. First, with this method, the SNR of the perfusion measurement will likely be reduced because of imperfections in the amplitude-modulated pulse. Second, the power of the amplitude-modulated pulse has to be adjusted manually to match that of the spin-tagging pulse, making the method difficult to use and susceptible to subjective error.

Considering the limitations of the one-coil CAST experiment, a two-coil method was developed by Zhang et al in 1995 (23,24), in which a separate neck coil, decoupled from the imaging coil, is used for AST. The geometric configuration of the neck coil was specially designed so that the RF power produced by this coil does not reach the brain. The two-coil configuration allows AST in the absence of MT and DORI effects, thus improving the SNRT of the perfusion measurements and enabling multiple-slice perfusion imaging. However, this experimental configuration requires two RF channels and other special hardware, and thus is inconvenient to use in practice. In addition, the use of the neck coil limits arterial tagging to spins in the carotid arteries only while leaving blood flowing in the vertebral arteries unaffected (24,51). Measurements of perfusion in posterior regions of the brain, or in animal experiments involving partial or complete carotid artery occlusion, are then compromised.

Previously, the equations for the perfusion calculation in the one-coil and the two-coil CAST experiments were developed separately (18,24). Equation [3.27] derived in this thesis is a general expression for f, valid for both the one-coil and the two-coil CAST experiments. In the one-coil CAST experiments, it is usually assumed that the macromolecule spins in the imaging slice are completely saturated instantaneously by the spin-tagging RF pulse, corresponding to $R_m=\infty$. In this case, Eq. [3.27] reduces to

$$f=\frac{\lambda}{T1_o}\left(\frac{M_b^{con}-M_b^{inv}}{2\alpha M_b^{con}}\right), \qquad [3.30]$$

agreeing with what was derived previously (18). In a two-coil CAST experiment, arterial blood is tagged in the absence of the MT/DORI effects in the imaging plane ($R_b=R_m=0$) so that Eq. [3.27] reduces to

$$f=\lambda\left(\frac{1}{T1_o}+\frac{k_{for}}{1+k_{rev}T1_m}\right)\left(\frac{M_b^{con}-M_b^{inv}}{2\alpha M_b^{con}}\right), \qquad [3.31]$$

consistent with the expression derived by Zhang et al (24).

Measurement of M_b^{inv} *and* M_b^{con}

Unless stated otherwise, all experiments described in this chapter were carried out on a Bruker Biospec/3 7 T/21 cm spectrometer equipped with actively-shielded gradient coils and a custom built 3 cm diameter saddle coil for both transmission and reception.

To obtain a perfusion image, M_b^{inv} and M_b^{con} are first prepared by CAST, and then determined with proton density weighted MR imaging. Conventional spin-echo (SE) (16,17,26), echo planar (28,50,52,53) and snapshot fast low angle shot (FLASH) imaging (54) have been used as the read-out procedures to determine M_b^{inv} and M_b^{con}. With SE imaging, AST has to be carried out for every phase-encoding step so that the total time to obtain a perfusion image is long, for example, at least 10 minutes to acquire a perfusion image with a matrix size of 128×128, not including the time to acquire the $T1_o$ image needed for perfusion calculation. With echo planar imaging (EPI) and snapshot FLASH imaging, images of M_b^{inv} and M_b^{con} can be obtained following only one magnetization preparation procedure, making these techniques much more time-efficient than the SE imaging technique. Theoretically, EPI is preferable to snapshot FLASH imaging because it acquires an image in one single shot. However, EPI requires specialized hardware and thus its use is limited. In the work described in this thesis, a snapshot FLASH imaging sequence was used to acquire the proton density weighted images and the detailed acquisition parameters will be given later when each individual experiment is described.

Measurement of α, $T1_o$ and Magnetization Transfer Parameters

In addition to M_b^{inv} and M_b^{con}, λ, α, $T1_o$, R_b and magnetization transfer parameters (i.e. k_{for}, k_{rev} and $T1_m$) must be determined in order to be able to use Eq. [3.27] to calculate *f*.

Measurement of α

The degree of spin labeling, α, can be determined experimentally by measuring the intensity of the arterial blood in the carotid arteries in a proton density weighted image with and without AST (25). In the work described in this thesis, α was measured using a gradient-refocused-echo imaging sequence with a repetition time (TR) of 530 ms, an echo time (TE) of 10 ms and a 90° flip angle excitation pulse. Images were acquired with a field of view (FOV) of 4.5×4.5 cm^2 and a 2 mm slice thickness. The acquisition matrix size was 128×128, and was zero-filled to 256×256 during reconstruction. The location of the detection plane for α measurement is shown in Fig. 3.3. To measure the proton density signal intensity of the arterial blood in the presence of AST, a 500 ms spin-tagging pulse along with an axial gradient was inserted into the TR period of the imaging sequence. The frequency of the spin-tagging pulse was adjusted according to the gradient strength applied so that the arterial blood was tagged in a plane that was about 5 mm upstream from the detection plane (Fig. 3.3).

Figure 3.4 shows magnitude-calculated neck images acquired for the measurement of α, in which the carotid arteries are indicated by arrows. Image A was acquired without AST and had the highest carotid artery intensities among all four images. Images B, C and D were acquired in the presence of AST with a constant spin-tagging gradient of 2 G/cm and a progressively increasing B_1 of 40, 75 and 150 mG. By measuring the carotid artery intensities and comparing them with that in image A, α can be calculated for each spin-

tagging condition by Eq. [3.1], and had a value of 0.30, 0.42 and 0.76 for images B, C and D respectively.

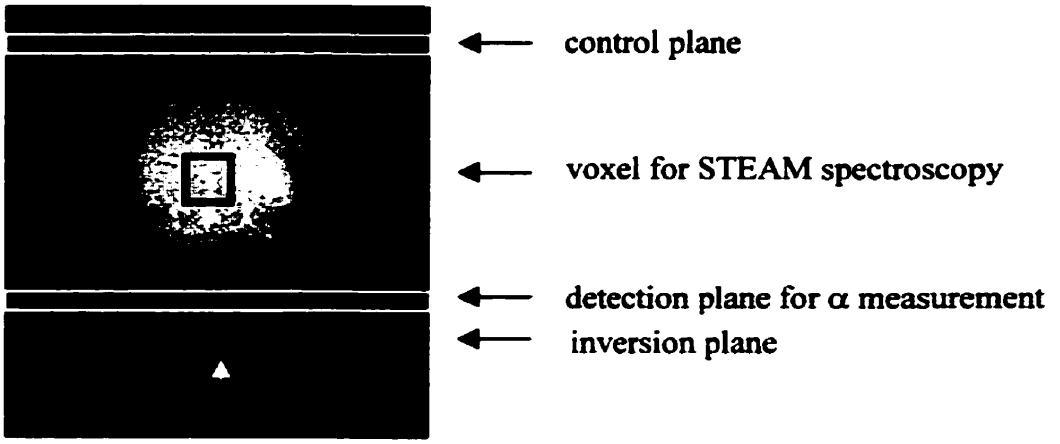

Figure 3.3 A transverse image of a rat brain showing the locations of the inversion plane, the control plane, the detection plane for α measurement and the voxel for STEAM spectroscopy.

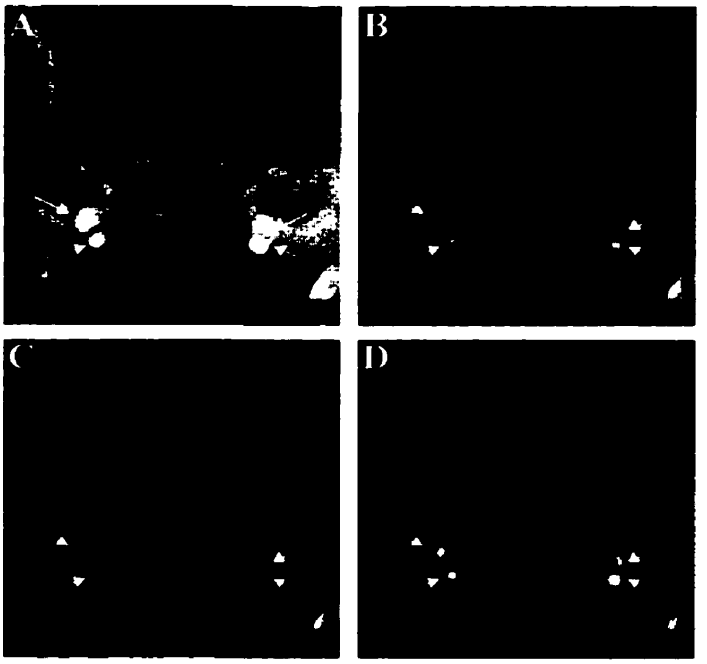

Figure 3.4 Gradient echo images of the carotid arteries (as indicated by arrows). Image A was acquired without arterial spin tagging (AST); Images B, C and D were acquired in the presence of AST with a constant spin-tagging gradient of 2 G/cm and a progressively increasing B_1 of 40, 75 and 150 mG. Carotid arteries are indicated by arrows.

Measurement of $T1_o$

From Eqs. [3.8] and [3.29], it can be seen that $T1_o$ can be measured using the slice-selective inversion-recovery method. In the work described in this thesis, the $T1_o$ maps used to calculate perfusion images were obtained using a slice-selective inversion-recovery snapshot FLASH sequence (55). Detailed acquisition parameters will be specified later when each individual experiment is described. A 5 ms sech pulse in the presence of a slice-selective gradient was used to invert the magnetization in the detection plane. A 1 ms gaussian was used as the excitation pulse for imaging. To correct for the difference in profiles of the inversion and imaging pulses (32,56), the gradient strength was adjusted so that the inverted slice was about 2.5 times the thickness of the imaged slice.

Measurement of Magnetization Transfer Parameters

In order to calculate a perfusion image precisely, k_{for}, k_{rev} and $T1_m$ maps must be used for each perfusion measurement. However, measurement of these maps for each experiment is impractical in most cases because of the constraint in the total acquisition time. Typically, δ is much less than $1/T1_o$ so that the calculation error introduced by imprecise values of k_{for}, k_{rev} and $T1_m$ is relatively small compared to that introduced by imprecise values of α or $1/T1_o$. Therefore, it is reasonable to use average values of k_{for}, k_{rev} and $T1_m$ determined separately under similar experimental conditions for perfusion calculations.

Average k_{for}, k_{rev} and $T1_m$ values were measured in brains of four normal rats using volume-localized ^1H spectra, with a $5\times5\times5$ mm^3 voxel whose location is shown in Fig. 3.3. Spectra were acquired using modified stimulated echo acquisition mode (STEAM) sequences. To determine k_{for}, magnetization transfer curves were obtained by acquiring a series of spectra with off-resonance RF pulses ($\Delta\omega$=8 kHz, B_1=100 mG) of varying length inserted into the TR period before the start of the STEAM sequence (24). Inversion-recovery experiments were used to determine $T1_m$ and k_{rev}. Following a hard 180° inversion pulse, a series of spectra was generated with varying delays TI between the inversion pulse and the STEAM sequence (24). $T1_m$, k_{for}, and k_{rev} were determined from the magnetization transfer and inversion-recovery curves. Each spectrum was obtained with 4 transients acquired into 2048 data points with TR=5 s, TE=20 ms and mixing time (TM) 10 ms. Free induction decays (FIDs) were zero-filled to 4096 data points and line-broadened by 5 Hz prior to Fourier transformation. Peak height was used to quantitate signal intensity.

Figure 3.5 shows a typical magnetization transfer curve (A) and an inversion recovery curve (B) of a voxel in a normal rat brain. An exponential fit to the magnetization transfer curve gave $k_{for}=1.67\pm0.07$ s^{-1}. Using this value and a double exponential fit (24) to the inversion recovery curve gave $T1_m=0.88\pm0.62$ s and $k_{rev}=20.1\pm7.5$ s^{-1}. A double exponential fit to the inversion recovery curve is significantly better than the commonly used single exponential fit, as shown by an F-test for nonlinear regression (57). Of the magnetization transfer parameters measured at 7 T in this work, k_{for} is larger than that measured at 4.7 T (1.67 vs. 1.32 s^{-1}), while k_{rev} is smaller (20.1 s^{-1} in this work compared to 33.5 s^{-1} at 4.7 T) (24).

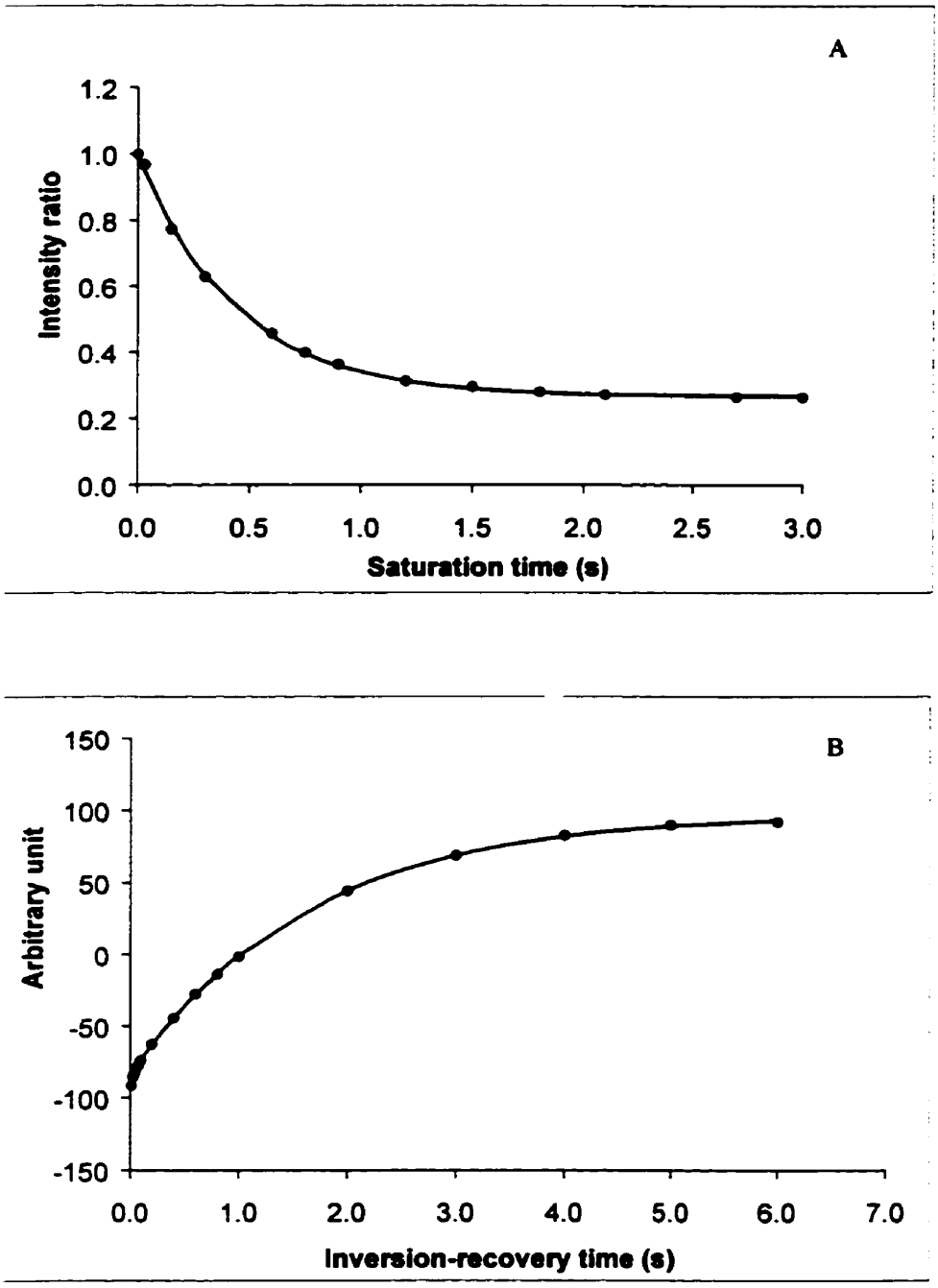

Figure 3.5 A magnetization transfer curve (A) and an inversion recovery curve (B) of a representative rat brain. Closed circles represent experimental data. The solid lines are least squares single exponential (A) or double exponential (B) fits to the experimental data.

Calculation of R_b and R_m

When off-resonance irradiation is applied, tissue water spins and macromolecule spins are saturated at different rates (R_i) given by (47)

$$R_i(2\pi\Delta\omega) = \pi\gamma^2 B_1^2 g_i(2\pi\Delta\omega) \qquad [3.32]$$

where the subscript i is b or m, $\Delta\omega$ is the frequency offset in Hz and $g(2\pi\Delta\omega)$ is the absorption lineshape. For brain tissue water spins, the extreme narrowing condition applies so that the absorption lineshape is Lorentzian and

$$g_b(2\pi\Delta\omega) = \frac{T2_b}{\pi}\frac{1}{\left[1+(2\pi\Delta\omega T2_b)^2\right]} \qquad [3.33]$$

where $T2_b$ is the transverse relaxation time for the brain tissue water spins.

For macromolecule spins, the mobility of the protons is restricted so that the averaged spin-spin dipolar interactions are not zero and the absorption lineshape is Gaussian or super-Lorentzian (47). Because of its simplicity, a Gaussian absorption lineshape is assumed for the macromolecule spins in this thesis and

$$g_m(2\pi\Delta\omega) = \frac{T2_m}{\sqrt{2\pi}}\exp\left(\frac{-(2\pi\Delta\omega T2_m)^2}{2}\right) \qquad [3.34]$$

where $T2_m$ is the transverse relaxation time for macromolecule spins.

Factors Affecting Perfusion Quantification in a Continuous Arterial Spin Tagging Experiment

In theory, the method of MR perfusion imaging using CAST is capable of measuring absolute CBF, and absolute CBF measurements with this method have already been

validated in normal rat brain using the radioactive microsphere method (58). In practice, however, there are a number of factors which may potentially affect the CBF measurement with this method, and which must be taken into account in order to determine CBF precisely.

Effects of Magnetization Transfer Parameters

Because average MT parameters are used to calculate the perfusion images, regional errors will result if there is a significant spatial variation of those parameters across the brain. For example, after focal ischemia, k_{for} of infarcted brain tissue decreases by up to 50% (59). In this case, using a k_{for} value that is measured from normal brain tissue to calculate f will overestimate CBF by an amount that is dependent upon the relative sizes of δ and $1/T1_o$. Since, commonly, δ is much less than $1/T1_o$, the size of such an error usually does not exceed 10%.

Asymmetrical Magnetization Transfer Effect

The use of Eq. [3.27] to calculate f in the one-coil perfusion imaging method requires that the MT/DORI effects on the imaging slice produced by the spin-tagging pulse are matched perfectly by the control experiment. Since MT and DORI usually have much larger effects than AST on the proton density signal intensity of the brain tissue, the presence of even very little unbalanced MT/DORI effects will introduce a significant error into the perfusion quantification.

By assuming that the MT/DORI effects are symmetrical around the frequency of the brain tissue water, the control for MT/DORI effects has conventionally been done by applying the same spin-tagging gradient and an RF pulse whose frequency offset relative to the water frequency of the imaging slice is the same as that of the spin-tagging pulse, but with an opposite sign (16-18). However, it was found later that there is an apparent asymmetry in the MT/DORI effects around the water frequency and the use of the conventional method for control could result in either a positive or a negative systematic error in f, depending on the sign of the spin-tagging gradient (60). An alternative way to perform the control experiment, as suggested by Parker et al (60), is to reverse the direction of the spin-tagging gradient while keeping the control pulse the same as the spin-tagging pulse. Although this gives much better performance than the conventional method, it alone does not eliminate the asymmetry in the MT/DORI effects completely. To eliminate the asymmetrical MT/DORI effects completely, a four-step offset-gradient cycling protocol must be used (60,61).

Incomplete Saturation of Macromolecule Spins

Conventional one-coil CAST experiments assume that the macromolecule spins are completely saturated. In general, however, macromolecule spins are only partially saturated (60), and comparison of Eqs. [3.27] and [3.30] shows that Eq. [3.30] underestimates f by an amount depending on R_m under such circumstances. With typical values for k_{for}, $T1_m$, k_{rev}, $T1_b$ and a R_m value calculated using Eq. [3.34] with B_1=100 mG, $\Delta\omega$=10 kHz and $T2_m$ =20.0 μs, the underestimation of f due to incomplete saturation of macromolecule spins is

about 5%. In studies using lower B_1 (≤50 mG) (26,53,60), the underestimation of f could be as much as 10%.

Determination of α

α can either be measured experimentally by imaging the carotid arteries (25) or calculated theoretically by numerically integrating the Bloch equations (62,63). Two concerns have been raised for the experimental method of measuring α. First, α values measured at the carotid arteries can not be used directly for perfusion calculations because of the vascular transit time effect (see below). Second, to measure α, the proton density signal intensity of the arterial blood is averaged over the cross-section of the carotid arteries, and will over-emphasize the contribution from the slowly flowing spins since most of the blood flow in the carotid arteries is carried by blood traveling at high velocities if laminar blood flow is assumed. The effects of vascular transit time and velocity distribution on α can be taken into account when numerical simulation is used to evaluate α (62). However, the existing numerical methods usually oversimplify the real situation by neglecting factors that might contribute significantly to the precise determination of α, such as the MT effect of the spin-tagging pulse on the arterial blood (64,65). As a result, α values calculated by numerical simulation are often higher than those obtained from experimental measurements with similar spin-tagging and relaxation parameters. In this thesis, experimentally determined α values are used for perfusion calculations.

Extraction Fraction for Water

Equation [3.27] was derived based on the assumption that water is a freely diffusible tracer. In other words, it was assumed that all the tagged water molecules in the arterial blood can diffuse out of the vasculature and exchange with the brain tissue water instantaneously after their arrival at the capillary bed of the imaging slice. In rat brain, such an assumption seems to be valid when CBF is normal or lower than normal (<1.5 $ml \cdot g^{-1} \cdot min^{-1}$). However, as the CBF increases, this assumption becomes invalid since there is now only a fraction (E) of the tagged water molecules that can diffuse out of the vasculature and exchange with the brain tissue water (66). E is usually referred to as the "extraction fraction" for water. The assumption of water as a freely diffusible tracer corresponds to E=1. The effect of the extraction fraction for water on perfusion quantification has been investigated theoretically by Silva et al (66). Generally, assuming water behaves as a freely diffusible tracer when it is not truly freely diffusible underestimates f by a factor of 1/E. In order to measure f precisely at high flow rates, it is therefore necessary to evaluate the dependence of E on CBF using independent methods.

Brain:Blood Partition Coefficient λ

For simplicity, a global λ value of 0.9 ml/g is usually used to calculate f for the entire brain. Because λ is not homogeneous across the brain, the use of a global λ will introduce regional errors in perfusion. For example, in normal human brain, λ values for gray matter and white matter are 0.98 and 0.82 (67-69). The calculation of perfusion using a

global λ value of 0.9, therefore, underestimates f in the grey matter and overestimates f in the white matter. Furthermore, the average λ value of 0.9 ml/g is measured from normal brain, and it may not be correct under all physiological circumstances. For example, higher brain tissue water content in neonatal or edematous brain usually results in a higher λ, while a decrease in hematocrit increases the blood water content, and thus results in a lower λ (69). Therefore, when f is measured in physiologically-perturbed brain tissue, caution must be exercised in choosing the correct λ value for a perfusion calculation.

Artifacts from Flowing Spins

A proton density image of the brain includes contributions from water protons in brain tissue as well as water protons in blood so that

$$M^{con} - M^{inv} = (M_b^{con} - M_b^{inv}) + (M_{blood}^{con} - M_{blood}^{inv}) \qquad [3.35]$$

where M^{con} and M^{inv} are the measured proton density signal intensities in the control and the spin-tagging experiments, and M_{blood}^{con} and M_{blood}^{inv} are the proton density signal intensities of the blood in the control and the spin-tagging experiments.

In large arteries, $M_{blood}^{con} - M_{blood}^{inv}$ gives rise to very high intensity "foci" in the perfusion image, interfering with the perfusion measurement in the surrounding regions (54). In smaller blood vessels and the capillary bed, $M_{blood}^{con} - M_{blood}^{inv}$ does not give rise to bright "foci", but contributes to the proton density signal difference observed in the spin-tagging and the control experiments and causes an overestimation of f (52,70). Although the blood

volume in normal brain is small (less than 5%) (71,72), the size of $M^{con}_{blood} - M^{inv}_{blood}$ is usually comparable to that of $M^{con}_{b} - M^{inv}_{b}$ so that vascular artifacts will affect the perfusion measurement significantly if not eliminated. In experiments using conventional SE imaging or EPI, the vascular artifacts can be eliminated by applying bipolar crusher gradients around the refocusing pulse which dephase the magnetization of moving spins (70). With snapshot FLASH imaging, the use of crusher gradients is not possible, and the vascular artifacts can be suppressed by inserting a post-tagging delay that is longer than the vascular transit time (see below) between the spin-tagging pulse and the imaging sequence so that all tagged vascular spins will flow out of the imaging plane before imaging (52). Figure 3.6 shows four $(M^{con} - M^{inv})/M^{con}$ images obtained with different post-tagging delays. With no post-tagging delay (A), artifacts with high intensities are apparent at the sites where major blood vessels are located (as indicated by the arrows). Images B, C and D were acquired with a post-tagging delay of 280 ms, 400 ms and 600 ms respectively. With the increase in post-tagging delay, the vascular artifacts from major blood vessels are suppressed progressively and eliminated when the post-tagging delay reaches 600 ms (D). The overall intensities of the images B, C and D are lower than that in A, due to both the suppression of the vascular artifacts from small blood vessels and T1 relaxation of the brain tissue water during the post-tagging delay (see below).

Vascular Transit Time

When measuring perfusion with CAST, the arterial spins are tagged at the carotid arteries. After tagging, the spins have to travel from the plane where they are tagged to

the imaging plane before they can exchange with the brain tissue water (73). The interval between the time just after the arterial spins are tagged and the time just before they start to exchange with the brain tissue water in the imaging plane is usually referred as the "vascular transit time". It is worthwhile to pointed out that, the vascular transit time, by this definition, is different from the "mean transit time" defined in the first pass bolus tracking experiment. The vascular transit time affects perfusion quantification through its effects on α which results from T1 relaxation of the tagged blood water spins. If the effect of the vascular transit time is not accounted for, the use of the α value at the tagging plane to calculate f will underestimate the perfusion rate. The vascular transit time in normal rat brain is about 200 ms (73). The vascular transit time in human brain is somewhat longer and has a range of about 600-1000 ms (52), so that the effects of vascular transit time on perfusion quantification in a CAST experiment are more significant in humans than in rats.

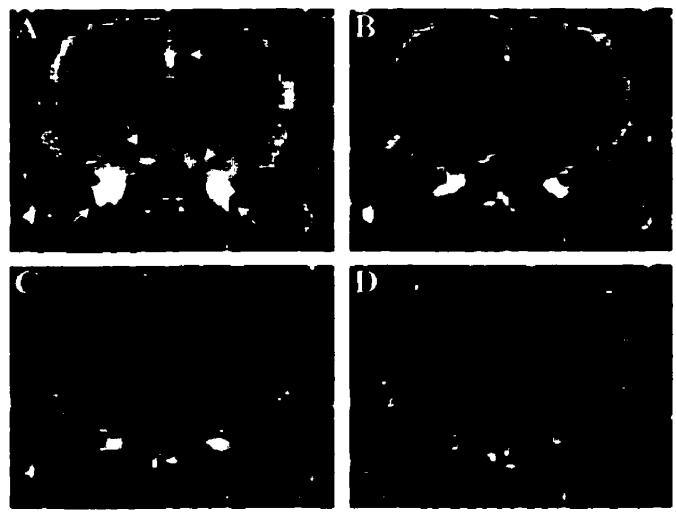

Figure 3.6 Perfusion weighted images acquired without post-tagging delay (A) and with a post-tagging delay of 280 ms (B), 400 ms (C) and 600 ms (D). White arrows indicate the locations of major blood vessels.

The value of the vascular transit time also depends on CBF (73). Compared to brain regions with lower CBF, brain regions with higher CBF usually have a shorter vascular transit time, thus a higher effective α value in the imaging plane so that the underestimation of CBF in these regions is smaller if α at the tagging plane is used to calculate CBF. As a result, sensitivity of the vascular transit time to CBF will cause regional errors in the perfusion determination whenever there is a significant variation in perfusion rate across the brain (52).

The vascular transit time sensitivity of a perfusion measurement using CAST can be eliminated by inserting a post-tagging delay between the spin-tagging pulse and the imaging sequence which is longer than the longest vascular transit time observed in the imaging plane (52). A mathematical model has been developed for perfusion measurements by CAST with the use of a post-tagging delay, in which a correction factor that can be determined experimentally is used to account for the vascular transit time effect on α as well as the T1 relaxation of the brain tissue water during the post-tagging delay (52).

Although T1 relaxation of the brain tissue water during the post-tagging delay decreases the sensitivity of the perfusion measurement, the use of a post-tagging delay is essential to remove the vascular artifacts and vascular transit time sensitivity to obtain accurate perfusion measurements. When a snapshot FLASH imaging sequence is used, phase-

encoding steps are acquired sequentially so that the effective post-tagging delay varies among the k_y line in k-space[1]. For example, if the total imaging time is 550 ms and the post-delay for the first k_y line is 400 ms, then the effective post-tagging is 675 ms for the central k_y line and 950 ms for the final k_y line. One solution to this problem is to calculate the correction factor using an apparent post-tagging delay which corresponds to the effective post-tagging delay of the k_y=0 line. It should be noted that this approximation only applies when the total imaging time is short relative to $T1_b$. When the total imaging time becomes comparable to $T1_b$ (e.g. for a large imaging matrix), this variation in the post-tagging delay over k-space could significantly affect the calculated perfusion rate. In such cases, segmented acquisition may become necessary.

Magnetization Recovery During Acquisition

Unlike EPI, snapshot FLASH is a multiple-shot imaging technique with a typical imaging time of 200-1200 ms depending on the spatial resolution of the image and TR. Because of the multiple-shot nature, it is a requirement that all phase-encoding steps have an identical amount of longitudinal magnetization in order to give an artifact-free image. When the initial longitudinal magnetization is at its equilibrium value, this requirement can often be fulfilled by carefully adjusting the flip angle of the excitation pulse (θ) and TR. However, due to the effect of T1 relaxation, this is often impossible when the initial longitudinal magnetization is not at its equilibrium value. The evolving longitudinal magnetization during acquisition will then distort the point spread function and result in

[1] *k*-space: a reciprocal space in which a vector represents the Fourier Transform of a vector in spatial coordinates [P. Mansfield, *J. Phys. E.* **21**, 18, (1988)].

blurring or edge enhancing artifacts that can not be eliminated by using the central phase encoding scheme (74,75).

In perfusion imaging experiments using CAST, $M_b^{inv} \neq M_b^{con} < M_b^0$. When a snapshot FLASH imaging sequence is used to acquire the proton density weighted images, the longitudinal magnetization prepared by CAST evolves during acquisition through two mechanisms with opposite effects: T1 relaxation and progressive saturation (74,75). Furthermore, the courses of this evolution are different in the tagging experiment and in the control experiment. As a result, the evolving longitudinal magnetization during acquisition will introduce edge enhancing artifacts on the proton density weighted images and these artifacts will be propagated into the perfusion image through calculation. To illustrate this, numerical simulation was performed on a fictitious phantom and the result of the simulation is shown in Fig. 3.7. The phantom was composed of 128 pixels among which pixels 33 to 96 were the region of interest having an assumed uniform perfusion rate with $M_b^{inv}=0.30$ and $M_b^{con}=0.35$. It was also assumed that $M_b^0=1.0$, TR=4.3 ms, $\theta=12^\circ$, $T1_b=1.70$ s and a 128-step linear phase-encoding scheme was used. Parameters were chosen to resemble the situation in a real perfusion measurement. T1 recovery curves of M_b^{inv} and M_b^{con} are shown in Fig. 3.7A, illustrating the different levels of longitudinal magnetization for different phase-encoding steps in the spin-tagging and the control experiments. Fig. 3.7B compares the real perfusion profile (solid line) and the "measured" perfusion profile (dashed line) of the phantom. The intensity of $M_b^{con} - M_b^{inv}$ was used as a measure of perfusion. The "measured" perfusion profile was calculated by inverse Fourier-transforming the distorted *k*-

space data, which were generated by filtering the actual *k*-space data with functions shown in Fig. 3.7A. From Fig. 3.7B, three types of perfusion artifacts caused by T1 relaxation during acquisition can be identified. First, the "measured" perfusion profile has a lower intensity than the real perfusion profile across the entire region of interest. Second, underestimation of the perfusion rate at the center of the region of interest is larger than that at the edges of the region, demonstrating the presence of the edge enhancing effect. Third, artificial perfusion is evident outside the region of interest.

Two measures can be used, theoretically, to correct for these artifacts. The first solution is to use variable flip angle FLASH imaging instead of snapshot FLASH imaging to acquire the data, with the flip angle of the excitation pulse for each phase-encoding step adjusted to counterbalance the decreasing longitudinal magnetization (76,77). The second solution involves dividing the data acquired with snapshot FLASH imaging by a calibration function prior to reconstruction, a process that numerically equalizes the amount of the transverse magnetization observed among different phase encoding steps (75). However, in practice both methods require complicated experimental protocols and are thus often inconvenient to use.

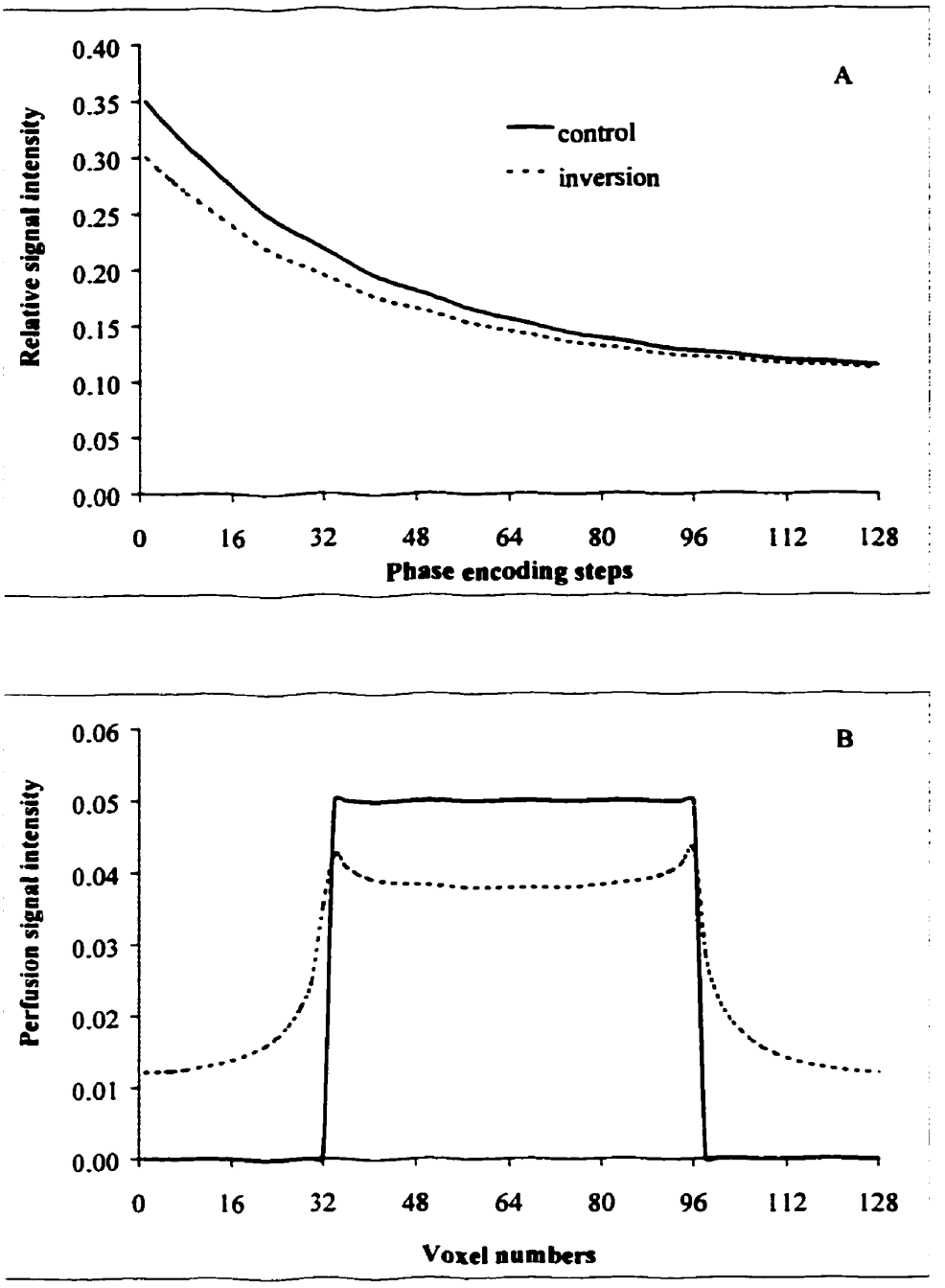

Figure 3.7 Evolution of the longitudinal magnetization during the acquisition period in an arterial spin tagging perfusion imaging using snapshot FLASH as a read-out (A); this evolution of longitudinal magnetization during acquisition introduces edge-enhancing artifacts to the perfusion image (B).

Error Propagation Analysis for MR Perfusion Imaging Using Continuous Arterial Spin Tagging

The precision with which f can be determined depends on the SNR of the perfusion image (SNR_{perfu}). Because the perfusion image is calculated algebraically from proton density weighted images, assessment of SNR_{perfu} requires an error propagation analysis.

In a CAST experiment, the expression for the perfusion is Eq. [3.27]. For simplicity, define the normalized difference in proton density signal intensities (β),

$$\beta = \frac{M_b^{con} - M_b^{inv}}{M_b^{con}} = \frac{2\alpha f}{\lambda}\left(\frac{1}{T1_o} + \delta\right)^{-1}. \qquad [3.36]$$

The variation in β ($\Delta\beta$) resulting from random noise in M_b^{con} (ΔM_b^{con}) and M_b^{inv} (ΔM_b^{inv}) is

$$\Delta\beta = \sqrt{\left(\frac{\partial\beta}{\partial M_b^{con}}\Delta M_b^{con}\right)^2 + \left(\frac{\partial\beta}{\partial M_b^{inv}}\Delta M_b^{inv}\right)^2}. \qquad [3.37]$$

Assuming that $T1_o$ and α can be determined precisely, and that $\Delta M_b^{con} = \Delta M_b^{inv} = N$, Eqs. [3.36] and [3.37] give

$$\Delta\beta = \frac{N}{M_b^{con}}\sqrt{1 + \left(1 - \frac{2\alpha f}{\lambda}\left(\frac{1}{T1_o} + \delta\right)^{-1}\right)^2}$$

and since the SNR of the proton density images (SNR_{image}) is

$$\frac{1}{SNR_{image}} = \frac{N}{M_b^{con}},$$

$$\Delta\beta = \frac{1}{SNR_{image}}\sqrt{1 + \left(1 - \frac{2\alpha f}{\lambda}\left(\frac{1}{T1_o} + \delta\right)^{-1}\right)^2}. \qquad [3.38]$$

Because $2\alpha f(1/T1_o+\delta)^{-1}/\lambda<<1$ (typically about 0.07) even when the perfusion rate is very high, Eq. [3.38] can be simplified to

$$\Delta\beta = \frac{\sqrt{2}}{SNR_{image}}. \qquad [3.39]$$

Then from Eqs. [3.36] and [3.39],

$$SNR_{perfu} = \frac{\beta}{\Delta\beta} = \sqrt{2}SNR_{image}\frac{\alpha f}{\lambda}\left(\frac{1}{T1_o} + \frac{k_{for}}{1+k_{rev}T1_m + R_m T1_m}\right)^{-1}. \qquad [3.40]$$

SNR_{perfu} is therefore proportional to both α and SNR_{image}. With typical values for α, λ, $T1_o$, $T1_m$, k_{for}, k_{rev}, and R_m, Eq. [3.40] shows that SNR_{perfu} is reduced about 20 fold compared to SNR_{image}, even when blood flow is high. Then proton density weighted images with SNR_{image} as high as 100:1 can generate a perfusion image with SNR_{perfu} only about 5:1, and the precision with which f can be determined can then be no better than ±20%.

A Strategy to Optimize the Signal-to-Noise Ratio in One-Coil MR Perfusion Imaging Using Continuous Arterial Spin Tagging

Introduction

Improved precision in determining f requires high SNR_{perfu}. In a conventional one-coil CAST experiment, it is usually assumed that MT effects arise from complete saturation of macromolecule spins in the imaging plane, and effects due to direct irradiation of water spins are usually ignored. Accurate determination of cerebral perfusion then requires that B_1 and the offset ($\Delta\omega$, which is determined by the gradient strength G_l applied during spin tagging) of the spin-tagging RF pulse be chosen to saturate the macromolecule spins

completely while not directly affecting water spins in the imaging plane. However, complete saturation of macromolecule spins does not occur under typical experimental conditions. Even so, the resulting MT and DORI effects can reduce image intensity by as much as 70% (24), and in turn decrease SNR_{perfu} by the same amount (Eq. [3.40]).

Improved SNR_{perfu} requires increases in either α or SNR_{image}. Typically α is about 0.6-0.8, and non-laminar arterial flow and longitudinal relaxation of labeled spins in transit from the labeling plane to the imaging plane limits the extent to which α can be increased. The most straightforward way to increase SNR_{image} is to increase the number of averages. However, the resulting increase in total acquisition time may make this impractical. SNR_{image} can also be increased by reducing the MT/DORI effects, as long as α is not affected. This can be accomplished by decreasing B_1, or by increasing $\Delta\omega$ by increasing G_l. However, simply decreasing B_1 or increasing G_l alone will decrease the right side of the inequality required to satisfy the adiabatic-fast-passage condition. Then α will decrease. However, it is possible to increase the brain tissue water signal without compromising the adiabatic-fast-passage requirements if both B_1 and G_l are increased.

For example, with typical values of k_{for}=1.35 s^{-1}, k_{rev}=33.65 s^{-1}, $T1_b$=1.71 s, $T1_m$=1.32 s, f=1.98 ml·min^{-1}·g^{-1}, α=0.7, and λ=0.9 ml/g, and with calculated R values, magnetization transfer curves in the presence of perfusion can be simulated from Eq. [3.19] (Fig. 3.8). With commonly used experimental parameters B_1=100 mG, G_l=1 G/cm and $\Delta\omega$=10 kHz, M_b^{inv}/M_b^0 is about 0.30 and the inequalities in Eq. [3.2] are satisfied (12.0<<100.0<<428.8) if V=10.0 cm/s and $1/T2_a$=12.0 s^{-1} are assumed. Increasing B_1 to 150 mG, G_l to 2 G/cm,

and $\Delta\omega$ to 20 kHz, M_b^{inv}/M_b^0 is increased by a factor of about 1.6, to about 0.47. Both inequalities in Eq. [3.2] remain satisfied (12.0<<133.3<<643.2), so that α will not decrease, and may even increase slightly. The net result is a theoretical 1.6-fold increase in SNR_{image} and therefore in SNR_{perfu}.

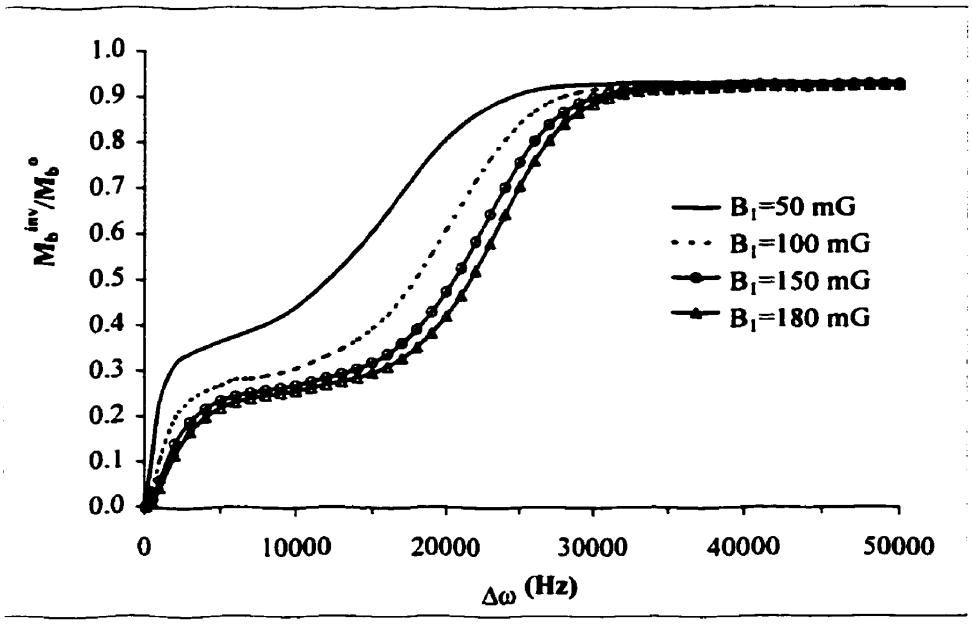

Figure 3.8 Magnetization transfer curves in the presence of perfusion generated using Eq. [3.19], showing the dependence of the steady state water signal intensity on the offset $\Delta\omega$ and strength B_1 of the off-resonance irradiation.

Materials and Methods

The experiments used 4 male Sprague-Dawley rats, 250-300 g, anesthetized with 1.0-1.5% halothane in 30/70 O_2/N_2O administered via a nose cone. Volume-localized ^1H spectra acquired using a STEAM sequence were used to demonstrate the effect of B_1 and $\Delta\omega$ on signal intensity M_b^{inv} with a voxel size of 5×5×5 mm^3. A 3 s off-resonance RF pulse was inserted into the TR period before the STEAM sequence, using either B_1=100 mG, $\Delta\omega$=10

kHz or B_1=150 mG, $\Delta\omega$=20 kHz. Each spectrum was obtained with 4 transients acquired into 2048 data points with TR=5 s, TE=20 ms and TM=10 ms. FIDs were zero-filled to 4096 data points and line-broadened by 5 Hz prior to Fourier transformation. Peak height was used to quantitate signal intensity.

Perfusion imaging was done using a snapshot FLASH imaging sequence with a 5×5 cm^2 field of view, 2 mm thick slice excited using a 1 ms Gaussian pulse, 128×128 matrix size, TR=4.3 ms, TE=2.3 ms, 12° flip angle, and 28 averages. Arterial labelling was done using a 5 s RF pulse and a gradient in the slice selection direction applied before the imaging sequence, using either B_1=100 mG, G_l=1 G/cm, or B_1=150 mG, G_l=2 G/cm. The RF offset $\Delta\omega$ was adjusted to keep the labeling plane in the same location. A 400 ms delay was inserted between the labeling pulse and the start of the imaging sequence to eliminate transit time sensitivity and vascular artifact. Four sets of proton density images were acquired using a four-step offset-gradient cycling protocol to eliminate the asymmetrical magnetization transfer effect. Perfusion images were calculated using both Eq. [3.27] and Eq. [3.30] with λ=0.9 and R_m calculated using $T2_m$=20.0 μs (47), then corrected for post-tagging delay. The perfusion images were compared to show the effects of B_1 and G_l on perfusion quantification and SNR_{perfu}. For each animal, the mean perfusion rate over the entire brain, f_{mean}, was used, together with the average signal from extracranial muscle in the perfusion images as a measure of the noise (N) propagated from the proton density images through the perfusion calculation, to calculate SNR_{perfu} as f_{mean}/N.

The $T1_o$ map used to calculate the perfusion images was obtained using a slice-selective inversion-recovery snapshot FLASH sequence with acquisition parameters as above, except that only 6 averages were acquired. A set of 12 images with inversion-recovery delays ranging from 290 ms to 7.5 s was acquired. The effects of B_1 and G_1 on α were measured using a gradient-echo sequence with G_1=1 or 2 G/cm, and 7 values of B_1 ranging from 19 to 141 mG in each case. The offset $\Delta\omega$ was adjusted to keep the labelling plane in the same position.

Results

The labeling pulse decreased the H_2O peak height in the STEAM experiments. For B_1=100 mG, $\Delta\omega$=10 kHz, the relative steady state water signal intensity in the STEAM experiment was 0.324±0.016. For B_1=150 mG, $\Delta\omega$=20 kHz, the relative signal intensity increased by a factor of 1.6, to 0.510±0.068 ($p<0.002$, paired t-test), in agreement with theory.

Figure 3.9 shows how α changed with B_1 and G_1. Except at the extremes of the range studied, α was significantly higher ($p<0.05$, paired t-test) when G_1 was lower for a given value of B_1. Increasing B_1 stepwise by a factor of about 1.4 while simultaneously increasing G_1 from 1 to 2 G/cm maintained the same value of α.

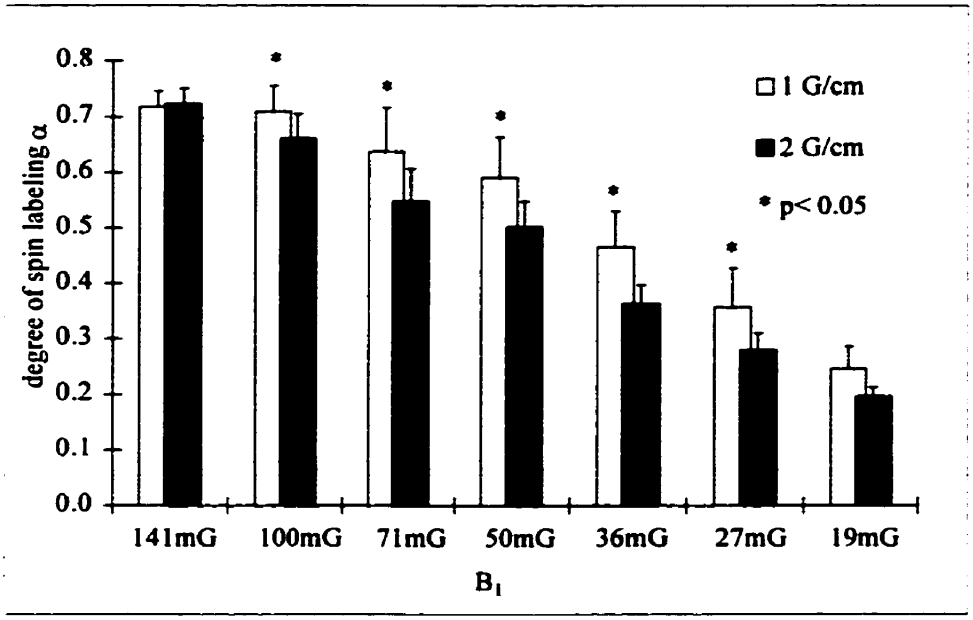

Figure 3.9 Measured values of the degree of spin labeling α in perfusion imaging experiments using different RF strengths and gradient offsets. Error bars represent standard deviations in measurements on 4 rats.

Table 3.1 Mean values of α, SNR_{perfu} and f_{mean} ($ml \cdot g^{-1} \cdot min^{-1}$) from measurements on 4 rats (±SD) at two different combinations of B_1 and G_1

measurement	B_1=100 mG G_1=1 G/cm	B_1=150 mG G_1=2 G/cm	two-tailed paired t-test
degree of labeling α	0.71±0.05	0.72±0.03	N.S.
SNR_{perfu}	2.70±0.53	4.04±0.75	p=0.045
f_{mean} calculated by Eq. [3.30]	2.03±0.10	1.75±0.07	p<0.0001
f_{mean} calculated by Eq. [3.27]	2.09±0.10	1.95±0.07	N.S.

Figure 3.10 shows perfusion images calculated using Eq. [3.30] (A, B) or Eq. [3.27] (C, D) for experiments with B_1=100 mG, G_1=1 G/cm, Δω=9000 Hz (A, C) or B_1=150 mG, G_1=2 G/cm, Δω=18000 Hz (B, D). As shown in Table 3.1, α was identical under the two experimental conditions. Increasing B_1 and G_1 increased the SNR in the perfusion images by

a factor of about 1.5, in good agreement with theory. The perfusion rate calculated using Eq. [3.27] (A,B) was not affected by the experimental conditions, while Eq. [3.30] underestimated f when B_1 and G_1 were increased in order to increase SNR_{perfu}.

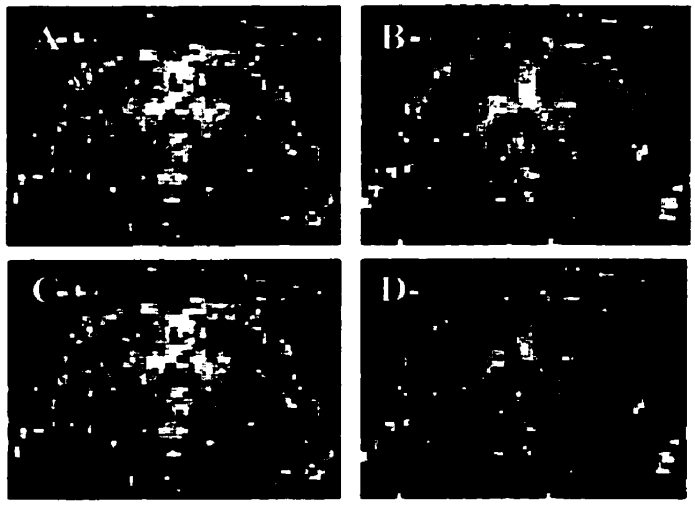

Figure 3.10 Perfusion images of rat brain calculated using Eq. [3.30] (A, B) or Eq. [3.27] (C, D) for experiments with B_1=100 mG, G_1=1 G/cm, $\Delta\omega$=9000 Hz (A, C) or B_1=150 mG, G_1=2 G/cm, $\Delta\omega$=18000 Hz (B, D).

Discussion

It has been shown both theoretically and experimentally that SNR_{perfu}, and hence the precision with which the perfusion rate f can be determined, can be significantly improved by simultaneously increasing the strength and offset of the labeling RF pulse, and this can be done without affecting the degree of arterial labeling α, but not without decreasing the degree of saturation of macromolecular spins in the brain. The result is that magnetization transfer effects to the brain water spins are decreased. Calculation of perfusion rates without considering this (for example using Eq. [3.30]) leads to an underestimation of f.

Temporal Resolution of MR Perfusion Imaging Using CAST and Snapshot FLASH Imaging as a Read-out

When snapshot FLASH imaging is used as the read-out, the temporal resolution of the perfusion measurement depends on the number of averages accumulated for each proton density weighted image and TR of the sequence. To obtain quantitative perfusion images, sufficient signal averaging is often necessary to ensure sufficient SNR_{image} and thus SNR_{perfu} because of the intrinsic insensitivity of the perfusion measurement and the low flip angle excitation pulse associated with the snapshot FLASH sequence. TR of a perfusion imaging sequence using CAST is determined primarily by the length of the spin-tagging pulse, which usually has to be kept long enough to ensure that a steady-state longitudinal magnetization is reached at the end of spin tagging.

The temporal resolution of perfusion measurements using snapshot FLASH imaging can be increased by either improving SNRT of the perfusion measurement or shortening TR. For a given SNR, increasing SNRT will reduce the number of averages required and therefore improves the temporal resolution. Using the optimization strategy proposed, a 1.5 fold SNRT increase has been demonstrated, implying a potential 1.5 fold increase in temporal resolution for the perfusion measurement. Another way to improve temporal resolution is to shorten TR through decreasing the duration of the spin tagging pulse. It has been shown that TR can be reduced from the commonly-used value of 2.5 to 3.0 s to values as short as 1.5 s, without decreasing SNR or reducing the precision of the perfusion measurement significantly (19).

Using snapshot FLASH imaging as the readout, the temporal resolution of a dynamic perfusion measurement can be determined after acquisition through data processing. By acquiring the proton density weighted images rapidly and storing them into separate blocks, a given temporal resolution can always be obtained by averaging a set number of sequentially-acquired image blocks and shifting this process in the time domain. The only disadvantage of this method is the requirement of large disk space for data storage.

Recent Developments in MR Perfusion Imaging Using AST

Recently, four novel methods of MR perfusion imaging using AST were reported, which share the basic principles with the described MR perfusion imaging methods using AST, but have technical aspects which are quite different from what has been described in the earlier part of this chapter.

1. Normally, perfusion images are calculated using proton density weighted images. It was shown by Schwarzbauer et al (56) that T1 maps acquired with different inversion-recovery sequences can also be used to calculate both quantitative perfusion images and perfusion-weighted images. The quantification of perfusion using the T1 method is not complicated by the vascular transit time effect and the MT effect, thus it is, in principle, better than conventional methods. However, the inversion-recovery sequences used to acquire the T1 maps are generally very time-consuming so that the SNRT of this

technique is low compared to conventional methods and therefore its practical usefulness is often limited.

2. Several assumptions are made when the tracer kinetics in an AST experiment are modeled mathematically and any violation of those assumptions will potentially cause significant systematic errors in perfusion quantification. In order to relax those assumptions Buxton et al (40) developed a general kinetic model for perfusion quantification with convolution theory which is applicable to both the CAST and the PAST experiments. Using this method, perfusion is evaluated with the vascular transit time and the tissue T1 relaxation time simultaneously using a tissue response curve to a series of AST schemes. Although the usefulness of this method was demonstrated in the original report, further investigation is required to determine the precision of the perfusion measurement by this method.

3. Spin tagging in conventional MR perfusion imaging experiments is usually carried out in either the continuous or the pulsed mode, with which parameters such as α, $T1_0$ and vascular transit time needed for perfusion calculation usually have to be measured in separate experiments. By modifying the mathematical model used in a CAST experiment, it was shown in a recent study by Barbier et al (78) that perfusion can be quantified by analyzing the tissue response to a periodic perfusion-related perturbation such as an RF-driven time varying α. With this method, parameters such as $T1_0$ and the vascular transit time can actually be estimated simultaneously with perfusion, thus improving the perfusion quantification. However, the scanning time per perfusion measurement with

this method may be significantly longer than that with conventional methods, thus limiting the SNRT of the perfusion measurement if a constraint in the total scanning time applies.

4. In attempting to measure blood flow in the rat ovary, Tempel et al (31) recently proposed an interesting perfusion imaging method in which a steady-state measurement of the tissue response to pulsed AST is used. The method has advantages of both the CAST and the PAST experiments. For example, perfusion is more quantifiable in this method than in the conventional PAST methods. Compared to the conventional CAST experiment, this method does not require prolonged AST at major blood vessels and has smaller MT effects to decrease the SNR of the perfusion measurement, thus permitting higher temporal resolution. It is technically feasible to use this method to acquire three-dimensional perfusion images. Furthermore, the method also provides a precise way to measure the velocity of arterial blood flow in small blood vessels, which is usually difficult to assess using other methods.

References

1. C. S. Ewy, J. J. Ackerman and R. S. Balaban, Deuterium NMR cerebral imaging in situ, *Magn. Reson. Med.* **8**, 35, (1988).

2. J. A. Detre, V. H. Subramanian, M. D. Mitchell, D. S. Smith, A. Kobayashi, A. Zaman and J. S. J. Leigh, Measurement of regional cerebral blood flow in cat brain using intracarotid $^{2}H_2O$ and ^{2}H NMR imaging, *Magn. Reson. Med.* **14**, 389, (1990).

3. D. Fiat and S. Kang, Determination of the rate of cerebral oxygen consumption and regional cerebral blood flow by non-invasive ^{17}O in vivo NMR spectroscopy and magnetic resonance imaging: Part 1. Theory and data analysis methods, *Neurol. Res.* **14**, 303, (1992).

4. J. Pekar, L. Ligeti, Z. Ruttner, R. C. Lyon, T. M. Sinnwell, P. van Gelderen, D. Fiat, C. T. Moonen and A. C. McLaughlin, In vivo measurement of cerebral oxygen consumption and blood flow using ^{17}O magnetic resonance imaging, *Magn. Reson. Med.* **21**, 313, (1991).

5. K. K. Kwong, A. L. Hopkins, J. W. Belliveau, D. A. Chesler, L. M. Porkka, R. C. McKinstry, D. A. Finelli, G. J. Hunter, J. B. Moore and R. G. Barr , Proton NMR imaging of cerebral blood flow using $H_2(^{17})O$, *Magn. Reson. Med.* **22**, 154, (1991).

6. J. Pekar, T. Sinnwell, L. Ligeti, A. S. Chesnick, J. A. Frank and A. C. McLaughlin, Simultaneous measurement of cerebral oxygen consumption and blood flow using ^{17}O and ^{19}F magnetic resonance imaging, *J. Cereb. Blood Flow Metab.* **15**, 312, (1995).

7. J. Pekar, L. Ligeti, T. Sinnwell, C. T. Moonen, J. A. Frank and A. C. McLaughlin, ^{19}F magnetic resonance imaging of cerebral blood flow with 0.4 cc resolution, *J. Cereb. Blood Flow Metab.* **14**, 656, (1994).

8. C. A. Branch, J. R. Ewing, J. A. Helpern, R. J. Ordidge, S. Butt and K. M. Welch, Atraumatic quantitation of cerebral perfusion in cats by ^{19}F magnetic resonance imaging, *Magn. Reson. Med.* **28**, 39, (1992).

9. C. A. Branch, J. A. Helpern, J. R. Ewing and K. M. Welch, ^{19}F NMR imaging of cerebral blood flow, *Magn. Reson. Med.* **20**, 151, (1991).

10. D. Eidelberg, G. Johnson, P. S. Tofts, J. Dobbin, H. A. Crockard and D. Plummer, ^{19}F imaging of cerebral blood oxygenation in experimental middle cerebral artery occlusion: preliminary results, *J. Cereb. Blood Flow Metab.* **8**, 276, (1988).

11. J. W. Belliveau, B. R. Rosen, H. L. Kantor, R. R. Rzedzian, D. N. Kennedy, R. C. McKinstry, J. M. Vevea, M. S. Cohen, I. L. Pykett and T. J. Brady, Functional cerebral imaging by susceptibility-contrast NMR, *Magn. Reson. Med.* **14**, 538, (1990).

12. B. R. Rosen, J. W. Belliveau, B. R. Buchbinder, R. C. McKinstry, L. M. Porkka, D. N. Kennedy, M. S. Neuder, C. R. Fisel, H. J. Aronen and K. K. Kwong, Contrast agents and cerebral hemodynamics, *Magn. Reson. Med.* **19**, 285, (1991).

13. B. R. Rosen, J. W. Belliveau, J. M. Vevea and T. J. Brady, Perfusion imaging with NMR contrast agents, *Magn. Reson. Med.* **14**, 249, (1990).

14. A. Villringer, B. R. Rosen, J. W. Belliveau, J. L. Ackerman, R. B. Lauffer, R. B. Buxton, Y. S. Chao, V. J. Wedeen and T. J. Brady, Dynamic imaging with lanthanide chelates in normal brain: contrast due to magnetic susceptibility effects, *Magn. Reson. Med.* **6**, 164, (1988).

15. J. Kucharczyk, H. Asgari, J. Mintorovitch, Z. Vexler, M. Moseley, A. Watson and S. Rocklage, Magnetic resonance imaging of brain perfusion using the nonionic contrast agents Dy-DTPA-BMA and Gd-DTPA-BMA, *Invest. Radiol.* **26 Suppl 1**, S250, (1991).

16. J. A. Detre, J. S. Leigh Jr., D. S. Williams and A. P. Koretsky, Perfusion imaging, *Magn. Reson. Med.* **23**, 37, (1992).

17. D. S. Williams, J. A. Detre, J. S. Leigh Jr. and A. P. Koretsky, Magnetic resonance imaging of perfusion using spin inversion of arterial water , *Proc. Natl. Acad. Sci. U. S. A.* **89**, 212, (1992).

18. J. A. Detre, W. Zhang, D. A. Roberts, A. C. Silva, D. S. Williams, D. J. Grandis, A. P. Koretsky and J. S. Leigh Jr., Tissue specific perfusion imaging using arterial spin labeling, *NMR Biomed.* **7**, 75, (1994).

19. E. C. Wong, R. B. Buxton and L. R. Frank, A theoretical and experimental comparison of continuous and pulsed arterial spin labeling techniques for quantitative perfusion imaging, *Magn. Reson. Med.* **40**, 348, (1998).

20. M. L. Forbes, K. S. Hendrich, J. K. Schiding, D. S. Williams, C. Ho, S. T. DeKosky, D. W. Marion and P. M. Kochanek, Perfusion MRI assessment of cerebral blood flow and CO_2 reactivity after controlled cortical impact in rats, *Adv. Exp. Med. Biol.* **411**, 7, (1997).

21. M. L. Forbes, K. S. Hendrich, P. M. Kochanek, D. S. Williams, J. K. Schiding, S. R. Wisniewski, S. F. Kelsey, S. T. DeKosky, S. H. Graham, D. W. Marion and C. Ho, Assessment of cerebral blood flow and CO_2 reactivity after controlled cortical impact by perfusion magnetic resonance imaging using arterial spin-labeling in rats, *J. Cereb. Blood Flow Metab.* **17**, 865, (1997).

22. M. D. King, N. van Bruggen, A. L. Busza, J. Houseman, S. R. Williams and D. G. Gadian, Perfusion and diffusion MR imaging, *Magn. Reson. Med.* **24**, 288, (1992).

23. A. C. Silva, W. Zhang, D. S. Williams and A. P. Koretsky, Multi-slice MRI of rat brain perfusion during amphetamine stimulation using arterial spin labeling, *Magn. Reson. Med.* **33**, 209, (1995).

24. W. Zhang, A. C. Silva, D. S. Williams and A. P. Koretsky, NMR measurement of perfusion using arterial spin labeling without saturation of macromolecular spins, *Magn. Reson. Med.* **33**, 370, (1995).

25. W. Zhang, D. S. Williams and A. P. Koretsky, Measurement of rat brain perfusion by NMR using spin labeling of arterial water: in vivo determination of the degree of spin labeling, *Magn. Reson. Med.* **29**, 416, (1993).

26. D. A. Roberts, J. A. Detre, L. Bolinger, E. K. Insko and J. S. Leigh Jr., Quantitative magnetic resonance imaging of human brain perfusion at 1.5 T using steady-state inversion of arterial water, *Proc. Natl. Acad. Sci. U. S. A.* **91**, 33, (1994).

27. D. A. Roberts, J. A. Detre, L. Bolinger, E. K. Insko, R. E. Lenkinski, M. J. Pentecost and J. S. Leigh Jr., Renal perfusion in humans: MR imaging with spin tagging of arterial water, *Radiology* **196**, 281, (1995).

28. J. A. Detre, D. C. Alsop, L. R. Vives, L. Maccotta, J. W. Teener and E. C. Raps, Noninvasive MRI evaluation of cerebral blood flow in cerebrovascular disease, *Neurology* **50**, 633, (1998).

29. D. S. Williams, D. J. Grandis, W. Zhang and A. P. Koretsky, Magnetic resonance imaging of perfusion in the isolated rat heart using spin inversion of arterial water, *Magn. Reson. Med.* **30**, 361, (1993).

30. D. S. Williams, W. Zhang, A. P. Koretsky and S. Adler, Perfusion imaging of the rat kidney with MR, *Radiology* **190**, 813, (1994).

31. C. Tempel and M. Neeman, Perfusion of the rat ovary: application of pulsed arterial spin labeling MRI, *Magn. Reson. Med.* **41**, 113, (1999).

32. F. Calamante, S. R. Williams, N. van Bruggen, K. K. Kwong and R. Turner, A model for quantification of perfusion in pulsed labelling techniques, *NMR Biomed.* **9**, 79, (1996).

33. R. R. Edelman, B. Siewert, D. G. Darby, V. Thangaraj, A. C. Nobre, M. M. Mesulam and S. Warach, Qualitative mapping of cerebral blood flow and functional localization with echo-planar MR imaging and signal targeting with alternating radio frequency, *Radiology* **192**, 513, (1994).

34. S. G. Kim, Quantification of relative cerebral blood flow change by flow-sensitive alternating inversion recovery (FAIR) technique: application to functional mapping, *Magn. Reson. Med.* **34**, 293, (1995).

35. S. G. Kim and N. V. Tsekos, Perfusion imaging by a flow-sensitive alternating inversion recovery (FAIR) technique: application to functional brain imaging, *Magn. Reson. Med.* **37**, 425, (1997).

36. E. C. Wong, R. B. Buxton and L. R. Frank, Implementation of quantitative perfusion imaging techniques for functional brain mapping using pulsed arterial spin labeling, *NMR Biomed.* **10**, 237, (1997).

37. E. C. Wong, R. B. Buxton and L. R. Frank, Quantitative imaging of perfusion using a single subtraction (QUIPSS and QUIPSS II), *Magn. Reson. Med.* **39**, 702, (1998).

38. S. S. Berr and V. M. Mai, Extraslice spin tagging (EST) magnetic resonance imaging for the determination of perfusion, *J. Magn. Reson. Imaging* **9**, 146, (1999).

39. N. V. Tsekos, F. Zhang, H. Merkle, M. Nagayama, C. Iadecola and S. G. Kim, Quantitative measurements of cerebral blood flow in rats using the FAIR technique: correlation with previous iodoantipyrine autoradiographic studies, *Magn. Reson. Med.* **39**, 564, (1998).

40. R. B. Buxton, L. R. Frank, E. C. Wong, B. Siewert, S. Warach and R. R. Edelman, A general kinetic model for quantitative perfusion imaging with arterial spin labeling, *Magn. Reson. Med.* **40**, 383, (1998).

41. W. T. Dixon, L. N. Du, D. D. Faul, M. Gado and S. Rossnick, Projection angiograms of blood labeled by adiabatic fast passage, *Magn. Reson. Med.* **3**, 454, (1986).

42. D. A. Roberts, L. Bolinger, J. A. Detre, E. K. Insko, P. Bergey and J. S. Leigh Jr., Continuous inversion angiography, *Magn. Reson. Med.* **29**, 631, (1993).

43. K. K. Kwong, D. A. Chesler, R. M. Weisskoff and B. R. Rosen, *Abstr. Int. Soc. Magn. Reson. Med.*, 1005 (1994).

44. W. M. Luh, E. C. Wong, P. A. Bandettini and J. S. Hyde, QUIPSS II with thin-slice $T1_1$ periodic saturation: A method for improving accuracy of quantitative perfusion imaging using pulsed arterial spin tagging, *Magn. Reson. Med.* **41**, 1246, (1999).

45. J. Eng, T. L. Ceckler and R. S. Balaban, Quantitative ^1H magnetization transfer imaging in vivo, *Magn. Reson. Med.* **17**, 304, (1991).

46. B. S. Hu, S. M. Conolly, G. A. Wright, D. G. Nishimura and A. Macovski, Pulsed saturation transfer contrast, *Magn. Reson. Med.* **26**, 231, (1992).

47. C. Morrison, G. Stanisz and R. M. Henkelman, Modeling magnetization transfer for biological-like systems using a semi-solid pool with a super-Lorentzian lineshape and dipolar reservoir, *J. Magn. Reson. B.* **108**, 103, (1995).

48. D. Brooks, K. Kuwata and T. Schleich, Determination of proton magnetization transfer rate constants in heterogeneous biological systems, *Magn. Reson. Med.* **31**, 331, (1994).

49. A. C. McLaughlin, F. Q. Ye, J. J. Pekar, A. K. Santha and J. A. Frank, Effect of magnetization transfer on the measurement of cerebral blood flow using steady-state arterial spin tagging approaches: a theoretical investigation, *Magn. Reson. Med.* **37**, 501, (1997).

50. D. C. Alsop and J. A. Detre, Multisection cerebral blood flow MR imaging with continuous arterial spin labeling, *Radiology* **208**, 410, (1998).

51. G. Zaharchuk, P. J. Ledden, K. K. Kwong, T. G. Reese, B. R. Rosen and L. L. Wald, Multislice perfusion and perfusion territory imaging in humans with separate label and image coils, *Magn. Reson. Med.* **41**, 1093, (1999).

52. D. C. Alsop and J. A. Detre, Reduced transit-time sensitivity in noninvasive magnetic resonance imaging of human cerebral blood flow, *J. Cereb. Blood Flow Metab.* **16**, 1236, (1996).

53. F. Q. Ye, J. J. Pekar, P. Jezzard, J. Duyn, J. A. Frank and A. C. McLaughlin, Perfusion imaging of the human brain at 1.5 T using a single-shot EPI spin tagging approach, *Magn. Reson. Med.* **36**, 217, (1996).

54. C. M. Kerskens, M. Hoehn Berlage, B. Schmitz, E. Busch, C. Bock, M. L. Gyngell and K. A. Hossmann, Ultrafast perfusion-weighted MRI of functional brain activation in rats during forepaw stimulation: comparison with T2-weighted MRI, *NMR Biomed.* **9**, 20, (1996).

55. A. Haase, Snapshot FLASH MRI. Applications to T1, T2, and chemical-shift imaging, *Magn. Reson. Med.* **13**, 77, (1990).

56. C. Schwarzbauer, S. P. Morrissey and A. Haase, Quantitative magnetic resonance imaging of perfusion using magnetic labeling of water proton spins within the detection slice, *Magn. Reson. Med.* **35**, 540, (1996).

57. Z. H. Endre and R. G. Duggleby, Non-linear regression and variance ratio analysis of time based NMR data, *NMR. Biomed.* **6**, 130, (1993).

58. E. G. Walsh, K. Minematsu, J. Leppo and S. C. Moore, Radioactive microsphere validation of a volume localized continuous saturation perfusion measurement, *Magn. Reson. Med.* **31**, 147, (1994).

59. J. R. Ewing, Q. Jiang, M. Boska, Z. G. Zhang, S. L. Brown, G. H. Li, G. W. Divine and M. Chopp, T1 and magnetization transfer at 7 Tesla in acute ischemic infarct in the rat, *Magn. Reson. Med.* **41**, 696, (1999).

60. J. Pekar, P. Jezzard, D. A. Roberts, J. S. Leigh Jr., J. A. Frank and A. C. McLaughlin, Perfusion imaging with compensation for asymmetric magnetization transfer effects, *Magn. Reson. Med.* **35**, 70, (1996).

61. H. Lei and J. Peeling, A strategy to optimize signal-to-noise ratio in one-coil arterial spin tagging perfusion imaging, *Magn. Reson. Med.* **41**, 563, (1999).

62. L. Maccotta, J. A. Detre and D. C. Alsop, The efficiency of adiabatic inversion for perfusion imaging by arterial spin labeling, *NMR Biomed.* **10**, 216, (1997).

63. K. I. Marro, C. E. Hayes and M. J. Kushmerick, A model of inversion process in an arterial inversion experiment, *NMR Biomed.* **10**, 324, (1997).

64. L. Hernandez and C. A. Branch, *Abstr. Int. Soc. Magn. Reson. Med.*, 1753 (1997).

65. V. Dousset, P. Degreze, S. Mieze, M. Sesay, C. B. Basse and J. M. Caille, Magnetization transfer on in vitro circulating blood: implications for time-of-flight MR angiography, *J. Magn. Reson. Imaging* **5**, 786, (1995).

66. A. C. Silva, W. Zhang, D. S. Williams and A. P. Koretsky, Estimation of water extraction fractions in rat brain using magnetic resonance measurement of perfusion with arterial spin labeling, *Magn. Reson. Med.* **35**, 58, (1997).

67. D. A. Roberts, R. Rizi, R. E. Lenkinski and J. S. Leigh Jr., Magnetic resonance imaging of the brain: blood partition coefficient for water: application to spin-tagging measurement of perfusion, *J. Magn. Reson. Imaging* **6**, 363, (1996).

68. H. Iida, I. Kanno, S. Miura, M. Murakami, K. Takahashi and K. Uemura, A determination of the regional brain/blood partition coefficient of water using dynamic positron emission tomography, *J. Cereb. Blood Flow Metab.* **9**, 874, (1989).

69. P. Herscovitch and M. E. Raichle, What is the correct value for the brain--blood partition coefficient for water, *J. Cereb. Blood Flow Metab.* **5**, 65, (1985).

70. F. Q. Ye, V. S. Mattay, P. Jezzard, J. A. Frank, D. R. Weinberger and A. C. McLaughlin, Correction for vascular artifacts in cerebral blood flow values measured by using arterial spin tagging techniques, *Magn. Reson. Med.* **37**, 226, (1997).

71. F. Wittlich, K. Kohno, G. Mies, D. G. Norris and M. Hoehn Berlage, Quantitative measurement of regional blood flow with gadolinium diethylenetriaminepentaacetate bolus track NMR imaging in cerebral infarcts in rats: validation with the iodo[14C]antipyrine technique, *Proc. Natl. Acad. Sci. U. S. A.* **92**, 1846, (1995).

72. P. Sandor, P. J. Cox-van, W. de-Jong and D. de-Wied, Continuous measurement of cerebral blood volume in rats with the photoelectric technique: effect of morphine and naloxone, *Life Sci.* **39**, 1657, (1986).

73. W. Zhang, D. S. Williams, J. A. Detre and A. P. Koretsky, Measurement of brain perfusion by volume-localized NMR spectroscopy using inversion of arterial water spins: accounting for transit time and cross-relaxation, *Magn. Reson. Med.* **25**, 362, (1992).

74. F. M. W. Catherine and W. R. Thomas, Sources of artifact and systematic error in quantitative snapshot FLASH imaging and methods for their elimination, *Magn. Reson. Med.* **41**, 63, (1999).

75. J. Coremans, M. Spanoghe, L. Budinsky, J. Sterckx, R. Luypaert, H. Eisendrath and M. Osteaux, A comparison between different imaging strategies for diffusion measurements with the centric phase-encoded turboFLASH sequence , *J. Magn. Reson.* **124**, 323, (1997).

76. D. G. Mitchell, S. Vinitski, J. Burk-DL, D. Levy and M. D. Rifkin, Variable-flip-angle spin-echo MR imaging of the pelvis: more versatile T2-weighted images, *Radiology* **171**, 525, (1989).

77. S. Vinitski, D. G. Mitchell, J. Szumowski, J. Burk-DL and M. D. Rifkin, Variable flip angle imaging and fat suppression in combined gradient and spin-echo (GREASE) techniques, *Magn. Reson. Imaging* **8**, 131, (1990).

78. E. L. Barbier, A. C. Silva, D. S. Williams and A. P. Koretsky, Perfusion analysis using dynamic arterial spin labeling (DASL), *Magn. Reson. Med.* **41**, 299, (1999).

Chapter 4. Some Practical Applications of Magnetic Resonance Perfusion Imaging

There is an old Chinese saying, "*Practice is the only way to know the truth*." Sir Isaac Newton, the greatest scientist who ever lived, once wrote to one of the many critics of his theory of color what is considered by some to be the very foundation of modern science: "*The best and safest method of philosophizing seems to be, first to enquire diligently into the properties of things, and to establish those properties by experiments and then to proceed more slowly to hypotheses for the explanation of them.*" Although the exact words are different, the basic idea those great minds in history tried to tell, I believe, is the same. In the previous chapter, what was described is largely the theory or, in Newton's words, the *properties* of magnetic resonance (MR) perfusion imaging using arterial spin tagging (AST). In this chapter, the optimized one-coil MR perfusion imaging technique with continuous AST described in the last chapter is applied in several rather simple but practical experiments so that its performance and technical merits can be assessed. Only by such studies can a technique then be *established*. If looked at individually, some of the experiments to be described do nothing more than confirm older observations. Some of them, however, provide some new results in a self-contained way. Nevertheless, the main purpose of all these experiments is just to show that the AST perfusion imaging technique really works, and I hope to be able to say at the end of this chapter that my intended purpose has been well fulfilled.

Experiment 1. The Effect of Anesthetics on Cerebral Blood Flow

Introduction

Anesthetics affect cerebral blood flow (CBF) in both laboratory animals and humans (1). For example, volatile anesthetics, such as halothane, act as vasodilators and increase CBF (2-5), while intravenous anesthetics like pentobarbital act as vasoconstrictors and reduce CBF (5-9). In this experiment, AST perfusion imaging is used to measure CBF in rats under pentobarbital and halothane anesthesia and to examine the effects of different anesthetics on CBF.

Methods and Materials

The experiments used 4 male Sprague-Dawley rats, 250-300 g. Each rat was initially anesthetized by intraperitoneal (i. p.) injection of a high dose of pentobarbital (60 mg/kg) and then a catheter was placed in the right femoral artery for monitoring blood gases and blood pressure. After surgery, the rat was rapidly transferred to a MR probe ready for imaging. In the magnet bore, the rat was mechanically ventilated using pure oxygen delivered through a nose cone. The rate and the volume of ventilation were adjusted to maintain normal blood gases. Rectal temperature was controlled between 36.5 and 37.5 °C throughout the experiment. Heart rate, respiratory rate and blood pressure were monitored constantly. After the setup MR procedures such as positioning and shimming were carried out, baseline CBF under pentobarbital anesthesia was measured, usually starting about 1.5 hours after the initial injection.

Without waking up, the rat was then allowed to recover from pentobarbital, and anesthesia was maintained by changing the ventilating gas to 30/70 O_2/N_2O gas mixture containing 1.5% halothane. CBF was measured repeatedly during the switching process until it reached a new steady state which normally occurred 2.5-3.0 hours after pentobarbital injection.

MR experiments were carried out on a Bruker Biospec/3 7 T/21 cm spectrometer using a custom-built 3 cm-diameter saddle coil for both transmission and reception. Perfusion imaging was done using a snapshot fast low angle shot (FLASH) sequence with a 5×5 cm^2 field of view, 2 mm thick slice at caudoputamen level excited using a 1 ms Gaussian pulse, 128×128 matrix size, repetition time (TR) 4.3 ms, echo time (TE) 2.3 ms, 12° flip angle, and 48 averages. The power (about 150 mG) of the 2.5 s spin tagging pulse and the strength (2 G/cm) of the spin tagging gradient were optimized to increase the signal-to-noise ratio of the measurement (10), as described in the previous chapter. A 400 ms post-tagging delay was used to eliminate transit time sensitivity and vascular artifacts (11). Four sets of proton density images were acquired using a four-step gradient-offset cycling protocol to eliminate the asymmetrical magnetization transfer effect (12). Perfusion images were calculated using Eq. [3.27] and then corrected for the post-tagging delay. $T1_o$ maps used to calculate perfusion images were obtained using a slice-selective inversion-recovery snapshot FLASH sequence described in the previous chapter. The acquisition parameters for $T1_o$ imaging were the same as those used for perfusion imaging. A total of 8 inversion recovery images were acquired with the time of recovery (TI) ranging from 256 ms to 8.75 s. Six averages were accumulated. The degree of spin tagging (α) was measured using a gradient-echo sequence described in the previous chapter. Average CBF values over the

whole brain slice were compared. Statistical analysis was carried out using a two-tailed paired *t*-test.

Results

Average CBF values, α and blood gas data under pentobarbital and halothane anesthesia are listed in Table 4.1. No significant difference was found in either blood gas data or α between the two groups. Switching the anesthetic from pentobarbital to halothane resulted in a 1.54 fold CBF increase from 1.40±0.24 $ml \cdot g^{-1} \cdot min^{-1}$ to 2.15±0.12 $ml \cdot g^{-1} \cdot min^{-1}$.

Table 4.1 Average values of blood gas data, α and CBF (mean±SD) in rats under pentobarbital or halothane anesthesia.

	pentobarbital	halothane
pO_2 (mmHg)	134.1±22.1	112.7±24.9
pCO_2 (mmHg)	41.6±11.3	48.9±2.2
pH	7.343±0.032	7.323±0.021
α	0.73±0.03	0.75±0.05
CBF ($ml \cdot g^{-1} \cdot min^{-1}$)	1.40±0.24	2.15±0.12*

* significantly different from the pentobarbital group

Discussion

In rat, pentobarbital decreases the CBF in a region-dependent manner (6,8). In the striatum and cerebral cortex regions, which are the brain structures investigated in this study, pentobarbital has been consistently reported to cause a 20-60% reduction in regional blood

flow (6-9). The effects of halothane on CBF are strain dependent and concentration dependent (2,4), and are more controversial. Some studies have shown that halothane, alone or used in combination with nitrous oxide (N_2O), acts as a vasodilator and increases CBF (3,5). However, there are also reports suggesting that halothane has little or no effect on CBF (4,7). Switching the anesthetic from pentobarbital to halothane/N_2O, a 54% increase in CBF was observed in this study, in close agreement with previous results. However, because of the way the experiments were conducted, it is unclear whether this increase was due to the vasoconstriction effect of pentobarbital, to the vasodilatation effect of halothane, or to both.

The absolute perfusion rate values obtained in this study seemed higher than those obtained in other studies using non-MR methods for perfusion measurement (8,13). Recently, the perfusion rate measured by AST MR perfusion imaging has been correlated with the perfusion rate measured by other techniques such as the radioactive microsphere technique (14,15) and [^{14}C]iodoantipyrine autoradiography (16,17). A close correlation was found in those studies. However, AST MR perfusion imaging also systematically overestimates perfusion rate by as much as 0.79 $ml \cdot g^{-1} \cdot min^{-1}$ (14). This overestimation could be due to a number of factors which have already been analyzed comprehensively in the previous chapter. Among those, the most significant and relevant factor is probably incomplete elimination of vascular artifacts (18).

Experiment 2. The Effect of Prolonged Halothane Anesthesia on Cerebral Blood Flow

Introduction

As shown in the previous experiment and many other studies, halothane may act as a vasodilator and increase CBF. However, it remains an unanswered question whether the increase, if any, in CBF by halothane is maintained for a prolonged period of anesthesia. Clinically, answering this question could help improve patient management in surgeries involving prolonged inhalation of halothane or other volatile anesthetics. In experimental investigations, it is important to know whether prolonged halothane anesthesia causes any baseline CBF changes, especially when dynamic CBF measurement is of interest. Previous studies have yielded inconsistent results. In animals, some studies find that the halothane/isoflurane-induced CBF increase decreases gradually over time during prolonged anesthesia (19-22), while this was not observed in other studies (23,24). In humans, most studies showed there is no decrease in CBF during prolonged anesthesia with halothane or isoflurane (25-27). In this experiment, AST perfusion imaging is used to measure CBF in rat during 4 hours of halothane anesthesia.

Methods and Materials

The experiments used 5 male Sprague-Dawley rats, 250-300 g. Each rat was initially anesthetized with 5.0% halothane in 30/70 O_2/N_2O, and then intubated and mechanically ventilated with 1.5% halothane in 30/70 O_2/N_2O. In each rat, the tail artery was cannulated

for blood pressure monitoring and blood gas sampling. Rectal temperature was controlled between 36.5 and 37.5 °C using a water thermostat throughout the entire experiment. Heart rate, respiratory rate and blood pressure were monitored continuously. Blood gases were measured about every 40 minutes. CBF was measured with a temporal resolution of about 10 minutes for four consecutive hours. Perfusion imaging, $T1_o$ imaging and measurements of α were carried out as described for Experiment 1. Statistical analysis was carried out using a repeated measures analysis of variance (ANOVA).

Results

Blood gas data are listed in Table 4.2. No significant difference was found in any of the blood gas variables at any time point. Figure 4.1 shows the average CBF values during the four hours of halothane anesthesia. Repeated measures ANOVA showed no time dependent variations in CBF.

Table 4.2 Average (±SD) blood gases measured every 40 minutes in 5 rats during 4 hours of halothane anesthesia.

	pCO_2 (mmHg)	pO_2 (mmHg)	pH
40 minutes	53.1±6.0	135.5±16.9	7.262±0.041
80 minutes	53.6±6.4	141.5±9.6	7.270±0.035
120 minutes	51.7±5.5	126.6±12.2	7.286±0.035
160 minutes	53.8±7.5	131.9±12.8	7.294±0.035
200 minutes	49.7±7.5	123.4±11.2	7.315±0.035
240 minutes	48.3±5.8	117.5±10.1	7.319±0.035

Discussion

The results obtained in this experiment confirm that CBF remains constant during prolonged anesthesia of halothane in rat, at least for four hours. Although this agrees well with what has been observed in human brain (25-27), it is contrary to some earlier studies, mostly on canine and goat brain (19-22). As suggested by some authors (25), this discrepancy could, perhaps, simply be a result of the species differences, or it could be due to the different techniques used for CBF measurement.

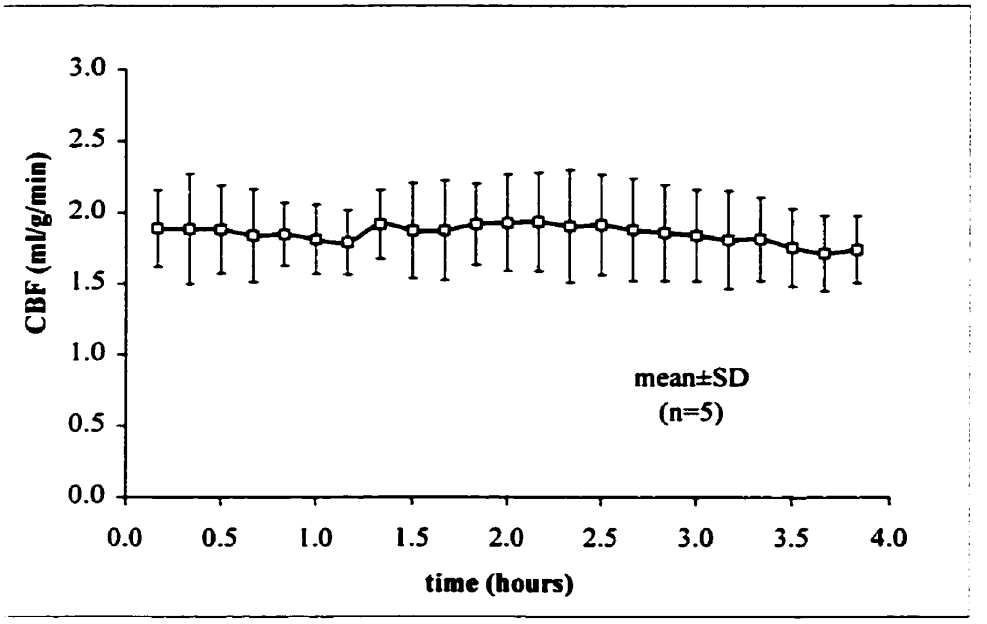

Figure 4.1 Mean cerebral blood flow in rats during 4 hours halothane anesthesia.

Experiment 3. The Effect of Acetazolamide on Cerebral Blood Flow

Introduction

Acetazolamide is a carbonic anhydrase inhibitor. Upon administration, it increases CBF globally without altering the tissue metabolic rate significantly (28). With a variety of CBF measuring techniques, an acetazolamide stimulation test has been performed to measure the cerebrovascular reserve capacity in both laboratory animals and humans (13,29-39). More recently, MR imaging techniques have been used in the acetazolamide stimulation test, including first pass bolus tracking perfusion imaging (31-33), blood oxygen level dependent (BOLD) based MR imaging (35-37) and $T2^*$-weighted gradient echo imaging (38). The feasibility of using AST MR perfusion imaging in the acetazolamide stimulation test, however, has not been investigated in either experimental animals or humans. In this experiment, AST perfusion imaging is used to measure CBF in rat before and after i. p. injection of acetazolamide.

Methods and Materials

The experiments used 6 male Sprague-Dawley rats, 250-300 g. Each rat was anesthetized, intubated, and mechanically ventilated (1.0-1.5% halothane in 30/70 O_2/N_2O). In each rat, the tail artery was cannulated for blood pressure monitoring and blood gas sampling, and a polyethylene tube was implanted into the abdominal cavity for acetazolamide injection. After surgery, the rat was quickly transferred into a MR probe ready for imaging. Inside the magnet bore, anesthesia was maintained using 1.0-1.5% halothane in 30/70 O_2/N_2O. Rectal temperature was controlled between 36.5 and 37.5 °C using a water thermostat throughout the entire experiment. Heart rate, respiratory rate and blood pressure were monitored continuously. After the rat was moved into the magnet, blood gases were checked and adjusted to normal

range (pO_2>100 mmHg, and pCO_2 between 35 to 50 mmHg) through altering the rate and the volume of the ventilation pump. When the rat was stabilized, baseline CBF was measured several times. Acetazolamide solution (2.0 ml, 25 mg/ml solution titrated with 1M NaOH to pH=9.2) was then injected intraperitoneally through the pre-implanted tube. Perfusion imaging began immediately upon injection and was repeated with a time interval of about 6 minutes for about one hour. Post-injection blood gas data were obtained 10 minutes after injection. Perfusion imaging, $T1_o$ imaging and measurement of α were carried out as described for Experiment 1. Statistical analysis was carried out using a two-tailed paired *t*-test.

Results

Blood gas data and α values before and after acetazolamide injection are listed in Table 4.3. After acetazolamide injection, pO_2 ($p<0.01$) and pCO_2 ($p<0.001$) of the blood increased significantly, while blood pH decreased significantly ($p<0.001$). No significant difference was found between the pre-injection and post-injection α values.

Table 4.3 Average values of α and blood gas data pre- and post acetazolamide injection (mean±SD).

	pre	post
α	0.76±0.07	0.72±0.07
pO_2 (mmHg)	116.3±7.3	147.5±21.0*
pCO_2 (mmHg)	41.2±5.3	61.6±5.3**
pH	7.360±0.029	7.199±0.030**

* significantly different from pre-injection value ($p<0.01$)
** significantly different from pre-injection values ($p<0.001$)

Figure 4.2 shows a set of MR perfusion images from a typical rat during the course of the experiment. All images were processed using the same intensity and contrast scale. The increase in the overall intensity from image A to F demonstrated a gradual global increase in CBF. Figure 4.3 shows the average time course of CBF increase in the regions of parietal cortex and striatum after acetazolamide injection. The time courses of post-injection CBF increase were similar for those two regions. CBF increased rapidly in the first 15 to 20 minutes after injection, followed by a very slow increase during the subsequent period of observation. After acetazolamide injection, the average CBF in parietal cortex increased 1.56 fold from 1.90±0.26 $ml \cdot g^{-1} \cdot min^{-1}$ to 2.96±0.13 $ml \cdot g^{-1} \cdot min^{-1}$ and CBF in striatum increased 1.65 fold from 1.45±0.26 $ml \cdot g^{-1} \cdot min^{-1}$ to 2.40±0.08 $ml \cdot g^{-1} \cdot min^{-1}$.

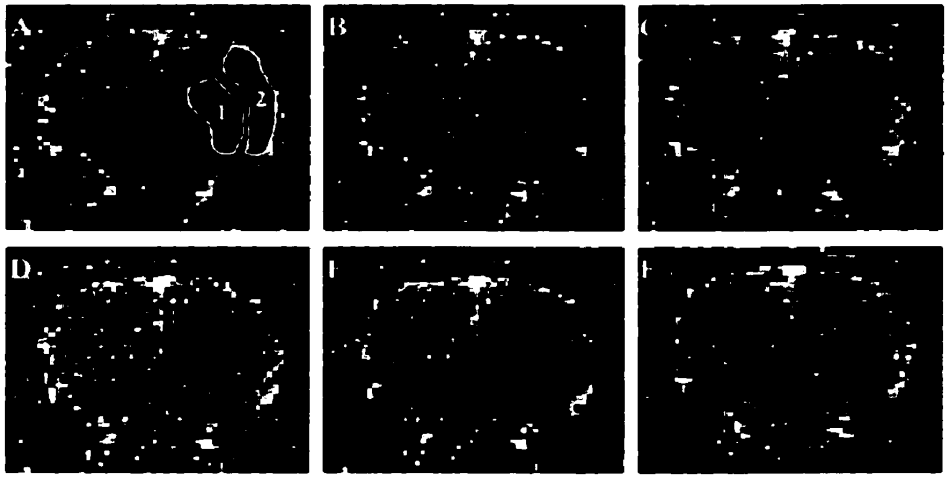

Figure 4.2 Perfusion images of a rat brain after i. p. injection of acetazolamide. CBF was measured in striatum (region 1) and parietal cortex (region 2).

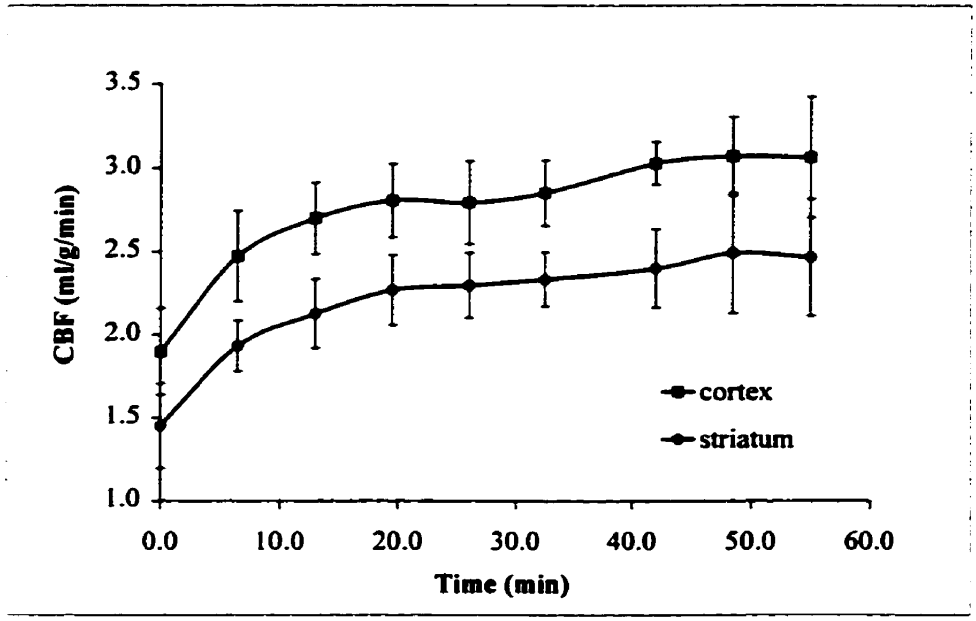

Figure 4.3 Time courses of cerebral blood flow increase in the parietal cortex and striatum after i. p. injection of acetazolamide.

Discussion

The baseline CBF values measured in parietal cortex and striatum were in close agreement with the results of other studies under similar conditions (40,41). In this experiment, CBF increased immediately after i. p. injection of acetazolamide. The increase was rapid in the first 15 to 20 minutes, then slowed down and the elevated blood flow lasted for at least 55 minutes, in good agreement with previous studies (28,42,43). The percentage increase in CBF induced by acetazolamide injection in rat has been previously reported to be between 60% and 120% at the parietal cortex and striatum regions (13,29,43,44). The percentage CBF increases (56.0% for parietal cortex and 65.1% for striatum) observed in this study are similar to or somewhat smaller than previous results. This may be due to the fact that CBF values measured after acetazolamide injection were underestimated. After acetazolamide

injection, CBF increases and usually exceeds 2.0 $ml \cdot g^{-1} \cdot min^{-1}$. Under such condition, water is no longer freely diffusible in rat brain and thus the effect of water extraction fraction on CBF quantification should be taken into account (45). Otherwise, CBF values calculated by Eq. [3.27] will be underestimated. Water extraction fraction was not measured in this experiment so that it can not be accounted for. However, with a pre-established relationship between water extraction fraction and absolute CBF value, it is, in principle, possible to correct for this effect semi-quantitatively (45).

In previous studies, only the averaged CBF changes over a period of time after acetazolamide injection were commonly measured to obtain information about the cerebrovascular reserve capacity. Few studies measured CBF changes dynamically after acetazolamide injection, probably because of the poor temporal resolution of the CBF measuring techniques used. In some cases such as hypertension, it has been shown that the time course of the CBF response to acetazolamide provides additional information about the pathophysiological state of the brain tissue (39). Therefore, it would be valuable to be able to measure not only the magnitude of the CBF changes but also the rate of CBF changes in an acetazolamide stimulation test. In this study, it has been demonstrated that MR perfusion imaging using AST can be used to measure CBF changes both quantitatively and dynamically in an acetazolamide stimulation test.

Experiment 4. Delayed Hyperemia In a Rat Model of Focal Ischemia

Introduction

Clinical and experimental transient cerebral ischemia is often followed by hyperemia, or "luxury perfusion" as defined by N. Lassen in his well-known 1966 report published in the *Lancet* (46). The mechanism underlying this is still unclear, as is its role in the development of cerebral infarction. Two types of postischemic hyperemia have been observed in a global ischemia model in rat, an initial reactive hyperemia that occurs immediately upon reperfusion and a delayed hyperemia that occurs 48 hours after ischemia in brain regions sustaining neuronal damage such as the striatum and hippocampus (47). The duration and the amplitude of the initial reactive hyperemia is related to the severity of the prior ischemia (48,49). Pre-treatment with N^G-nitro-L-arginine methylester (L-NAME), a non-selective nitric oxide synthase (NOS) inhibitor, reduces or depresses the hyperemia, indicating at least some involvement of nitric oxide (NO) in the mechanism of this hyperemia (50-52). A similar initial reactive hyperemia also occurs in transient focal ischemia models (53-56), the amplitude of which is correlated with both the severity of prior ischemia (56) the volume of the cortical infarction which develops later (53). Compared to the initial reactive hyperemia, delayed hyperemia is less well understood in both global and focal ischemia. In this study, AST MR perfusion imaging was used to evaluate and characterize delayed hyperemia 24 and 48 hours after ischemia/reperfusion in a transient focal ischemia model in rat.

Methods and Materials

The experiments used 6 male Sprague-Dawley rats, 250-300 g. Focal ischemia was induced by intracerebral injection of endothelin-1 (3 μl, 20 pmol/μl) just above the middle cerebral artery (MCA) distal to the striatal branches (57). Twenty-four and forty-eight hours after ischemia, each rat was anesthetized with 5.0% halothane in 30/70 O_2/N_2O, and then mechanically ventilated with 1.5% halothane in 30/70 O_2/N_2O. In each rat, the tail artery was cannulated for blood pressure monitoring and blood gas sampling. Rectal temperature was controlled between 36.5 and 37.5 °C using a water thermostat throughout the entire experiment. Heart rate, respiratory rate and blood pressure were monitored continuously. Perfusion imaging, $T1_0$ imaging and measurement of α were carried out as described for Experiment 1, but with the following exceptions: perfusion images and $T1_0$ image were acquired with a FOV of 4×4 cm^2, 96 averages were acquired for perfusion imaging and 8 averages were acquired for $T1_0$ imaging. For each rat, T2-weighted imaging was performed 48 hours after ischemia using a standard multiple-slice multiple-echo sequence to define the regions of brain infarction. Images from 10 contiguous 1 mm slices were acquired with 4 echoes (TE 20, 40, 60 and 80 ms, TR 1500 ms, matrix size 256×256, FOV 3.5×3.5 cm^2). Statistical analysis was carried out using a two-tailed paired *t*-test.

Results

Blood gas data and α values are listed in Table 4.4. No significant difference was found in either blood gases or α between the 24 hours and the 48 hours data. Figure 4.4 shows

perfusion images and T2-weighted (TE=80 ms) images of the same slice position in three rats. Twenty-four hours after ischemia, all three rats showed mild hyperemia in the ipsilateral striatum. However, the CBF pattern in the ipsilateral cortex was inconsistent among the rats. The cortical CBF in rat 1 is similar on the ipsilateral and contralateral sides while the ipsilateral cortex of rats 2 and 3 was hypoperfused compared to the respective contralateral sides. Forty-eight hours after ischemia, hyperemia was pronounced in both the ipsilateral striatum and the ipsilateral cortex in all three rats and the CBF pattern now became consistent among the rats. The regions with hyperemia 48 hours post-ischemia correlated well with the regions of cerebral infarction as defined by the regions with hyperintensity in the T2-weighted images. Quantitative CBF analysis averaged over all six rats is shown in Fig 4.5. In the striatum, CBF ratios (ipsilateral/contralateral) were 1.27±0.22 ($p<0.05$) and 1.72±0.52 ($p<0.01$) 24 hours and 48 hours after ischemia. In the cortex, CBF ratios were 0.96±0.40 (N.S.) and 1.53±0.45 ($p<0.01$) 24 hours and 48 hours after ischemia.

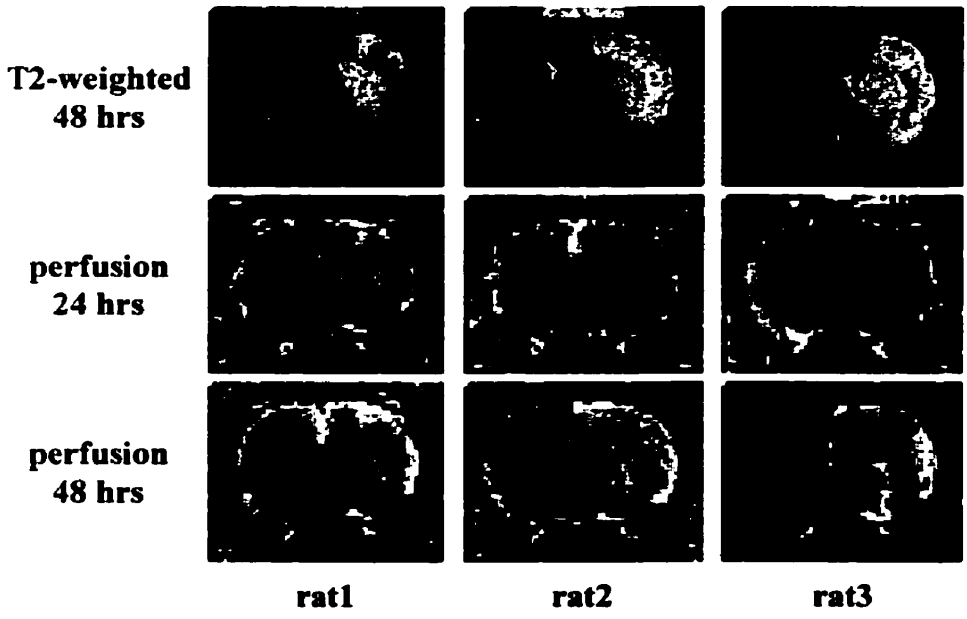

Figure 4.4 T2-weighted images and perfusion images of three rats 24 hours and 48 hours after transient focal ischemia.

Table 4.4 Average values of α and blood gas data 24 hours and 48 hours after transient focal ischemia (mean±SD).

	24 hrs	48 hrs
α	0.75±0.05	0.76±0.03
pO_2 (mmHg)	135.8±33.6	116.4±13.7
pCO_2 (mmHg)	38.8±10.1	30.5±2.8
pH	7.389±0.041	7.366±0.040

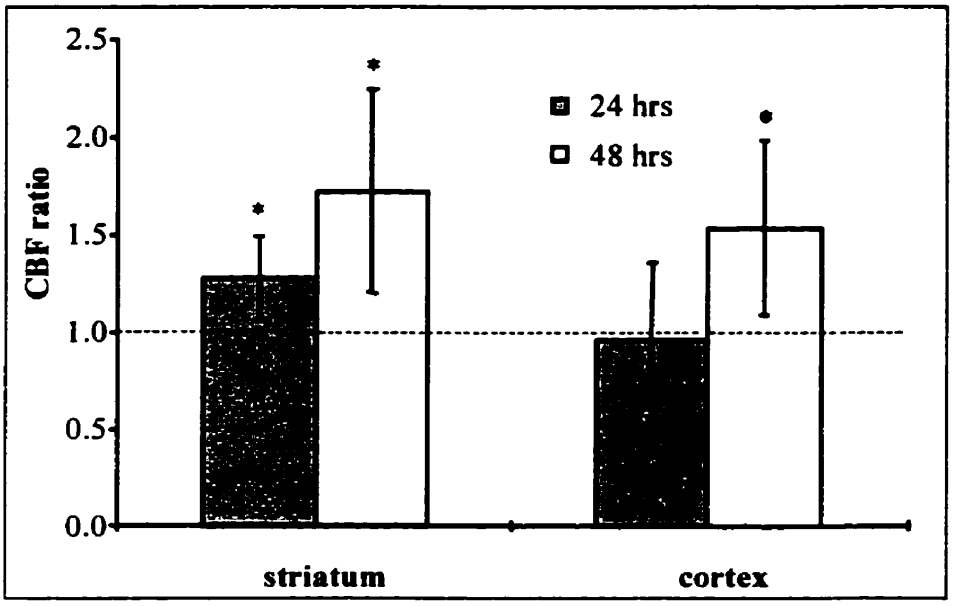

Figure 4.5 CBF ratios (ipsilateral/contralateral) in the striatum and cortex 24 and 48 hours after transient focal ischemia.

Discussion

Delayed postischemic hyperemia is apparent in the endothelin model of focal ischemia in rat. This hyperemia is distinct from the initial reactive hyperemia observed in previous studies (53-56) in the onset time, and probably also in the underlying mechanisms. The time course

of the development of this hyperemia is different for striatum and cortex. The exact mechanisms underlying this delayed hyperemia is unclear and probably multifactorial. First, the production of many vasodilating substances increases during ischemia/reperfusion. NO, a potent vasodilator, is likely the substance responsible for the reactive hyperemia observed in global ischemia (50-52), and it may also contribute to the delayed hyperemia observed in this study. In both permanent and transient focal ischemia, all three isoforms of NOS (endothelial NOS, neuronal NOS and inducible NOS) increase in ischemic brain tissue, and in turn cause an increase in NO production (58). In particular, the temporal profile of iNOS increase in a transient focal ischemia model with suture occlusion seems to be in accord with the time course of the delayed hyperemia observed here (59). Second, impaired autoregulation of CBF in the ischemic tissue will facilitate the development of any existing hyperemia (60). Third, it is also possible that the delayed hyperemia observed is a reflection of neovascularization in the ischemic tissues with increased capillary density and endothelial hypertrophy (61).

Whether postischemic hyperemia plays a beneficial or a detrimental role in the development of a cerebral infarct is controversial and clarifying this may direct the development of novel therapies for focal ischemia. In human, subacute hyperemia (less than 48 hours) tends to indicate rapid recanalization of occluded arteries and has been suggested to be beneficial (62). However, the situation in experimental animals is somewhat different and the presence of hyperemia in the ischemic tissue often indicates a greater chance of brain infarction (53,63). The reason for this discrepancy is unclear, probably due to the fact that the time window for tissue survival after cerebral ischemia might be shorter in experimental animals than in humans.

References

1. D. G. McDowall, The effects of general anaesthetics on cerebral blood flow and cerebral metabolism, *Br. J. Anaesth.* **37**, 236, (1965).

2. H. Takahashi, J. R. Kirsch, T. Okada and R. J. Traystman, Intensity of halothane- and hypercapnia-induced cerebral hyperemia is strain-dependent in rats, *Anesth. Analg.* **83**, 359, (1996).

3. T. D. Hansen, D. S. Warner, M. M. Todd and L. J. Vust, Effects of nitrous oxide and volatile anaesthetics on cerebral blood flow, *Br. J. Anaesth.* **63**, 290, (1989).

4. T. Brussel, W. Fitch, G. Brodner, I. Arendt and H. Van Aken, Effects of halothane in low concentrations on cerebral blood flow, cerebral metabolism, and cerebrovascular autoregulation in the baboon, *Anesth. Analg.* **73**, 758, (1991).

5. R. F. Albrecht, D. J. Miletich, R. Rosenberg and B. Zahed, Cerebral blood flow and metabolic changes from induction to onset of anesthesia with halothane or pentobarbital, *Anesthesiology* **47**, 252, (1977).

6. H. Goldman and L. A. Sapirstein, Brain blood flow in the conscious and anesthetized rat, *Am. J. Physiol.* **224**, 122, (1973).

7. T. Sooriyamoorthy, A. Livingston and P. V. Taberner, A comparison of the effect of some sedative and anaesthetic drugs on cerebral blood flow in the rat, *Gen. Pharmac.* **6**, 27, (1975).

8. T. Otsuka, L. Wei, V. R. Acuff, A. Shimizu, K. D. Pettigrew, C. S. Patlak and J. D. Fenstermacher, Variation in local cerebral blood flow response to high-dose pentobarbital sodium in the rat, *Am. J. Physiol.* **261**, H110, (1991).

9. M. Fillenz and J. P. Lowry, The relation between local cerebral blood flow and extracellular glucose concentration in rat striatum, *Exp. Physiol.* **83**, 233, (1998).

10. H. Lei and J. Peeling, A strategy to optimize signal-to-noise ratio in one-coil arterial spin tagging perfusion imaging, *Magn. Reson. Med.* **41**, 563, (1999).

11. D. C. Alsop and J. A. Detre, Reduced transit-time sensitivity in noninvasive magnetic resonance imaging of human cerebral blood flow, *J. Cereb. Blood Flow Metab.* **16**, 1236, (1996).

12. J. Pekar, P. Jezzard, D. A. Roberts, J. S. Leigh Jr., J. A. Frank and A. C. McLaughlin, Perfusion imaging with compensation for asymmetric magnetization transfer effects, *Magn. Reson. Med.* **35**, 70, (1996).

13. Y. Magata, H. Saji, S. R. Choi, K. Tajima, T. Takagaki, S. Sasayama, Y. Yonekura, H. Kitano, M. Watanabe, H. Okada and et al, Noninvasive measurement of cerebral blood flow and glucose metabolic rate in the rat with high-resolution animal positron emission tomography (PET): a novel in vivo approach for assessing drug action in the brains of small animals, *Biol. Pharm. Bull.* **18**, 753, (1995).

14. L. Hernandez, C. A. Branch and J. A. Helpern, *Abstr. Int. Soc. Magn. Reson. Med.*, 1193 (1998).

15. E. G. Walsh, K. Minematsu, J. Leppo and S. C. Moore, Radioactive microsphere validation of a volume localized continuous saturation perfusion measurement, *Magn. Reson. Med.* **31**, 147, (1994).

16. P. R. Allegrin, D. Bochelen, M. Eis, A. Sauter and M. Rudin, *Abstr. Int. Soc. Magn. Reson. Med.*, 377 (1998).

17. M. Hoehn-Berlage, K. Kruger, E. Busch and M. Franke, *Abstr. Int. Soc. Magn. Reson. Med.*, 1843 (1999).

18. F. Q. Ye, V. S. Mattay, P. Jezzard, J. A. Frank, D. R. Weinberger and A. C. McLaughlin, Correction for vascular artifacts in cerebral blood flow values measured by using arterial spin tagging techniques, *Magn. Reson. Med.* **37**, 226, (1997).

19. R. F. Albrecht, D. J. Miletich and L. R. Madala, Normalization of cerebral blood flow during prolonged halothane anesthesia, *Anesthesiology* **58**, 26, (1983).

20. D. M. Turner, N. F. Kassell, T. Sasaki, Y. G. Comair, D. J. Boarini and D. O. Beck, Time-dependent changes in cerebral and cardiovascular parameters in isoflurane-nitrous oxide-anesthetized dogs, *Neurosurgery* **14**, 135, (1984).

21. D. J. Boarini, N. F. Kassell, H. C. Coester, M. Butler and M. D. Sokoll, Comparison of systemic and cerebrovascular effects of isoflurane and halothane, *Neurosurgery* **15**, 400, (1984).

22. D. S. Warner, D. J. Boarini and N. F. Kassell, Cerebrovascular adaptation to prolonged halothane anesthesia is not related to cerebrospinal fluid pH, *Anesthesiology* **63**, 243, (1985).

23. O. K. Roald, M. Forsman and P. A. Steen, The effects of prolonged isoflurane anaesthesia on cerebral blood flow and metabolism in the dog, *Acta Anaesthesiol. Scand.* **33**, 210, (1989).

24. R. W. McPherson, J. R. Kirsch, J. R. Tobin, R. F. Ghaly and R. J. Traystman, Cerebral blood flow in primates is increased by isoflurane over time and is decreased by nitric oxide synthase inhibition, *Anesthesiology* **80**, 1320, (1994).

25. Y. Kuroda, M. Murakami, J. Tsuruta, T. Murakawa and T. Sakabe, Blood flow velocity of middle cerebral artery during prolonged anesthesia with halothane, isoflurane, and sevoflurane in humans, *Anesthesiology* **87**, 527, (1997).

26. J. B. Madsen, G. E. Cold, E. S. Hansen and B. Bardrum, The effect of isoflurane on cerebral blood flow and metabolism in humans during craniotomy for small supratentorial cerebral tumors, *Anesthesiology* **66**, 332, (1987).

27. E. Ornstein, W. L. Young, L. H. Fleischer and N. Ostapkovich, Desflurane and isoflurane have similar effects on cerebral blood flow in patients with intracranial mass lesions, *Anesthesiology* **79**, 498, (1993).

28. S. Vorstrup, L. Henriksen and O. B. Paulson, Effect of acetazolamide on cerebral blood flow and cerebral metabolic rate for oxygen, *J. Clin. Invest.* **74**, 1634, (1984).

29. Y. Kawata, K. Sako and Y. Yonemasu, Sequential changes in cerebrovascular reserve capacity in three-vessel occlusion rats, *Brain Res.* **739**, 330, (1996).

30. C. Yokota, Y. Hasegawa, K. Minematsu and T. Yamaguchi, Effect of acetazolamide reactivity and long-term outcome in patients with major cerebral artery occlusive diseases, *Stroke* **29**, 640, (1998).

31. F. J. Guckel, G. Brix, P. Schmiedek, Z. Piepgras, G. Becker, J. Kopke, H. Gross and M. Georgi, Cerebrovascular reserve capacity in patients with occlusive cerebrovascular disease: assessment with dynamic susceptibility contrast-enhanced MR imaging and the acetazolamide stimulation test, *Radiology* **201**, 405, (1996).

32. Y. Berthezene, N. Nighoghossian, R. Meyer, J. Damien, L. Cinotti, P. Adeleine, P. Trouillas and J. C. Froment, Can cerebrovascular reactivity be assessed by dynamic susceptibility contrast-enhanced MRI, *Neuroradiology* **40**, 1, (1998).

33. N. Nighoghossian, Y. Berthezene, R. Meyer, L. Cinotti, P. Adeleine, B. Philippon, J. C. Froment and P. Trouillas, Assessment of cerebrovascular reactivity by dynamic susceptibility contrast-enhanced MR imaging, *J. Neurol. Sci.* **149**, 171, (1997).

34. S. Gambhir, S. Inao, M. Tadokoro, M. Nishino, K. Ito, T. Ishigaki, H. Kuchiwaki and J. Yoshida, Comparison of vasodilatory effect of carbon dioxide inhalation and intravenous acetazolamide on brain vasculature using positron emission tomography, *Neurol. Res.* **19** , 139, (1997).

35. P. Hedera, S. Lai, J. S. Lewin, E. M. Haacke, D. Wu, A. J. Lerner and R. P. Friedland, Assessment of cerebral blood flow reserve using functional magnetic resonance imaging, *J. Magn. Reson. Imaging* **6**, 718, (1996).

36. G. D. Graham, J. Zhong, O. A. Petroff, R. T. Constable, J. W. Prichard and J. C. Gore, BOLD MRI monitoring of changes in cerebral perfusion induced by acetazolamide and hypercarbia in the rat, *Magn. Reson. Med.* **31**, 557, (1994).

37. A. Kleinschmidt, H. Steinmetz, M. Sitzer, K. D. Merboldt and J. Frahm, Magnetic resonance imaging of regional cerebral blood oxygenation changes under acetazolamide in carotid occlusive disease, *Stroke* **26**, 106, (1995).

38. H. Bruhn, A. Kleinschmidt, H. Boecker, K. D. Merboldt, W. Hanicke and J. Frahm, The effect of acetazolamide on regional cerebral blood oxygenation at rest and under stimulation as assessed by MRI, *J. Cereb. Blood Flow Metab.* **14**, 742, (1994).

39. A. Ficzere, A. Valikovics, B. Fulesdi, A. Juhasz, I. Czuriga and L. Csiba, Cerebrovascular reactivity in hypertensive patients: a transcranial Doppler study, *J. Clin. Ultrasound.* **25** , 383, (1997).

40. R. Tsuchidate, Q. P. He, M. L. Smith and B. K. Siesjo, Regional cerebral blood flow during and after 2 hours of middle cerebral artery occlusion in the rat, *J. Cereb. Blood Flow Metab.* **17**, 1066, (1997).

41. M. L. Forbes, K. S. Hendrich, P. M. Kochanek, D. S. Williams, J. K. Schiding, S. R. Wisniewski, S. F. Kelsey, S. T. DeKosky, S. H. Graham, D. W. Marion and C. Ho, Assessment of cerebral blood flow and CO_2 reactivity after controlled cortical impact by perfusion magnetic resonance imaging using arterial spin-labeling in rats, *J. Cereb. Blood Flow Metab.* **17**, 865, (1997).

42. E. B. Ringelstein, S. Van Eyck and I. Mertens, Evaluation of cerebral vasomotor reactivity by various vasodilating stimuli: comparison of CO_2 to acetazolamide, *J. Cereb. Blood Flow Metab.* **12**, 162, (1992).

43. J. C. LaManna and K. A. McCracken, Carbonic anhydrase inhibition and cerebral cortical oxygenation in the rat, *Adv. Exp. Med. Biol.* **277**, 335, (1990).

44. H. M. Frankel, E. Garcia, F. Malik, J. K. Weiss and H. R. Weiss, Effect of acetazolamide on cerebral blood flow and capillary patency, *J. Appl. Physiol.* **73**, 1756, (1992).

45. A. C. Silva, W. Zhang, D. S. Williams and A. P. Koretsky, Estimation of water extraction fractions in rat brain using magnetic resonance measurement of perfusion with arterial spin labeling, *Magn. Reson. Med.* **35**, 58, (1997).

46. N. A. Lassen, The luxury-perfusion syndrome and its possible relation to acute metabolic acidosis localised within the brain, *Lancet* **2**, 1113, (1966).

47. W. A. Pulsinelli, D. E. Levy and T. E. Duffy, Regional cerebral blood flow and glucose metabolism following transient forebrain ischemia, *Ann. Neurol.* **11**, 499, (1982).

48. J. K. Gourley and D. D. Heistad, Characteristics of reactive hyperemia in the cerebral circulation, *Am. J. Physiol.* **246**, H52, (1984).

49. N. V. Todd, P. Picozzi, H. A. Crockard and R. R. Russell, Reperfusion after cerebral ischemia: influence of duration of ischemia, *Stroke* **17**, 460, (1986).

50. R. S. Greenberg, M. A. Helfaer, J. R. Kirsch and R. J. Traystman, Effect of nitric oxide synthase inhibition on postischemic cerebral hyperemia, *Am. J. Physiol.* **269**, H341, (1995).

51. S. A. Humphreys and M. C. Koss, Role of nitric oxide in post-ischemic cerebral hyperemia in anesthetized rats, *Eur. J. Pharmacol.* **347**, 223, (1998).

52. C. L. Schleien, J. W. Kuluz and B. Gelman, Hemodynamic effects of nitric oxide synthase inhibition before and after cardiac arrest in infant piglets, *Am. J. Physiol.* **274**, H1378, (1998).

53. E. Morikawa, M. D. Ginsberg, W. D. Dietrich, R. C. Duncan, S. Kraydieh, M. Y. Globus and R. Busto, The significance of brain temperature in focal cerebral ischemia: histopathological consequences of middle cerebral artery occlusion in the rat, *J. Cereb. Blood Flow Metab.* **12**, 380, (1992).

54. H. Karibe, G. J. Zarow, S. H. Graham and P. R. Weinstein, Mild intraischemic hypothermia reduces postischemic hyperperfusion, delayed postischemic hypoperfusion, blood-brain barrier disruption, brain edema, and neuronal damage volume after temporary focal cerebral ischemia in rats, *J. Cereb. Blood Flow Metab.* **14**, 620, (1994).

55. A. J. de-Crespigny, M. F. Wendland, N. Derugin, E. Kozniewska and M. E. Moseley, Real-time observation of transient focal ischemia and hyperemia in cat brain, *Magn. Reson. Med.* **27**, 391, (1992).

56. H. Traupe, E. Kruse and W. D. Heiss, Reperfusion of focal ischemia of varying duration: postischemic hyper- and hypo-perfusion, *Stroke* **13**, 615, (1982).

57. J. Sharkey, I. M. Ritchie and P. A. Kelly, Perivascular microapplication of endothelin-1: a new model of focal cerebral ischaemia in the rat, *J. Cereb. Blood Flow Metab.* **13**, 865, (1993).

58. A. F. Samdani, T. M. Dawson and V. L. Dawson, Nitric oxide synthase in models of focal ischemia, *Stroke* **28**, 1283, (1997).

59. C. Iadecola, F. Zhang, R. Casey, H. B. Clark and M. E. Ross, Inducible nitric oxide synthase gene expression in vascular cells after transient focal cerebral ischemia, *Stroke* **27**, 1373, (1996).

60. U. Dirnagl and W. Pulsinelli, Autoregulation of cerebral blood flow in experimental focal brain ischemia, *J. Cereb. Blood Flow Metab.* **10**, 327, (1990).

61. T. Yamaguchi, Regional cerebral blood flow in experimental cerebral infarction, with special reference to hyperemia in the ischemic cerebral hemisphere, *Int. J. Neurol.* **11**, 162, (1977).

62. G. Marchal, A. R. Young and J. C. Baron, Early postischemic hyperperfusion: pathophysiological insights from positron emission tomography, *J. Cereb. Blood Flow Metab.* **19**, 467, (1999).

63. W. D. Heiss, R. Graf, J. Lottgen, K. Ohta, T. Fujita, R. Wagner, M. Grond and K. Weinhard, Repeat positron emission tomographic studies in transient middle cerebral artery occlusion in cats: residual perfusion and efficacy of postischemic reperfusion, *J. Cereb. Blood Flow Metab.* **17**, 388, (1997).

Chapter 5. *In vivo* Proton Magnetic Resonance Spectroscopy

Although magnetic resonance imaging (MRI) provides anatomical pictures as well as information about other properties of biological tissue (i.e. water content, relaxation times, water diffusion coefficient and perfusion), it does not yield biochemical information which is useful in assessing the metabolic profile of the tissue. *In vivo* magnetic resonance spectroscopy (MRS) observes the resonances of different metabolites and can be used to measure the concentrations of these metabolites, thus offering a valuable complement to MRI. The combined use of MRI and MRS in recent years has greatly improved our understanding of the pathogenesis of a number of diseases.

The first magnetic resonance (MR) spectrum on intact biological tissue was recorded using red blood cells and phosphorus-31 (^{31}P) MRS in 1973 by Moon and Richards (1). This was followed by a study in 1974 by Hoult et al who also used ^{31}P MRS to investigate muscle bioenergetics (2). In 1978, Chance et al reported the first *in vivo* ^{31}P spectrum of whole animal head (3). *In vivo* MRS thrived after the invention of the surface coil in 1980 (4) because now there was a way to acquire a spectrum from a confined region of interest without sticking the whole specimen, sometimes the whole body, into a MR probe! Inspired by the success of ^{31}P MRS, the usefulness of carbon-13 (^{13}C), nitrogen-15 (^{15}N), sodium-23 (^{23}Na) and fluorine-19 (^{19}F) MRS for *in vivo* applications was soon examined. MRS of all these nuclei has now become routine and has found many applications in the field of biomedicine. For example, *in vivo* ^{31}P MRS has been used to obtain information regarding tissue energetics, glucose metabolism, intracellular pH and intracellular magnesium ion

concentration (1-8); *in vivo* ^{13}C and ^{15}N MRS have been applied mainly to study tricarboxylic acid (TCA) cycle and ammonia metabolism (9-16); *in vivo* ^{23}Na MRS has been utilized to monitor trans-membrane ion transport (17-19); *in vivo* ^{19}F MRS has been employed for measurement of intracellular pH, quantification of intracellular metal ions and studies on metabolism of glucose and a variety of drugs (20-27).

The proton (^{1}H) has the highest sensitivity of stable MR-sensitive nuclei and is also the most abundant nucleus encountered in biological tissue. ^{1}H MRS therefore provides enormous potential for *in vivo* applications. Figure 5.1 compares *in vivo* ^{1}H (A and B), ^{31}P (C), and ^{23}Na (D and E) spectra acquired from rat brain at 7 T. It can be seen from the figure that the number of metabolites that can be detected by *in vivo* ^{1}H MRS is larger than the number of metabolites that can be detected by either ^{31}P or ^{23}Na MRS. Historically, the first ^{1}H MRS study on intact biological tissue was conducted at the very beginning of the 1980s when Brown and Campbell recorded the ^{1}H MR spectrum of red blood cells (28). By showing that MR signals were observable from almost a dozen metabolites, they also appreciated and suggested the potential of ^{1}H MRS for *in vivo* applications. However, the development of ^{1}H MRS was somewhat slower than the development of MRS of other nuclei. The earliest "high resolution" ^{1}H MR spectra of whole brain were not recorded, as far as I am aware, until the mid 1980s (29). In addition to the common problems encountered in all *in vivo* MRS such as the intrinsic insensitivity of MRS, poor B_0 homogeneity and short transverse relaxation times (T2), there are two problems that are unique for ^{1}H MRS. First, intense water and lipid signals usually dominate the *in vivo* ^{1}H MR spectra, if not suppressed, and interfere with the observation of other metabolites with low concentrations. Second, ^{1}H resonances of many

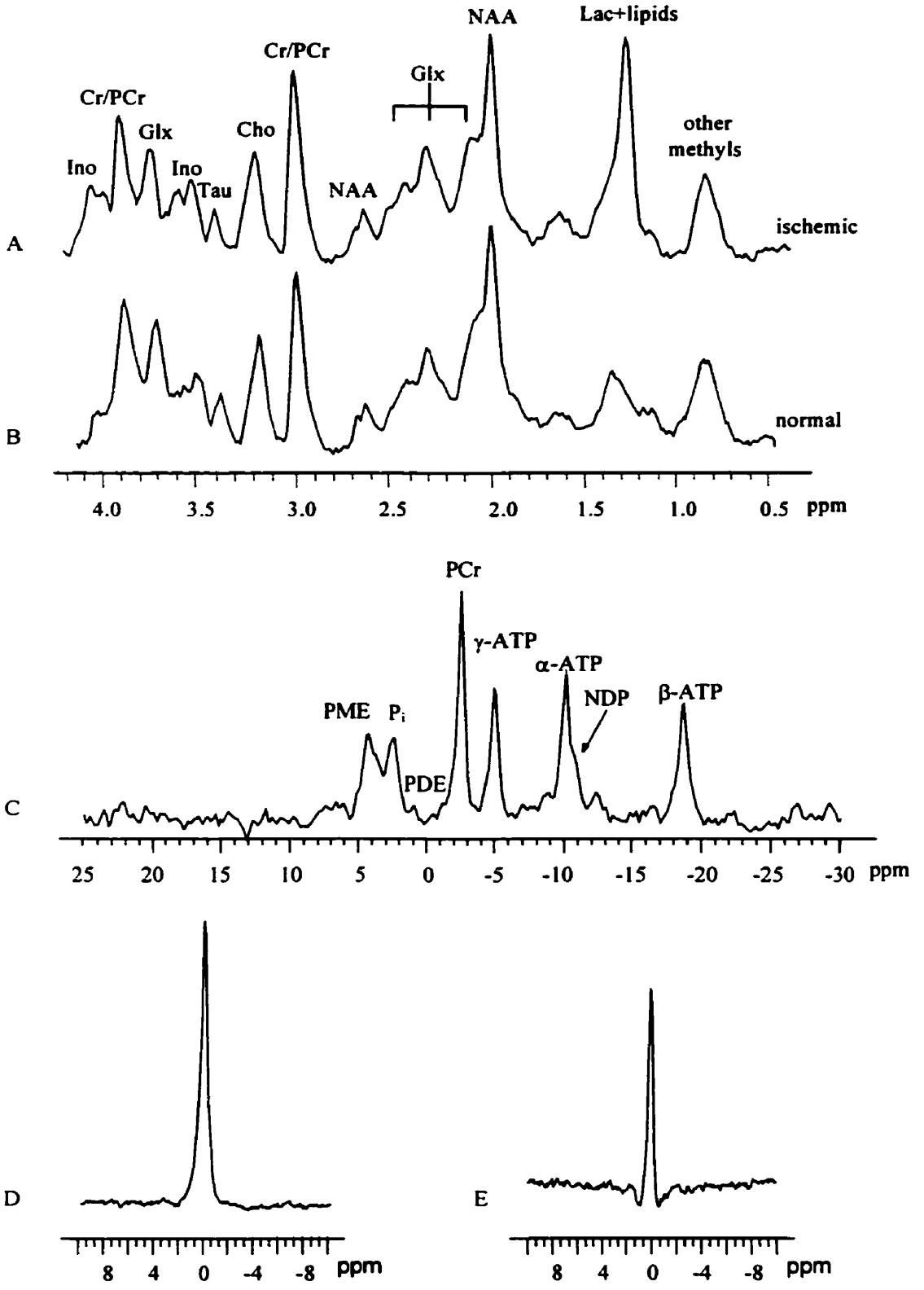

Figure 5.1 *In vivo* ^{1}H, (B) ,^{31}P (C), and single quantum (D) and double quantum (E) ^{23}Na spectra of normal rat brain at 7 T. ^{1}H spectra A was acquired from an ischemic rat brain.

metabolites all appear in a narrow spectral range (i.e. 0.0-6.0 ppm) and overlap with each other, making unequivocal observation of one particular metabolite difficult. Considerable progress has been made, and still has to be made, to overcome these problems.

Table 5.1 Metabolites of common interest in *in vivo* proton magnetic resonance spectroscopy

Metabolite	Chemical Shift [a]	Metabolite Concentration [b]
water	4.70	----
myo-inositol (Ino)/inositol	3.56	2.52
glycine	3.54	----
glucose (Glc)	3.43 + 3.80	----
taurine (Tau)	3.41	1.57
choline (Cho)[c]	3.21	4.79
creatine (Cr)[d]	3.03 + 3.95	9.35
glutamate (Glu)/glutamine (Gln)	2.10-2.50 + 3.76	6.08/3.58
γ-aminobutyric acid (GABA)	1.91, 2.31, 3.02	1.71
N-acetylaspartate (NAA)	2.01	6.37
aspartate (Asp)	2.69, 2.82, 3.90	2.69
alanine (Ala)	1.46	1.52
lactate (Lac)	1.33	3.03 ± 0.19
lipids	0.5-1.5	----

[a] values represent the chemical shift (ppm) frequently examined *in vivo*
[b] values are given as the mean metabolite concentration (μmol/g) in normal rat brain
[c] includes choline, phosphocholine and glycerophosphocholine
[d] includes creatine and phosphocreatine (PCr)
courtesy Dr. K. Malisza (31)

Because of the intrinsic insensitivity of MR, only metabolites with a concentration greater than about 1 mmol/L can be detected by ^{1}H MRS *in vivo* (30). This, as usual, implies some good news and some bad news. The good news is that, because the resonances from

metabolites having very low concentrations show no or only little signal intensity, the appearance of the observed *in vivo* ^{1}H MR spectrum is therefore greatly simplified, making assignment of the resonances much easier. The bad news is that observation of some metabolites which are of physiological significance but at low concentrations, such as some amino acids, is difficult by *in vivo* ^{1}H MRS, therefore limiting the usefulness of the technique. The metabolites of common interest which are readily detected in brain tissue by *in vivo* ^{1}H MRS are listed in Table 5.1, adapted from a recent review by Malisza et al (31).

Among the metabolites listed, other than water and lipids, only N-acetylaspartate (NAA), creatine and choline are generally observed by conventional ^{1}H MRS techniques. The reasons for that are 1) these metabolites have relatively high concentrations in brain; 2) the methyl resonances of these metabolites are uncoupled so that the intensity of these resonances is not attenuated by so-called J-modulation in the long echo-time pulse sequences commonly used; 3) it is possible to observe the methyl resonances of these metabolites unequivocally using conventional pulse sequences. Lactate is an important metabolic product of glycolysis and usually is associated with ischemia, and its role in the pathophysiology of a number of neurological diseases has been well documented. *In vivo* observation of lactate by ^{1}H MRS, however, is often hindered by overlapping of the lactate methyl peaks with the lipid resonances at about 1.33 ppm (Fig. 5.1). Development of ^{1}H MRS techniques which can be used for unequivocal observation of lactate by suppressing or eliminating the lipid resonances has been and continues to be a focus of considerable research. If selective observation of lactate represents a major problem for *in vivo* ^{1}H MRS, selective observation of other metabolites such as γ-aminobutyric acid (GABA), taurine, glutamate and glutamine

by *in vivo* ^{1}H MRS provides an even greater challenge. That is because these amino acids usually have low concentrations, and have complex spin systems which give rise to resonances which often overlap with each other and with the resonances of other metabolites such as NAA, creatine and choline.

Even so, the use of *in vivo* ^{1}H MRS has proven useful and the information it provides has gained us new understandings of a number of neurological diseases. For example, it is suggested that NAA exists only in neurons in the mature brain, and thus can be used as a specific marker for neuronal viability (32). Decreases in NAA concentrations, as detected by *in vivo* ^{1}H MRS, are observed in both humans and animals under pathological conditions such as stroke (33-37), brain tumor (38-42), multiple sclerosis (43-45) and Alzheimer's disease (46-48). The choline resonances observed by *in vivo* ^{1}H MRS include the contributions from free choline, phosphocholine and glycerophosphocholine (49). Alterations in choline level are observed in hepatic encephalopathy (50,51), brain tumor (38,40,42) and diseases involving membrane damage such as multiple sclerosis (44) and leukodystrophies (52). Both creatine and phosphocreatine contribute to the creatine peak observed by *in vivo* ^{1}H MRS, and the total creatine levels in brain are relatively uniform among different brain structures and are unchanged in many pathological processes, thus providing a good reference for the quantification of other metabolites (49). *In vivo* ^{1}H MRS can be used to detect changes in the steady state lactate concentrations in physiologically perturbed tissues (53,54), and to follow the kinetics of dynamic lactate changes in cerebral ischemia models (55,56). Alterations in the concentrations of other metabolites such as *myo*-inositol (51,52,57) and GABA (58-60) have also been seen, as observed by *in vivo* ^{1}H MRS, in a

limited number of studies.

Another interesting feature of *in vivo* ^{1}H MRS is that most studies have been on human brain at low field strength (49). The reason *in vivo* MRS is not as popular in experimental animals (i.e. rodents) as it is in humans is simply because the volume of tissue available for sampling in experimental animals is smaller so that there is often not enough signal-to-noise (SNR) for the measurement. Although acquiring spectra at higher field strength offers some well known advantages such as higher SNR and a more dispersed spectrum, there are also a number of difficulties that either are not encountered at lower field strength or are exaggerated with the increase in field strength (61). For example, the greater chemical shift dispersion at higher field strength on one hand helps in resolving the resonances of different metabolites, but on the other hand it increases the error associated with chemical-shift-dependent spatial displacement when localized spectra are acquired. This will be discussed in detail in the next chapter. Other difficulties in performing *in vivo* ^{1}H MRS at high field strength include the shorter T2 values for metabolites and higher demands on hardware, for instance, a more powerful radiofrequency (RF) amplifier.

Although the volume of research on *in vivo* ^{1}H MRS has been growing steadily (30), it is fair to say that most of the techniques developed so far do not have the reliability and the robustness required for routine applications even though their advantages were demonstrated in the original reports. It is also disappointing to see that a large portion of the current *in vivo* ^{1}H MRS studies on neurological diseases show nothing more than an increased lactate level and/or a decreased NAA level in spite of the fact that these various diseases may be quite

different from one another in terms of their pathophysiology. Increases in applications and particularly in more elaborate applications for *in vivo* ^{1}H MRS requires improvements in the current methodology. This is the main objective of the second part of this thesis which includes this chapter and the next four chapters. It is my hope and determination that, with the contributions made by all members of the *in vivo* MRS community including myself, *in vivo* ^{1}H MRS will continue to develop as a valuable tool with many practical applications.

References

1. R. B. Moon and J. H. Richards, Determination of intracellular pH by ^{31}P magnetic resonance, *J. Biol. Chem.* **248**, 7276, (1973).

2. D. I. Hoult, S. J. Busby, D. G. Gadian, G. K. Radda, R. E. Richards and P. J. Seeley, Observation of tissue metabolites using ^{31}P nuclear magnetic resonance, *Nature* **252**, 285, (1974).

3. B. Chance, S. Eleff and J. Leigh Jr, Noninvasive, nondestructive approaches to cell bioenergetics, *Proc. Natl. Acad. Sci. U. S. A.* **77**, 7430, (1980).

4. J. J. Ackerman, T. H. Grove, G. G. Wong, D. G. Gadian and G. K. Radda, Mapping of metabolites in whole animals by ^{31}P NMR using surface coils, *Nature* **283**, 167, (1980).

5. R. K. Deuel, G. M. Yue, W. R. Sherman, D. J. Schickner and J. J. Ackerman, Monitoring the time course of cerebral deoxyglucose metabolism by ^{31}P nuclear magnetic resonance spectroscopy, *Science* **228**, 1329, (1985).

6. R. K. Gupta, P. Gupta, W. D. Yushok and Z. B. Rose, On the noninvasive measurement of intracellular free magnesium by ^{31}P NMR spectroscopy, *Physiol. Chem. Phys. Med. NMR* **15**, 265, (1983).

7. J. W. Prichard, J. R. Alger, K. L. Behar, O. A. Petroff and R. G. Shulman, Cerebral metabolic studies in vivo by ^{31}P NMR, *Proc. Natl. Acad. Sci. U. S. A.* **80**, 2748, (1983).

8. E. A. Shoubridge, R. W. Briggs and G. K. Radda, ^{31}P NMR saturation transfer measurements of the steady state rates of creatine kinase and ATP synthetase in the rat brain, *FEBS Lett.* **140**, 289, (1982).

9. P. C. van-Zijl and D. Rothman, NMR studies of brain ^{13}C-glucose uptake and metabolism: present status, *Magn. Reson. Imaging* **13**, 1213, (1995).

10. J. W. Prichard and R. G. Shulman, NMR spectroscopy of brain metabolism in vivo, *Annu. Rev. Neurosci.* **9**, 61, (1986).

11. N. R. Sibson, J. Shen, G. F. Mason, D. L. Rothman, K. L. Behar and R. G. Shulman, Functional energy metabolism: in vivo ^{13}C-NMR spectroscopy evidence for coupling of cerebral glucose consumption and glutamatergic neuronalactivity, *Dev. Neurosci.* **20**, 321, (1998).

12. G. F. Mason, K. L. Behar and J. C. Lai, The ^{13}C isotope and nuclear magnetic resonance: unique tools for the study of brain metabolism, *Metab. Brain Dis.* **11**, 283, (1996).

13. G. F. Mason, R. Gruetter, D. L. Rothman, K. L. Behar, R. G. Shulman and E. J. Novotny, Simultaneous determination of the rates of the TCA cycle, glucose utilization, alpha-ketoglutarate/glutamate exchange, and glutamine synthesis in human brain by NMR, *J. Cereb. Blood Flow Metab.* **15**, 12, (1995).

14. K. Kanamori and B. D. Ross, Steady-state in vivo glutamate dehydrogenase activity in rat brain measured by ^{15}N NMR, *J. Biol. Chem.* **270**, 24805, (1995).

15. K. Kanamori and B. D. Ross, ^{15}N n.m.r. measurement of the in vivo rate of glutamine synthesis and utilization at steady state in the brain of the hyperammonaemic rat, *Biochem. J.* **293**, 461, (1993).

16. N. A. Farrow, K. Kanamori, B. D. Ross and F. Parivar, A ^{15}N-n.m.r. study of cerebral, hepatic and renal nitrogen metabolism in hyperammonaemic rats, *Biochem. J.* **270**, 473, (1990).

17. G. S. Payne, A. M. Seymour, P. Styles and G. K. Radda, Multiple quantum filtered ^{23}Na NMR spectroscopy in the perfused heart, *NMR Biomed.* **3**, 139, (1990).

18. R. L. Tyson, G. R. Sutherland and J. Peeling, ^{23}Na nuclear magnetic resonance spectral changes during and after forebrain ischemia in hypoglycemic, normoglycemic, and hyperglycemic rats, *Stroke* **27**, 957, (1996).

19. Y. Boulanger and P. Vinay, Nuclear magnetic resonance monitoring of sodium in biological tissues, *Can. J. Physiol. Pharmacol.* **67**, 820, (1989).

20. C. J. Deutsch and J. S. Taylor, Intracellular pH as measured by ^{19}F NMR, *Ann. N. Y. Acad. Sci.* **508**, 33, (1987).

21. S. K. Song, R. S. Hotchkiss, J. Neil, J. Morris-PE, C. Y. Hsu and J. J. Ackerman, Determination of intracellular calcium in vivo via fluorine-19 nuclear magnetic resonance spectroscopy, *Am. J. Physiol.* **269**, C318, (1995).

22. L. A. Levy, E. Murphy, B. Raju and R. E. London, Measurement of cytosolic free magnesium ion concentration by ^{19}F NMR, *Biochemistry* **27**, 4041, (1988).

23. T. Nakada, I. L. Kwee, P. J. Card, N. A. Matwiyoff, B. V. Griffey and R. H. Griffey, Fluorine-19 NMR imaging of glucose metabolism, *Magn. Reson. Med.* **6**, 307, (1988).

24. I. L. Kwee, T. Nakada and P. J. Card, Noninvasive demonstration of in vivo 3-fluoro-3-deoxy-D-glucose metabolism in rat brain by ^{19}F nuclear magnetic resonance spectroscopy: suitable probe for monitoring cerebral aldose reductase activities, *J. Neurochem.* **49**, 428, (1987).

25. T. Nakada, I. L. Kwee and C. B. Conboy, Noninvasive in vivo demonstration of 2-fluoro-2-deoxy-D-glucose metabolism beyond the hexokinase reaction in rat brain by ^{19}F nuclear magnetic resonance spectroscopy, *J. Neurochem.* **46**, 198, (1986).

26. W. Wolf, V. Waluch and C. A. Presant, Non-invasive ^{19}F-NMRS of 5-fluorouracil in pharmacokinetics and pharmacodynamic studies, *NMR Biomed.* **11**, 380, (1998).

27. E. Hanusovska, I. Dovinova, I. Tkac and L. Novotny, Application of NMR spectroscopy in biochemical studies of tumor cells sensitive and resistant to anticancer drugs, *Neoplasma* **45**, 187, (1998).

28. F. F. Brown and I. D. Campbell, N.m.r. studies of red cells, *Philos. Trans. R. Soc. Lond. B Biol. Sci.* **289**, 395, (1980).

29. P. A. Bottomley, J. Hart-HR, W. A. Edelstein, J. F. Schenck, L. S. Smith, W. M. Leue, O. M. Mueller and R. W. Redington, Anatomy and metabolism of the normal human brain studied by magnetic resonance at 1.5 Tesla, *Radiology* **150**, 441, (1984).

30. R. A. Kauppinen and S. R. Williams, Nuclear magnetic resonance spectroscopy studies of the brain, *Prog. Neurobiol.* **44**, 87, (1994).

31. K. Malisza, P. Kozlowski and J. Peeling, A review of in vivo ^{1}H magnetic resonance spectroscopy of cerebral ischemia in rats, *Biochem. Cell Biol.* **76**, 487, (1998).

32. D. L. Birken and W. H. Oldendorf, N-acetyl-L-aspartic acid: a literature review of a compound prominent in ^{1}H-NMR spectroscopic studies of brain, *Neurosci. Biobehav. Rev.* **13**, 23, (1989).

33. G. D. Graham, P. Kalvach, A. M. Blamire, L. M. Brass, P. B. Fayad and J. W. Prichard, Clinical correlates of proton magnetic resonance spectroscopy findings after acute cerebral infarction, *Stroke* **26**, 225, (1995).

34. H. Lanfermann, H. Kugel, W. Heindel, K. Herholz, W. D. Heiss and K. Lackner, Metabolic changes in acute and subacute cerebral infarctions: findings at proton MR spectroscopic imaging, *Radiology* **196**, 203, (1995).

35. K. M. Welch, S. R. Levine, G. Martin, R. Ordidge, L. A. Vande and J. A. Helpern, Magnetic resonance spectroscopy in cerebral ischemia, *Neurol. Clin.* **10**, 1, (1992).

36. T. Higuchi, S. H. Graham, E. J. Fernandez, W. D. Rooney, H. L. Gaspary, M. W. Weiner and A. A. Maudsley, Effects of severe global ischemia on N-acetylaspartate and other metabolites in the rat brain, *Magn. Reson. Med.* **37**, 851, (1997).

37. T. N. Sager, H. Laursen and A. J. Hansen, Changes in N-acetyl-aspartate content during focal and global brain ischemia of the rat, *J. Cereb. Blood Flow Metab.* **15**, 639, (1995).

38. J. P. Usenius, R. A. Kauppinen, P. A. Vainio, J. A. Hernesniemi, M. P. Vapalahti, L. A. Paljarvi and S. Soimakallio, Quantitative metabolite patterns of human brain tumors: detection by ^{1}H NMR spectroscopy in vivo and in vitro, *J. Comput. Assist. Tomogr.* **18**, 705, (1994).

39. P. B. Barker, S. J. Blackband, J. C. Chatham, B. J. Soher, M. A. Samphilipo, C. A. Magee, J. D. Hilton, J. D. Strandberg and J. H. Anderson, Quantitative proton spectroscopy and histology of a canine brain tumor model, *Magn. Reson. Med.* **30**, 458, (1993).

40. M. J. Fulham, A. Bizzi, M. J. Dietz, H. H. Shih, R. Raman, G. S. Sobering, J. A. Frank, A. J. Dwyer, J. R. Alger and G. Di-Chiro, Mapping of brain tumor metabolites with proton MR spectroscopic imaging: clinical relevance, *Radiology* **185**, 675, (1992).

41. M. L. Gyngell, B. M. Hoehn, O. Kloiber, T. Michaelis, R. I. Ernestus, D. Horstermann and J. Frahm, Localized proton NMR spectroscopy of experimental gliomas in rat brain in vivo, *NMR Biomed.* **5**, 335, (1992).

42. H. Kugel, W. Heindel, R. I. Ernestus, J. Bunke, M. R. du and G. Friedmann, Human brain tumors: spectral patterns detected with localized H-1 MR spectroscopy, *Radiology* **183**, 701, (1992).

43. D. L. Arnold, P. M. Matthews, G. Francis and J. Antel, Proton magnetic resonance spectroscopy of human brain in vivo in the evaluation of multiple sclerosis: assessment of the load of disease, *Magn. Reson. Med.* **14**, 154, (1990).

44. H. B. Larsson, P. Christiansen, M. Jensen, J. Frederiksen, A. Heltberg, J. Olesen and O. Henriksen, Localized in vivo proton spectroscopy in the brain of patients with multiple sclerosis, *Magn. Reson. Med.* **22**, 23, (1991).

45. J. S. Wolinsky, P. A. Narayana and M. J. Fenstermacher, Proton magnetic resonance spectroscopy in multiple sclerosis, *Neurology* **40**, 1764, (1990).

46. D. J. Meyerhoff, S. MacKay, J. M. Constans, D. Norman, C. Van-Dyke, G. Fein and M. W. Weiner, Axonal injury and membrane alterations in Alzheimer's disease suggested by in vivo proton magnetic resonance spectroscopic imaging, *Ann. Neurol.* **36**, 40, (1994).

47. R. A. Moats, T. Ernst, T. K. Shonk and B. D. Ross, Abnormal cerebral metabolite concentrations in patients with probable Alzheimer disease, *Magn. Reson. Med.* **32**, 110, (1994).

48. T. K. Shonk, R. A. Moats, P. Gifford, T. Michaelis, J. C. Mandigo, J. Izumi and B. D. Ross, Probable Alzheimer disease: diagnosis with proton MR spectroscopy, *Radiology* **195**, 65, (1995).

49. F. A. Howe, R. J. Maxwell, D. E. Saunders, M. M. Brown and J. R. Griffiths, Proton spectroscopy in vivo, *Magn. Reson. Q.* **9**, 31, (1993).

50. R. Kreis, B. D. Ross, N. A. Farrow and Z. Ackerman, Metabolic disorders of the brain in chronic hepatic encephalopathy detected with H-1 MR spectroscopy, *Radiology* **182**, 19, (1992).

51. B. D. Ross, S. Jacobson, F. Villamil, J. Korula, R. Kreis, T. Ernst, T. Shonk and R. A. Moats, Subclinical hepatic encephalopathy: proton MR spectroscopic abnormalities, *Radiology* **193**, 457, (1994).

52. B. Kruse, F. Hanefeld, H. J. Christen, H. Bruhn, T. Michaelis, W. Hanicke and J. Frahm, Alterations of brain metabolites in metachromatic leukodystrophy as detected by localized proton magnetic resonance spectroscopy in vivo, *J. Neurol.* **241**, 68, (1993).

53. J. W. Hugg, J. H. Duijn, G. B. Matson, A. A. Maudsley, J. S. Tsuruda, D. F. Gelinas and M. W. Weiner, Elevated lactate and alkalosis in chronic human brain infarction observed by ^{1}H and ^{31}P MR spectroscopic imaging, *J. Cereb. Blood Flow Metab.* **12**, 734, (1992).

54. G. D. Graham, A. M. Blamire, A. M. Howseman, D. L. Rothman, P. B. Fayad, L. M. Brass, O. A. Petroff, R. G. Shulman and J. W. Prichard, Proton magnetic resonance spectroscopy of cerebral lactate and other metabolites in stroke patients, *Stroke* **23**, 333, (1992).

55. H. P. Hetherington, M. J. Tan, K. L. Luo, G. M. Pohost, J. H. Halsey and K. A. Conger, Evaluation of lactate production and clearance kinetics by ^{1}H NMR in a model of brief repetitive cerebral ischemia, *J. Cereb. Blood Flow Metab.* **14**, 591, (1994).

56. H. Lei and J. Peeling, Effect of temperature on the kinetics of lactate production and clearance in a rat model of forebrain ischemia, *Biochem. Cell Biol.* **76**, 503, (1998).

57. B. L. Miller, R. A. Moats, T. Shonk, T. Ernst, S. Woolley and B. D. Ross, Alzheimer disease: depiction of increased cerebral myo-inositol with proton MR spectroscopy, *Radiology* **187**, 433, (1993).

58. O. A. Petroff, K. L. Behar, R. H. Mattson and D. L. Rothman, Human brain gamma-aminobutyric acid levels and seizure control following initiation of vigabatrin therapy, *J. Neurochem.* **67**, 2399, (1996).

59. B. Y. Choe, T. S. Suh, K. S. Shinn, C. W. Lee, C. Lee and I. H. Paik, Observation of metabolic changes in chronic schizophrenia after neuroleptic treatment by *in vivo* hydrogen magnetic resonance spectroscopy, *Invest. Radiol.* **31**, 345, (1996).

60. O. Petroff, D. Rothman, K. Behar and R. H. Mattson, Low brain GABA level is associated with poor seizure control, *Ann. Neurol.* **40**, 908, (1996).

61. H. P. Hetherington, J. W. Pan, W. J. Chu, G. F. Mason and B. R. Newcomer, Biological and clinical MRS at ultra-high field, *NMR Biomed.* **10**, 360, (1997).

Chapter 6. Spectral Editing and Spatial Localization in Proton Magnetic Resonance Spectroscopy

Spectral discrimination and spatial localization are important for all *in vivo* magnetic resonance spectroscopy (MRS) studies. Without spectral discrimination, metabolites can not be observed unequivocally, complicating interpretation of the experimental results. With no spatial localization, spectra can not be acquired from a well-defined region of interest. In this chapter, the current spectral editing and spatial localization techniques are briefly reviewed.

Spectral Editing

Two problems are often encountered when proton MRS is applied to biological samples. First, proton MR resonances from various metabolites all appear in a very narrow spectroscopic range, and often overlap with one another. Secondly, intense water and fat resonances and broad spectral lines due to tissue heterogeneity often complicate the observation of resonances of specific metabolites of interest. Therefore, to be able to monitor subtle changes in metabolites of low concentrations, it is essential to not only suppress water and fat signals, but also eliminate the spectral overlap. Two-dimensional MRS and spectral editing techniques have been developed for such purposes. The two-dimensional MRS techniques often require a long acquisition time which is unacceptable in many cases, and thus they are generally considered inappropriate for *in vivo* studies. Spectral editing is a simplification technique which exploits some unique properties of the spin systems (other than chemical shift) to allow selective observation of the resonances of interest. One

commonly used spin property for spectral editing is scalar J coupling which arises from spin interactions through covalent bonds. In recent years, a family of spectral editing techniques has been developed, including J-modulated echo difference (1-9), multiple-quantum/zero-quantum coherence filtering (10-13), polarization transfer (14-17) and longitudinal spin order (18-21). Among those techniques, the first two are the most commonly used for *in vivo* applications and will be discussed in detail in this thesis. To lay the basis for further discussion, the product operator formalism and the selection of coherence transfer pathways by pulsed magnetic field gradients are first described.

Product Operator Formalism

Virtually all magnetic resonance (MR) experiments are now performed in the pulsed Fourier transform mode. To understand the MR response of a spin system to a pulse sequence, a description of the behavior of the spins in the pulse sequence is required. Over the years, two different approaches have been developed for this purpose, with one that takes advantage of a simple vector model and the other that utilizes quantum mechanics calculations. Although the simple vector model is useful in many cases, in general, it is not adequate in describing more sophisticated MR experiments such as multiple quantum and multiple-dimensional MRS. In such cases, the use of a quantum mechanics approach becomes essential. The density matrix formalism was among the first used quantum mechanics formalisms to describe a multiple-pulse MR experiment (22). Although it provides a rigorous and comprehensive analysis for the spin behavior, the density matrix formalism soon becomes extremely cumbersome with increasing numbers of pulses and precession periods, and thus is

inconvenient to use in practice. Currently, the method of choice for describing a sophisticated MR experiment is the product operator formalism, which is a derivative of the density matrix formalism and surprisingly easy to learn and use (23).

The product operators in a product operator formalism are a set of orthogonal matrices. Each of the product operators represents an orthogonal component of the magnetization and their linear combination forms the complete density matrix. In the past, different product operator formalisms have been developed using different basis sets of product operators, and each of them has advantages and disadvantages (23-29). In the work described in this thesis, the product operator formalisms for the weakly and strongly coupled spin I=1/2 systems in the spherical basis will be used (28,29). For example, 16 spherical basis product operators, **1**, $\mathbf{I_0}$, $\mathbf{I_+}$, $\mathbf{I_-}$, $\mathbf{S_0}$, $\mathbf{S_+}$, $\mathbf{S_-}$, $\mathbf{I_+S_0}$, $\mathbf{I_-S_0}$, $\mathbf{I_0S_+}$, $\mathbf{I_0S_-}$, $\mathbf{I_0S_0}$, $\mathbf{I_+S_+}$, $\mathbf{I_+S_-}$, $\mathbf{I_-S_+}$ and $\mathbf{I_-S_-}$, are required to describe a weakly-coupled two-spin-1/2 system (IS), and Table 6.1 shows the evolution of these product operators under the effects of radiofrequency (RF) pulses, free precession and J coupling (28).

Coherence Transfer Pathways

The concept of "coherence" is a generalization of the notion of transverse magnetization (30). In a MR experiment, coherence can be associated with a transition between two eigenstates with arbitrary difference (p) in magnetic quantum numbers, and p itself is also a quantum number which is usually called the "order" of the coherence. The conventional concept of transverse magnetization corresponds to a particular type of coherence with $p=\pm1$, often

termed single quantum coherence (SQC). Double quantum coherence (DQC) corresponds to $p=\pm 2$, and triple quantum coherence (TQC) corresponds to $p=\pm 3$, and so on. Only SQC (i.e. $p=-1$) is directly observable in a MR experiment. Coherences with other quantum numbers can be generated in a multiple-pulse sequence, but are not physically observable. Longitudinal magnetization is not a coherence, but has properties that resemble those of zero quantum coherences (ZQC).

Table 6.1 Evolution of spherical product operators for an weakly coupled IS spin system under the effects of RF pulses, free precession and J coupling.

1. Pulse with a flip angle of θ and a phase angle of ϕ
$\mathbf{I}_0 \rightarrow \mathbf{I}_0 \cos\theta - \frac{i}{\sqrt{2}}\mathbf{I}_+ \cos\theta \exp(-i\phi) - \frac{i}{\sqrt{2}}\mathbf{I}_- \cos\theta \exp(i\phi)$
$\mathbf{I}_+ \rightarrow \frac{1}{2}\mathbf{I}_+(\cos\theta + 1) - \frac{i}{\sqrt{2}}\mathbf{I}_0 \sin\theta \exp(i\phi) + \frac{1}{2}\mathbf{I}_-(\cos\theta - 1)\exp(2i\phi)$
$\mathbf{I}_- \rightarrow \frac{1}{2}\mathbf{I}_-(\cos\theta + 1) - \frac{i}{\sqrt{2}}\mathbf{I}_0 \sin\theta \exp(-i\phi) + \frac{1}{2}\mathbf{I}_+(\cos\theta - 1)\exp(-2i\phi)$
2. Precession about the z axis with a frequency of ω
$\mathbf{I}_0 \rightarrow \mathbf{I}_0$ $\mathbf{I}_+ \rightarrow \mathbf{I}_+ \exp(-i\omega t)$ $\mathbf{I}_- \rightarrow \mathbf{I}_- \exp(i\omega t)$
3. J coupling with a coupling constant of J
$\mathbf{I}_0 \rightarrow \mathbf{I}_0$ $\mathbf{I}_+ \rightarrow \mathbf{I}_+ \cos 2\pi Jt - i\mathbf{I}_+\mathbf{S}_0 \sin 2\pi Jt$ $\mathbf{I}_- \rightarrow \mathbf{I}_- \cos 2\pi Jt + i\mathbf{I}_-\mathbf{S}_0 \sin 2\pi Jt$

Coherence can be viewed as a non-equilibrium state of a coherent superposition of two eigenstates (30). RF pulses can induce a transition between two coherences, and may change

the order of the coherences. Free precession of a coherence, however, conserves the coherence order. In a multiple-pulse sequence, each RF pulse perturbs the spin system in a coherent state and results in coherence transfer steps which mix coherences of different order. A particular sequence of coherences successively generated in the pulse sequence then forms a coherence transfer pathway which can be represented by a vector **P**,

$$\mathbf{P}=(p_1, p_2, \ldots p_j, \ldots p_n) \qquad [6.1]$$

where p_j is the order of the coherence generated in the jth coherence transfer step.

Selection of Coherence Transfer Pathways by Pulsed Magnetic Field Gradients

Numerous coherence transfer pathways can occur simultaneously in a multiple-pulse sequence. It is therefore necessary in many cases to observe selectively a particular coherence transfer pathway or a family of coherence transfer pathways which corresponds to the spin interactions that are of interest, while eliminating the rest. The selection of coherence transfer pathway(s) can be performed using either phase cycling (31) or filters comprised of pulsed magnetic field gradients (32). For *in vivo* MRS, using pulsed gradients is usually preferable to using phase cycling in selecting coherence transfer pathway(s) because the latter method requires addition/subtraction of sequentially acquired spectra, making it more susceptible to motion artifacts.

Under the influence of a magnetic field gradient, a homonuclear coherence precesses about the z-axis and acquires a position-dependent phase factor (ϕ_r^p) that is proportional to the coherence order p,

$$\phi_r^p = \gamma p \mathrm{Grt} \qquad [6.2]$$

where γ is the gyromagnetic ratio, G is the gradient strength, r is the spatial coordinate, t is the duration of the gradient and a rectangular waveform for the gradient is assumed. Because only MR signals with coherent phase are observable, the different sensitivities of coherences with different orders to the presence of the gradients can then be exploited to select coherence transfer pathway(s) through dephasing/rephasing.

Suppose there is a pulse sequence which involves n coherence transfer steps with a gradient pulse applied during each of those steps. The overall gradient train can be represented as a vector (**G**),

$$\mathbf{G}=(G_1t_1, G_2t_2, \ldots G_jt_j, \ldots G_nt_n). \qquad [6.3]$$

and the overall effect of **G** on an arbitrary coherence transfer pathway **P** is,

$$\sigma(r)_+^{\mathbf{P}} = \exp\left[-i\gamma r\left(\sum_{j=1}^{n} p_j G_j t_j\right)\right]\sigma(r)_-^{\mathbf{P}}. \qquad [6.4]$$

where $\sigma(r)_+^{\mathbf{P}}$ and $\sigma(r)_-^{\mathbf{P}}$ are the density operator components of **P** after and before the gradient pulse train at location r. Integrating over the entire sample, the contribution of **P** to the total signal intensity observed, S(**P**), is

$$S(\mathbf{P}) = \int_{-\infty}^{+\infty} \exp\left[-i\gamma r\left(\sum_{j=1}^{n} p_j G_j t_j\right)\right]\sigma(r)_-^{\mathbf{P}} dr \qquad [6.5]$$

For a particular coherence transfer pathway or pathways that satisfy

$$\sum_{j=1}^{n} p_j G_j t_j = 0 \qquad [6.6]$$

the phase term on the right side of Eq. [6.5] vanishes for all positions over the entire sample and consequently a coherence transfer echo is formed (33). However, for coherence transfer

pathways that do not satisfy Eq. [6.6], the gradient train will introduce a position-dependent phase accumulation and cause a phase dispersion over the entire sample. Coherences with different phases often interfere with each other destructively and the contribution from those coherence transfer pathways to the final signal intensity is therefore eliminated. A full analysis of the principles of using gradient trains to select coherence transfer pathway(s) is beyond the scope of this thesis and can be found elsewhere (32).

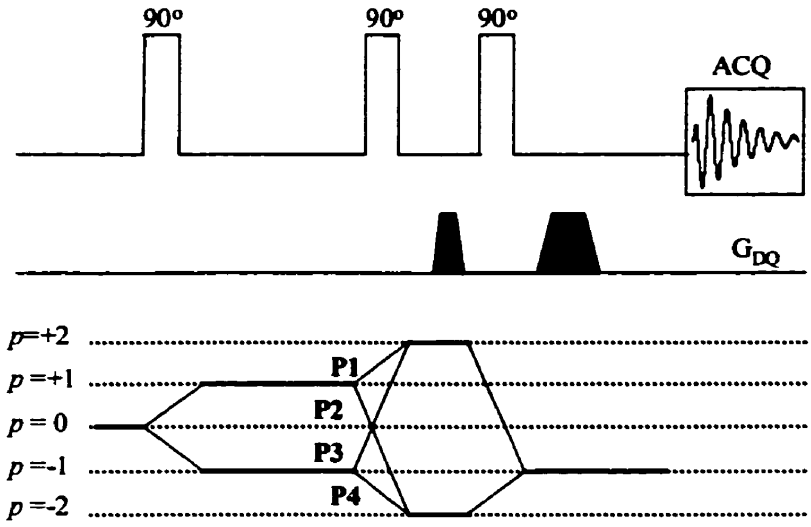

Figure 6.1 A three-pulse double quantum (DQ) coherence transfer experiment. **P1**, **P2**, **P3** and **P4** are the four possible coherence transfer pathways involving DQ coherences. With the gradient pulses (G_{DQ}) shown in the figure, only **P1** and **P3** are selected.

One disadvantage of using gradient pulses to select coherence transfer pathway(s) is the potential reduction in detection sensitivity in the case when more than one coherence transfer pathway is relevant (34-36). For example, in a three-pulse double quantum spectroscopy experiment (Fig. 6.1), four coherence transfer pathways, $\mathbf{P}_1$=(0, 1, 2, -1), $\mathbf{P}_2$=(0, 1, -2, -1), $\mathbf{P}_3$=(0, -1, 2, -1) and $\mathbf{P}_4$=(0, -1, -2, -1), involve double quantum coherence, and have to be selected simultaneously in order to recover the full sensitivity. However, the gradient train

shown in the figure selects only $\mathbf{P}_1$ and $\mathbf{P}_3$, but not $\mathbf{P}_2$ and $\mathbf{P}_4$, thus reducing the detection sensitivity by 50%. It has been demonstrated that, compared to phase cycling, at best only half of the relevant coherence transfer pathways can be selected at a time when gradients are used for signal selection (35,36).

Spectral Editing Using J-Modulated Echo Difference

In a Hahn-echo experiment (Fig. 6.2A), the evolution of product operators for a single spin-1/2 (**I**) is as follows. For simplicity, only terms leading to observable signals are considered and T2 relaxation is neglected.

$$\mathbf{I}_0 \xrightarrow{90^\circ_I} -\frac{i}{\sqrt{2}}\mathbf{I}_+ - \frac{i}{\sqrt{2}}\mathbf{I}_- \qquad [6.7]$$

$$\xrightarrow{\tau} -\frac{i}{\sqrt{2}}\mathbf{I}_+ \exp[-i(\omega_I + \Delta B_0)\tau] - \frac{i}{\sqrt{2}}\mathbf{I}_- \exp[i(\omega_I + \Delta B_0)\tau] \qquad [6.8]$$

$$\xrightarrow{\theta_I} -\frac{i}{2\sqrt{2}}(\cos\theta_I - 1)\mathbf{I}_- \exp[-i(\omega_I + \Delta B_0)\tau] - \frac{i}{2\sqrt{2}}(\cos\theta_I + 1)\mathbf{I}_- \exp[i(\omega_I + \Delta B_0)\tau] \qquad [6.9]$$

$$\xrightarrow{\tau} -\frac{i}{2\sqrt{2}}(\cos\theta_I - 1)\mathbf{I}_- - \frac{i}{2\sqrt{2}}(\cos\theta_I + 1)\mathbf{I}_- \exp[2i(\omega_I + \Delta B_0)\tau] \qquad [6.10]$$

When θ_I=180°, Eq. [6.10] reduces to,

$$\xrightarrow{\tau} \frac{i}{\sqrt{2}}\mathbf{I}_- \qquad [6.11]$$

where subscript I represents the spin **I**, ω is the chemical shift, θ is the flip angle of the refocusing pulse and ΔB_0 is the B_0 inhomogeneity. Eq. [6.11] shows that signal intensity of the Hahn echo is independent of τ, and both the chemical shift and the B_0 inhomogeneity are refocused provided the flip angle of the refocusing pulse is exactly 180°.

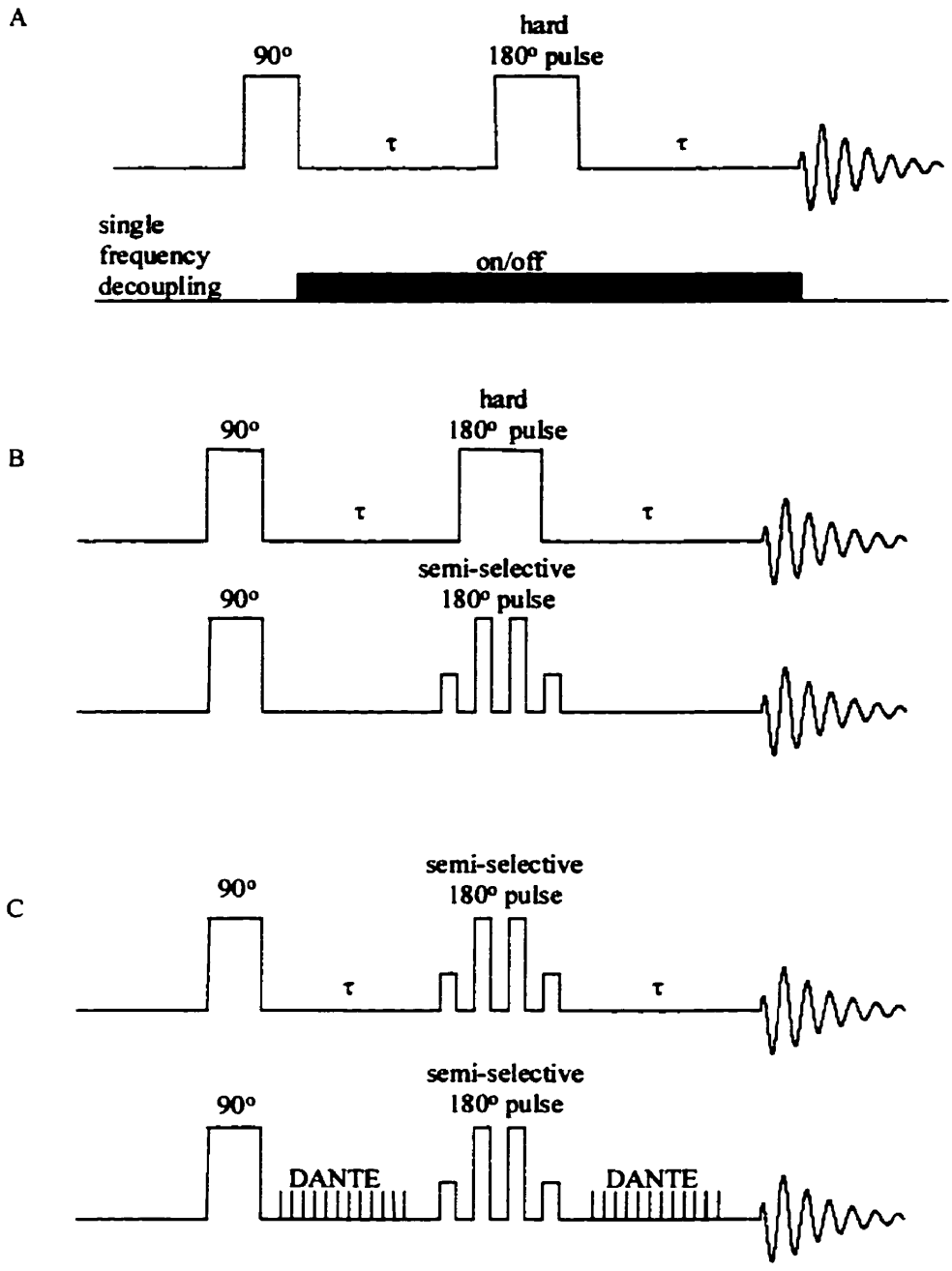

Figure 6.2 Pulse sequences for spectral editing using J-modulated Hahn echoes.

For a weakly-coupled two-spin-1/2 system **IS**, its response to the Hahn-echo sequence is different from that of the uncoupled spin. Considering only the terms that are originated from the spin **I** and lead to observable signals, and neglecting the effect of T2 relaxation,

$$\mathbf{I}_0 \xrightarrow{90^\circ_{I+S}} -\frac{i}{\sqrt{2}}\mathbf{I}_+ \qquad [6.12]$$

$$\xrightarrow{\tau} -\frac{i}{\sqrt{2}}\mathbf{I}_+ \cos \pi J\tau \exp[-i(\omega_I + \Delta B_0)] - \sqrt{2}\mathbf{I}_+\mathbf{S}_0 \sin \pi J\tau \exp[-i(\omega_I + \Delta B_0)] \qquad [6.13]$$

$$\xrightarrow{180^\circ_{I+S}} \frac{i}{\sqrt{2}}\mathbf{I}_- \cos \pi J\tau \exp[-i(\omega_I + \Delta B_0)] - \sqrt{2}\mathbf{I}_-\mathbf{S}_0 \sin \pi J\tau \exp[-i(\omega_I + \Delta B_0)] \qquad [6.14]$$

$$\xrightarrow{\tau} \frac{i}{\sqrt{2}}\mathbf{I}_- \cos 2\pi J\tau \qquad [6.15]$$

where 180°_{I+S} represents a 180° refocusing pulse which refocuses the resonances of both the **I** and **S** spins. Eq. [6.15] shows that, unlike chemical shift and ΔB_0, J-coupling is not refocused in the Hahn echo experiment and the signal intensity of the Hahn echo for the weakly coupled spin **I** is modulated by a factor of $\cos 2\pi J\tau$. When $\tau = 1/2J$, Eq. [6.15] becomes

$$\xrightarrow{\tau} -\frac{i}{\sqrt{2}}\mathbf{I}_- \qquad [6.16]$$

so that the Hahn echo is 180° out of phase relative to that of an uncoupled spin.

Instead of using a refocusing pulse that refocuses the resonances of both the **I** and **S** spins, the use of a refocusing pulse that acts on the resonance of the **I** spin only (180°_I) will inhibit the J-coupling effect and result in a Hahn echo whose intensity is not modulated by τ,

$$\xrightarrow{180^\circ_I} \frac{i}{\sqrt{2}}\mathbf{I}_- \cos \pi J\tau \exp[-i(\omega_I + \Delta B_0)] + \sqrt{2}\mathbf{I}_-\mathbf{S}_0 \sin \pi J\tau \exp[-i(\omega_I + \Delta B_0)] \qquad [6.17]$$

$$\xrightarrow{\tau} \frac{i}{\sqrt{2}}\mathbf{I}_{-}. \qquad [6.18]$$

Under such conditions, the weakly coupled **I** spin behaves the same as if it is uncoupled.

The use of the J-modulated echo difference sequence to edit proton MR spectra was proposed originally by Campbell et al (1). Rothman et al (2) first applied this principle to edit a number of metabolites *in vivo*. Rothman's editing sequence is shown in Fig. 6.2A. Two Hahn echoes are acquired with τ=1/2J (for doublets or quartets) or τ=1/4J (for triplets), one in the absence and the other in the presence of a single frequency decoupling. In the presence of decoupling, the coupled spin behaves exactly the same as an uncoupled spin and produces a Hahn echo that is 180° out of phase relative to the echo produced in the absence of decoupling. For uncoupled spins, the phases of the two Hahn echoes remain the same regardless of the presence or the absence of decoupling. Subtraction of the two spectra will therefore retain the signals from the coupled spins only, while eliminating the signals from the uncoupled spins.

In view of the technical inconvenience of using single frequency decoupling, a number of alternative editing sequences using J-modulated echo difference were developed soon after Rothman's work (3-5). In those sequences, two Hahn echoes were acquired, one with a "non-selective" refocusing pulse that acts on the resonances of all the spins in the coupled spin system and the other with a selective refocusing pulse that acts on the resonance of the target spin only, and subtraction of these two echoes will result in a spectrum of the edited spin only. Two typical sequences of this kind are shown in Fig. 6.2B and 6.2C. In both sequences 6.2B and 6.2C, a binomial refocusing pulse serves as the semi-selective refocusing pulse with which the J-coupling effect is inhibited. To produce "non-selective" refocusing, either a hard

180° pulse (Fig. 6.2B) or a combination of a binomial refocusing pulse and a delays alternating with nutations for tailored excitation (DANTE) pulse train (Fig. 6.2C) is used. Compared to the sequence 6.2A, sequences 6.2B and 6.2C provide better water suppression and are less susceptible to frequency and pulse power missetting.

Imperfection of the refocusing pulses affects the outcome of an editing experiment using J-modulated echo difference. If instead of being exactly 180°, the flip angles of the refocusing pulse(s) for **I** and **S** spins are θ_I and θ_S, then when τ=1/2J, Eqs. [6.16] and [6.18] become

$$\xrightarrow{\tau} -\frac{i}{2\sqrt{2}}(\cos\theta_I - 1)\cos\theta_S \mathbf{I}_- + \frac{i}{2\sqrt{2}}(\cos\theta_I + 1)\cos\theta_S \mathbf{I}_- \exp[2i(\omega_I + \Delta B_0)\tau] \qquad [6.19]$$

and

$$\xrightarrow{\tau} -\frac{i}{2\sqrt{2}}(\cos\theta_I - 1)\mathbf{I}_- + \frac{i}{2\sqrt{2}}(\cos\theta_I + 1)\mathbf{I}_- \exp[2i(\omega_I + \Delta B_0)\tau] \qquad [6.20]$$

so that the detection sensitivity decreases by a factor of $\frac{1}{4}(\cos\theta_S - 1)(\cos\theta_I - 1)$ relative to the ideal case. Also the chemical shift and B_0 inhomogeneity are not refocused perfectly so that the phase of the observed signals will be slightly distorted (9). Moreover, because of the phase mismatch caused by the imperfection of the refocusing pulses, simple sequences such as those shown in Figs. 6.2B and 6.2C often are not adequate to provide perfect cancellation of unwanted signals, thus compromising the editing efficiency of those sequences. Phase cycling or order cycling of the refocusing pulse(s) circumvents this problem (37), and using adiabatic refocusing pulses also helps (9,38).

Besides Hahn echo spectroscopy, spectral editing using J-modulated echo difference spectroscopy can also be done with double spin echo (6,7) and stimulated echo spectroscopy

(8). In these methods, the phase dependence of the echo on the echo time (TE) or the mixing time (TM) is exploited for spectral editing. Among existing spectral editing techniques, spectral editing using J-modulated echo difference provides the highest possible detection sensitivity. For example, in the case of editing for lactate (9) and γ-aminobutyric acid (GABA) (39-42) which are two metabolites most commonly observed by this technique *in vivo*, the theoretical detection sensitivities are 100% and 50% respectively, higher than those of other editing techniques. One major disadvantage of this technique is that it requires addition/subtraction of sequentially acquired spectra, and thus is susceptible to motion artifacts when used *in vivo*.

Spectral Editing Using Multiple Quantum Filtering

Generation of multiple quantum coherences (MQC) from an uncoupled spin system is generally forbidden except in special situations such as in the case of high field multiple quantum (MQ) echoes (43,44). On the contrary, for a coupled spin system, MQC can always be generated in a multiple-pulse experiment and the creation and the evolution of such MQC during the pulse sequence depends on the coupling properties of the spin system. Therefore, by selectively observing coherence transfer pathway(s) that involve MQC, it is possible to differentiate between uncoupled spin systems and coupled spin systems, and between coupled spin systems with different coupling properties, thus achieving the purpose of spectral editing. Although MQC are not directly observable, it is always possible to convert MQC into SQC and observe them indirectly.

MQ filtering (MQF) has long been used in high resolution MRS for spectral editing. Adaptation of such a concept to *in vivo* MRS started in the late 1980s when much effort was made in searching for a MRS technique for the selective observation of lactate (10,11,45), an important glycolysis metabolite, *in vivo*. A number of MQF sequences have been developed and compared in the past (10,12), and it has been concluded that a double quantum filtering (DQF) sequence with a symmetric excitation/detection RF scheme provides the best compromise among detection sensitivity, water/fat suppression and motion sensitivity, and thus is most suitable for *in vivo* applications. A schematic representation of such a DQF sequence is shown in Fig. 6.3.

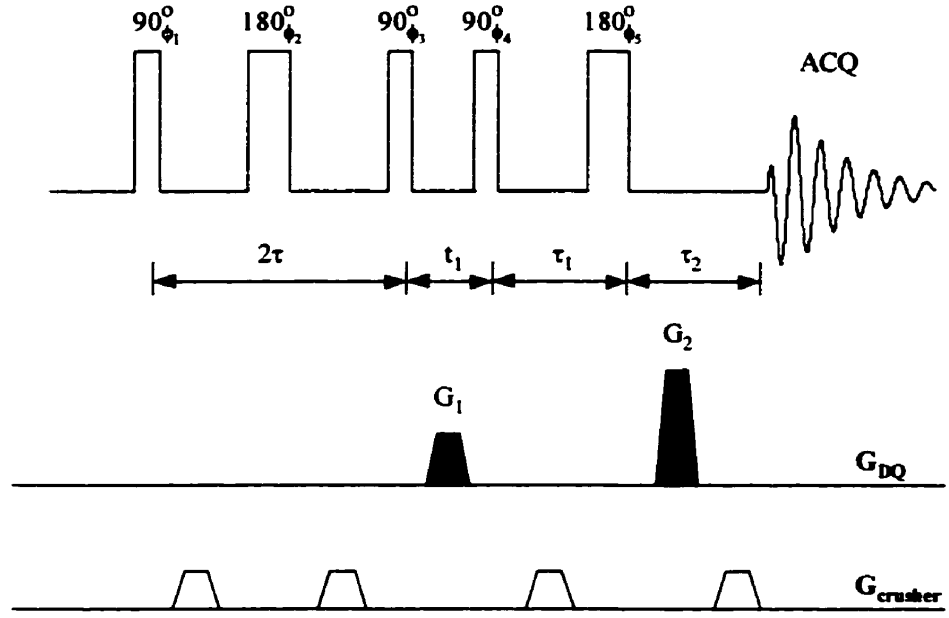

Figure 6.3 A conventional double quantum coherence transfer sequence for spectral editing.

Using a product operator formalism in spherical basis (28), the response of a weakly-coupled spin system **IS** to the pulse sequence shown in Fig. 6.3 is analyzed as follows. Only the terms which originate from the **I** spin and lead to observable signals are considered and, for

simplicity, T2 relaxation is ignored. With the first 90° and 180° pulses, the longitudinal magnetization is prepared into a so-called antiphase state which is represented by the operators $\mathbf{I}_-\mathbf{S}_0$ and $\mathbf{I}_+\mathbf{S}_0$.

$$\mathbf{I}_0 \xrightarrow{90^\circ_{\phi_1}} -\frac{i}{\sqrt{2}}\mathbf{I}_+ \exp[-i\phi_1] - \frac{i}{\sqrt{2}}\mathbf{I}_- \exp[i\phi_1]$$

$$\xrightarrow{\tau} \xrightarrow{180^\circ_{\phi_2}} \xrightarrow{\tau}$$

$$\frac{i}{\sqrt{2}}(\mathbf{I}_- \cos 2\pi J\tau + 2i\mathbf{I}_-\mathbf{S}_0 \sin 2\pi J\tau)\exp[-i(\phi_1 - 2\phi_2)]$$

$$+\frac{i}{\sqrt{2}}(\mathbf{I}_+ \cos 2\pi J\tau + 2i\mathbf{I}_+\mathbf{S}_0 \sin 2\pi J\tau)\exp[i(\phi_1 - 2\phi_2)]$$

Note that chemical shift and B_0 inhomogeneity are refocused at the end of the second τ period. The second 90° pulse is the DQ creation pulse which converts the antiphase magnetization into DQC ($\mathbf{I}_+\mathbf{S}_+$ and $\mathbf{I}_-\mathbf{S}_-$) and ZQC ($\mathbf{I}_+\mathbf{S}_-$ and $\mathbf{I}_-\mathbf{S}_+$).

$$\xrightarrow{90^\circ_{\phi_3}} -\frac{i}{2}\sin 2\pi J\tau \mathbf{I}_+\mathbf{S}_+ \exp[i(\phi_1 - 2\phi_2 - \phi_3)] - \frac{i}{2}\sin 2\pi J\tau \mathbf{I}_+\mathbf{S}_+ \exp[-i(\phi_1 - 2\phi_2 + 3\phi_3)]$$

$$+\frac{i}{2}\sin 2\pi J\tau \mathbf{I}_-\mathbf{S}_- \exp[i(\phi_1 - 2\phi_2 + 3\phi_3)] + \frac{i}{2}\sin 2\pi J\tau \mathbf{I}_-\mathbf{S}_- \exp[-i(\phi_1 - 2\phi_2 - \phi_3)]$$

$$-\frac{i}{2}\sin 2\pi J\tau \mathbf{I}_+\mathbf{S}_- \exp[i(\phi_1 - 2\phi_2 + \phi_3)] - \frac{i}{2}\sin 2\pi J\tau \mathbf{I}_+\mathbf{S}_- \exp[-i(\phi_1 - 2\phi_2 + \phi_3)]$$

$$+\frac{i}{2}\sin 2\pi J\tau \mathbf{I}_-\mathbf{S}_+ \exp[i(\phi_1 - 2\phi_2 + \phi_3)] + \frac{i}{2}\sin 2\pi J\tau \mathbf{I}_-\mathbf{S}_+ \exp[-i(\phi_1 - 2\phi_2 + \phi_3)]$$

The terms for ZQC will be ignored from now on since they will be dephased by the coherence transfer pathway selection gradients. During the t_1 evolution period, the amplitude of the DQC is modulated by a factor of $\cos^2\pi Jt_1$ and the phase of the DQC is affected by B_0 inhomogeneity (12).

$$\xrightarrow{t_1} -\frac{i}{2}\cos^2\pi Jt_1\sin 2\pi J\tau \mathbf{I}_+\mathbf{S}_+\exp[i(\phi_1-2\phi_2-\phi_3-2\Delta B_0t_1)]$$
$$-\frac{i}{2}\cos^2\pi Jt_1\sin 2\pi J\tau \mathbf{I}_+\mathbf{S}_+\exp[-i(\phi_1-2\phi_2+3\phi_3+2\Delta B_0t_1)]$$
$$+\frac{i}{2}\cos^2\pi Jt_1\sin 2\pi J\tau \mathbf{I}_-\mathbf{S}_-\exp[i(\phi_1-2\phi_2+3\phi_3+2\Delta B_0t_1)]$$
$$+\frac{i}{2}\cos^2\pi Jt_1\sin 2\pi J\tau \mathbf{I}_-\mathbf{S}_-\exp[-i(\phi_1-2\phi_2-\phi_3-2\Delta B_0t_1)]$$

The third 90° pulse is the DQ read pulse which converts DQC back to the observable SQC. If a non-selective DQ read pulse is used, which acts on the resonances of both the **I** and **S** spins

$$\xrightarrow{90^\circ_{\phi_4}} -\frac{i}{4\sqrt{2}}\cos^2\pi Jt_1\sin 2\pi J\tau \mathbf{I}_+\mathbf{S}_0\exp[i(\phi_1-2\phi_2-\phi_3+\phi_4-2\Delta B_0t_1)]$$
$$-\frac{i}{4\sqrt{2}}\cos^2\pi Jt_1\sin 2\pi J\tau \mathbf{I}_+\mathbf{S}_0\exp[-i(\phi_1-2\phi_2+3\phi_3-\phi_4+2\Delta B_0t_1)]$$
$$-\frac{i}{4\sqrt{2}}\cos^2\pi Jt_1\sin 2\pi J\tau \mathbf{I}_+\mathbf{S}_0\exp[i(\phi_1-2\phi_2+3\phi_3-3\phi_4+2\Delta B_0t_1)]$$
$$-\frac{i}{4\sqrt{2}}\cos^2\pi Jt_1\sin 2\pi J\tau \mathbf{I}_+\mathbf{S}_0\exp[-i(\phi_1-2\phi_2-\phi_3+3\phi_4-2\Delta B_0t_1)]$$

The final 180° pulse serves as a refocusing pulse.

$$\xrightarrow{\tau_1}\xrightarrow{180^\circ_{\phi_5}}\xrightarrow{\tau_2}$$
$$-\frac{i}{8\sqrt{2}}\cos^2\pi Jt_1\sin 2\pi J\tau\sin[\pi J(\tau_1+\tau_2)]\mathbf{I}_-\exp[i(\phi_1-2\phi_2-\phi_3+\phi_4+2\phi_5+\Delta B_0(\tau_2-\tau_1-2t_1))]$$
$$-\frac{i}{8\sqrt{2}}\cos^2\pi Jt_1\sin 2\pi J\tau\sin[\pi J(\tau_1+\tau_2)]\mathbf{I}_-\exp[-i(\phi_1-2\phi_2+3\phi_3-\phi_4-2\phi_5-\Delta B_0(\tau_2-\tau_1-2t_1))]$$
$$-\frac{i}{8\sqrt{2}}\cos^2\pi Jt_1\sin 2\pi J\tau\sin[\pi J(\tau_1+\tau_2)]\mathbf{I}_-\exp[i(\phi_1-2\phi_2+3\phi_3-3\phi_4+2\phi_5+\Delta B_0(\tau_2-\tau_1+2t_1))]$$
$$-\frac{i}{8\sqrt{2}}\cos^2\pi Jt_1\sin 2\pi J\tau\sin[\pi J(\tau_1+\tau_2)]\mathbf{I}_-\exp[-i(\phi_1-2\phi_2-\phi_3+3\phi_4-2\phi_5-\Delta B_0(\tau_2-\tau_1+2t_1))]$$

Each of the four terms above represents a theoretically observable signal generated from a particular coherence transfer pathway with the first one from **P1**=(0, -1, +1, +2, +1, -1), the second one from **P2**=(0, +1, -1, +2, +1, -1), the third one from **P3**=(0, -1, +1, -2, +1, -1) and

the fourth one from **P4**=(0, +1, -1, -2, +1, -1). With the coherence transfer selection gradients shown in Fig. 6.3, however, only the signals generated from **P1** and **P2** are selected. A symmetric excitation/detection RF scheme means $\tau_1+\tau_2=2\tau$, and if τ_1 and τ_2 are set to be $\tau-t_1$ and $\tau+t_1$, thus $\tau_2-\tau_1-2t_1=0$, to refocus the B_0 inhomogeneity, the expression for the final signal, F(**I**), is

$$F(\mathbf{I}_-) =$$

$$-\frac{i}{8\sqrt{2}}\cos^2\pi Jt_1\sin^2 2\pi J\tau \mathbf{I}_- \exp[i(\phi_1-2\phi_2-\phi_3+\phi_4+2\phi_5)]$$

$$-\frac{i}{8\sqrt{2}}\cos^2\pi Jt_1\sin^2 2\pi J\tau \mathbf{I}_- \exp[-i(\phi_1-2\phi_2+3\phi_3-\phi_4+2\phi_5)]$$

The phases of the RF pulses can be chosen so that the phase factors in both terms are zero and if 2τ is 1/2J and t_1 modulation is ignored,

$$F(\mathbf{I}_-) = -\frac{i}{4\sqrt{2}}\mathbf{I}_- . \qquad [6.21]$$

Recall that the signal intensity for **I** spin immediately after a 90° pulse is

$$F(\mathbf{I}_-) = -\frac{i}{\sqrt{2}}\mathbf{I}_- . \qquad [6.22]$$

Comparison of Eqs. [6.21] and [6.22] shows that, at best, only 25% of the total signal intensity available can pass through the DQ filter shown in Fig. 6.3

If a frequency selective DQ read pulse which acts on the **S** spin only is used,

$$\xrightarrow{90^\circ_{\phi_4}} -\frac{1}{2\sqrt{2}}\cos^2\pi Jt_1\sin 2\pi J\tau \mathbf{I}_+\mathbf{S}_0 \exp[i(\phi_1-2\phi_2-\phi_3+\phi_4-2\Delta B_0 t_1)]$$

$$-\frac{1}{2\sqrt{2}}\cos^2\pi Jt_1\sin 2\pi J\tau \mathbf{I}_+\mathbf{S}_0 \exp[-i(\phi_1-2\phi_2+3\phi_3-\phi_4+2\Delta B_0 t_1)]$$

Then, after the 180° refocusing pulse,

$$\xrightarrow{\tau_1} \xrightarrow{180^\circ_{\phi_5}} \xrightarrow{\tau_2}$$

$$-\frac{i}{4\sqrt{2}}\cos^2\pi Jt_1 \sin 2\pi J\tau \sin[\pi J(\tau_1+\tau_2)]\mathbf{I}_- \exp[i(\phi_1 - 2\phi_2 - \phi_3 + \phi_4 + 2\phi_5 + \Delta B_0(\tau_2 - \tau_1 - 2t_1))]$$

$$-\frac{i}{4\sqrt{2}}\cos^2\pi Jt_1 \sin 2\pi J\tau \sin[\pi J(\tau_1+\tau_2)]\mathbf{I}_- \exp[-i(\phi_1 - 2\phi_2 + 3\phi_3 - \phi_4 - 2\phi_5 - \Delta B_0(\tau_2 - \tau_1 - 2t_1))]$$

In this case, a new expression for F(**I**$_-$) can be derived in analogy to Eq. [6.21]

$$F(\mathbf{I}_-) = -\frac{i}{2\sqrt{2}}\mathbf{I}_- . \qquad [6.23]$$

Equation [6.23] shows that the detection sensitivity is improved from 25% to 50% if a frequency selective DQ read pulse is used. The 50% intrinsic signal loss is due to the dephasing of ZQC by the coherence transfer pathway selection gradient pulses. In theory, full detection sensitivity can be obtained by means of selective-pulse filtering of both DQC and ZQC (46,47). However, in practice, those pulse sequences require either phase cycling to eliminate the fat signals (46) or addition/subtraction of sequentially acquired spectra in order to recover the full detection sensitivity (47), making their usefulness limited for *in vivo* applications.

The pulse sequence shown in Fig. 6.3 in principle can be used to edit for any metabolites when it is adjusted to optimize the detection sensitivity of the target metabolite while eliminating spectral overlap efficiently. Previously, DQF methods have been applied to the selective observation of lactate (10,11), GABA (48,49), citrate (50), glucose (51), N-acetylaspartate (NAA) (52), taurine (53) and glutamate (54) *in vivo*.

Spatial Localization

Because of the heterogeneity of biological tissues, the need for spatial localization in *in vivo* MRS is apparent. When *in vivo* MRS is used for diagnostic purposes, spatial localization is particularly essential to locate the origin of pathogenesis and to differentiate the healthy tissue from the tissue undergoing physiological perturbation. The development of spatial localization techniques commenced at the beginning of the 1980s, soon after the demonstration of the usefulness of MRS *in vivo*. A great number of spatial localization techniques have been developed and refined over the years, and many of them have become available for routine uses.

Localized spectroscopy can be performed with either single voxel localization or multiple voxel localization. Single voxel techniques allow spectra to be acquired from a single volume of interest (VOI) while multiple voxel techniques, which are usually referred as spectroscopic imaging (SI), acquire spectra from a number of VOIs, usually a matrix of volume elements, simultaneously. Although single voxel localization is sufficient in some cases, SI is generally preferred because, in practice, there is often no a *priori* knowledge available about the exact localization of the VOI.

Spatial Localization Based on B_1 Gradient

The spatial localization techniques for *in vivo* MRS can be divided into two categories: techniques based on B_1 gradient and techniques based on B_0 gradient. The idea of using B_1

gradients for spatial encoding was originally proposed by Hoult in 1979 (55), and was soon adapted by Cox and Styles for spatially localized spectroscopy (56). This technique was later referred to as rotating frame spectroscopy (RFS) which gained its name from the title of Hoult's original paper "rotating frame zeugmatography" (57). Usually, RFS is used to acquire one-dimensional (1D) spectroscopic images although in principle single voxel localization is also achievable with Fourier series analysis (58-60). Besides RFS, spatial localization with B_1 gradients can also be obtained by using a surface coil, first introduced to *in vivo* MRS by Ackerman et al (61). A surface coil generates an inhomogeneous B_1 field and receives MR signals originating from a sensitive volume only. The shape and the size of the sensitive volume are usually not well-defined, and are determined by the geometry of the surface coil itself and, to some extent, by experimental settings. Because spatial localization achieved by surface coil itself is not exact, it is therefore not sufficient in many cases. Surface coil localization can be refined further by using depth pulses which incorporate composite pulses and phase cycling schemes (62) and by using B_0 gradients such as in the case of depth resolved surface coil spectroscopy (DRESS) (63).

An apparent advantage of localization techniques based on B_1 gradient is that no B_0 switching is needed, which becomes significant for systems suffering eddy current problems and for experiments in which extremely short TE is required. Another feature of the techniques based on B_1 gradient is that the spatial localization achieved is always relative to the coil itself so that it is not susceptible to motion artifacts. Furthermore, spatial localization by B_1 gradient is not subject to errors such as those caused by chemical shift dispersion and other off-resonance effects that can occur in the techniques based on B_0 gradient. In spite of

the advantages, spatial localization techniques using B_1 gradients are losing their popularity due to some significant disadvantages. First, localization by B_1 gradients is often not exact. Second, spatial localization achieved to date by this technique has generally been limited to one dimension only, although in principle three-dimensional localization is possible. Third, localization by RFS requires a specialized RF coil which, technically, is difficult to make. Finally, the correlation between localized spectra and a MR image is not straightforward, making visualization of the VOI difficult.

Spatial Localization Based on B_0 Gradient

The two basic principles for spatial localization with B_0 gradients, slice selective excitation (64) and phase encoding (65), were both proposed in the mid 1970s. However, localization techniques based on those principles only started to emerge about ten years later. The localization techniques based on B_0 gradient can be divided into three groups.

1. Topical Magnetic Resonance

Topical magnetic resonance (TMR) was first used by Gordon et al in 1980 (66). In this technique, the main field is profiled using nonlinear static field gradients so that high field homogeneity remains only in a small volume which is the VOI. Protons that reside outside the VOI experience a highly inhomogeneous B_0 field and therefore have very broad resonances and do not contribute to the final signals observed. The spectra acquired with TMR often suffer from poor spectral resolution, and the technique does not allow free control

of the volume and the position of the VOI. Thus the method is now seldom used. However, the idea of using nonlinear field gradients to spoil MR signals outside the VOI has survived and has been used in some applications with surface coil localization (67).

2. Localization with Phase Encoding

The phase acquired by a precessing magnetization depends on the strength of the magnetic field it experiences. With a B_0 gradient applied during a free precession period, the magnetizations at different spatial coordinates experience different field strengths and thus acquire different phases during the precession. By performing experiments with a number of gradient strengths or durations, spatially resolved information can be extracted, by Fourier transformation in most cases, from the data acquired. This is the basic idea of phase-encoding proposed by Kumar et al in 1975 (65), and is a fundamental principle for both MR imaging and chemical shift spectroscopic imaging (CSI). *In vivo* CSI was first demonstrated in the early 1980s (68,69) and has found many applications since. CSI is capable of generating images reflecting the spatial distribution of metabolites, which in conjunction with the anatomical images are very useful in studying regional tissue metabolism and have the potential to be used as a tool for clinical diagnosis.

CSI by itself can be used for full three-dimensional localization when phase encoding is performed in all three directions. However, two-dimensional CSI techniques are the most commonly used in view of reducing the total acquisition time, with localization in the third dimension usually achieved by slice selective excitation or refocusing. CSI is often combined

with other localization techniques such as outer volume suppression to achieve more precise localization (70-72). Decoding of the phase-encoded data for CSI is usually performed by Fourier transformation. Recently, another decoding method, spectral localization by imaging (SLIM) (73), was proposed by Lauterber's group, although the usefulness of the method requires further investigation.

CSI offers flexible spatial localization (the voxel matrix can be shifted post-acquisition) that is independent of chemical shift, and theoretically provides the same signal-to-noise per unit time (SNRT) as the single voxel techniques. The major concern with CSI for *in vivo* applications is the long acquisition time it is often associated with. For example, for a two-dimensional CSI experiment with a 16×16 matrix size, a repetition time of 2.5 s and four averages, the total acquisition time is about 42 minutes. With CSI, a large matrix size is usually necessary in order to avoid inter-voxel signal leakage via so-called Gibbs artifacts. A larger matrix size corresponds to a greater number of phase encoding steps, and therefore a longer acquisition time. Since the acquisition time is long, any motion and system instability during acquisition will degrade the outcome of the experiment.

3. Localization with Slice Selection

Localization with slice selection is the most popular technique for spatial localization in *in vivo* MRS. The main reason for its popularity is that it allows, with the direct guidance of a MR image, free control of the size and the position of the VOI. These are generally single voxel techniques, with the exception of Hadamard encoding which will be discussed

separately in chapter 9. Based on the technical features, these methods can be further divided into three categories.

The first category of methods achieves spatial localization by destroying the magnetization outside the VOI through excitation/dephasing while retaining the magnetization within the VOI for observation, and these are normally single-shot methods. The earliest method of this category is volume selective excitation (VSE) proposed by Aue et al in 1984 (74). In Aue's method, localization in each of the three dimensions is attained by using a three-pulse train containing a hard 90° pulse and two 45° slice selective pulses along with a slice-selective gradient to destroy the magnetization outside the slice of interest (74-76). Other methods of this category using different pulse trains or pulse sandwiches to prepare the magnetization include spatially resolved spectroscopy (SPARS) (77), localization of unaffected spins (LOCUS) (78), spatial and chemical-shift-encoded excitation (SPACE) (79) and discrete isolation from gradient-governed elimination of resonances (DIGGER) (80). Despite the earlier success, spatial localization by destroying the magnetization outside the VOI has already lost its popularity for the following reasons. First, such methods usually require a considerable number of RF pulses with precise flip angles, and any imperfection or mis-caliberation of these pulses will result in significant localization error. Second, T1 relaxation during the magnetization preparation period leads to contamination from regions outside the VOI. Third, phase cycling is necessary in some of the methods so that they become sensitive to sample motion.

The second category of localization includes methods in which sequentially acquired spectra are added/subtracted to obtain a spatially localized spectrum from the VOI. One of the most successful methods of this category is imaging selected *in vivo* spectroscopy (ISIS) which was first proposed by Ordidge et al in 1986 (81). The basic ISIS pulse sequence is shown in Fig. 6.4 (82). The sequence begins with a magnetization preparation period during which the longitudinal magnetization is encoded spatially by slice-selective inversion. The preparation period is followed by a stabilization period for eddy currents to decay, then by a read-out period for signal observation. In order to achieve three-dimensional localization for a cubic volume, a total of eight ISIS scans are required in which the three slice selective inversion pulses are switched between "On" and "Off" in alternating scans and the FIDs are combined in such a way that only the signals from the VOI are added coherently while the signals from elsewhere cancel. By using slice selective refocusing, the number of scans required to achieve three-dimensional localization with ISIS can be reduced from 8 to 4, as is the case with frequency-interval-selective volume localization (FRIVOL) (83).

The ISIS method imposes no T2 weighting on the signals observed, and thus is especially suitable for the experiments involving metabolites with short T2, such as *in vivo* ^{31}P spectroscopy. Precise localization with ISIS requires perfect cancellation of the signals from regions outside the VOI. This may be difficult to achieve in practice for the following three reasons (84-87). First, spatial localization is not achieved in a single-shot and consequently any motion that occurs between the scans will degrade the precision of localization. Second, when a short repetition time (less than 5 times T1) is used, as is usually the case due to the restraint in the total acquisition time, a significant amount of contamination arising from

regions outside the VOI can occur. Optimizing the order of the ISIS scans (88) or incorporating outer-volume suppression into the basic ISIS sequence (89) can help alleviate this problem, but by no means provide a perfect solution. Finally, imperfections in the inversion and observation pulses also result in localization imprecision. Moreover, shimming on the VOI and optimization of the receiver gain are difficult with ISIS because of its multiple-shot nature.

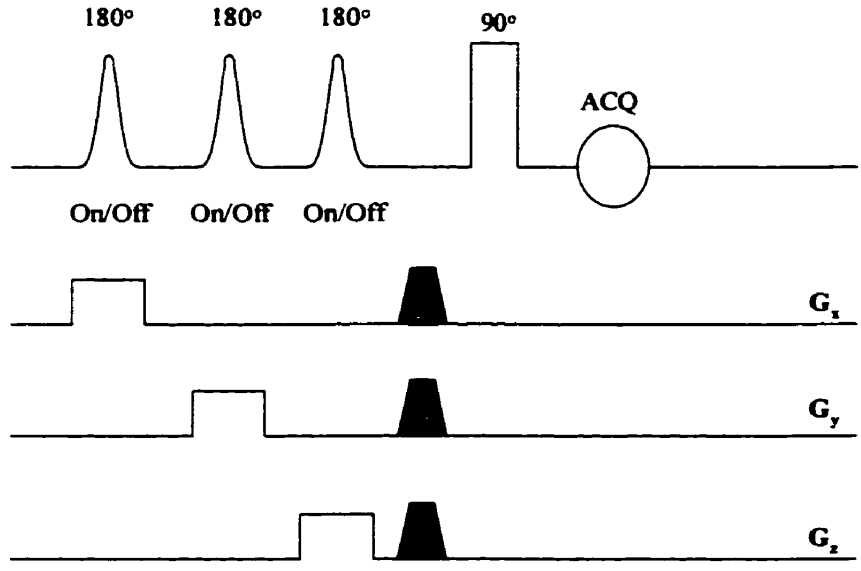

Figure 6.4 A pulse sequence for image selected *in vivo* spectroscopy (ISIS).

The last category of localization methods using slice selection is those which use direct excitation or refocusing of the spins inside the VOI. These methods acquire a localized spectrum in a single shot, and thus are less susceptible to motion artifacts than ISIS. Early methods in this category include volume selective refocusing (VSR) (90), volume selective spectral editing (VOSING) (91) and volume of interest by selective inversion, excitation and refocusing (VOISINER) (92-94). Currently, the most commonly used methods in this

category are point resolved spectroscopy (PRESS) (95,96) and stimulated echo acquisition mode (STEAM) (97,98) which is also known as volume excitation using stimulated echo (VEST) (99), volume-selective spectroscopy (VOSY) (100), and acquiring combined echoes (ACE) (101). Both STEAM and PRESS employ three slice-selective excitation or refocusing pulses to obtain an echo from the VOI and the protons outside the VOI are either never excited or dephased immediately after excitation by gradients. Figures 6.5 and 6.6 show the pulse sequences for PRESS and STEAM.

With the product operator formalism for a single spin-1/2, the intensity of the stimulated echo observed in a STEAM experiment is,

$$F(\mathbf{I}_-) = \frac{i}{2\sqrt{2}} \sin\theta_1 \sin\theta_2 \sin\theta_3 \mathbf{I}_- \qquad [6.24]$$

and the intensity of the Carr-Purcell echo observed in a PRESS experiment is,

$$F(\mathbf{I}_-) = -\frac{i}{4\sqrt{2}} \sin\theta_1 (1-\cos\theta_2)(1-\cos\theta_3) \mathbf{I}_- \qquad [6.25]$$

where θ_1, θ_2 and θ_3 are the flip angles of the first, the second and the third RF pulses respectively. When the flip angles of the pulses are adjusted to give the maximum signal intensity in each of experiments (i.e. $\theta_1=\theta_2=\theta_3=90^\circ$ for STEAM; $\theta_1=90^\circ$ and $\theta_2=\theta_3=180^\circ$ for PRESS), PRESS provides twice the signal as STEAM, although it has been shown recently that it is possible to reverse the half signal loss in STEAM by refocusing the stimulated echo and the stimulated anti-echo simultaneously (102). Both STEAM and PRESS acquire spectra with T2-weighting, and thus are not the methods of choice when metabolites with extremely short T2 are observed. The minimum echo time that can be obtained in STEAM is always shorter than that in PRESS because additional crusher gradients are needed in PRESS to

eliminate unwanted echoes generated from outside the VOI, reducing the signal loss through T2 relaxation in STEAM. Comprehensive comparison of these two methods is not the purpose of this thesis and in any case can be found in the literature (103).

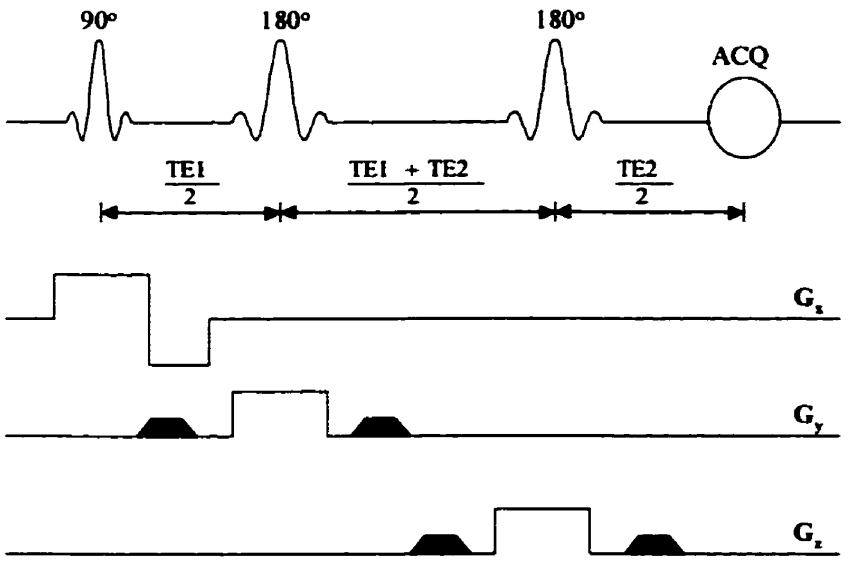

Figure 6.5 A pulse sequence for point resolved spectroscopy (PRESS).

There are two problems associated with spatial localization using slice selection with B_0 gradients. First, spatial localization achieved by slice selection depends on the chemical shift so that there is a spatial displacement for those resonances that are off-resonance relative to the carrier frequency. The amount (Δx) of this spatial displacement is given by

$$\Delta x = \frac{\Delta\omega}{\gamma G_x} \qquad [6.26]$$

where $\Delta\omega$ is the angular frequency offset and G_x is the gradient strength applied for slice selection. One way to reduce this chemical-shift-dependent spatial displacement is to increase the strength of the slice selection gradients. However, in order to accommodate the increase in gradient strength, the bandwidth as well as the RF power of the slice selection

pulse have to be increased accordingly for the selection of a volume with the same size, a process usually limited by system hardware specifications. Another practical solution to this problem is to use frequency offset-corrected pulses along with shaped gradients for slice selection, and the usefulness of this method in ISIS localization has been demonstrated (104). Other problems associated with spatial localization using slice selection, especially with the methods using direct excitation or refocusing, are the J coupling effects. J coupling not only causes a spatial displacement, as is produced by chemical shift dispersion, but also results in modulation of the observed signal intensity, depending on the timing of the pulse sequence used for localization. A vector description of the J coupling effects in volume-localized spectroscopy has been given by Yablonskiy et al (105) who also described several strategies to avoid such problems. Other solutions to the problems caused by J coupling in volume-localized spectroscopy include multi-echo volume selective spectroscopy (106) and J-refocused spectroscopy (107).

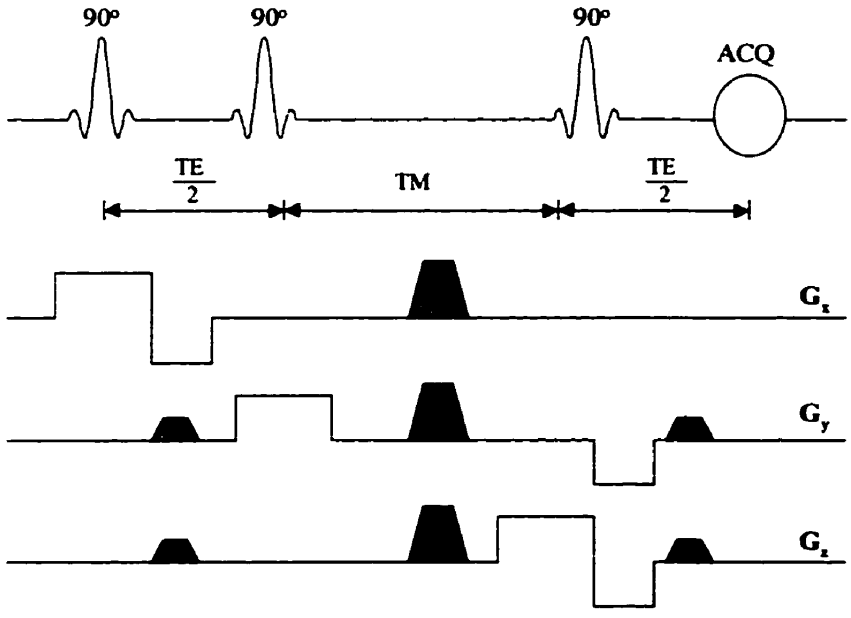

Figure 6.6 A pulse sequence for stimulated echo acquisition mode (STEAM).

A general disadvantage associated with all localization techniques using B_0 gradients is the production of eddy currents resulting from the rapidly switched B_0 gradients. The eddy currents adversely affect the quality of the spectra acquired, if not avoided. However, this problem is becoming less significant with the development of advanced technology such as actively shielded gradient sets.

References

1. I. D. Campbell and C. M. Dobson, The application of high resolution nuclear magnetic resonance to biological systems, *Methods Biochem. Anal.* **25**, 1, (1979).

2. D. L. Rothman, K. L. Behar, H. P. Hetherington and R. G. Shulman, Homonuclear ^{1}H double-resonance difference spectroscopy of the rat brain in vivo, *Proc. Natl. Acad. Sci. U. S. A.* **81**, 6330, (1984).

3. H. P. Hetherington, M. J. Avison and R. G. Shulman, ^{1}H homonuclear editing of rat brain using semi-selective pulses, *Proc. Natl. Acad. Sci. U. S. A.* **82**, 3115, (1985).

4. S. R. Williams, D. G. Gadian and E. Proctor, A method for lactate detection in vivo by spectral editing without the need for double irradiation, *J. Magn. Reson.* **66**, 562, (1986).

5. C. C. Hanstock, M. R. Bendall, H. P. Hetherington, D. P. Boisvert and P. S. Allen, Localized in vivo proton spectroscopy using depth-pulse spectral editing, *J. Magn. Reson.* **71**, 349, (1987).

6. T. Jue, Two for one: Simultaneously windowing the ^{13}C-^{1}H and ^{12}C-^{1}H signals using only ^{1}H pulses, *J. Magn. Reson.* **73**, 524, (1987).

7. M. Bunse, W.-I. Jung, F. Schick, G. J. Dietze and O. Lutz, HOPE, a new lactate editing method, *J. Magn. Reson. B* **109**, 270, (1995).

8. C. H. Sotak and D. M. Freeman, A method for volume-localized lactate editing using zero-quantum coherence created in a stimulated-echo pulse sequence, *J. Magn. Reson.* **77**, 382, (1988).

9. D. G. Schupp, H. Merkle, J. M. Ellermann, Y. Ke and M. Garwood, Localized detection of glioma glycolysis using edited ^{1}H MRS, *Magn. Reson. Med.* **30**, 18, (1993).

10. R. E. Hurd and D. M. Freeman, Metabolite specific proton magnetic resonance imaging, *Proc. Natl. Acad. Sci. U. S. A.* **86**, 4402, (1989).

11. C. H. Sotak, D. M. Freeman and R. E. Hurd, The unequivocal determination of in vivo lactic acid using two dimensional double-quantum coherence-transfer spectroscopy, *J. Magn. Reson.* **78**, 355, (1988).

12. J. E. van Dijk, A. F. Mehlkopf and W. M. Bovee, Comparison of double and zero quantum NMR editing techniques for in vivo use, *NMR Biomed.* **5**, 75, (1992).

13. P. S. Allen, R. B. Thompson and A. H. Wilman, Metabolite-specific NMR spectroscopy in vivo, *NMR Biomed.* **10**, 435, (1997).

14. C. J. Hardy and C. L. Dumoulin, Lipid and water suppression by selective ^{1}H homonuclear polarization transfer, *Magn. Reson. Med.* **5**, 58, (1987).

15. C. L. Dumoulin, Suppression of water and other noncoupled spins by homonuclear polarization transfer in magnetic resonance imaging, *Magn. Reson. Med.* **3**, 90, (1986).

16. A. Knuttel and R. Kimmich, Single-scan volume-selective spectral editing by homonuclear polarization transfer, *Magn. Reson. Med.* **9**, 254, (1989).

17. M. von Kienlin, J. P. Albrand, B. Authier, P. Blondet, S. Lotito and M. Decorps, Spectral editing in vivo by homonuclear polarization transfer, *J. Magn. Reson.* **75**, 371, (1987).

18. I. M. Brereton, G. J. Galloway, S. E. Rose and D. M. Doddrell, Metabolite editing via correlated 2-order with total inherent coherence, *J. Magn. Reson.* **83**, 190, (1989).

19. I. M. Brereton, S. E. Rose, G. J. Galloway, L. N. Moxon and D. M. Doddrell, In vivo volume-selective metabolite editing via correlated z-order, *Magn. Reson. Med.* **16**, 460, (1990).

20. R. Reddy, V. H. Subramanian, B. J. Clark and J. S. Leigh Jr., In-vivo lactate editing in the presence of inhomogeneous B1 fields, *J. Magn. Reson. B* **102**, 20, (1993).

21. R. Reddy, V. H. Subramanian, B. J. Clark and J. S. Leigh Jr., Longitudinal spin-order-based pulse sequence for lactate editing, *Magn. Reson. Med.* **19**, 477, (1991).

22. R. R. Ernst, G. Bodenhausen and A. Wokaun, Principles of Nuclear Magnetic Resonance in One or Two Dimensions, Oxford University Press, London, 1987.

23. O. W. Sorensen, G. W. Eich, M. H. Levitt, G. Bodenhausen and R. R. Ernst, Product operator formalism for the description of NMR pulse experiments, *Prog. NMR Spectrosc.* **16**, 163, (1983).

24. M. A. Howarth, L. Y. Lian, G. E. Hawkes and K. D. Sales, Formalisms for the description of multiple-pulse NMR experiments, *J. Magn. Reson.* **68**, 433, (1986).

25. L. R. Brown and J. Bremer, A unified product operator formalism. Application to uniform excitation in heteronuclear correlation 2D NMR, *J. Magn. Reson.* **68**, 217, (1986).

26. D. Graveron-Demilly, A. Diop, A. Briguet and B. Fenet, Product-operator algebra for strongly coupled spin systems, *J. Magn. Reson. A* **101**, 233, (1993).

27. T. T. Nakashima and R. E. D. McClung, Simulation of two-dimensional NMR spectra using product operators in the spherical basis, *J. Magn. Reson.* **70**, 187, (1986).

28. J. Shriver, Product operators and coherence transfer in multiple-pulse NMR experiments, *Concepts Magn. Reson.* **4**, 1, (1992).

29. L. E. Kay and R. E. D. McCLung, A product operator description of AB and ABX spin systems, *J. Magn. Reson.* **77**, 258, (1988).

30. G. Bodenhausen, H. Kogler and R. R. Ernst, Selection of coherence-transfer pathways in NMR pulse experiments, *J. Magn. Reson.* **58**, 370, (1984).

31. A. D. Bian, Coherence levels and coherence pathways in NMR. A simple way to design phase cycling procedures, *J. Magn. Reson.* **56**, 418, (1984).

32. P. B. Kingsley, Magnetic field gradients and coherence-pathway elimination, *J. Magn. Reson. B* **109**, 243, (1995).

33. A. Maudsley, A. Wokaun and R. R. Ernst, Coherence transfer echoes, *Chem. Phys. Lett.* **55**, 9, (1978).

34. G. Kontaxis, J. Stonehouse, E. D. Laue and J. Keeler, The sensitivity of experiments which use gradient pulses for coherence-pathway selection, *J. Magn. Reson. A* **111**, 70, (1994).

35. L. Mitschang, Signal selection in high-resolution NMR by pulsed field gradients, *J. Magn. Reson.* **137**, 1, (1999).

36. D. J. Thomas, L. Mitschang, B. Simon and H. Oschkinat, Signal selection in high-resolution NMR by pulsed field gradients, *J. Magn. Reson.* **137**, 10, (1999).

37. H. P. Hetherington and D. L. Rothman, Phase cycling of composite refocusing pulses to eliminate dispersive refocusing magnetization, *J. Magn. Reson.* **65**, 348, (1985).

38. M. Garwood, B. Nease, Y. Ke, R. A. de Graaf and H. Merkle, Simultaneous compensation for B_1 inhomogeneity and resonance offsets by a multiple-quantum NMR sequence using adiabatic pulses, *J. Magn. Reson. A* **112**, 272, (1995).

39. R. H. Mattson, O. A. Petroff, D. Rothman and K. Behar, Vigabatrin: effect on brain GABA levels measured by nuclear magnetic resonance spectroscopy, *Acta Neurol. Scand. Suppl.* **162**, 27, (1995).

40. O. A. Petroff, K. L. Behar, R. H. Mattson and D. L. Rothman, Human brain gamma-aminobutyric acid levels and seizure control following initiation of vigabatrin therapy, *J. Neurochem.* **67**, 2399, (1996).

41. O. A. Petroff, D. L. Rothman, K. L. Behar and R. H. Mattson, Initial observations on effect of vigabatrin on in vivo ^{1}H spectroscopic measurements of gamma-aminobutyric acid, glutamate, and glutamine in human brain, *Epilepsia* **36**, 457, (1995).

42. D. L. Rothman, O. A. Petroff, K. L. Behar and R. H. Mattson, Localized ^{1}H NMR measurements of gamma-aminobutyric acid in human brain in vivo, *Proc. Natl. Acad. Sci. U. S. A.* **90**, 5662, (1993).

43. W. Richter, S. H. Lee, W. S. Warren and Q. H. He, Imaging with intermolecular multiple-quantum coherences in solution nuclear-magnetic-resonance, *Science* **267**, 654, (1995).

44. R. Bowtell, R. M. Bowley and P. Glover, Multiple spin echoes in liquids in a high magnetic field, *J. Magn. Reson.* **88**, 643, (1990).

45. W. Nosel, L. A. Trimble, J. F. Shen and P. S. Allen, On the use of double-quantum coherence from an AX3 system (protons in lactate) for spectral editing, *Magn. Reson. Med.* **11**, 398, (1989).

46. L. A. Trimble, J. F. Shen, A. H. Wilman and P. S. Allen, Lactate editing by means of selective-pulse filtering of both zero- and double-quantum coherence signals, *J. Magn. Reson.* **86** , 191, (1990).

47. Q. He, D. C. Shungu, P. C. van Zijl, Z. M. Bhujwalla and J. D. Glickson, Single-scan in vivo lactate editing with complete lipid and water suppression by selective multiple-quantum-coherence transfer (Sel-MQC) with application to tumors, *J. Magn. Reson. B* **106**, 203, (1995).

48. A. H. Wilman and P. S. Allen, In vivo NMR detection strategies for gamma-aminobutyric acid, utilizing proton spectroscopy and coherence-pathway filtering with gradients, *J. Magn. Reson. B* **101**, 165, (1993).

49. J. R. Keltner, L. L. Wald, B. D. Frederick and P. F. Renshaw, In vivo detection of GABA in human brain using a localized double-quantum filter technique, *Magn. Reson. Med.* **37**, 366, (1997).

50. A. H. Wilman and P. S. Allen, Double-quantum filtering of citrate for in vivo observation, *J. Magn. Reson. B* **105**, 58, (1994).

51. J. R. Keltner, L. L. Wald, P. J. Ledden, Y. C. Chen, R. T. Matthews, E. H. Kuestermann, J. R. Baker, B. R. Rosen and B. G. Jenkins, A localized double-quantum filter for the in *vivo* detection of brain glucose, *Magn. Reson. Med.* **39**, 651, (1998).

52. A. H. Wilman and P. S. Allen, Observing N-acetyl aspartate via both its N-acetyl and its strongly coupled aspartate groups in in vivo proton magnetic resonance spectroscopy, *J. Magn. Reson. B* **113**, 203, (1996).

53. D. L. Hardy and T. J. Norwood, Spectral editing technique for the in vitro and in vivo detection of taurine, *J. Magn. Reson.* **133**, 70, (1998).

54. R. B. Thompson and P. S. Allen, A new multiple quantum filter design procedure for use on strongly coupled spin systems found in vivo: its application to glutamate, *Magn. Reson. Med.* **39**, 762, (1998).

55. D. I. Hoult, Rotating frame zeugmatography, *J. Magn. Reson.* **33**, 183, (1979).

56. S. J. Cox and P. Styles, Towards biochemical imaging, *J. Magn. Reson.* **40**, 209, (1980).

57. D. I. Hoult, C.-N. Chen and L. K. Hedges, Spatial localization by rotating frame techniques, *Ann. N. Y. Acad. Sci.* **508**, 366, (1987).

58. K. R. Metz and R. W. Briggs, Spatial localization of NMR spectra using Fourier series analysis, *J. Magn. Reson.* **64**, 172, (1985).

59. M. Garwood, T. Schleich, B. D. Ross, G. B. Matson and W. D. Winters, A modified rotating frame experiment based on a Fourier series window function. Application to in vivo spatially localized NMR spectroscopy, *J. Magn. Reson.* **65**, 239, (1985).

60. J. Pekar, J. S. Leigh Jr. and B. Chance, Harmonically analyzed sensitivity profile. A novel approach to depth pulses for surface coils, *J. Magn. Reson.* **64**, 115, (1985).

61. J. J. Ackerman, T. H. Grove, G. G. Wong, D. G. Gadian and G. K. Radda, Mapping of metabolites in whole animals by ^{31}P NMR using surface coils, *Nature* **283**, 167, (1980).

62. M. R. Bendall and R. E. Gordon, Depth and refocusing pulses designed for multipulse NMR with surface coil, *J. Magn. Reson.* **53**, 365, (1983).

63. P. A. Bottomley, T. B. Foster and R. D. Darrow, Depth-resolved surface-coil spectroscopy (DRESS) for in vivo ^{1}H, ^{31}P, and ^{13}C NMR, *J. Magn. Reson.* **59**, 338, (1984).

64. A. N. Garroway, P. K. Grannell and P. Mansfield, Image formation in NMR by a selective irradiative process, *J. Phys. C: Solid State Phys.* **7**, L457, (1974).

65. A. Kumar, D. Welti and R. R. Ernst, NMR Fourier zeugmatography, *J. Magn. Reson.* **18**, 69, (1975).

66. R. E. Gordon, P. E. Hanley, D. Shaw, D. G. Gadian, G. K. Radda, P. Styles, P. J. Bore and L. Chan, Localization of metabolites in animals using ^{31}P topical magnetic resonance, *Nature* **287**, 736, (1980).

67. W. Chen and J. J. Ackerman, Surface coil single-pulse localization in vivo via inhomogeneous surface spoiling magnetic gradient, *NMR Biomed.* **1**, 205, (1989).

68. T. R. Brown, B. M. Kincaid and K. Ugurbil, NMR chemical shift imaging in three dimensions, *Proc. Natl. Acad. Sci. U. S. A.* **79**, 3523, (1982).

69. A. A. Maudsley, S. K. Hilal, W. H. Perman and H. E. Simon, Spatially resolved high resolution spectroscopy by "four-dimensional" NMR, *J. Magn. Reson.* **51**, 147, (1983).

70. Y. J. Chen, S. Rachamadugu and E. J. Fernandez, Three dimensional outer volume suppression for short echo time *in vivo* ^{1}H spectroscopic imaging in rat brain, *Magn. Reson. Imaging* **15**, 839, (1997).

71. O. Gonen, J. Hu, R. Stoyanova, J. S. Leigh Jr., G. Goelman and T. R. Brown, Hybrid three dimensional (1D-Hadamard, 2D-chemical shift imaging) phosphorus localized spectroscopy of phantom and human brain, *Magn. Reson. Med.* **33**, 300, (1995).

72. O. Gonen, F. A. Mendoza and G. Goelman, 3D localized in vivo ^{1}H spectroscopy of human brain by using a hybrid of 1D-Hadamard with 2D-chemical shift imaging, *Magn. Reson. Med.* **37**, 644, (1997).

73. J. A. Kmiecik, C. D. Gregory, Z.-P. Liang, D. E. Hrad, P. C. Lauterbur and M. J. Dawson, Quantitative lactate-specific MR imaging and ^{1}H spectroscopy of skeletal muscle at macroscopic and microscopic resolutions using zero-quantum/double-quantum coherence filter and SLIM/GSLIM localization, *Magn. Reson. Med.* **37**, 840, (1997).

74. W. P. Aue, S. Muller, T. A. Cross and J. Seelig, Volume-selective excitation. A novel approach to topical NMR, *J. Magn. Reson.* **56**, 350, (1984).

75. W. P. Aue, S. Muller and J. Seelig, Localized ^{13}C NMR spectra with enhanced sensitivity obtained by volume-selective excitation, *J. Magn. Reson.* **61**, 392, (1985).

76. S. Muller, W. P. Aue and J. Seelig, NMR imaging and volume-selective spectroscopy with a single surface coil, *J. Magn. Reson.* **63**, 530, (1985).

77. P. R. Luyten, J. A. Denhollander, A. J. H. Marien and B. Sijtsma, Solvent-suppressed spatially resolved spectroscopy - An approach to high-resolution NMR on a whole-body MR system, *J. Magn. Reson.* **67**, 148, (1986).

78. A. Haase, Localization of unaffected spins in NMR imaging and spectroscopy (LOCUS Spectroscopy), *Magn. Reson. Med.* **3**, 963, (1986).

79. D. M. Doddrell, H. Baddeley, W. M. Brooks, J. M. Bulsing, J. Field and M. G. Irving, Spatial and chemical-shift-encoded excitation - SPACE, a new technique for volume-selected NMR spectroscopy, *J. Magn. Reson.* **68**, 367, (1986).

80. D. M. Doddrell, H. Baddeley, W. M. Brooks, J. M. Bulsing, J. Field, G. J. Galloway and M. Irving, Discrete isolation from gradient-governed elimination of resonances - DIGGER, a new technique for in vivo volume-selected NMR spectroscopy, *J. Magn. Reson.* **70**, 319, (1986).

81. R. J. Ordidge, A. Connelly and J. A. B. Lohman, Image-selected in vivo spectroscopy (ISIS). A new technique for spatially selective NMR spectroscopy, *J. Magn. Reson.* **66**, 283, (1986).

82. R. J. Ordidge, R. M. Bowley and G. McHale, A general approach to selection of multiple cubic volume elements using the ISIS technique, *Magn. Reson. Med.* **8**, 323, (1988).

83. A. Volk, B. Tiffon, J. Mispelter and J. M. Lhoste, High-Resolution localized spectroscopy at 4.7 Tesla by frequency-interval-selective volume localization (FRIVOL), *J. Magn. Reson.* **76**, 386, (1988).

84. S. F. Keevil, D. A. Porter and M. A. Smith, Experimental characterization of the ISIS technique for volume selected NMR spectroscopy, *NMR. Biomed.* **5**, 200, (1992).

85. P. R. Luyten, J. P. Groen, J. W. Vermeulen and J. A. den Hollander, Experimental approaches to image localized human ^{31}P NMR spectroscopy, *Magn. Reson. Med.* **11**, 1, (1989).

86. N. M. Yongbi, G. S. Payne, D. J. Collins and M. O. Leach, Quantification of signal selection efficiency, extra volume suppression and contamination for ISIS, STEAM and PRESS localized ^{1}H NMR spectroscopy using an EEC localization test object, *Phys. Med. Biol.* **40**, 1293, (1995).

87. G. B. Matson, D. J. Meyerhoff, T. J. Lawry, R. S. Lara, J. Duijn, R. F. Deicken and M. W. Weiner, Use of computer simulations for quantitation of ^{31}P ISIS MRS results, *NMR. Biomed.* **6**, 215, (1993).

88. C. Burger, R. Buchli, G. McKinnon, D. Meier and P. Boesiger, The impact of the ISIS experiment order on spatial contamination, *Magn. Reson. Med.* **26**, 218, (1992).

89. A. Connelly, C. Counell, J. A. B. Lohman, and R. J. Ordidge, Outer volume suppressed image related in vivo spectroscopy (ORIRIS), a high-sensitivity localization technique, *J. Magn. Reson.* **78**, 519, (1988);

90. G. C. Mckinnon and P. Bosiger, Localized double-quantum filter and correlation spectroscopy experiments, *Magn. Reson. Med.* **6**, 334, (1988).

91. A. Knuttel, E. Rommel, M. Clausen and R. Kimmich, Integrated volume-selective spectral editing ^{1}H NMR and post detection signal processing for the sensitive determination of lactate, *Magn. Reson. Med.* **8**, 70, (1988).

92. J. Briand and L. D. Hall, Spatially localized NMR with the VOISINER sequence, *J. Magn. Reson.* **94**, 234, (1991).

93. J. Briand and L. D. Hall, VOISINER, a new method for spatially resolved NMR spectroscopy, *J. Magn. Reson.* **80**, 559, (1988).

94. J. Briand and L. D. Hall, Volume-selective measurements of spin-lattice relaxation times using the VOISINER sequence, *J. Magn. Reson.* **82**, 180, (1989).

95. P. A. Bottomley, Selective volume method for performing localized NMR spectroscopy, *U. S. Patent* 4 480 228, (1984).

96. P. A. Bottomley, Spatial localization in NMR spectroscopy in vivo, *Ann. N. Y. Acad. Sci.* **508**, 333, (1987).

97. J. Frahm, H. Bruhn, W. Hanicke, K. D. Merboldt, K. Mursch and E. Markakis, Localized proton NMR spectroscopy of brain tumors using short-echo time STEAM sequences, *J. Comput. Assist. Tomogr.* **15**, 915, (1991).

98. J. Frahm, K. D. Merboldt and W. Hanicke, Localized proton spectroscopy using stimulated echoes, *J. Magn. Reson.* **72**, 502, (1987).

99. J. Granot, Selected volume excitation using stimulated echoes (VEST) - Applications to spatially localized spectroscopy and imaging, *J. Magn. Reson.* **70**, 488, (1986).

100. R. Kimmich and D. Hoepfel, Volume-selective multiple spin-echo spectroscopy, *J. Magn. Reson.* **72**, 379, (1987).

101. J. J. van-Vaals, A. H. Bergman, J. H. den-Boef, H. J. van-den-Boogert and P. H. van-Gerwen, ACE: a single-shot method for water-suppressed localization and editing of spectra, images, and spectroscopic images, *Magn. Reson. Med.* **19**, 136, (1991).

102. J. M. Zhu and I. C. P. Smith, Stimulated anti-echo selection in spatially localized NMR spectroscopy, *J. Magn. Reson.* **136**, 1, (1999).

103. C. T. Moonen, M. von-Kienlin, P. C. van-Zijl, J. Cohen, J. Gillen, P. Daly and G. Wolf, Comparison of single-shot localization methods (STEAM and PRESS) for in vivo proton NMR spectroscopy, *NMR Biomed.* **2**, 201, (1989).

104. R. J. Ordidge, M. Wylezinska, J. W. Hugg, E. Butterworth and F. Franconi, Frequency offset corrected inversion (FOCI) pulses for use in localized spectroscopy, *Magn. Reson. Med.* **36** , 562, (1996).

105. D. A. Yablonskiy, J. J. Neil, M. E. Raichle and J. J. Ackerman, Homonuclear J coupling effects in volume localized NMR spectroscopy: pitfalls and solutions, *Magn. Reson. Med.* **39**, 169, (1998).

106. J. Hennig, T. Thiel and O. Speck, Improved sensitivity to overlapping multiplet signals in in vivo proton spectroscopy using a multiecho volume selective (CPRESS) experiment, *Magn. Reson. Med.* **37**, 816, (1997).

107. H. K. Lee, A. Yaman and O. Nalcioglu, Homonuclear J-refocused spectral editing technique for quantification of glutamine and glutamate by 1H NMR spectroscopy, *Magn. Reson. Med.* **34**, 253, (1995).

Chapter 7. A Localized Double Quantum Filter for *In Vivo* Detection of Taurine

Introduction

Spectral editing with double quantum (DQ) coherence transfer has been successfully applied to the selective observation of a number of metabolites *in vivo*, including lactate (1-3), γ-aminobutyric acid (GABA) (4,5), citrate (6), glucose (7), N-acetylaspartate (NAA) (8), and glutamate (9). Taurine is an important metabolic product of sulfur amino acid catabolism (10-12), whose roles in the central nervous system may include neurotransmission (13), osmoregulation (14), buffering of acidosis (15,16), and neuroprotection during cerebral ischemia (17). Previously, noninvasive observation of taurine *in vivo* has been conducted using conventional one-dimensional (1D) magnetic resonance (MR) spectroscopy (18-20), two-dimensional (2D) J-correlated spectroscopy (COSY) (21-23) and a spectral editing method with J-modulated echo difference spectroscopy (24). Severe overlap of the taurine resonances and the resonances of other metabolites such as choline, *myo*-inositol and glucose hinders direct observation of taurine using conventional 1D MR spectroscopy (25,26). Assignment of taurine peaks solely on the basis of chemical shift is difficult and measurements made in this manner are susceptible to significant errors. 2D COSY spectroscopy can resolve overlapping resonances from different metabolites, and its use in selective detection of taurine has been demonstrated (21-23). One shortcoming of 2D COSY spectroscopy is that the acquisition time required can be very long, making it unacceptable for many *in vivo* applications. The J-modulated echo difference spectral editing method can

also be used to observe taurine selectively (24). However, such a method requires subtraction of sequentially acquired spectra and thus is susceptible to motion artifacts.

In view of all these difficulties, a non-localized double quantum filtering (DQF) sequence for taurine editing has been described recently and its performance has been demonstrated in rat brain extracts and homogenates (27), but not *in vivo*. In this chapter, an alternative DQF sequence incorporating spatial localization for taurine editing is described, and its performance is demonstrated in phantoms and in rat brain *in vivo*. The results show that the sequence proposed not only provides excellent three dimensional spatial localization but also has a 42% higher detection sensitivity than the previous DQF sequence for taurine editing while still eliminating most of the overlapping resonances substantially.

Taurine

Taurine contains two methylene groups which give rise to two multiplets in the proton MR spectrum at 3.27 ($N\text{-}CH_2$) ppm and 3.43 ppm ($S\text{-}CH_2$) (25). The scalar coupling constant (J) between the two methylene groups is 6.7 Hz (25). Unless the magnetic field strength exceeds 9.4 T, the chemical shift difference $\Delta\upsilon$ (in Hz) between the two taurine methylene groups (i.e. 64 Hz at 9.4 T) is of the same order of magnitude (i.e. $0.1<J/\Delta\upsilon<1.0$) as the scalar coupling constant. Therefore, taurine should normally be treated as a strongly coupled spin system (i.e. A_2B_2), not a weakly coupled spin system (i.e. A_2X_2).

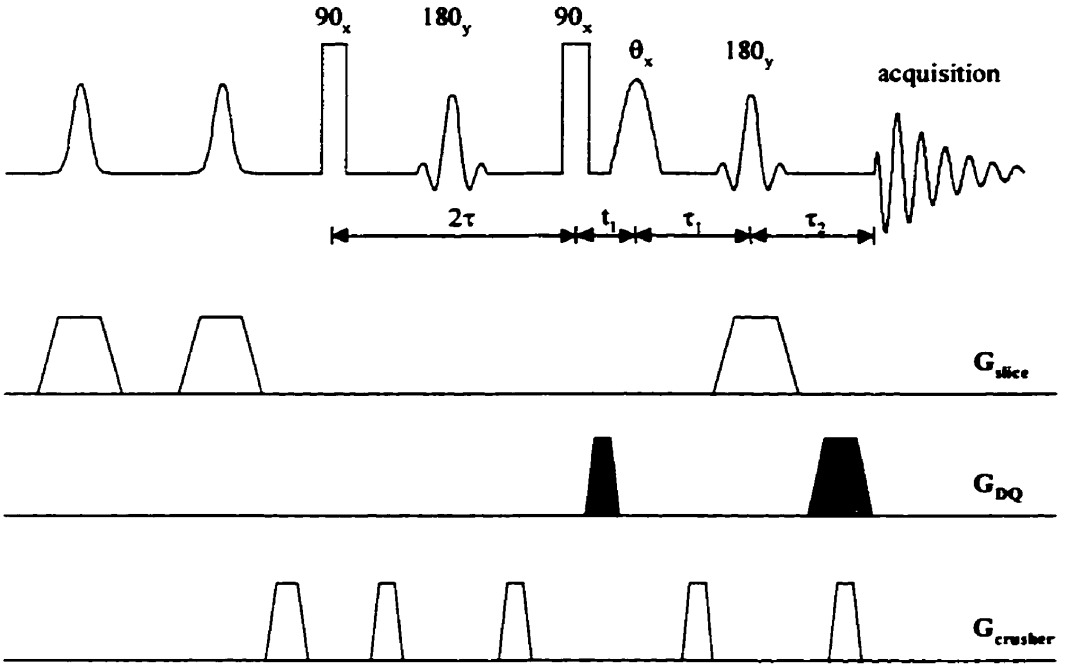

Figure 7.1 Double quantum filtering pulse sequence for taurine editing, incorporating three dimensional spatial localization. The first two hyperbolic secant pulses are for spatial localization and the remaining five pulses form the double quantum filter. For taurine editing, 2τ=37.5 ms, t_1=7.5 ms, τ_1= 11.25 ms, τ_2= 26.25 ms.

Pulse Sequence

The localized DQF sequence for taurine editing is shown in Fig. 7.1. The last five pulses comprise the conventional DQ filter (28). In this sequence, spatial localization in the slice direction is achieved by making the second 180° refocusing pulse of the DQ filter slice-selective. The two slice-selective hyperbolic secant pulses (29) at the beginning of the sequence provide 2D in-plane spatial localization in a manner that resembles the image-selected *in vivo* spectroscopy (ISIS) localization strategy (30). The frequency selectivity and the flip angle of the DQ read pulse as well as the duration of the DQ coherence creation

period (2τ) are chosen to optimize the sensitivity for taurine detection and the efficiency for eliminating overlapping resonances. The detection periods τ_1 and τ_2 are set to τ-t_1 and τ+t_1 respectively in order to simultaneously refocus the taurine coherence transfer echo and the B_0 inhomogeneity experienced by the taurine DQ coherence during the t_1 period (28). All crusher gradients and coherence transfer pathway selection gradients are adjusted to a near magic-angle setting to maximize the efficiency of water suppression (31), and to avoid the formation of gradient echoes. The flip angles of all the pulses are calibrated using a method proposed by Perman et al (32).

Optimization of Double Quantum Filter for Taurine Detection

To optimize the DQ filter for taurine detection, the first step is to choose an optimal 2τ value because it affects both the detection sensitivity (i.e. via inherent yield and signal loss through transverse relaxation) and the lineshape of the DQ filtered signals (9). For weakly coupled spin systems and simple strongly coupled spin systems such as AB and ABX, the optimal 2τ value can be calculated theoretically with product operator formalisms (6,8,33,34). In the case of taurine, however, theoretical calculation of the exact 2τ dependence to a DQF sequence is difficult because the product operator formalism for an A_2B_2 spin system is yet to be developed. Treating taurine as a weakly coupled (A_2X_2) spin system tends to oversimplify the real picture and results in a large deviation between the theoretical response and the experimental response to the DQF sequence (27).

Although exact calculation is difficult, the 2τ dependence of taurine, as a strongly coupled A_2B_2 spin system, to the DQF sequence can be calculated approximately as follows. For a DQF sequence with $\tau_1+\tau_2 = 2\tau$, the 2τ dependence of the fractional signal intensity passing through the DQ filter for an AB spin system is (6,35)

$$f(2\tau)=\frac{1}{2}\left\{\left[\left(\frac{\Delta\omega}{\Lambda}\right)^2+\left(\frac{\pi J}{\Lambda}\right)^2\cos(2\Lambda\tau)\right]\sin(2\pi J\tau)-\left(\frac{\pi J}{\Lambda}\right)\sin(2\Lambda\tau)\cos(2\pi J\tau)\right\}^2\exp(-\frac{4\tau}{T2}) \qquad [7.1]$$

where $\Delta\omega=(\omega_A-\omega_B)/2$ is the one-half the chemical shift difference (in $rad\cdot s^{-1}$) between A and B and $\Lambda = [\Delta\omega^2+(\pi J)^2]^{1/2}$ is the strong coupling frequency. For a weakly coupled A_2X_2 spin system, $f(2\tau)$ is identical to that for an AX system except that the period of the sin/cos modulation for the A_2X_2 system is twice that for an AX spin system (36). Assuming this also applies to strongly coupled spins systems, $f(2\tau)$ for the A_2B_2 spin system (i.e. taurine) can then be written

$$f(2\tau)=\frac{1}{2}\left\{\left[\left(\frac{\Delta\omega}{\Lambda}\right)^2+\left(\frac{\pi J}{\Lambda}\right)^2\cos(4\Lambda\tau)\right]\sin(4\pi J\tau)-\left(\frac{\pi J}{\Lambda}\right)\sin(4\Lambda\tau)\cos(4\pi J\tau)\right\}^2\exp(-\frac{4\tau}{T2}) \qquad [7.2]$$

where T2 is the transverse relaxation time for taurine. It is worthwhile to point out that Eq. [7.2] is only an approximation because Eq. [7.1] is not a regular periodic function as is that for weakly coupled spin system. A numerical simulation of Eq. [7.2] for taurine at 7 T is shown in Fig. 7.2A with an assumed T2 value of 178 ms.

The duration of the evolution period (t_1) also influences the detection sensitivity (via so-called J-modulation) and the signal lineshape (9,28). In order to minimize the effects of J-modulation, t_1, in theory, should be kept as short as possible, but has a minimum value in

practice, depending on the length of the DQ excitation and read pulses and the duration of the DQ coherence selection gradient pulse (Fig. 7.1).

The flip angle of the DQ coherence observation pulse also affects the detection sensitivity (6,9,37). When a non-frequency-selective read pulse and a DQ coherence selection gradient pair of the same polarity are used, the fractional signal intensity passing through the DQ filter as a function of θ for an AX (37) or an AB (6) system is

$$f(\theta) = \sin(\theta)\cos^2(\frac{\theta}{2}) \ . \qquad [7.3]$$

As the two methylene groups of taurine have similar chemical shift, in practice it is difficult to use a frequency selective DQ read pulse to excite only one methylene group. A read pulse that converts the DQ coherence originating from both methylene groups into single quantum coherence can therefore be considered to be a "non-frequency-selective" read pulse. With the pulse sequence shown in Fig. 7.1, it is therefore expected that $f(\theta)$ for taurine also follows Eq. [7.3] and has a maximal value when $\theta=60^\circ$.

The dependence of the detection sensitivity for taurine on 2τ and on θ was determined experimentally. A 2.5 cm diameter vial phantom containing 20 mM taurine in saline was used for this purpose. Measurements were done using the sequence in Fig. 7.1, but without spatial localization. 1024 data points were acquired with a spectral bandwidth of 4000 Hz, repetition time (TR) 2.0 sec, and 32 averages. Hard 180° pulses were used as the refocusing pulses and a 12 ms single lobe sinc pulse with a bandwidth of 90 Hz was used as the DQ coherence read pulse. A practical minimum of 7.5 ms was used for t_1. With $\theta=90^\circ$, the

intensity of the DQ filtered taurine signals was measured as 2τ was varied in fifty steps from 30 to 210 ms. With the optimum value of 2τ (37.5 ms) determined from these experiments, the DQ filtered taurine peak intensity was measured as θ was taken through 22 steps from 5 to 150 degrees. All subsequent taurine-edited spectra were acquired using the resulting optimized values of 2τ and θ (60°).

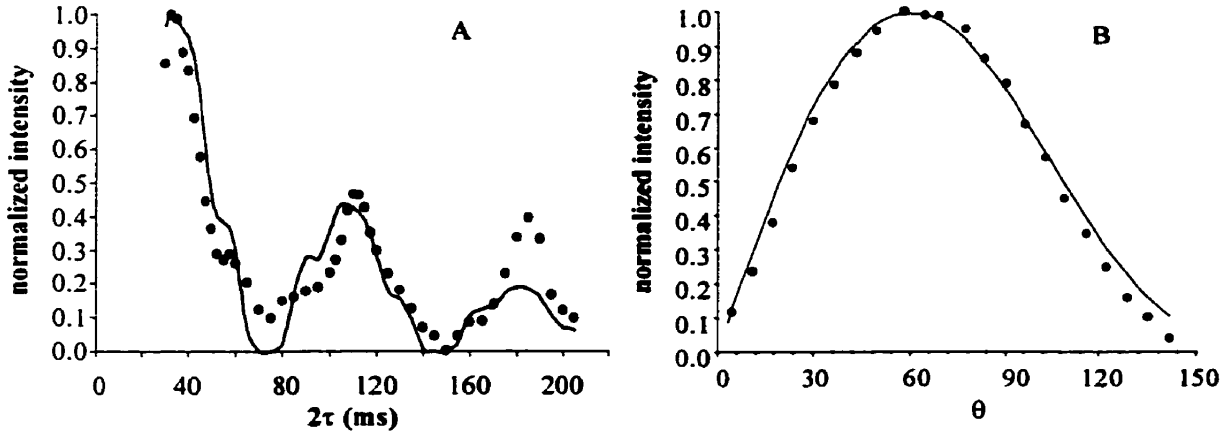

Figure 7.2 The dependence of the intensity of the taurine signal passing through the DQ filter on the DQ creation time 2τ (A) and on the flip angle (θ) of the DQ read pulse (B). Signal intensity was normalized to the maximum in each curve. In both A and B, the filled circles represent experimental data, while the solid lines were simulated using Eq. [7.2] with T_2=178 msec (A) and Eq. [7.3] (B).

Figure 7.2 shows the normalized intensity of the taurine signal passing through the DQ filter as a function of 2τ (Fig. 7.2A) and θ (Fig. 7.2B). In both A and B, the filled circles represent experimental data, while the solid lines were simulated using Eq. [7.2] (A) and Eq. [7.3] (B). Over the observable range, the experimental intensity of the taurine signal is maximum at 2τ=37.5 ms (Fig. 7.2A), with two additional local maxima at 2τ =112.5 and 185.0 ms and two local minima at 2τ =75.0 and 150.0 ms. The product operator simulation reproduces the experimental features for 2τ<180 ms; in particular, the position of the calculated intensity

maximum, lower local maxima, and local minima agree with experiment (i.e. at $2\tau = (2k+1)/4J$ and $2\tau = \pi k/\Lambda$, where k=0, 1, 2, 3 ···). The experimental intensity of the taurine signal is maximum when $\theta = 60^\circ$ (Fig. 7.2B), higher by a factor of 1.30 than the intensity for $\theta = 90^\circ$; this is reproduced by the simulation. When a hard pulse is used as the read pulse, the maximum taurine signal intensity has been reported to occur when the flip angle is 90° (27). The cause for this difference is unclear.

Spatial Localization and Elimination of Overlapping Resonances

Although it is important to optimize the detection sensitivity of the DQF sequence for taurine, it is also essential for the optimized DQF sequence to be efficient in filtering out major overlapping resonances from other metabolites, particularly those from choline, GABA, *myo*-inositol and glucose. Phantom experiments were designed to test whether effective filtering can be accomplished by the sequence proposed and to verify the precision of spatial localization with this sequence.

Three two-compartment phantoms were used for these experiments. Each consisted of a 2.5 cm diameter vial filled with 20 mM taurine in saline and a 1.2 cm diameter vial inserted concentrically into the larger vial. The inner vial of phantoms I and II contained choline, GABA and *myo*-inositol, 20 mM each, and 2 mM lactate, in saline. The inner vial of phantom II also contained 20 mM taurine. The inner vial of phantom III contained 20 mM glucose in saline.

For experiments involving spatial localization, scout images were obtained using a snapshot fast low angle shot (FLASH) imaging sequence. Volume-localized non-edited ^{1}H MR spectra were acquired using a stimulated echo acquisition mode (STEAM) sequence (38) with a voxel size of 5×5×5 mm^3. Each STEAM spectrum was obtained with 128 transients acquired into 2048 data points with a spectral bandwidth of 2500 Hz, TR=2.0 s, TE=20 ms and mixing time (TM) 30 ms. Volume-localized taurine-edited proton MR spectra were acquired using the pulse sequence shown in Fig. 7.1 with a spectral bandwidth of 4000 Hz and TR 2.0 s. Thirty-two averages were accumulated into 1024 data points for each of the four ISIS-like steps, resulting in a total of 128 acquisitions. Hyperbolic secant pulses (5 ms) with a bandwidth of 2200 Hz were used as the inversion pulses for spatial localization, and 1 ms sinc-gaussian pulses (half-width at half-maximum) were used as the refocusing pulses. The read pulse, gradients, t_1, τ_1, and τ_2 were adjusted as described above. For both the STEAM and the taurine edited spectra, post-acquisition processing included zero-filling the free induction decays (FIDs) to 4096 data points and applying 5 Hz exponential line-broadening prior to Fourier transformation.

Figure 7.3 shows localized non-edited (A and C) and taurine-edited (B and D) spectra acquired from identical voxels in the inner vials of phantoms I (A and B) and II (C and D). No taurine resonances at 3.43 and 3.27 ppm are apparent in A or B, indicating that effective localization is achieved. With taurine editing, the intense choline methyl singlet (3.20 ppm) is effectively suppressed in B and D, as are the *myo*-inositol peaks between 3.20 and 3.50 ppm (B). However, the GABA triplet at 3.00 ppm, the *myo*-inositol multiplets between 3.50 and 3.70 ppm, and the *myo*-inositol [H2] and choline methylene peaks at 4.06 ppm remain in the

spectrum, all with modulated phase. Spectrum D shows taurine signals at 3.43 and 3.27 ppm in addition to the background signals observed in C.

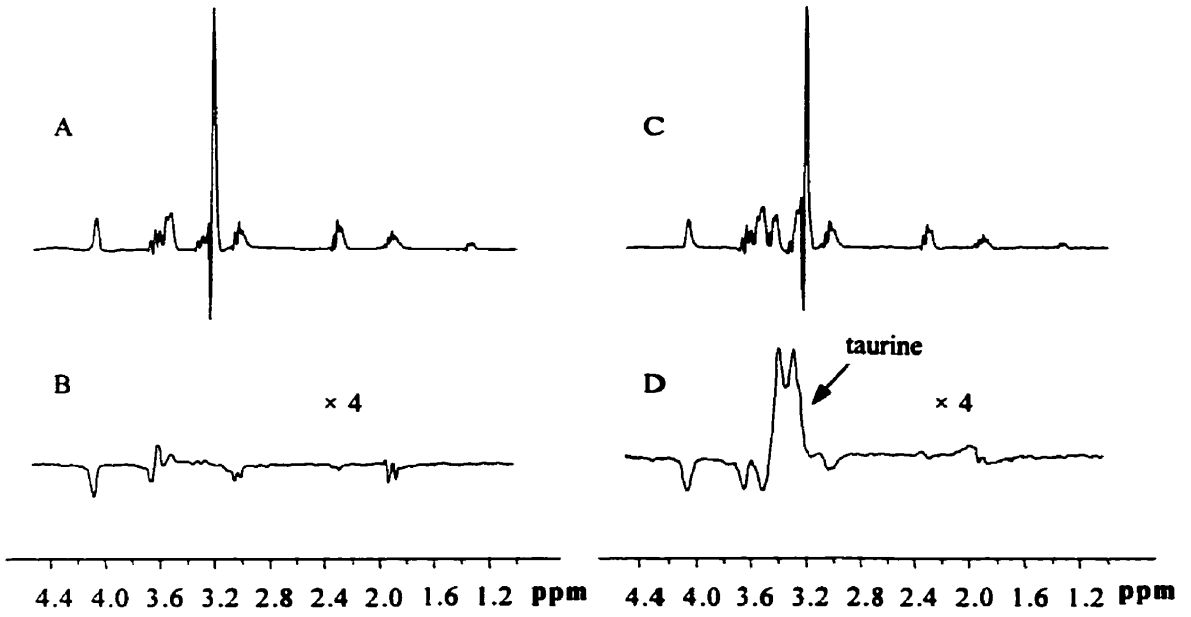

Figure 7.3 STEAM spectra without editing (A and C) and taurine-edited spectra (B and D) acquired from the same voxels located in the inner vial of the phantom I (A and B) and II (C and D).

Non-edited and taurine-edited spectra acquired from the same voxel located in the inner vial of phantom III are shown in Fig. 7.4A and 7.4B, respectively. Fig. 7.4C shows a taurine-edited spectrum acquired from a voxel with the same size located in the outer vial of the same phantom. Comparing the integrated intensity between 3.10 ppm and 3.50 ppm in B and C, the relative detection sensitivity of the DQF sequence for glucose and taurine is about 1:8.

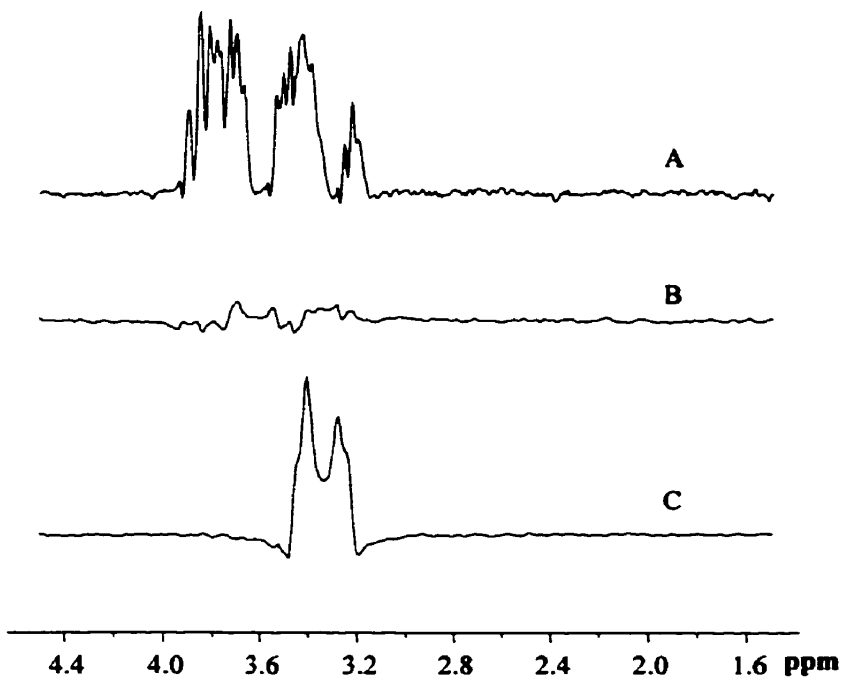

Figure 7.4 A STEAM spectrum acquired without taurine editing from a voxel located in the inner vial of phantom III (A) and a taurine edited spectrum acquired from the same voxel (B), showing residual glucose signals passing through the taurine editing DQ filter. A taurine edited spectrum from a voxel of the same size located in the outer vial of the phantom is shown for comparison (C).

Several mechanisms contribute to the efficient filtering. First, because of the nature of DQ filtering, all singlets in the spectrum including those from choline at about 3.20 ppm will be suppressed completely. Second, the DQ coherence read pulse is made frequency-selective and excites only a narrow frequency window (90 Hz) around the taurine resonances so that the signals from coupled systems whose resonances do not all fall into that window will be completely suppressed (such as lactate, and the choline methylene resonances at 3.54 ppm) or attenuated (*myo*-inositol, GABA and glucose). Third, by using 2τ optimized for taurine, signals from metabolites falling into this window but having coupling constants different from that in taurine will be attenuated. Thus the signal from [H5] of *myo*-inositol at 3.28 ppm, which is coupled by 9.0 Hz to [H4,6] at 3.62 ppm (25,39), is suppressed almost

completely. Substantial attenuation of glucose signals is also achieved through this mechanism since most of its J-coupling constants differ from those of taurine (7). Although most of the resonances that overlap with the taurine signals are suppressed through these three mechanisms, some remain in the edited spectra, albeit with substantially reduced intensity. These include *myo*-inositol resonances at 3.59 ppm and 4.06 ppm, choline methylene resonances at 4.06 ppm, GABA resonances at 3.00 ppm and glucose resonances between 3.20 and 3.80 ppm. Except for the glucose resonances, these all differ in chemical shift from the taurine resonances. Unless the shimming is very poor, they will not interfere with the observation of taurine and can be eliminated through a baseline simplification procedure using time domain fitting (4). Some of the glucose resonances which pass through the DQ filter have the same chemical shift as the taurine resonances and can obscure taurine observation. However, the relative detection sensitivity of the DQF sequence for glucose is only one-eighth of that for taurine. Furthermore, in tissues such as brain, the taurine concentration is higher than that of glucose under normal physiological conditions (e.g. 5.5 μmol/g (14,40-42) vs. about 2.4 μmol/g (43) for rat brain). Under these conditions the contribution of glucose to the *in vivo* MR spectrum of rat brain is probably only about 5%.

The first 90° pulse and the two 180° refocusing pulses in a DQF sequence can be made slice-selective to achieve single-shot three dimensional (3D) localization in a manner that is similar to point resolved spectroscopy (PRESS) (1,4,9). However, the problem of phase accumulation induced by slice-selective excitation/refocusing often creates difficulties in implementation (1). A phase correction procedure (4) and the use of self-refocusing pulses (9) have been proposed to solve this problem, but the robustness of these methods has not

been demonstrated. The DQF sequence has also been combined with ISIS to achieve single voxel spatial localization (44). In the DQF sequence described here, slice-selective refocusing combined with the ISIS strategy is used to achieve effective 3D localization. Making the second 180° refocusing pulse of the DQ filter slice selective does not introduce a frequency offset-dependent (i.e. position dependent) modulation of the edited signal intensity, so that no phase adjustment for the RF pulses is needed (1). By using two slice selective inversion pulses, in-plane localization is achieved in a manner that resembles ISIS. This localization strategy has advantages over conventional 3D ISIS. First, the use of two slice selective inversion pulses instead of three reduces T1 relaxation effects, thus improving sensitivity. Second, only four ISIS steps are required instead of eight to achieve 3D localization, thus reducing sensitivity to motion. Moreover, by switching the single band inversion pulses to multiple band inversion pulses and using Hadamard encoding (45), taurine editing with multiple-voxel in-plane localization can be obtained.

Comparison with a Previous DQF Sequence for Taurine Editing

Figure 7.5 compares taurine edited spectra acquired using the sequence in Fig. 7.1 (A) with taurine edited spectra obtained using a previous DQF sequence (27) incorporating Gaussian pulses for excitation and DQ coherence creation and a hard 90° pulse for the DQ read pulse (B). The two spectra were acquired from the same voxel located in the inner vial of phantom II. Common acquisition parameters were kept the same, and other parameters for each pulse sequence were carefully adjusted to give the maximum taurine signal intensities. The

spectrum in B shows less contamination with resonances of GABA, choline, and *myo*-inositol, but at the cost of a reduction in signal intensity of about 42%.

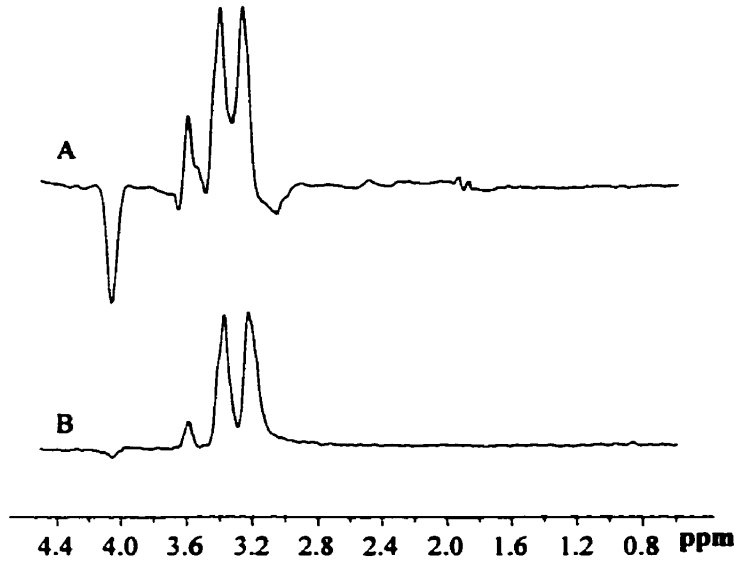

Figure 7.5 Taurine edited spectra acquired from a voxel located in the inner vial of the phantom II. Spectrum A was acquired using the DQF sequence depicted in Fig. 7.1, while spectrum B was acquired using a DQF sequence which uses Gaussian pulses for excitation and DQ coherence creation and a hard DQ coherence read pulse (27)). The intensities of the taurine peaks in A are 1.42-fold higher than those in B.

The sequence shown in Fig. 7.1 provides improved sensitivity over a previous DQF sequence for taurine editing (27). This can be important for *in vivo* applications. Long shaped pulses interact with J-coupled spin systems in a way that is quite different from short hard pulses (46). Non-negligible unwanted coherences can be generated if soft pulses are used in a DQF sequence, reducing the efficiency of coherence transfer and resulting in significant signal loss, depending on the pulse time, coupling constants and chemical shifts (46,47). Thus the use of more hard pulses as in the DQF sequence described here may produce more efficient coherence transfer and improved sensitivity. Furthermore, because a shorter shaped pulse is

used, t_1 can be reduced, providing additional sensitivity through minimizing J-modulation effects during the t_1 period (28).

Localized Double Quantum Taurine Editing In Vivo

Localized taurine editing *in vivo* was performed in normal rat brain. Three male Sprague-Dawley rats weighting 275-325g were used. Each rat was anesthetized with 1.0-1.5% halothane in 30/70 O_2/N_2O administered via a nose cone. Rectal temperature was controlled between 36.5 and 37.5 °C using a thermostated water blanket. For each rat, a volume-localized STEAM spectrum was obtained from an 8×8×5 mm^3 voxel centered in the brain, with 128 transients acquired into 2048 data points, a spectral bandwidth of 2500 Hz, TR=2.0 s, TE=20 ms and TM=30 ms. Localized taurine-edited spectra were acquired from the same voxel using the parameters described above for the phantom experiments. FIDs were zero-filled to 4096 data points and line-broadened by 15 Hz prior to Fourier transformation.

Non-edited (A) and taurine-edited (B) spectra acquired from the same voxel of a rat brain *in vivo* are shown in Fig. 7.6, together with a taurine-edited spectrum acquired from another rat (C). The localized taurine-edited spectra are reproducible, and display features similar to those in spectra from phantoms.

The DQ filter described in this chapter is optimized for the selective observation of taurine at high field strength (7 T). Whether this sequence is applicable to human studies at lower field strength requires further investigation. The response of taurine to the DQ filter is field

strength-dependent, as are the responses of *myo*-inositol and glucose. Therefore, at lower field strength, the experimental parameters for optimized taurine editing could be different from those described here. Longer T2 for the metabolites at lower field strength and the larger voxel size that can be used on human subjects will effectively increase the detection sensitivity.

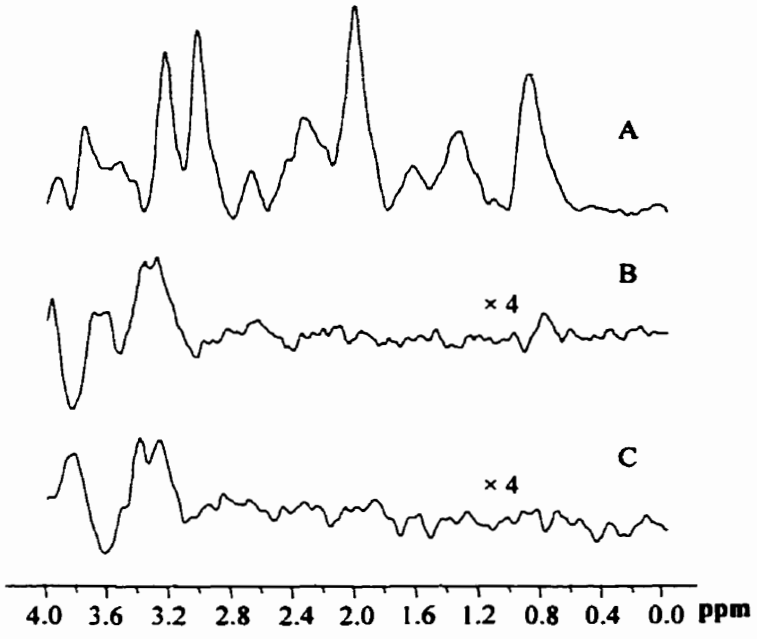

Figure 7.6 A STEAM spectrum obtained without spectral editing (A) from a rat brain *in vivo* and a taurine edited spectrum (B) acquired from the same voxel. Spectrum C shows a taurine-edited spectrum acquired from an identical voxel in the brain of another rat. The intensity scale in B and C is 4 times that in A.

Conclusion

In summary, a localized spectral editing sequence based on double quantum filtering has been developed for *in vivo* detection of taurine. The sequence recovers taurine signals with optimized sensitivity while eliminating overlapping resonances substantially, and provides

excellent three dimensional spatial localization. The performance of the sequence was demonstrated both in phantoms and in rat brain *in vivo*.

References

1. L. Jouvensal, P. G. Carlier and G. Bloch, Practical implementation of single-voxel double-quantum editing on a whole-body NMR spectrometer: localized monitoring of lactate in the human leg during and after exercise, *Magn. Reson. Med.* **36**, 487, (1996).

2. Q. He, Z. M. Bhujwalla and J. D. Glickson, Proton detection of choline and lactate in EMT6 tumors by spin-echo-enhanced selective multiple-quantum-coherence transfer, *J. Magn. Reson. B* **112**, 18, (1996).

3. Q. He, D. C. Shungu, P. C. van Zijl, Z. M. Bhujwalla and J. D. Glickson, Single-scan in vivo lactate editing with complete lipid and water suppression by selective multiple-quantum-coherence transfer (Sel-MQC) with application to tumors, *J. Magn. Reson. B* **106**, 203, (1995).

4. J. R. Keltner, L. L. Wald, B. D. Frederick and P. F. Renshaw, In vivo detection of GABA in human brain using a localized double-quantum filter technique, *Magn. Reson. Med.* **37**, 366, (1997).

5. J. Shen, D. C. Shungu and D. L. Rothman, In vivo chemical shift imaging of γ-aminobutyric acid in the human brain, *Magn. Reson. Med.* **41**, 35, (1999).

6. A. H. Wilman and P. S. Allen, Double-quantum filtering of citrate for in vivo observation, *J. Magn. Reson. B* **105**, 58, (1994).

7. J. R. Keltner, L. L. Wald, P. J. Ledden, Y. C. Chen, R. T. Matthews, E. H. Kuestermann, J. R. Baker, B. R. Rosen and B. G. Jenkins, A localized double-quantum filter for the in vivo detection of brain glucose, *Magn. Reson. Med.* **39**, 651, (1998).

8. A. H. Wilman and P. S. Allen, Observing N-acetyl aspartate via both its N-acetyl and its strongly coupled aspartate groups in in vivo proton magnetic resonance spectroscopy, *J. Magn. Reson. B* **113**, 203, (1996).

9. R. B. Thompson and P. S. Allen, A new multiple quantum filter design procedure for use on strongly coupled spin systems found in vivo: its application to glutamate, *Magn. Reson. Med.* **39**, 762, (1998).

10. R. J. Huxtable, J. Azuma, K. Kuriyama, M. Nakagawa, and A. Baba, Eds., Taurine 2: Basic and clinical aspects. Adv. Exp. Med. Biol. **403**, (1995);

11. R. J. Huxtable and D. Michalk, Eds., Taurine in health and disease. Adv. Exp. Med. Biol. **359**, (1993);

12. J. B. Lombardini, S. W. Schaffer, and J. Azuma, Eds., Taurine: Nutritional value and mechanisms of action. Adv. Exp. Med. Biol. **315**, (1991);

13. R. J. Huxtable, Taurine in the central nervous system and the mammalian actions of taurine, *Prog. Neurobiol.* **32**, 471, (1989).

14. M. Puka, K. Sundell, J. W. Lazarewicz and A. Lehmann, Species differences in cerebral taurine concentrations correlate with brain water content, *Brain Res.* **548**, 267, (1991).

15. T. Nakada, K. Hida and I. L. Kwee, Brain pH and lactic acidosis: quantitative analysis of taurine effect, *Neurosci. Res.* **15**, 115, (1992).

16. T. Nakada, K. Hida and I. L. Kwee, pH-lactate dissociation during anoxic insult: taurine effect, *Neuroreport* **2**, 325, (1991).

17. P. Saransaari and S. S. Oja, Mechanisms of ischemia-induced taurine release in mouse hippocampal slices, *Brain Res.* **807**, 118, (1998).

18. T. Michaelis, K. D. Merboldt, W. Hanicke, M. L. Gyngell, H. Bruhn and J. Frahm, On the identification of cerebral metabolites in localized ^{1}H NMR spectra of human brain in vivo, *NMR Biomed.* **4**, 90, (1991).

19. T. E. Bates, S. R. Williams, D. G. Gadian, J. D. Bell, R. K. Small and R. A. Iles, ^{1}H NMR study of cerebral development in the rat, *NMR Biomed.* **2**, 225, (1989).

20. K. Hida, I. L. Kwee and T. Nakada, In vivo ^{1}H and ^{31}P NMR spectroscopy of the developing rat brain, *Magn. Reson. Med.* **23**, 31, (1992).

21. S. Brulatout, P. Meric, I. Loubinoux, J. Borredon, J. L. Correze, P. Roucher, B. Gillet, G. Berenger, J. C. Beloeil, B. Tiffon, J. Mispelter and J. Seylaz, A one-dimensional (proton and phosphorus) and two-dimensional (proton) in vivo NMR spectroscopic study of reversible global cerebral ischemia, *J. Neurochem.* **66**, 2491, (1996).

22. B. Barrere, M. Peres, B. Gillet, S. Mergui, J. C. Beloeil and J. Seylaz, 2D COSY ^{1}H NMR: a new tool for studying in situ brain metabolism in the living animal, *FEBS Lett.* **264**, 198, (1990).

23. C. Remy, C. Arus, A. Ziegler, E. S. Lai, A. Moreno, Y. Le Fur and M. Decorps, In vivo, ex vivo, and in vitro one- and two-dimensional nuclear magnetic resonance spectroscopy of an intracerebral glioma in rat brain: assignment of resonances, *J. Neurochem.* **62**, 166, (1994).

24. D. L. Rothman, K. L. Behar, H. P. Hetherington and R. G. Shulman, Homonuclear ^{1}H double-resonance difference spectroscopy of the rat brain in vivo, *Proc. Natl. Acad. Sci. U. S. A.* **81**, 6330, (1984).

25. K. L. Behar and T. Ogino, Assignment of resonance in the ^{1}H spectrum of rat brain by two-dimensional shift correlated and J-resolved NMR spectroscopy, *Magn. Reson. Med.* **17**, 285, (1991).

26. J. Frahm, H. Bruhn, W. Hanicke, K. D. Merboldt, K. Mursch and E. Markakis, Localized proton NMR spectroscopy of brain tumors using short-echo time STEAM sequences, *J. Comput. Assist. Tomogr.* **15**, 915, (1991).

27. D. L. Hardy and T. J. Norwood, Spectral editing technique for the in vitro and in vivo detection of taurine, *J. Magn. Reson.* **133**, 70, (1998).

28. J. E. van Dijk, A. F. Mehlkopf and W. M. Bovee, Comparison of double and zero quantum NMR editing techniques for in vivo use, *NMR Biomed.* **5**, 75, (1992).

29. M. S. Silver, R. I. Joseph and D. I. Hoult, Highly selective $\pi/2$ and π pulse generation, *J. Magn. Reson.* **59**, 347, (1984).

30. R. J. Ordidge, R. M. Bowley and G. McHale, A general approach to selection of multiple cubic volume elements using the ISIS technique, *Magn. Reson. Med.* **8**, 323, (1988).

31. P. C. van Zijl, M. O. Johnson, S. Mori and R. E. Hurd, Magic-angle-gradient double-quantum-filtered COSY, *J. Magn. Reson. A* **113**, 265, (1995).

32. W. H. Perman, M. A. Bernstein and J. C. Sandstrom, A method for correctly setting the rf flip angle, *Magn. Reson. Med.* **9**, 16, (1989).

33. W. Nosel, L. A. Trimble, J. F. Shen and P. S. Allen, On the use of double-quantum coherence from an AX3 system (protons in lactate) for spectral editing, *Magn. Reson. Med.* **11**, 398, (1989).

34. A. H. Wilman and P. S. Allen, In vivo NMR detection strategies for gamma-aminobutyric acid, utilizing proton spectroscopy and coherence-pathway filtering with gradients, *J. Magn. Reson. B* **101**, 165, (1993).

35. L. E. Kay and R. E. D. McCLung, A product operator description of AB and ABX spin systems, *J. Magn. Reson.* **77**, 258, (1988).

36. J. F. Shen and P. S. Allen, Reduced length for double-quantum filtering sequences, *J. Magn. Reson.* **92**, 398, (1991).

37. J. F. Shen and P. S. Allen, Enhancement of double-quantum-filtered signals using optimized tip angle RF pulses, *J. Magn. Reson.* **90**, 606, (1990).

38. J. Frahm, K. D. Merboldt and W. Hanicke, Localized proton spectroscopy using stimulated echoes, *J. Magn. Reson.* **72**, 502, (1987).

39. S. Cerdan, R. Parrilla, J. Santoro and M. Rico, ^{1}H NMR detection of cerebral myo-inositol, *FEBS Lett.* **187**, 167, (1985).

40. A. G. Chapman, E. Westerberg, M. Premachandra and B. S. Meldrum, Changes in regional neurotransmitter amino acid levels in rat brain during seizures induced by L-allylglycine, bicuculline, and kainic acid, *J. Neurochem.* **43**, 62, (1984).

41. E. R. Korpi and R. J. Wyatt, Effects of chronic D-amphetamine and phenylethylamine on the concentrations of neurotransmitter amino acids in the rat brain, *Int. J. Neurosci.* **18**, 239, (1983).

42. T. A. Durkin, G. M. Anderson and D. J. Cohen, High-performance liquid chromatographic analysis of neurotransmitter amino acids in brain, *J. Chromatogr.* **428**, 9, (1988).

43. S. R. Wagner and W. L. Lanier, Metabolism of glucose, glycogen, and high-energy phosphates during complete cerebral ischemia. A comparison of normoglycemic, chronically hyperglycemic diabetic, and acutely hyperglycemic nondiabetic rats, *Anesthesiology* **81**, 1516, (1994).

44. M. A. Thomas, H. P. Hetherington, D. J. Meyerhoff and D. B. Twieg, Localized double-quantum-filtered ^{1}H NMR spectroscopy, *J. Magn. Reson.* **93**, 485, (1991).

45. G. Goelman, G. Walter and J. S. Leigh Jr., Hadamard spectroscopic imaging technique as applied to study human calf muscles, *Magn. Reson. Med.* **25**, 349, (1992).

46. J. Slotboom, A. F. Mehlkopf and W. M. Bovee, The effects of frequency-selective RF pulses on J-coupled spin-1/2 systems, *J. Magn. Reson. A.* **108**, 38, (1994).

47. R. B. Thompson and P. S. Allen, Sources of variability in the response of coupled spins to the PRESS sequence and their potential impact on metabolite quantification, *Magn. Reson. Med.* **41**, 1162, (1999).

Chapter 8. Spectral Editing with the Recovery of More Than One Metabolite

Introduction

A general problem with magnetic resonance (MR) spectral editing techniques is that they recover spectra of only one metabolite at a time, and thus are inefficient in acquiring data if more than a single metabolite is of interest. Furthermore, the final spectrum does not contain peaks from other metabolites such as N-acetylaspartate (NAA) or creatine (Cr) that can serve as internal concentration standards. It would therefore be useful in many cases to be able to observe the signals from edited metabolite and such other metabolites simultaneously. A lactate editing technique using a J-modulated echo difference sequence has been described which allows simultaneous acquisition of the lactate methyl signals and singlets from choline, creatine, NAA, and lipids (1). Simultaneous spectral editing for lactate and γ-aminobutyric acid (GABA) using J-modulated echo difference method has also been reported (2). Two other techniques based on gradient-selected double quantum (DQ) coherence transfer have been described for detection of edited lactate and other metabolites in a single scan (3,4). In those techniques, a DQ filtered coherence transfer echo of lactate and a spin echo of the other metabolites are formed and detected either in one prolonged acquisition window (3) or in two sequential acquisition windows (4).

In this chapter, two spectral editing pulse sequences which are capable of recovering signals from more than one metabolite are described. The first one is a stimulated-echo enhanced selective DQ editing sequence which allows simultaneous observation of lactate and other

metabolites in a single scan while leaving fat and water signals suppressed. The second sequence is a double-editing sequence which in principle can be used to observe edited signals from any two metabolites simultaneously. A pulse sequence for simultaneous editing for GABA and taurine is used as an example here to demonstrate the performance and to illustrate the potential and the pitfalls of such a double-editing sequence.

Simultaneous Lactate Editing and Observation of Other Metabolites Using a Stimulated-Echo Enhanced Selective DQ Filter

Theory

A conventional DQ coherence transfer sequence for lactate editing is shown in Fig. 8.1A. Switching the first two hard 90° pulses in sequence A to frequency selective pulses (Fig. 8.1B) results in a selective DQ coherence transfer editing sequence (5). Because of frequency selective excitation, sequence B usually has better water suppression than sequence A. For lactate editing, the frequency selective excitation pulses (i.e. the first two 90° pulses) are set to excite narrow frequency windows around 1.33 and 4.11 ppm, and the frequency selective DQ read pulse (i.e. the third 90° pulse) is centered at 4.11 ppm. The magnetization outside these regions remains oriented along the z axis during the sequence. It is convenient to choose $\tau_1=\tau-t_1$ and $\tau_2=\tau+t_1$ in order to refocus simultaneously the coherence transfer echo and B_0 inhomogeneity experienced by the DQ coherence during the t_1 period (6). In practice, t_1 should be kept as short as possible to minimize effects of J-modulation (6), but has a minimum of about 10 ms, depending on the length of the frequency-selective excitation pulse and DQ read pulse and the duration of G_1. When 2τ has a conventional value of 68 ms (7-9),

τ_2 is at least 44 ms, and this time is available to obtain MR signals from the non-edited metabolites simultaneously with the edited lactate signals.

One sequence that can be used to do so is shown in Fig 8.1C. The insertion of three identical frequency selective 90° pulses into the τ_2 period forms a stimulated-echo window and generates a stimulated echo from the magnetization of un-edited metabolites whose resonances fall within that window (10). The stimulated-echo window can be shifted along the chemical shift axis by adjusting the carrier frequency and the bandwidth of these three 90° pulse as long as the lactate methyl resonance and lipid resonance at about 1.33 ppm, the lactate methine resonance at about 4.11 ppm, and the water resonance at about 4.7 ppm are not affected. A pair of echo-time (TE) crusher gradient pulses and a mixing-time (TM) crusher gradient pulse (10), adjusted so that the single quantum lactate coherence is not affected, are used to select the stimulated echo. Timing of the stimulated echo window can be adjusted so that the stimulated echo is generated at the end of τ_2, together with the coherence transfer echo of lactate.

Materials and Methods

All phantom experiments were performed on a Bruker Biospec spectrometer using a 9.4 T/21 cm Magnex magnet equipped with a custom-made actively-shielded field gradient coil. An inductively coupled Alderman-Grant RF probe with a 35 mm inner diameter was used for both transmission and reception. The performance of the sequence shown in Fig. 8.1C was tested on two phantoms. Each phantom consisted of a 1.2 cm diameter vial, phantom I containing lactate and GABA in saline and phantom II containing lactate and NAA in saline.

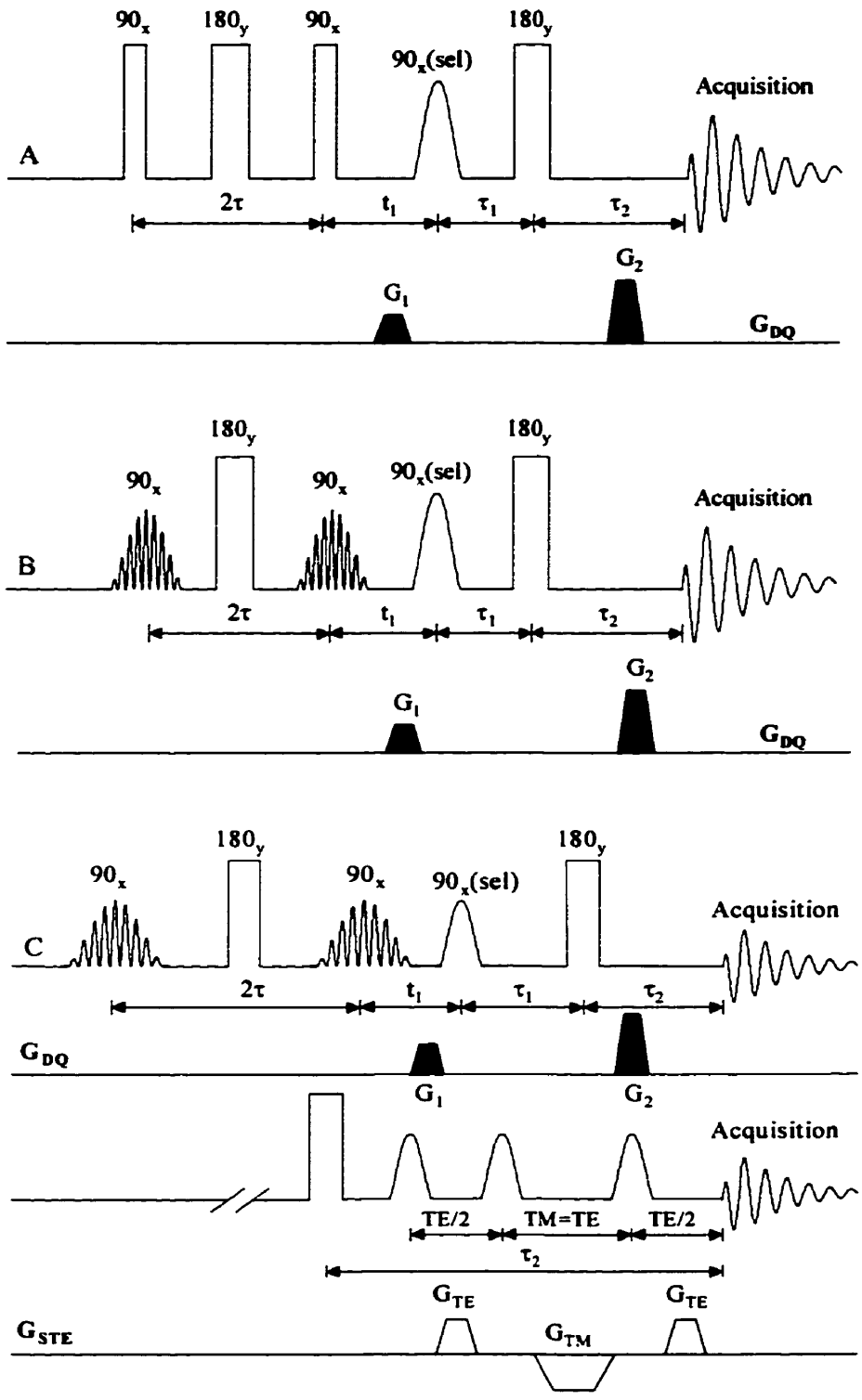

Figure 8.1 Conventional (A), selective (B) and stimulated-echo-enhanced selective (C) double quantum coherence transfer sequences for lactate editing.

For lactate editing, a 20 ms sine-modulated single lobe sinc pulse with double excitation bands having half-height bandwidths of 120 Hz was used as the frequency-selective excitation pulse (11). The sine modulation and carrier frequency were adjusted so that the two excitation bands were centered at the $-CH_3$ and -CH- resonances of lactate. An 8 ms single lobe sinc pulse with a half-height bandwidth of about 250 Hz was used as the frequency selective observation pulse. Either a 9 ms single-lobe (half-height bandwidth of about 180 Hz) or a 9 ms three-lobe (half-height bandwidth of about 700 Hz) sinc pulse was used as the stimulated echo excitation pulse. The flip angles of all pulses were carefully calibrated (12), and all crusher gradients and coherence transfer pathway selection gradients were adjusted experimentally to a near magic-angle setting to maximize the efficiency of water/fat suppression (13). Each spectrum was acquired with 16 transients into 1024 data points with a repetition time of 2.0 s. Spectral processing included zero-filling free induction decays (FIDs) to 4096 data points and a 5 Hz exponential line-broadening.

In vitro experiments on rat brain were carried out on a Bruker Biospec/3 7 T/21 cm spectrometer equipped with actively-shielded gradients. A homebuilt 3 cm-diameter saddle coil was used for both transmission and reception. Rat brain tissue was homogenized and placed in a 1.2 cm diameter vial for MR spectroscopy. All experimental settings for lactate editing in the *in vitro* experiments were the same as those used in the phantom experiments. For observation of creatine and choline resonances, an 11 ms single-lobe sinc pulse was used as the stimulated-echo excitation pulse with the carrier frequency set to 520 Hz downfield of the lactate methyl resonances.

Results

A lactate edited spectrum from phantom I acquired using pulse sequence 8.1B is shown in Fig. 8.2A. The water signal and GABA signals are completely suppressed due to selective coherence transfer. Figure 8.2B to 8.2D show spectra acquired using sequence 8.1C with the simulated echo windows centered on the γ-, α-, and β- GABA resonances respectively, while in spectrum 8.2E, the 1.8 ppm wide stimulated-echo window covers all three GABA resonances. The amplitudes of the γ- and β- GABA peaks in E are less than those in spectra B and C because of imperfections in the excitation profile of the sinc pulse. The variation in the amplitude of lactate peaks among spectra A to E is less than 2%.

Figure 8.3 show the results from phantom II. For spectrum 8.3A, the stimulated-echo window was centered on the 2.02 ppm NAA resonance. As expected, both the lactate methyl signal at 1.33 ppm and the NAA singlet at 2.02 ppm were recovered. For spectrum 8.3B, the power of the two lactate excitation pulses was reduced to a minimum, so that NAA was observed via the stimulated-echo window without lactate editing. As shown, the NAA methyl peak was recovered while no peak at 1.33 ppm was observed, demonstrating that the stimulated-echo window for NAA at 2.02 ppm did not excite the lactate methyl resonance. For spectrum 8.3C, the carrier frequency was switched to "edit" the NAA singlet at 2.02 ppm while putting the stimulated-echo window on the lactate methyl peak. The lactate methyl peak was recovered and no intensity for NAA at 2.02 ppm was found, verifying that the editing efficiency was not degraded by the stimulated-echo window.

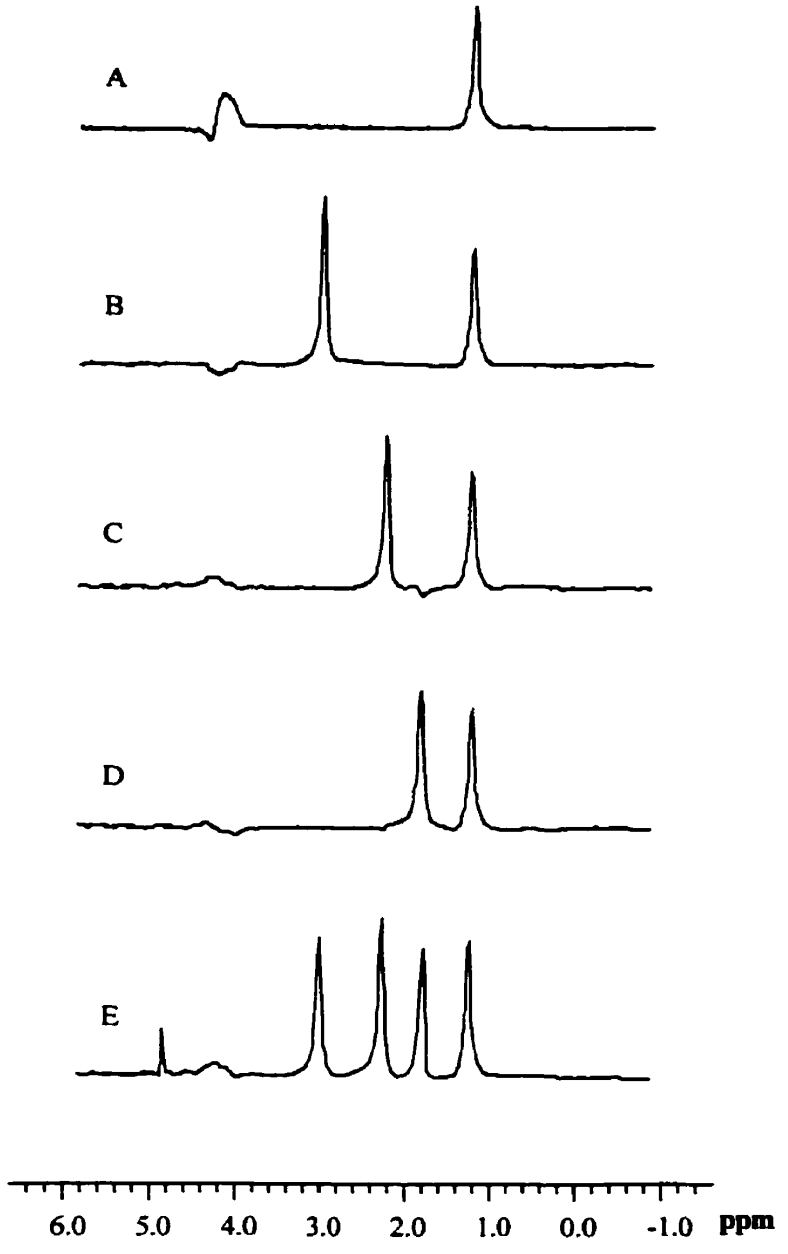

Figure 8.2 Spectra obtained from phantom I (solution of lactate and GABA in saline) using pulse sequence 8.1B (A) and 8.1C (B-E). Spectra B, C and D were acquired with the simulated-echo windows (9 ms single lobe sinc pulses) centered on the γ-, α-, and β- GABA resonances respectively. For spectrum E, the stimulated-echo window was formed by using three 9 ms three-lobe sinc pulses with the carrier frequency at 470 Hz downfield of the lactate methyl resonance (i.e. about 2.5 ppm).

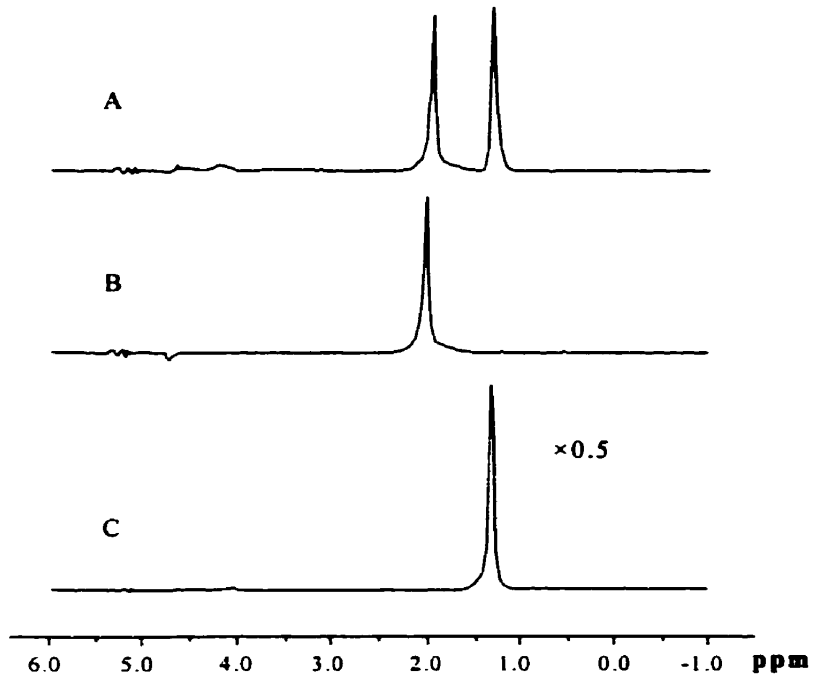

Figure 8.3 Spectra obtained from phantom II using pulse sequence 8.1C with the stimulated-echo window formed by three 9 ms single-lobe sinc pulses with the carrier frequency centered on the NAA methyl peak at 2.02 ppm (A, B), or on the lactate methyl peaks at 1.33 ppm (C). Spectra were acquired with (A) or without (B) lactate editing or with "NAA editing" (C).

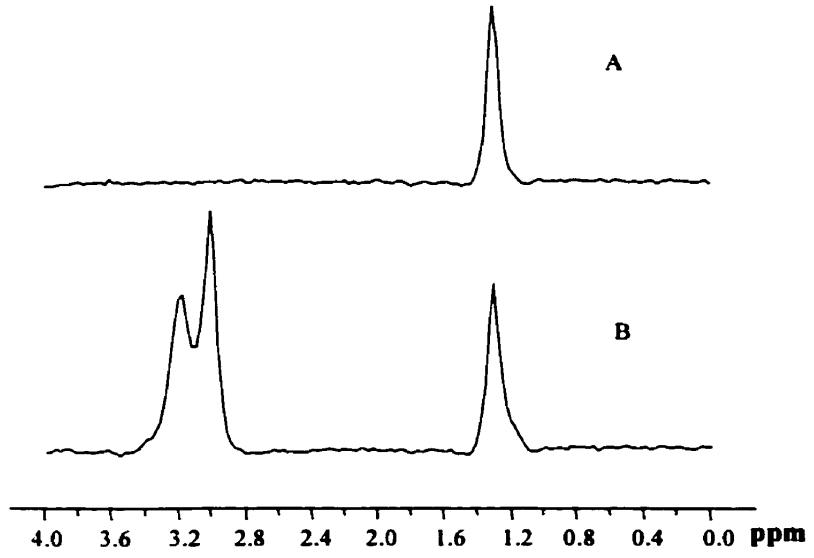

Figure 8.4 Spectra obtained from rat brain *in vitro* using pulse sequences 8.1B (A) and 8.1C (B), with the stimulated-echo window formed by three 11 ms single-lobe sinc pulses with the carrier frequency centered at 3.12 ppm.

Spectra from rat brain tissue are shown in Fig 8.4. Spectrum 8.4A was acquired using sequence 8.1B, and only lactate signals are present in the spectrum. Spectrum 8.4B was acquired using sequence 8.1C with the frequency of the stimulated echo excitation pulses centered between the creatine and choline resonances. As expected, both creatine and choline singlets were recovered together with the edited lactate signals.

Discussion

Lactate editing in combination with recovery of resonances of other metabolites has been reported previously using spin-echo enhanced selective DQ coherence transfer (SEE-SelDQC) (3,4). An alternative sequence using stimulated-echo enhanced selective DQ coherence transfer (STE-SelDQC) has been presented above. Compared with SEE-SelDQC, STE-SelDQC has several advantages. First, in the previously described SEE-SelDQC sequences, it takes extra time to generate the spin echo, while it is possible to incorporate the entire stimulated echo part of the sequence into the τ_2 duration of the editing sequence in STE-SelDQC. Therefore no extra time is needed. Second, in SEE-SelDQC, the minimum TE for the non-edited metabolites is long (i.e. about 160-170 ms) so that only resonances from metabolites with long T2 can be recovered. On the other hand, using STE-SelDQC, shorter TE (18-22 ms) is possible, depending on the duration of the frequency-selective pulses used to excite the stimulated echo. Third, using SEE-SelDQC, the lactate coherence transfer echo and the spin echo of other metabolites cannot be refocused simultaneously. Consequently, the acquisition windows must be prolonged (3) or two acquisition windows (4) must be used to accommodate the two echoes. In STE-SelDQC, the timing of the stimulated echo window can be adjusted so that the lactate coherence transfer echo and the stimulated echo are

refocused simultaneously. Finally, the STE-SelDQC sequence is more flexible than the SEE-SelDQC sequence in terms of recovering non-edited metabolites. For example, the excitation frequency and the bandwidth of the stimulated-echo excitation pulse can be adjusted to create a stimulated-echo window which captures any desired metabolite resonances as long as the lactate, lipid and water resonances do not fall into the simulated-echo window.

However, there are also some limitations to the STE-SelDQC sequence. First, because the stimulated echo frequency selective pulses are long (typically 8-10 ms), t_1 must be increased in order that the τ_2 period be long enough to incorporate the entire stimulated echo part of the sequence and refocus the lactate coherence transfer echo and the stimulated echo simultaneously ($\tau_2=\tau+t_1$). Without the stimulated echo part, t_1 can be as short as 10 ms, while adding the stimulated echo sequence requires that t_1 be increased to at least 18 ms. Because the edited lactate signal is modulated by a factor of $\cos^2(\pi J t_1)$ (6), this increase in t_1 results in a lactate signal loss of about 13%. Second, because the lactate single quantum coherence must experience the TM and TE crusher gradients during τ_2, the lactate signal intensity will be decreased by spin diffusion effects (14). However, because the amplitudes of the TM and TE crusher gradients were small (about 15 mT/m) and the duration was short (1 ms) in this study, spin-diffusion effects were minor, as can be see by comparing the lactate peaks in spectra 8.2A and 8.2B. Third, because resonances of non-edited metabolites are excited and observed during τ_2, it is essential to ensure that the magnetization of those metabolites remains intact at the beginning of τ_2 in order to obtain maximum sensitivity. Theoretically, transverse magnetization of non-edited metabolites is not excited during the first part of the sequence. However, because of RF pulse imperfections and T1 relaxation between the first

and the second 180° refocusing pulses, a 10% signal loss was found in the present study for the non-edited metabolites when the editing part of the sequence was added ahead of the stimulated echo window. To some extent, this problem can be avoided by carefully tuning the power and bandwidth of the RF pulses used for lactate editing, particularly for the two hard refocusing pulses. Fourth, using the stimulated-echo sequence and balanced TM and TE crusher gradients, two signals are refocused at the end of the stimulated-echo window, namely the stimulated echo and FID1 (the FID generated by the first 90° pulse of the three 90° pulses). However, the B_0 inhomogeneity experienced by FID1 is not refocused during the subsequent part of the sequence, and $T2^*$ is normally short enough for FID1 to decay completely before acquisition. This can be seen from Figs. 8.2B to 8.2D. The absence of any phase distortion in the GABA peaks demonstrates that only the stimulated echo was observed.

Both the DQ coherence transfer and the stimulated echo sequences recover 50% of the signal intensity. However, the edited lactate resonance can experience further reductions in intensity due to spin diffusion effects and to J-modulation during t_1, as described above. Furthermore, the resonance of lactate and those of metabolites excited by the stimulated-echo sequence experience significantly different echo times, so that differences in the extent of T2 relaxation can also affect the relative signal intensities. Direct comparison of signal intensities to assess relative concentrations must take these features into account.

Spatial localization of the STE-SelDQC sequence can be achieved by chemical shift imaging (CSI) (3,7,15). Two or three phase-encoding gradients can be placed between the last

stimulated-echo excitation pulse and the data acquisition window. If two-dimensional CSI is used, the spatial localization in the third dimension can be achieved by longitudinal Hadamard encoding, in which a Hadamard encoding RF pulse is applied at the beginning of the sequence to encode the longitudinal magnetization of both lactate and other metabolites (16).

Simultaneous Spectral Editing for GABA and Taurine Using Double Quantum Coherence Transfer

Theory

A DQ coherence transfer sequence for metabolite editing is shown in Fig. 8.1A. To edit a particular metabolite, the frequency selectivity and the flip angle (θ) of the DQ read pulse as well as the duration of the DQ coherence creation period (2τ) are adjusted to optimize the sensitivity of detection of the target metabolite while eliminating spectral overlap. Usually t_1 is kept as short as possible to minimize signal loss through J-modulation, and τ_1 and τ_2 are usually set to τ-t_1 and τ+t_1 respectively in order to refocus simultaneously the coherence transfer echo and B_0 inhomogeneity experienced by the DQ coherence during the t_1 period (6).

For *in vivo* DQ GABA editing, the γ-GABA resonance at 3.01 ppm is usually the target resonance (17-20). The γ protons are weakly coupled to the β protons at 1.91 ppm by 7.3 Hz (21). Using a product operator formalism, an optimized DQ filtering sequence for *in vivo*

GABA editing has been designed, with $2\tau=1/4J=34$ ms and a 90° frequency selective pulse which excites only the β-GABA resonance for the DQ coherence read pulse (18).

As described in the last chapter, taurine is a strongly coupled A_2B_2 spin system with chemical shifts of 3.27 ($N-CH_2$) ppm and 3.43 ppm ($S-CH_2$) and J=6.7 Hz (21). The signal intensity passing through a DQ filter for taurine is maximum at $2\tau=37.5$ ms, similar to the optimum value for GABA editing. As the two taurine methylene groups have similar chemical shifts, in practice it is difficult to use a frequency-selective DQ read pulse to excite only one methylene group. A read pulse that converts the DQ coherence originating from both methylene groups into single quantum coherence can therefore be considered to be a "non-frequency-selective" read pulse. For taurine, the maximum edited signal intensity passing through the DQ filter occurs when $\theta=60°$ when a DQ coherence selection gradient pair of the same polarity is used.

Since the optimum values of 2τ are similar for GABA and taurine, a dual-band DQ read pulse can be used to convert the DQ coherence from both GABA and taurine into single quantum coherence. One wave form for such a dual-band pulse is

$$RF(t) = A(t) \times \{W_{GABA}\,[\exp[-i(\omega_{GABA}\,t)] + W_{tau}\exp[-i(\omega_{tau}\,t + \Delta\phi)]\} \qquad [8.1]$$

where $A(t)$ is the amplitude envelop function, W_{GABA} and W_{tau} are the amplitude weighting coefficients for GABA and taurine excitation bands, ω_{GABA} and ω_{tau} are the frequency offsets of the β-GABA and taurine resonances relative to the carrier frequency, and $\Delta\phi$ is the relative phase between the GABA and taurine excitation bands. For the 12 ms DQ read pulse used for the experiments, $A(t)$ is a single-lobe sinc function; $W_{GABA}=1.0$ and $W_{tau}=0.667$ so that the

flip angle of the taurine excitation band is 60° when that of the GABA excitation band is 90°; the carrier frequency is on resonance for the γ peaks of GABA, so that ω_{GABA}=-332 Hz and ω_{tau}=75 Hz at 7 T; and Δϕ can be determined experimentally to give in-phase GABA and taurine signals. The real and imaginary wave forms of this pulse are shown in Fig. 8.5.

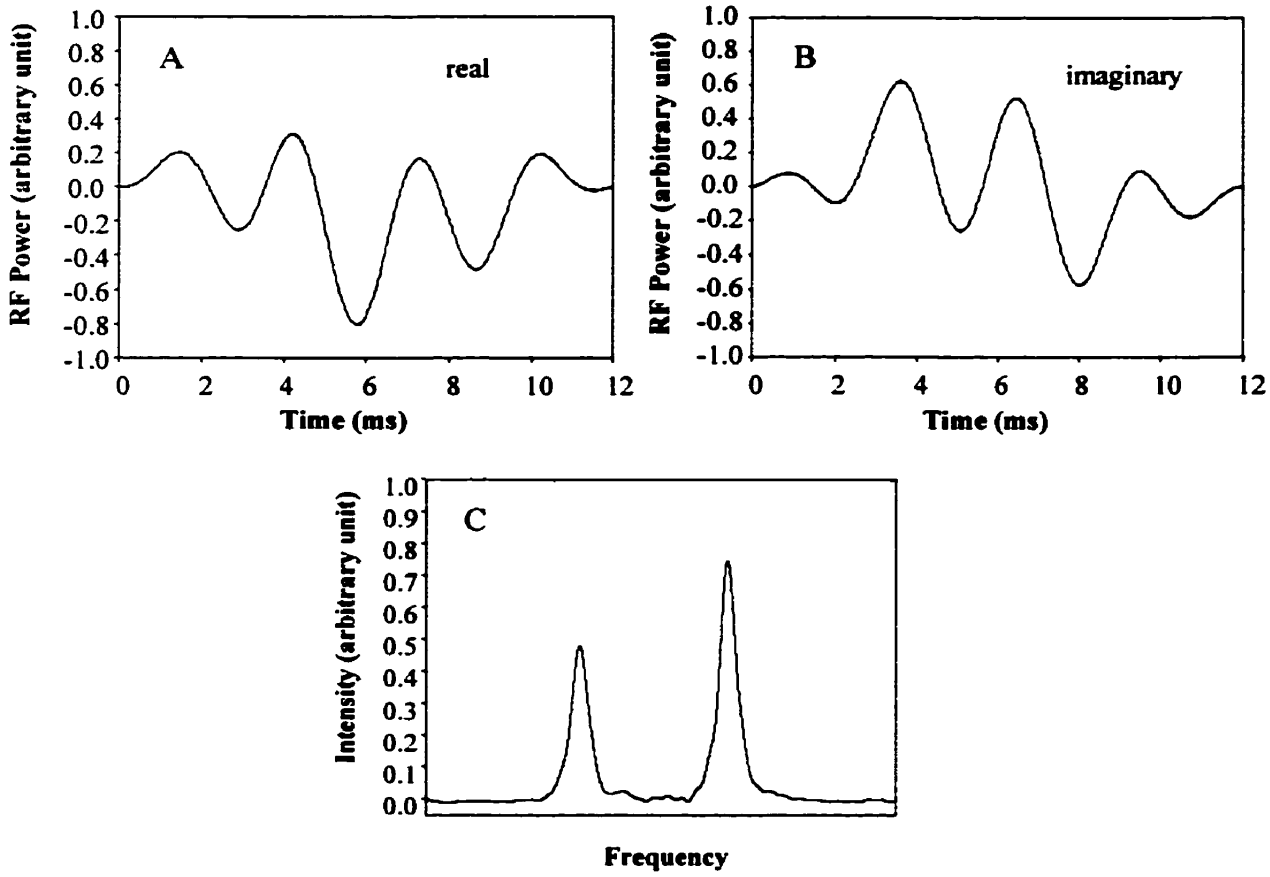

Figure 8.5 Real (A) and imaginary (B) waveforms, and the excitation profile (C) of the dual-band double quantum coherence read pulse for simultaneous GABA and taurine editing.

Materials and Methods

All experiments were carried out on a Bruker Biospec/3 7 T/21 cm spectrometer equipped with actively shielded gradients. A homebuilt 3 cm-diameter saddle coil was used for both transmission and reception. The flip angles of all pulses were carefully calibrated (12), and all crusher gradients and coherence transfer pathway selection gradients were adjusted experimentally to a near magic-angle setting to maximize the efficiency of water suppression (13).

Experiments were performed using a 2.5 cm diameter vial phantom containing 15 mM creatine and 20 mM each of choline, GABA and taurine in saline solution, and a 1.2 cm diameter vial containing homogenized rat brain tissue. Spectra were acquired without editing, and with editing for GABA, for taurine, and for GABA and taurine simultaneously. Non-edited spectra were acquired using a STEAM sequence, with a spectral bandwidth of 2500 Hz, 2048 data points, 16 averages, TR=2.0 s, TE=20 ms and TM=30 ms. Edited spectra were acquired with the DQ filtering sequence shown in Fig. 8.1A, with TR=2.0 s, t_1=7.5 ms, a spectral bandwidth of 4000 Hz and 1024 data points. For GABA editing, 2τ=34 ms and the read pulse was a 12 ms single lobe sinc pulse with the frequency on the β-GABA resonance and a 90° flip angle. For taurine editing, 2τ=37.5 ms and the read pulse was a 12 ms single lobe sinc pulse with the frequency on the taurine resonance at 3.27 ppm and a 60° flip angle. For simultaneous GABA and taurine editing, 2τ=34 ms and the read pulse was a dual-band pulse with one frequency on the β-GABA resonance giving a flip angle of 90° (GABA band), and the other frequency on the taurine resonance at 3.27 ppm giving a flip angle of 60° (taurine

band). Edited spectra were acquired using 16 and 256 averages for the phantom and brain rat tissue respectively. Post-acquisition spectral processing included zero-filling FIDs to 4096 data points and applying a 5 Hz exponential line-broadening prior to Fourier transformation.

Results

Figure 8.6 shows non-edited (A), GABA-edited (B), taurine-edited (C) and GABA- plus taurine-edited spectra (D) acquired from the solution phantom. In the non-edited spectrum (A), the γ-GABA resonance at 3.01 ppm is hidden beneath the creatine methyl singlet, the taurine resonance at 3.27 ppm is hidden beneath the choline methyl singlet, and the taurine resonance at 3.43 ppm overlaps that of the choline α-methylene protons. With GABA editing (B), the γ-GABA resonance is observed, along with the α- and distorted β-GABA resonances. The signals from creatine, choline and taurine are suppressed completely. With taurine editing (C), the creatine and choline singlets are suppressed completely, and the γ-GABA resonance and the choline α-methylene resonance at 3.54 ppm are attenuated significantly, both with distorted phase. The choline β-methylene resonance at 4.06 ppm passes through the filter. With simultaneous GABA and taurine editing (D), both the γ-GABA resonances and the taurine resonances are recovered, with signal intensities indistinguishable from those in B and C.

Figure 8.7 shows the non-edited (A), GABA-edited (B), taurine-edited (C) and GABA- plus taurine-edited spectra (D) acquired from rat brain tissue. Without spectral editing (A), the γ-GABA resonance and the taurine resonances are not resolved from the creatine and choline

resonances. With spectral editing, the interfering creatine and choline resonances are suppressed along with the resonances of other metabolites, and the γ-GABA resonance (B) and the taurine resonances (C) are observed unequivocally. With simultaneous GABA and taurine editing (D), both the γ-GABA resonances and the taurine resonances are recovered, with signal intensities indistinguishable from those in B and C. Distorted signals at about 2.3 ppm in B and D are probably GABA, NAA, and glutamate signals that pass through the DQ filter. Signals with distorted phase between 3.5 and 4.0 ppm in C and D are residual signals from *myo*-inositol, creatine and glucose that pass through the DQ filter.

Discussion

The ability to obtain edited spectra from more than one metabolite in an *in vivo* ^{1}H MRS experiment may be useful in many situations, for example when metabolically coupled compounds are of interest, or when changes in more than a single observable metabolite are potential markers for disease staging or diagnosis. In addition, it is often convenient to obtain information about a metabolite whose concentration is unchanged and so can serve as an internal reference compound. In the present study the possibility of simultaneous DQ editing for more than one metabolite is demonstrated, using a DQ filtering sequence with a composite dual-band DQ coherence read pulse to edit for GABA and taurine together. GABA is an important inhibitory neurotransmitter in brain, and dysregulation of GABA metabolism has been implicated in the pathophysiology of disorders such as stroke, epilepsy and schizophrenia (22-28). Taurine is a metabolic product of sulfur amino acid catabolism, whose role may include neurotransmission, osmoregulation, buffering of acidosis, and

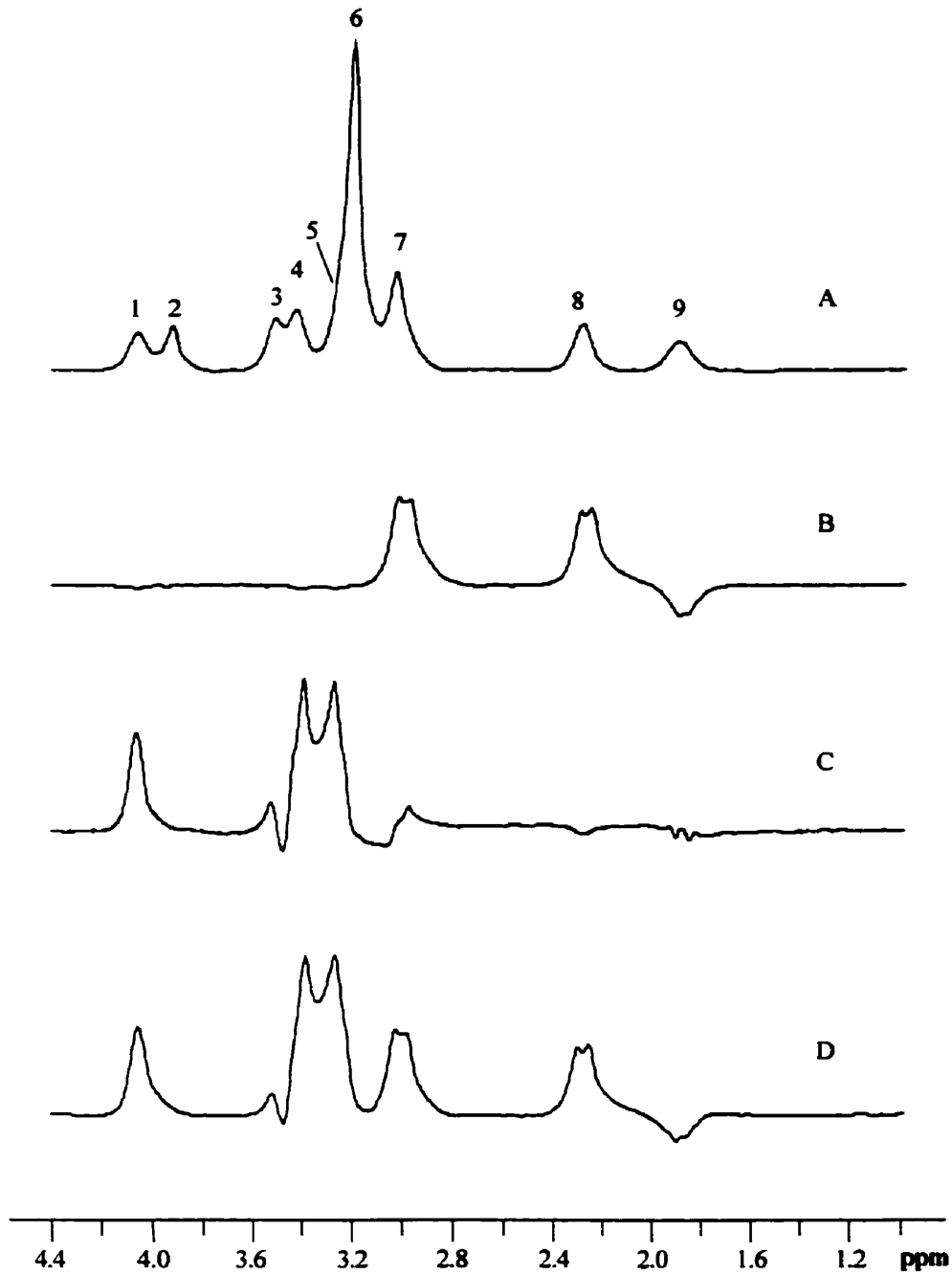

Figure 8.6 Spectra acquired from the solution phantom without spectral editing (A), and with editing for GABA (B), taurine (C), or GABA and taurine together. The scaling factors for B, C, and D are twice that for A. Peak assignments; 1) choline (β-CH_2); 2) creatine, (CH_2); 3) choline, (α-CH_2); 4) taurine, (S-CH_2); 5) taurine (N-CH_2); 6) choline (CH_3); 7) creatine (CH_3)+GABA (γ-CH_2); 8) GABA (α-CH_2) and 9) GABA (β-CH_2).

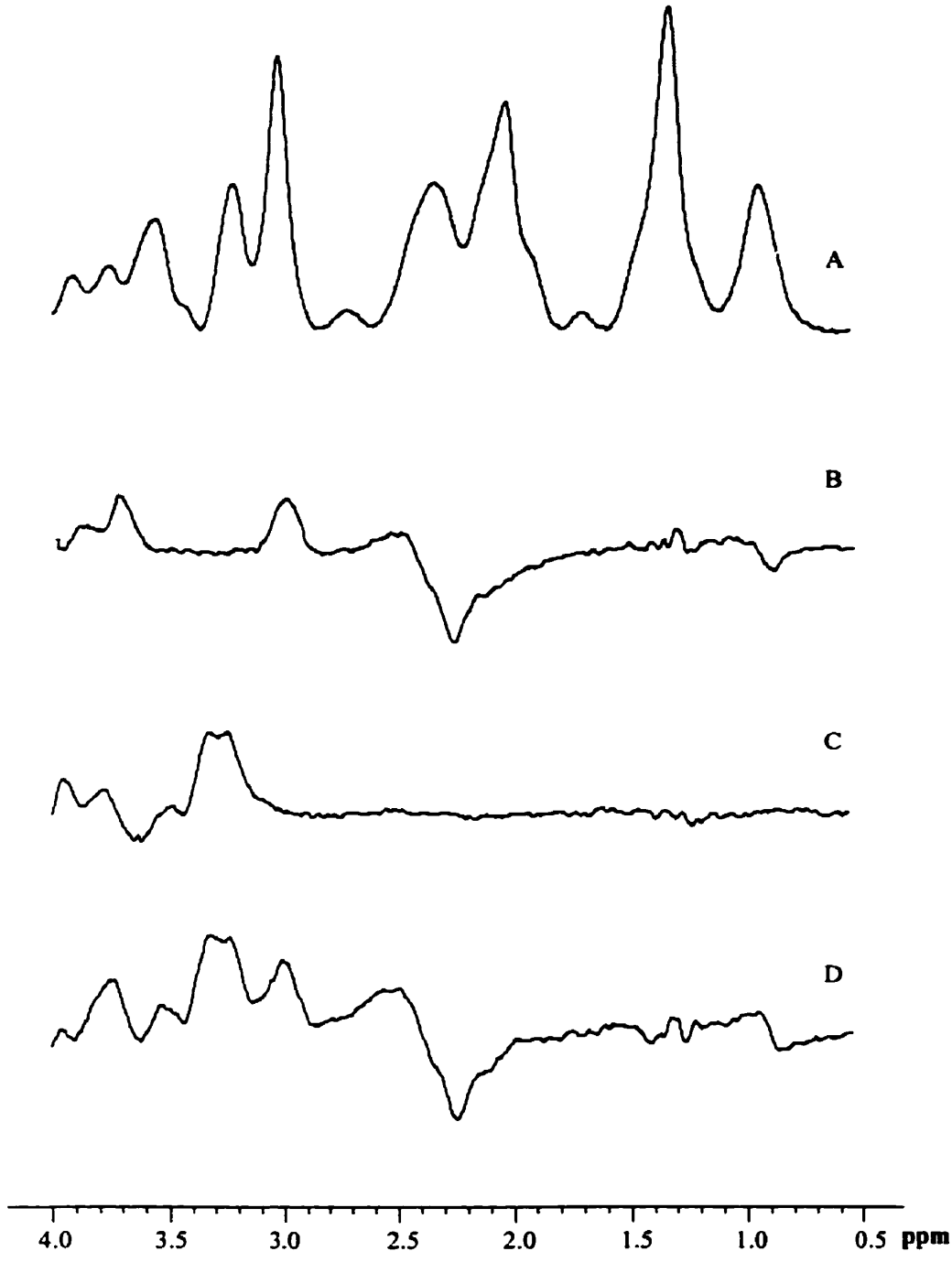

Figure 8.7. Spectra acquired from rat brain tissue *in vitro* without spectral editing (A), and with editing for GABA (B), taurine (C), or GABA and taurine simultaneously. The scaling factor for A is twice those for B, C, and D.

neuroprotection during cerebral ischemia (references see last chapter). *In vivo* observation of both GABA and taurine by conventional proton MR spectroscopy is hindered by severe spectral overlap of their resonances with those of a number of other metabolites such as creatine, choline, *myo*-inositol and glucose (21). The sequence described here permits observation of GABA and taurine in a single experiment without interference from the resonances of other metabolites.

When a DQ filtering sequence is used to observe a single metabolite, all experimental parameters can be adjusted to optimize the detection sensitivity and editing efficiency for that particular metabolite. However, compromise is necessary when two metabolites are edited simultaneously so that, theoretically, the detection sensitivity for both metabolites may be lower than when they are edited individually. With the study described, the detection sensitivity for GABA may be reduced due to the use of the dual-band DQ read pulse required for the double editing. Leakage of the taurine excitation band of the dual-band DQ read pulse into the γ-GABA resonance will decrease the detection sensitivity for GABA since the maximum detection sensitivity is obtained when the DQ read pulse excites only the β-GABA resonance (18). Some residual γ-GABA signal intensity is observed in the taurine edited spectrum (Fig. 8.6C), confirming the presence of such leakage. However, the effect on the GABA detection sensitivity is small (about 3%), as can be seen by comparing the GABA signal intensities in Figs. 8.6B and 8.6D, or 8.7B and 8.7D.

With the study described, the experimental settings for double editing were adjusted to optimize the sensitivity for GABA detection, at the cost of potentially compromised

detection sensitivity for taurine. Since the carrier frequency was set on the γ-GABA resonance, the taurine resonances are affected in two ways by off-resonance effects. First, off-resonance excitation and refocusing compromise the efficiency of the coherence transfer, reducing the detection sensitivity for taurine (6). Because the frequency difference between the γ-GABA resonance and the taurine resonance is small (about 75 Hz) at the field strength used here (7 T), no reduction in the intensity of the taurine resonances was observed. However, when two metabolites with a larger chemical shift difference are edited simultaneously, this effect may become important. Second, the DQ coherences of taurine and GABA precess with different DQ frequencies during t_1, resulting in a phase difference that will be carried through to the final spectrum and will affect the detection of both metabolites if not corrected. However, the relative phase between the GABA and the taurine excitation bands of the dual-band DQ read pulse can always be adjusted experimentally until the final spectrum gives in-phase signals for both GABA and taurine. The taurine detection sensitivity may also be reduced by the use of 2τ=34 ms, which is optimized for GABA editing, rather than 37.5 ms which is optimum for taurine editing. Again, any such reduction in taurine detection sensitivity appears to be unimportant in the experiments reported here (less than 5%), as can be seen by comparing the taurine signal intensities in Figs. 8.6C and 8.6D, or 8.7C and 8.7D.

The double editing strategy described can in principle be used to edit for any two metabolites for which the optimum values of 2τ are similar. The optimum 2τ value for a coupled spin system is determined mainly by the J coupling constant(s) and the transverse relaxation time, and also on the chemical shift difference(s) and the field strength in the case of strong

coupling. For many metabolites of common interest in *in vivo* proton MR spectroscopy, J is about 7 Hz and the optimum 2τ values that have been reported lie around 40 ms. For example, the optimum 2τ values are 34-44 ms for lactate and alanine (8,29,30), 34 ms for GABA (18), 36 ms for glutamate at 3 T (31), 34 ms for glucose at 4.7 T (32), and 37.5 ms for taurine at 7.1 T. One problem that might prevent the generalization of this sequence for editing for any pair of metabolites is the off-resonance effects discussed above; these effects must be considered in designing and optimizing a DQ filter for the detection of more than a single metabolite. Technically, the off-resonance effects can potentially be circumvented by using selective on-resonance double pulses (33) or resonance-offset compensated adiabatic pulses as the excitation/refocusing pulses (34). However, to fully understand how the off-resonance excitation/refocusing affects the outcome of a DQ editing experiment requires a rigorous theoretical treatment which has yet to be developed.

Since the proposed double editing sequence differs from conventional DQ sequences only in the DQ read pulse, it can be combined with spatial localization strategies previously developed for conventional DQ filtering, including point resolved spectroscopy (PRESS) (19,31,32,35), image-selected in vivo spectroscopy (ISIS) (36), and conventional or Hadamard- encoded chemical shift imaging (CSI) (3,7,15,16,30). However, when used with PRESS, caution must be exercised in setting the phase of the DQ read pulse relative to other pulses as well as the relative phase between the two excitation bands of the DQ pulse because of the loss of phase coherence through slice selective excitation/refocusing (35).

References

1. E. Adalsteinsson, D. M. Spielman, G. A. Wright, J. M. Pauly, C. H. Meyer and A. Macovski, Incorporating lactate/lipid discrimination into a spectroscopic imaging sequence, *Magn. Reson. Med.* **30**, 124, (1993).

2. M. Mescher, H. Merkle, J. Kirsch, M. Garwood and R. Gruetter, Simultaneous in vivo spectral editing and water suppression, *NMR Biomed.* **11**, 266 (1998).

3. Q. He, Z. M. Bhujwalla and J. D. Glickson, Proton detection of choline and lactate in EMT6 tumors by spin-echo-enhanced selective multiple-quantum-coherence transfer, *J. Magn. Reson. B* **112**, 18, (1996).

4. A. H. Wilman, M. Astridge, R. E. Snyder and P. S. Allen, Same-scan acquisition of both edited J-coupled multiplets and singlet resonances of uncoupled spins for proton MRS, *J. Magn. Reson. B.* **109**, 202, (1995).

5. D. L. Hardy, C. J. Webb and T. J. Norwood, *Abstr. Int. Soc. Magn. Reson. Med.*, 1352 (1997).

6. J. E. van Dijk, A. F. Mehlkopf and W. M. Bovee, Comparison of double and zero quantum NMR editing techniques for in vivo use, *NMR Biomed.* **5**, 75, (1992).

7. R. E. Hurd and D. M. Freeman, Metabolite specific proton magnetic resonance imaging, *Proc. Natl. Acad. Sci. U. S. A.* **86**, 4402, (1989).

8. C. H. Sotak, D. M. Freeman and R. E. Hurd, The unequivocal determination of in vivo lactic acid using two dimensional double-quantum coherence-transfer spectroscopy, *J. Magn. Reson.* **78**, 355, (1988).

9. W. Nosel, L. A. Trimble, J. F. Shen and P. S. Allen, On the use of double-quantum coherence from an AX3 system (protons in lactate) for spectral editing, *Magn. Reson. Med.* **11**, 398, (1989).

10. J. Frahm, K. D. Merboldt and W. Hanicke, Localized proton spectroscopy using stimulated echoes, *J. Magn. Reson.* **72**, 502, (1987).

11. D. C. Shungu and J. D. Glickson, Band-selective spin echoes for in vivo localized ^{1}H NMR spectroscopy, *Magn. Reson. Med.* **32**, 277, (1994).

12. W. H. Perman, M. A. Bernstein and J. C. Sandstrom, A method for correctly setting the rf flip angle, *Magn. Reson. Med.* **9**, 16, (1989).

13. P. C. van Zijl, M. O. Johnson, S. Mori and R. E. Hurd, Magic-angle-gradient double-quantum-filtered COSY, *J. Magn. Reson. A* **113**, 265, (1995).

14. K. D. Merboldt, W. Hanicke and J. Frahm, Diffusion imaging using stimulated echoes, *Magn. Reson. Med.* **19**, 233, (1991).

15. Q. He, D. C. Shungu, P. C. van Zijl, Z. M. Bhujwalla and J. D. Glickson, Single-scan in vivo lactate editing with complete lipid and water suppression by selective multiple-quantum-coherence transfer (Sel-MQC) with application to tumors, *J. Magn. Reson. B* **106**, 203, (1995).

16. G. Goelman, G. Walter and J. S. Leigh Jr., Hadamard spectroscopic imaging technique as applied to study human calf muscles, *Magn. Reson. Med.* **25**, 349, (1992).

17. A. H. Wilman and P. S. Allen, In vivo NMR detection strategies for gamma-aminobutyric acid, utilizing proton spectroscopy and coherence-pathway filtering with gradients, *J. Magn. Reson. B* **101**, 165, (1993).

18. A. H. Wilman and P. S. Allen, Yield enhancement of a double-quantum filter sequence designed for the edited detection of GABA, *J. Magn. Reson. B.* **109**, 169, (1995).

19. J. R. Keltner, L. L. Wald, B. D. Frederick and P. F. Renshaw, In vivo detection of GABA in human brain using a localized double-quantum filter technique, *Magn. Reson. Med.* **37**, 366, (1997).

20. J. Shen, D. C. Shungu and D. L. Rothman, In vivo chemical shift imaging of γ-aminobutyric acid in the human brain, *Magn. Reson. Med.* **41**, 35, (1999).

21. K. L. Behar and T. Ogino, Assignment of resonance in the ^{1}H spectrum of rat brain by two-dimensional shift correlated and J-resolved NMR spectroscopy, *Magn. Reson. Med.* **17**, 285, (1991).

22. K. Gale, GABA and epilepsy: basic concepts from preclinical research, *Epilepsia* **33 Suppl 5**, S3, (1992).

23. W. D. Lust, H. M. Assaf, A. J. Ricci, R. A. Ratcheson and L. L. Sternau, A role for gamma-aminobutyric acid (GABA) in the evolution of delayed neuronal death following ischemia, *Metab. Brain Dis.* **3**, 287, (1988).

24. P. D. Lyden, GABA and neuroprotection, *Int. Rev. Neurobiol.* **40**, 233, (1997).

25. D. A. McCormick, GABA as an inhibitory neurotransmitter in human cerebral cortex, *J. Neurophysiol.* **62** , 1018, (1989).

26. F. M. Sherif and S. S. Ahmed, Basic aspects of GABA-transaminase in neuropsychiatric disorders, *Clin. Biochem.* **28**, 145, (1995).

27. D. P. van Kammen, F. Petty, M. E. Kelley, G. L. Kramer, E. J. Barry, J. K. Yao, J. A. Gurklis and J. L. Peters, GABA and brain abnormalities in schizophrenia, *Psychiatry Res.* **82**, 25, (1998).

28. H. F. Bradford, Glutamate, GABA and epilepsy, *Prog. Neurobiol.* **47**, 477, (1995).

29. J. F. Shen and P. S. Allen, Reduced length for double-quantum filtering sequences, *J. Magn. Reson.* **92** , 398, (1991).

30. H. Lei and J. Peeling, Multiple-voxel double-quantum lactate edited spectroscopy using two dimensional longitudinal Hadamard encoding, *Magn. Reson. Med.* **42**, 19, (1999)

31. R. B. Thompson and P. S. Allen, A new multiple quantum filter design procedure for use on strongly coupled spin systems found in vivo: its application to glutamate, *Magn. Reson. Med.* **39**, 762, (1998).

32. J. R. Keltner, L. L. Wald, P. J. Ledden, Y. C. Chen, R. T. Matthews, E. H. Kuestermann, J. R. Baker, B. R. Rosen and B. G. Jenkins, A localized double-quantum filter for the in *vivo* detection of brain glucose, *Magn. Reson. Med.* **39**, 651, (1998).

33. V. Blechta and J. Schraml, Selective on-resonance double pulses applied to an IS spin system, *J. Magn. Reson. A* **112**, 30, (1995).

34. M. Garwood, B. Nease, Y. Ke, R. A. de Graaf and H. Merkle, Simultaneous compensation for B_1 inhomogeneity and resonance offsets by a multiple-quantum NMR sequence using adiabatic pulses, *J. Magn. Reson. A* **112**, 272, (1995).

35. L. Jouvensal, P. G. Carlier and G. Bloch, Practical implementation of single-voxel double-quantum editing on a whole-body NMR spectrometer: localized monitoring of lactate in the human leg during and after exercise, *Magn. Reson. Med.* **36**, 487, (1996).

36. M. A. Thomas, H. P. Hetherington, D. J. Meyerhoff and D. B. Twieg, Localized double-quantum-filtered ^{1}H NMR spectroscopy, *J. Magn. Reson.* **93**, 485, (1991).

Chapter 9. Spatially Localized Spectral Editing with Two-Dimensional Longitudinal Hadamard Encoding

Introduction

Lactate, a metabolite of glycolysis, may play important roles in the pathophysiology of many neurological diseases. In general, observation of lactate *in vivo* by proton magnetic resonance spectroscopy (MRS) is hindered by interference from lipids which usually give rise to intense resonances that happen to have virtually the same chemical shift as that of the lactate methyl group in proton MR spectra. Over the past two decades, many lactate editing techniques have been developed to differentiate lactate signals from those of lipids so that lactate can be determined unequivocally (1-17). Among these, gradient selected double-quantum (DQ) lactate editing techniques provide a good compromise between lipid/water suppression, detection sensitivity and motion sensitivity, and thus are considered the most useful for practical applications (7,14-16). However, combining DQ lactate editing techniques with spatial localization, another key element for *in vivo* MRS, is not straightforward. Single-voxel methods using stimulated echo acquisition mode (STEAM) (1,2) and volume selective spectral editing (VOSING) (5) localization generally cannot recover the maximum signal generated by the editing sequence, thus reducing the detection sensitivity for lactate. Point resolved spectroscopy (PRESS) based sequences (7,18,19) can recover the maximum signal, but voxel localization is restricted because of phase problems caused by the slice selective excitation/refocusing (7). DQ lactate editing has also been combined with image selected *in vivo* spectroscopy (ISIS) (6), spatial and chemical shift encoded excitation (SPACE) (3) and volume selective refocusing (VSR) (4) to achieve single voxel spatial localization. Chemical

Chemical shift imaging (CSI) and other imaging sequences with lactate editing capability have been reported (14-17), but they generally suffer from low signal-to-noise ratio per unit time (SNRT), so that acquisition times become unacceptably long for *in vivo* applications.

Hadamard encoding has been proposed as an alternative to conventionally used localization strategies (20-25). Compared to single-voxel techniques, Hadamard encoding has the advantage of multiple-voxel localization. Compared with CSI and other imaging techniques, it provides spectra with higher SNRT in practice and the capability to acquire spectra from a smaller matrix (e.g. 3×3) without suffering Gibbs artifact (21-25). Hadamard encoding can be divided into transverse Hadamard encoding and longitudinal Hadamard encoding. With longitudinal Hadamard encoding, all spatial information is encoded in the longitudinal direction. It can then be combined with spectral editing sequences requiring frequency-selective excitation pulses while avoiding the phase problems encountered with slice-selective excitation (7). In this chapter, multiple-voxel localized DQ lactate editing using two-dimensional longitudinal Hadamard encoding localization is described.

Hadamard Encoding

The use of longitudinal Hadamard encoding for multiple-volume localization in MR spectroscopy and imaging was first introduced by Bolinger and Leigh (20). Hadamard encoding is based on Hadamard matrices, and it in principle recovers n volume elements in n scans. The basic ideas underlying Hadamard encoding and decoding are illustrated in Fig. 9.1. Suppose spatial localization is required for 4 volume elements (i.e. slices 1, 2, 3 and 4)

which together form a matrix **S**. Hadamard encoding is mathematically equivalent to multiplying **S** with a respective Hadamard matrix **H**, a 4×4 matrix in this case. The four columns in **H** correspond to the four volume elements while the four rows represent four encoding steps. The notations "1" and "-1" in **H** indicate whether the longitudinal magnetization of one particular volume element should be inverted ("-1") or not ("1") in one particular encoding step. For example, **H**[2,4] is "-1", and this means that the longitudinal magnetization of slice 4 should be inverted in the second encoding step. In each encoding step, a specially designed multiple-band inversion pulse along with a slice-selective gradient are used to encode the longitudinal magnetization of the sample according to the corresponding row in **H**. Then the encoded longitudinal magnetization is observed in the form of a free induction decay (FID) or an echo with a designated read-out procedure. The four FIDs or echoes acquired in the four encoding steps together form another matrix **F**. An inverse Hadamard transformation on **F** (i.e. diagonalizing **H**) then gives the localized response from each of the volume elements. Two-dimensional (2D) Hadamard encoding is just a straightforward extension of one-dimensional Hadamard encoding by performing Hadamard encoding steps independently in two orthogonal directions. For example, for a two- dimensional 4th order Hadamard encoding experiment, a total of 4×4=16 encoding steps have to be performed to form a 4×4 **F** matrix. Two-dimensional inverse Hadamard transformation of such an **F** matrix gives the localized response from a total of 4×4=16 volume elements.

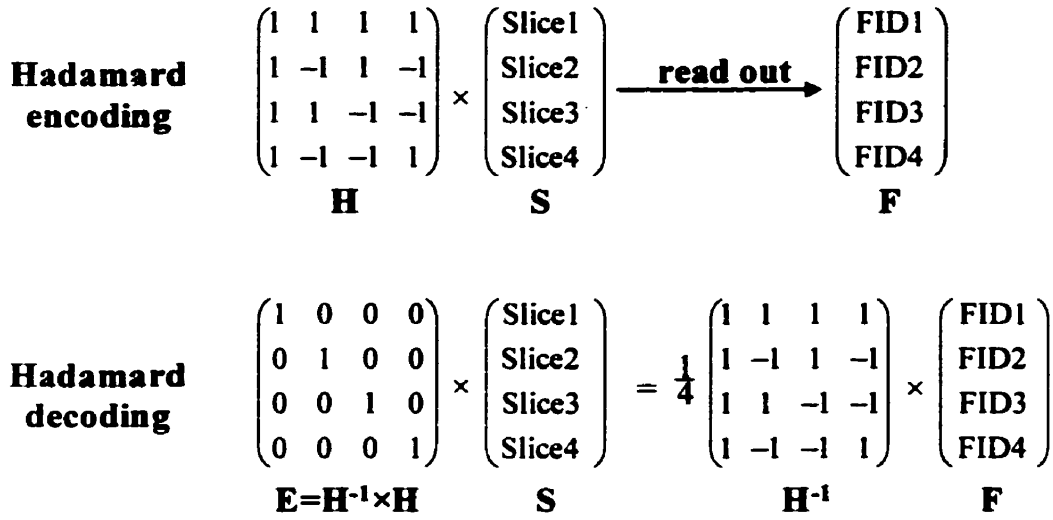

Figure 9.1 A schematic representation of one-dimensional 4th order Hadamard encoding and decoding.

Verification of the Precision of Spatial Localization Using Longitudinal Hadamard Encoding

The first set of experiments was done to verify the precision of spatial localization using longitudinal Hadamard encoding. Multiple-band inversion pulses used for longitudinal Hadamard encoding were numerically synthesized from single band inversion pulses (24),

$$RF(t) = \sum_j A(t)e^{i\phi(t)}e^{-i\omega_j t} \qquad [9.1]$$

where RF(t) is the complex wave form for the multiple-band Hadamard inversion pulse, A(t) and $\phi(t)$ are the amplitude envelop function and phase function for the composite single band inversion pulses, and ω_j is the frequency at the center of the jth desired inversion band. In this study, adiabatic hyperbolic secant pulses (26)

$$A(t) = A_1\,\mathrm{sech}(\beta t) \qquad \phi(t) = \mu \ln[\mathrm{sech}(\beta t)] \qquad [9.2]$$

were used to synthesize the 10 ms 4th order Hadamard pulses with μ=5, β=412 s^{-1}, a bandwidth of 2200 Hz for each inversion band, and A_1 adjusted to optimize the pulse profile.

The inversion profiles of the synthesized Hadamard pulses were measured on a 2.5 cm diameter vial filled with saline using a one-dimensional spin-echo imaging sequence. Figure 9.2A shows the axial profile of the longitudinal magnetization of the phantom with no inversion pulse applied. Figures 9.2B to 9.2D show the inversion profiles of the Hadamard inversion pulses corresponding to the second, the third and the fourth rows of the Hadamard matrix **H** respectively. Slice profiles (E-H) were generated by performing inverse Hadamard transformation on the profiles A-D. There is minor (<5%) inter-slice leakage and overlap of the slice profiles in F-H. The slice profile in E shows contamination from the area outside the region of interest and the gaps between the slices.

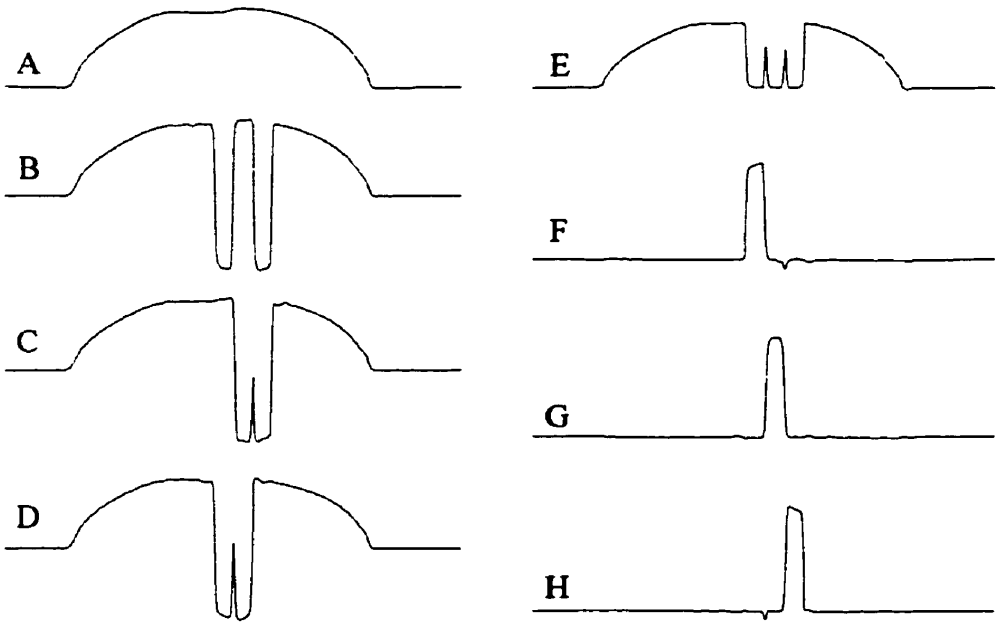

Figure 9.2 Inversion profiles (one-dimensional spin-echo images) of the 4th order Hadamard inversion pulses (A-D) and the slice profiles generated by their inverse Hadamard transformation (E-H).

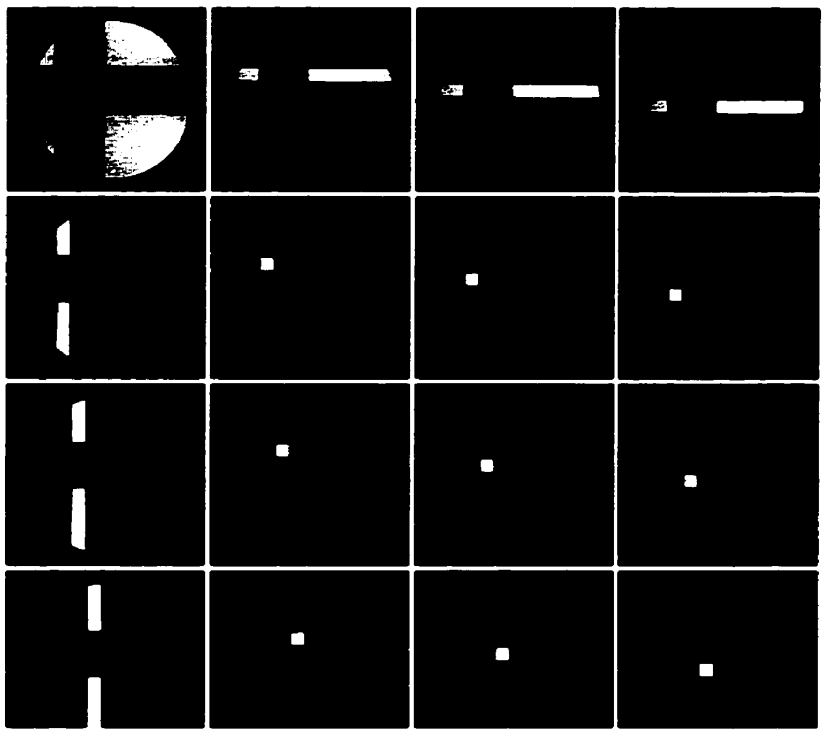

Figure 9.3 Snapshot FLASH images showing spatial localization with two-dimensional 4th order longitudinal Hadamard encoding.

The precision of spatial localization with two-dimensional 4th order longitudinal Hadamard encoding was verified on the same phantom and the results are shown in Fig. 9.3. To obtain those images, 16 proton density weighted images were acquired with a modified snapshot fast low angle shot (FLASH) imaging sequence. The images were acquired with a 5×5 cm^2 field of view (FOV), 128×128 matrix size, 2 mm slice thickness, repetition time (TR) 4.3 ms, echo time (TE) 2.3 ms, two averages and a gaussian excitation pulse with a 12° flip angle. Two 10 ms dual-band Hadamard inversion pulses were inserted before the imaging sequence, encoding the longitudinal magnetization according to the Hadamard matrix as described previously. An inverse Hadamard transformation on the 16 images obtained gave the images shown in Fig. 9.3, with each individual image showing localized signal intensity from one volume element only. Spatial localization in the lower-right 3×3 matrix of voxels is

excellent, showing no sign of contamination. However, it can been seen from the figure that localization of the volume elements in the first row and the first column is not satisfactory because of the contamination resulting from regions outside the volume of interest and the gaps between the volume elements.

Pulse Sequence for Multiple-Voxel Localized DQ Lactate Editing

A conventional DQ coherence transfer sequence for lactate editing is shown in Fig. 9.4A. The first 90° pulse and the two 180° refocusing pulses of the sequence can be made slice selective (Fig. 9.4B) to achieve three-dimensional localization in a manner that is similar to PRESS (7,18,19). However, the lactate signal intensity recovered from such a sequence was found to be dependent on the positioning of the voxel, or in other words, on the frequency offset of the slice-selective 90° pulse and the first slice-selective 180° refocusing pulse (7). As a result, an extra phase correction procedure has to be performed experimentally to correct for this effect, making this localization strategy inconvenient to use in practice (18).

A pulse sequence to acquire multiple-voxel localized lactate-edited spectra without encountering this phase problem is shown in Fig. 9.4C. Two localization strategies are used in this sequence. First, localization in the slice direction is achieved by making the second 180° refocusing pulse of the DQ filter slice selective; making this pulse slice-selective does not introduce a frequency offset-dependent (i.e. position dependent) modulation of the lactate signal intensity (7), so that no phase adjustment is needed (18). Second, multiple-voxel in-plane localization is achieved by two-dimensional longitudinal Hadamard encoding with two Hadamard inversion pulses inserted before the DQ filter along with slice-selective gradients.

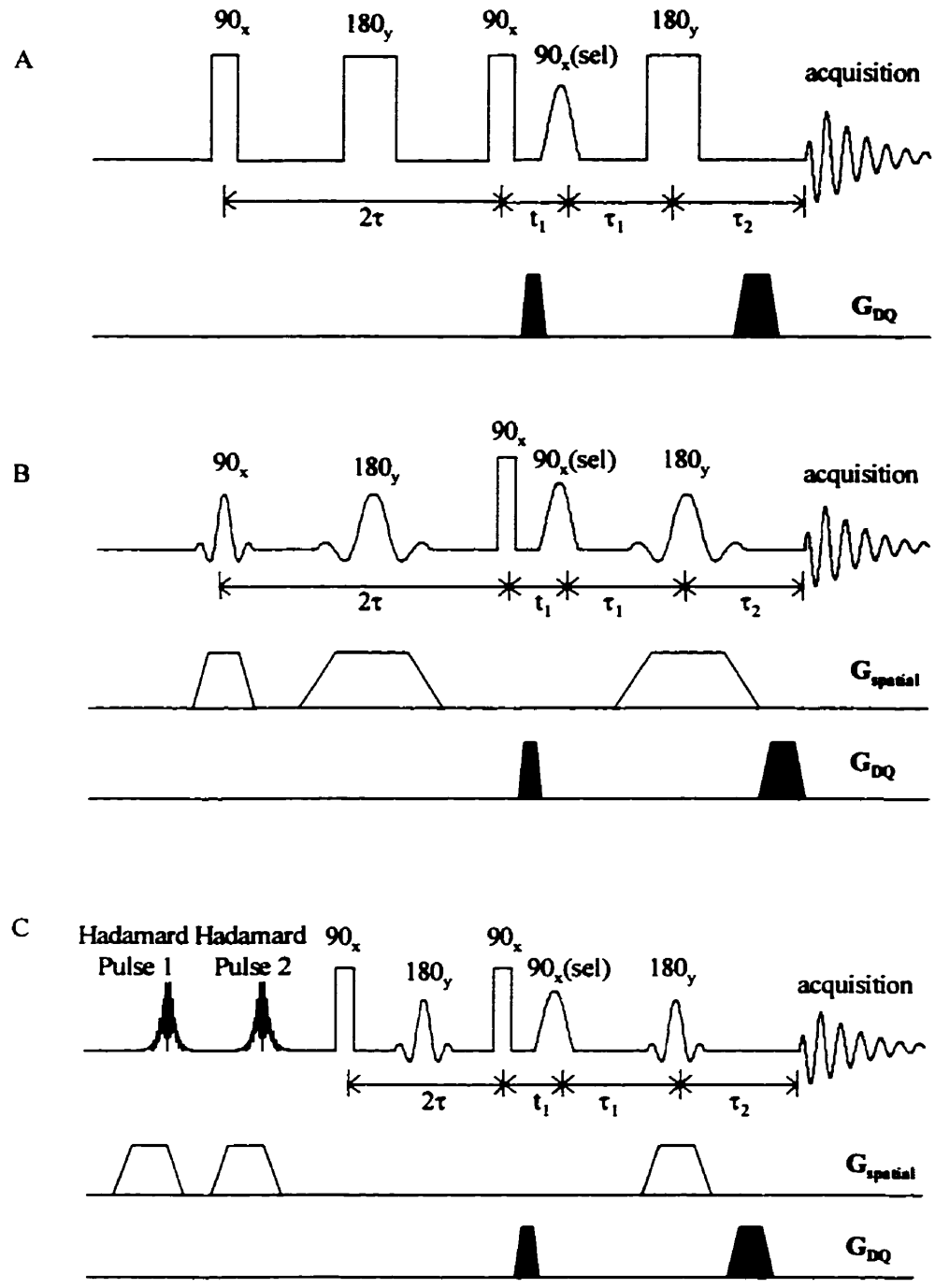

Figure 9.4 A conventional DQ lactate editing sequence (A), a DQ lactate editing sequence combined with PRESS spatial localization (B), and a pulse sequence for DQ lactate editing with two dimensional longitudinal Hadamard encoding and slice selective refocusing to achieve multiple voxel localization. $G_{spatial}$ and G_{DQ} are the gradient pulses used to achieve spatial localization and to select DQ coherence transfer pathways respectively.

Although changing the last refocusing pulse of the DQ filter from a hard pulse to a slice selective pulse does not cause frequency offset-dependent modulation of the lactate signal intensity, caution still must be exercised in choosing the duration and the shape of the pulse, especially for *in vivo* applications (19,27). In the studies described in this chapter, 1 ms sinc-gaussian pulses (half-width at half-maximum) were used as the refocusing pulses, giving good sensitivity and a good slice profile. Fig. 9.5C shows the refocusing profile of the sinc-gaussian pulse used. The refocusing profiles of a 1 ms three-lobe sinc pulse (B) and a 1 ms gaussian pulse (A) are also shown in Fig. 9.5 for comparison.

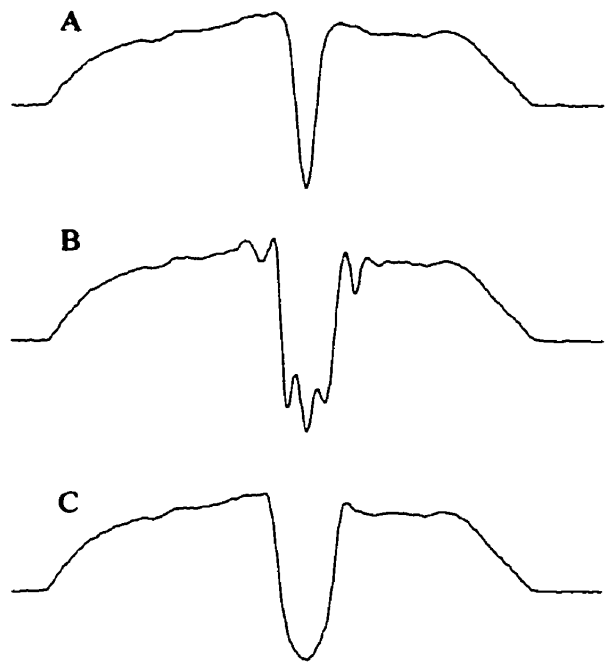

Figure 9.5 Refocusing profiles of a 1 ms gaussian pulse (A), a 1 ms 3-lobe sinc pulse (B) and a 1 ms sinc-gaussian pulse with half-width at half-maximum (C).

Materials and Methods

Phantom Experiments

Experiments on phantoms were performed on a Bruker Biospec spectrometer using a 9.4 T/21 cm Magnex magnet equipped with custom-made actively-shielded field gradient coils. An inductively coupled Alderman-Grant probe with a 35 mm inner diameter was used for both transmission and reception. A two-compartment phantom consisting of a 1.2 cm diameter vial containing pure olive oil in a 2.5 cm diameter vial containing 15 mM lactate and 15 mM N-acetylaspartate (NAA) in saline was used. For the DQ editing part of the sequence, 2τ=68 ms, t_1=12 ms, τ_1=8 ms, and τ_2 was adjusted experimentally so that only the second half of the coherence transfer echo was acquired. DQ coherence transfer pathways were selected using 5 ms gradient pulses with amplitudes of 2.5 G/cm and 5.0 G/cm. Crusher gradients and coherence transfer pathway selection gradients were experimentally adjusted to a near magic-angle setting to maximize the efficiency of water/fat suppression (28). 1 ms sinc-gaussian pulses (half-width at half-maximum) served as the refocusing pulses. The flip angles of the RF pulses were carefully calibrated (29). Eight scans were accumulated for each of the 16 Hadamard encoding steps. To remove the DC offset and spuriously refocused signals, a two-step (0^o-180^o) phase cycling of the last 180^o pulse in synchrony with the receiver was employed. Data were acquired into 1024 points using a spectral bandwidth of 5000 Hz. The FIDs resulting from inverse Hadamard transformation of the acquired FID matrix were zero-filled to 4096 data points, multiplied by a 10 Hz exponential line-broadening function, and Fourier transformed. After excluding the contaminated first row and column, nine 6×6×5 mm^3 voxels were recovered.

In Vivo Experiments

The performance of the sequence shown in Fig. 9.4C was tested on a globally ischemic rat brain and a focally ischemic rat brain. Male Sprague-Dawley rats weighting 250-300 g were used. Global ischemia was produced by cardiac arrest with the injection of 3 ml 20% KCl solution into the tail artery. To induce focal cerebral ischemia in rats the middle cerebral artery was occluded using an intraluminal suture (30). MR measurements on rat brain were carried out on a Bruker Biospec/3 spectrometer using a 7 T/21 cm magnet equipped with actively-shielded gradient coils. A home-built 3 cm diameter RF saddle coil was used for both transmission and reception. For DQ lactate editing, 2τ=40 ms, t_1=6.5 ms, τ_1=13.5 ms, and τ_2 =26.5 ms; in order to refocus the B_0 inhomogeneity experienced by the DQ lactate coherence during the t_1 period, τ_1 and τ_2 were taken as τ-t_1 and τ+t_1 respectively (31). The use of a shorter 2τ value than the conventionally-used 68 ms been reported before (2) and has been dealt with theoretically by Shen et al (32). DQ coherence transfer pathways were selected using 1 ms gradient pulses with amplitudes of 3.5 G/cm and 7.0 G/cm. TR was 2.0 s. For experiments on globally ischemic and focally ischemic rat brain, 64 scans and 80 scans for each of the 16 Hadamard encoding steps were accumulated, giving an experiment time of 36 minutes and 45 minutes respectively. Other acquisition parameters and procedures were the same as those used for phantom experiments. Post-transformation processing included zero filling to 4096 data points and a 20 Hz line broadening. The voxels were 4.5×4.5×5 mm^3 in size.

Results

A snapshot FLASH scout image of the lactate/oil phantom in which the water/oil chemical shift artifact has been corrected manually is shown in Fig. 9.6A. The grid overlying the image shows the in-plane localization. The 0.0-3.0 ppm portion of the spectra obtained from the nine voxels in A is shown in B. The NAA singlet at 2.02 ppm is absent from all spectra, demonstrating successful suppression of uncoupled spins. The lactate methyl resonance is observed with high signal-to-noise ratio (SNR) in the spectra from voxels 3, 6, 7, 8 and 9, containing the lactate/NAA solution, and with low intensity in the spectra from voxels 1, 2, 4 and 5 containing mainly olive oil. There is a significant correlation (r=0.93) between the number of lactate-containing pixels of each voxel and the integrated lactate peak intensity from that voxel. The oil methylene resonances around 1.3 ppm are suppressed.

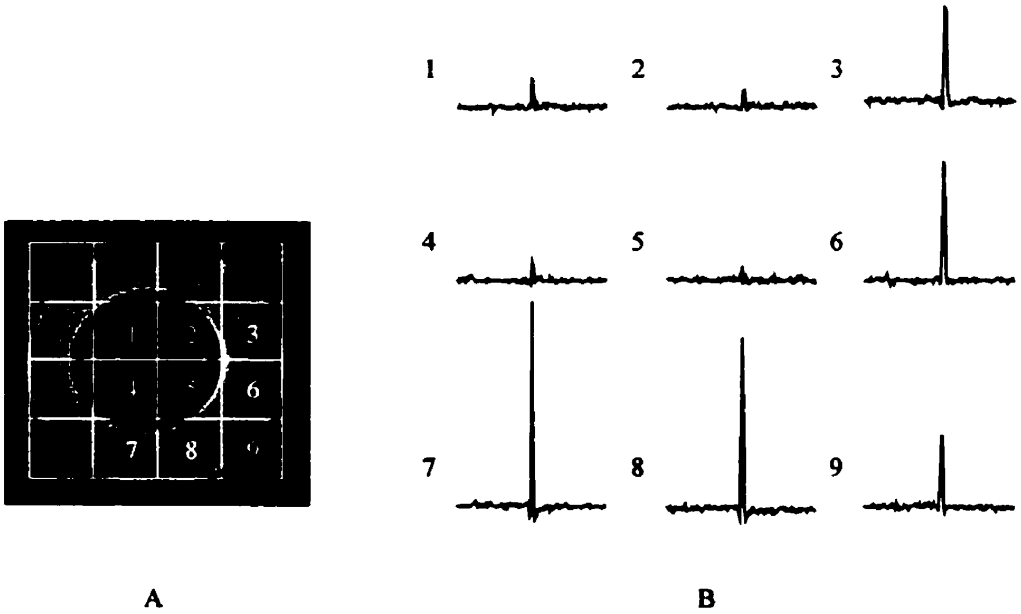

Figure 9.6 Snapshot FLASH image of a phantom of a vial of pure olive oil in a larger vial containing an aqueous solution of lactate and NAA (A). The oil/water chemical shift artifact in A was corrected manually. The grid overlaying the image shows the positions of the nine voxels, whose DQ edited spectra are shown in B.

Figures 9.7A and 9.7B are snapshot FLASH images from a globally ischemic rat brain. The dark bands on the images showing the locations of the slice (A) and the in-plane voxels (B) were produced by preceding the snapshot FLASH imaging sequence with a slice selective refocusing pulse (A) or Hadamard inversion pulses corresponding to the second row of the Hadamard matrix (B). The noise bands appearing on these images are artifacts resulting from the central phase-encoding scheme used for imaging. Figure 9.7C shows a lactate edited spectrum acquired from the whole slice shown in A. Singlet peaks from NAA, creatine, and choline are absent, demonstrating successful suppression of uncoupled spins. The lactate methyl peak at 1.33 ppm is sharp and without phase modulation, showing no contribution from lipid signals. Water suppression by the DQ filter is good. Figure 9.7D shows localized spectra from the nine voxels shown in B. The variation in the integrated signal intensity among the lactate peaks in the nine voxels was about 10%. The lactate peaks from voxels 3, 6 and 9 are broader than those from the other voxels, probably a result of poorer shimming at these voxels.

Figure 9.8A is a snapshot FLASH scout image of a focally ischemic rat brain. The lactate-edited spectra obtained from the voxels shown on the scout image are shown in Fig. 9.8B. Singlet peaks from NAA, creatine, and choline are absent, demonstrating successful suppression of uncoupled spins. Water suppression by the DQ filter is good. The lactate methyl peak is prominent only in spectra from voxels from the region of the brain (i.e. striatum in the right hemisphere) subjected to ischemia.

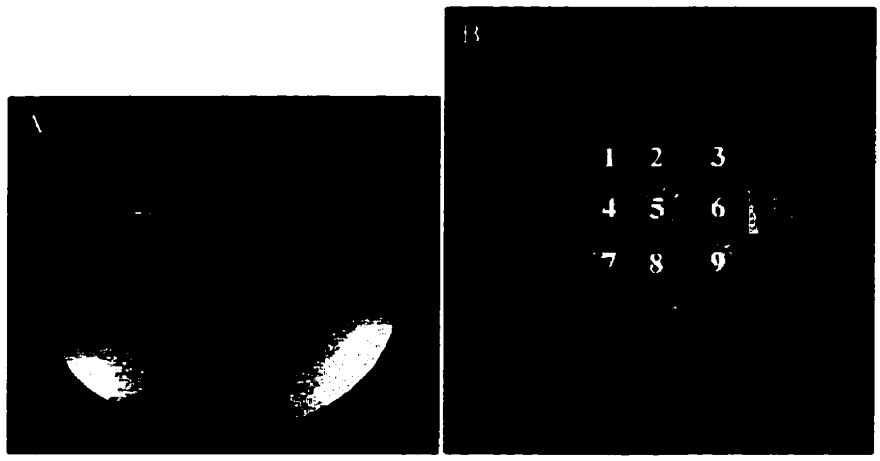

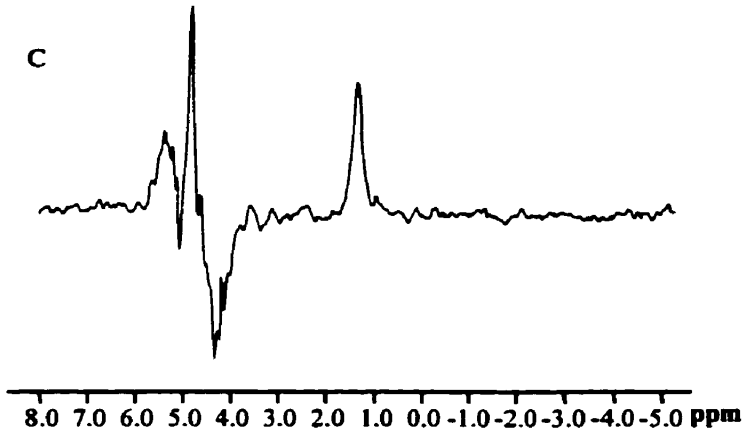

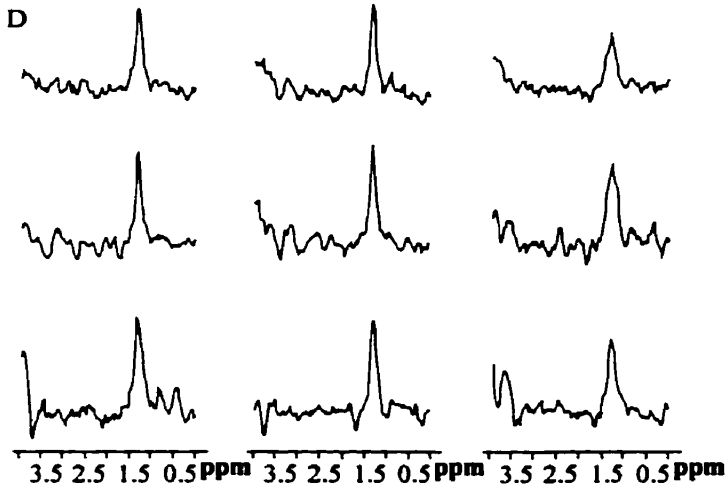

Figure 9.7 Snapshot FLASH images from a globally ischemic rat brain (A-B). The lactate edited spectrum in C was acquired from the whole slice in A. Localized DQ lactate edited spectra from the nine voxels shown in B are given in D.

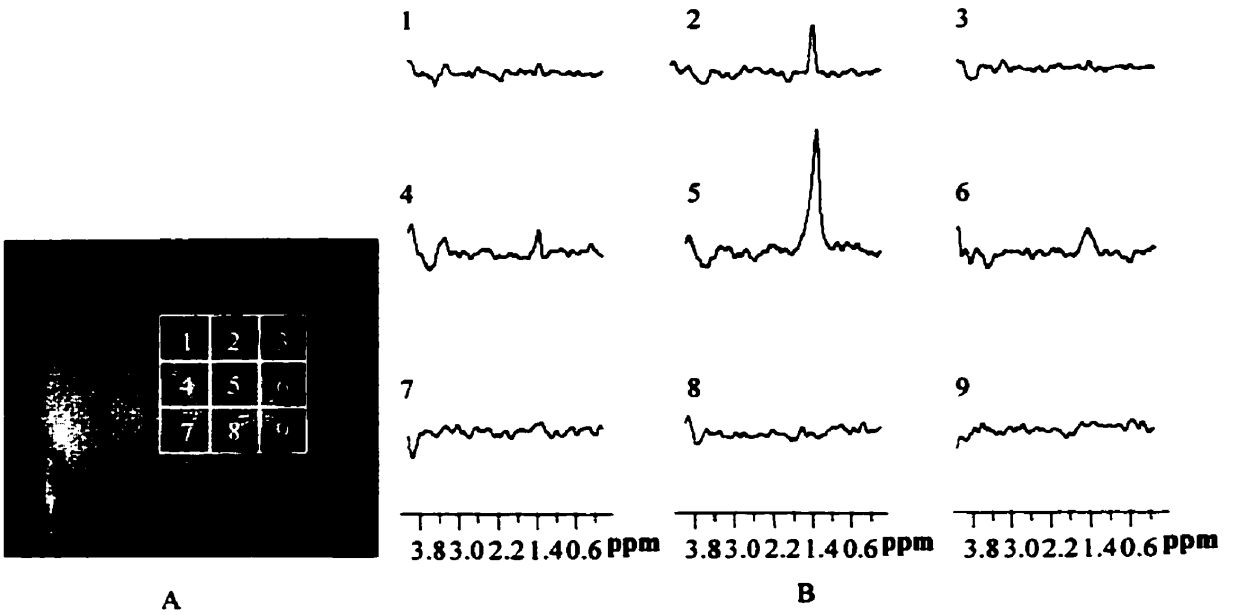

Figure 9.8 Snapshot FLASH scout image (A) and localized DQ lactate edited spectra (B) from a rat brain with focal ischemia in the right hemisphere. The grid overlying the image shows the in-plane voxels from which the spectra were obtained.

Discussion

Combining DQ lactate editing with spatial localization is challenging. Long slice-selective pulses interact with J-coupled spin systems in a way that is quite different from short hard pulses (33). Then in a DQ lactate editing experiment, unwanted coherences can be generated if the hard pulses used for excitation/refocusing are switched to soft slice selective pulses, affecting coherence transfer and the outcome of the experiment. Localization procedures must therefore be introduced into the editing sequence without affecting coherence transfer. This has been done using SPACE (3), VSR (4) or ISIS (6). Longitudinal Hadamard encoding is another localization technique that can be incorporated into a DQ editing sequence without affecting coherence transfer since all spatial information is encoded in the longitudinal

direction in a way that resembles ISIS.

The full discussion of the advantages of using Hadamard encoding as a localization strategy can be found in the literature (22,23,34,35) and are only briefly summarized here: (i) multiple voxel localization is possible; (ii) a small matrix size can be used without significant inter-voxel leakage; (iii) the quality of the spatial localization with longitudinal Hadamard encoding is insensitive to B_1 imperfections and the repetition time; (iv) the method gives spectra with high SNRT; (v) data can be recovered if acquisition is interrupted.

There are also limitations to the use of longitudinal Hadamard encoding. First, multiple-band Hadamard inversion pulses require high RF peak power, requiring a high performance RF amplifier. Careful optimization of the pulse design can help minimize the required peak power (36). Second, because of contamination from outside the region of interest and gaps between the slices, the first volume element in each encoded direction must be discarded, compromising the efficiency of the technique. For example, in a two dimensional 4th order longitudinal Hadamard encoding experiment, after excluding the first row and column, only 3×3=9 voxels out of a total of 16 can be recovered. This problem can potentially be solved by using outer volume suppression (37) along with a no-gap Hadamard pulse design (38) to eliminate the sources of contamination. Third, because localization is not achieved in a single scan, the accuracy of localization may be more susceptible to motion artifacts than single-shot techniques such as PRESS. However, the editing efficiency of the DQ sequence will not be degraded by motion since the lactate-edited signals are acquired in a single shot. Finally, because acquisition does not begin immediately after the Hadamard pulses, some

longitudinal relaxation occurs between the last Hadamard pulse and the start of acquisition (about 100 ms for an *in vivo* lactate editing experiment). This does not degrade the precision of spatial localization (22,23), but it does reduce the overall detection sensitivity by about 10%, taking T1 of lactate *in vivo* to be 1.75 s at 7 T (39).

With spectral editing, metabolite(s) of interest can be observed unequivocally, but usually at the cost of reduced sensitivity. Although the DQF sequence shown in Fig. 9.4A has a high detection sensitivity relative to similar lactate editing sequences, it recovers at best 50% of the lactate signal intensity (16). Lactate signals passing through the DQ filter are further attenuated by mechanisms such as spin-diffusion, J-modulation, transverse relaxation, and RF pulse imperfections (15). In this study the DQF sequence probably recovers only 30-35% of the lactate signal intensity. Even so, Hadamard encoded lactate editing may be useful for clinical studies. At lower fields (e.g. 1.5 T), T2 of lactate is likely significantly longer than that at the high fields used in this study, so that signal loss through transverse relaxation during the DQ creation and detection periods will be reduced. Signal losses due to J-modulation could be reduced by using a binomial pulse (40) rather than a longer shaped pulse as the DQ read pulse to shorten t_1. Finally, clinical studies will use a larger voxel size, effectively increasing the sensitivity.

References

1. C. H. Sotak and D. M. Freeman, A method for volume-localized lactate editing using zero-quantum coherence created in a stimulated-echo pulse sequence, *J. Magn. Reson.* **77**, 382, (1988).

2. C. H. Sotak, D. M. Freeman and R. E. Hurd, The unequivocal determination of in vivo lactic acid using two dimensional double-quantum coherence-transfer spectroscopy, *J. Magn. Reson.* **78**, 355, (1988).

3. S. Crozier, I. M. Brereton, S. E. Rose, J. Field, G. F. Shannon and D. M. Doddrell, Application of volume-selected, two-dimensional multiple-quantum editing in vivo to observe cerebral metabolites, *Magn. Reson. Med.* **16**, 496, (1990).

4. G. C. McKinnon and P. Boesiger, A one-shot lactate-editing sequence for localized whole-body spectroscopy, *Magn. Reson. Med.* **8**, 355, (1988).

5. A. Knuttel and R. Kimmich, Double-quantum filtered volume-selective NMR spectroscopy, *Magn. Reson. Med.* **10**, 404, (1989).

6. M. A. Thomas, H. P. Hetherington, D. J. Meyerhoff and D. B. Twieg, Localized double-quantum-filtered ^{1}H NMR spectroscopy, *J. Magn. Reson.* **93**, 485, (1991).

7. L. Jouvensal, P. G. Carlier and G. Bloch, Practical implementation of single-voxel double-quantum editing on a whole-body NMR spectrometer: localized monitoring of lactate in the human leg during and after exercise, *Magn. Reson. Med.* **36**, 487, (1996).

8. D. L. Rothman, K. L. Behar, H. P. Hetherington and R. G. Shulman, Homonuclear ^{1}H double-resonance difference spectroscopy of the rat brain in vivo, *Proc. Natl. Acad. Sci. U. S. A.* **81**, 6330, (1984).

9. D. G. Schupp, H. Merkle, J. M. Ellermann, Y. Ke and M. Garwood, Localized detection of glioma glycolysis using edited ^{1}H MRS, *Magn. Reson. Med.* **30**, 18, (1993).

10. C. J. Hardy and C. L. Dumoulin, Lipid and water suppression by selective ^{1}H homonuclear polarization transfer, *Magn. Reson. Med.* **5**, 58, (1987).

11. A. Knuttel and R. Kimmich, Single-scan volume-selective spectral editing by homonuclear polarization transfer, *Magn. Reson. Med.* **9**, 254, (1989).

12. C. L. Dumoulin, Suppression of water and other noncoupled spins by homonuclear polarization transfer in magnetic resonance imaging, *Magn. Reson. Med.* **3**, 90, (1986).

13. M. von Kienlin, J. P. Albrand, B. Authier, P. Blondet, S. Lotito and M. Decorps, Spectral editing in vivo by homonuclear polarization transfer, *J. Magn. Reson.* **75**, 371, (1987).

14. Q. He, Z. M. Bhujwalla and J. D. Glickson, Proton detection of choline and lactate in EMT6 tumors by spin-echo-enhanced selective multiple-quantum-coherence transfer, *J. Magn. Reson. B* **112**, 18, (1996).

15. Q. He, D. C. Shungu, P. C. van Zijl, Z. M. Bhujwalla and J. D. Glickson, Single-scan in vivo lactate editing with complete lipid and water suppression by selective multiple-quantum-coherence transfer (Sel-MQC) with application to tumors, *J. Magn. Reson. B* **106**, 203, (1995).

16. R. E. Hurd and D. M. Freeman, Metabolite specific proton magnetic resonance imaging, *Proc. Natl. Acad. Sci. U. S. A.* **86**, 4402, (1989).

17. J. A. Kmiecik, C. D. Gregory, Z.-P. Liang, D. E. Hrad, P. C. Lauterbur and M. J. Dawson, Quantitative lactate-specific MR imaging and ^{1}H spectroscopy of skeletal muscle at macroscopic and microscopic resolutions using zero-quantum/double-quantum coherence filter and SLIM/GSLIM localization, *Magn. Reson. Med.* **37**, 840, (1997).

18. J. R. Keltner, L. L. Wald, B. D. Frederick and P. F. Renshaw, In vivo detection of GABA in human brain using a localized double-quantum filter technique, *Magn. Reson. Med.* **37**, 366, (1997).

19. R. B. Thompson and P. S. Allen, A new multiple quantum filter design procedure for use on strongly coupled spin systems found in vivo: its application to glutamate, *Magn. Reson. Med.* **39**, 762, (1998).

20. L. Bolinger and J. S. Leigh Jr., Hadamard spectroscopic imaging (HSI) for multiple-volume localization, *J. Magn. Reson.* **80**, 162, (1988).

21. G. Goelman, Fast Hadamard spectroscopic imaging techniques, *J. Magn. Reson. B* **104**, 212, (1994).

22. G. Goelman and J. S. Leigh Jr., B_1-insensitive Hadamard spectroscopic imaging technique, *J. Magn. Reson.* **91**, 93, (1991).

23. G. Goelman and J. S. Leigh Jr., Hadamard spectroscopic imaging technique insensitive to pulse imperfections, *J. Magn. Reson. A* **105**, 78, (1993).

24. G. Goelman and J. S. Leigh Jr., Multiband adiabatic inversion pulses, *J. Magn. Reson. A* **101**, 136, (1993).

25. G. Goelman, G. Walter and J. S. Leigh Jr., Hadamard spectroscopic imaging technique as applied to study human calf muscles, *Magn. Reson. Med.* **25**, 349, (1992).

26. M. S. Silver, R. I. Joseph and D. I. Hoult, Highly selective $\pi/2$ and π pulse generation, *J. Magn. Reson.* **59**, 347, (1984).

27. R. B. Thompson and P. S. Allen, Sources of variability in the response of coupled spins to the PRESS sequence and their potential impact on metabolite quantification, *Magn. Reson. Med.* **41**, 1162, (1999).

28. P. C. van Zijl, M. O. Johnson, S. Mori and R. E. Hurd, Magic-angle-gradient double-quantum-filtered COSY, *J. Magn. Reson. A* **113**, 265, (1995).

29. W. H. Perman, M. A. Bernstein and J. C. Sandstrom, A method for correctly setting the rf flip angle, *Magn. Reson. Med.* **9**, 16, (1989).

30. E. Z. Longa, P. R. Weinstein, S. Carlson and R. Cummins, Reversible middle cerebral artery occlusion without craniotomy in rats, *Stroke* **20**, 84, (1989).

31. J. E. van Dijk, A. F. Mehlkopf and W. M. Bovee, Comparison of double and zero quantum NMR editing techniques for in vivo use, *NMR Biomed.* **5**, 75, (1992).

32. J. F. Shen and P. S. Allen, Reduced length for double-quantum filtering sequences, *J. Magn. Reson.* **92** , 398, (1991).

33. J. Slotboom, A. F. Mehlkopf and W. M. Bovee, The effects of frequency-selective RF pulses on J-coupled spin-1/2 systems, *J. Magn. Reson. A* **108**, 38, (1994).

34. W. Dreher and D. Leibfritz, Double-echo multislice proton spectroscopic imaging using Hadamard slice encoding, *Magn. Reson. Med.* **31**, 596, (1994).

35. O. Gonen, F. A. Mendoza and G. Goelman, 3D localized in vivo ^{1}H spectroscopy of human brain by using a hybrid of 1D-Hadamard with 2D-chemical shift imaging, *Magn. Reson. Med.* **37**, 644, (1997).

36. G. Goelman, Two methods for peak RF power minimization of multiple inversion-band pulses, *Magn. Reson. Med.* **37**, 658, (1997).

37. Y. J. Chen, S. Rachamadugu and E. J. Fernandez, Three dimensional outer volume suppression for short echo time in vivo ^{1}H spectroscopic imaging in rat brain, *Magn. Reson. Imaging* **15**, 839, (1997).

38. C. H. Cunningham and M. L. Wood, *Abstr. Int. Soc. Magn. Reson. Med.*, 2062 (1998).

39. W. D. Rooney, T. Ebisu, A. Mancuso, S. Graham, M. W. Weiner and A. A. Maudsley, Metabolite ^{1}H relaxation in normal and hyponatremic brain, *Magn. Reson. Med.* **35**, 688, (1996).

40. P. J. Hore, Solvent suppression in Fourier transform nuclear magnetic resonance, *J. Magn. Reson.* **55**, 283, (1983).

Chapter 10. Summary and Prospects

The thesis is composed of two parts. Part one involved developing, implementing and applying a one-coil magnetic resonance (MR) perfusion imaging technique using continuous arterial spin tagging (CAST), while the development of a series of double quantum (DQ) coherence transfer magnetic resonance spectroscopy (MRS) techniques with possible *in vivo* applications was described in part two.

The technique of MR perfusion imaging using CAST was originally developed in 1992. Since then, there has been growing research interest in this subject because it is believed that this technique has the potential to provide a way of measuring cerebral blood flow (CBF) in experimental animals better than other techniques. Although significant progress has been made in the last several years, some problems must be solved before this technique can reach a point for more practical applications.

First of all, although a limited number of studies have shown that CBF measurements made by MR perfusion imaging using CAST correlate well with those made by other established techniques such as the radioactive microsphere technique (1,2) and autoradiography (3,4), the precision of this technique in measuring absolute CBF has not been rigorously evaluated, especially when the brain is not under normal conditions. There are many factors potentially affecting the precision with which CBF can be measured with this technique and, in my opinion, those factors have to be examined and then accounted for by either theoretical treatments or technical measures before the technique can be finally established. Although

improvement has been made lately (5-7), it is my perception that not all the factors I mentioned in chapter 3 have been receiving adequate attention in a way they should have. More studies are required to evaluate and improve the precision of the CBF measurements with this technique, and eventually to validate this technique.

The second problem associated with MR perfusion imaging using CAST, especially when used with a one-coil configuration, is the poor signal-to-noise ratio (SNR) and consequently the low accuracy with which CBF can be measured. Improving SNR of the CBF measurement (SNR_{perfu}) in one-coil CAST perfusion imaging is the central theme of part one of this thesis. Using a straightforward error propagation analysis, it was first shown that SNR_{perfu} is directly proportional to SNR of the proton density weighted images (SNR_{image}) used to calculate the perfusion images and to the degree of spin labeling (α). It was then realized that SNR_{perfu} can be improved by increasing SNR_{image} while not compromising α. In principle, this can be achieved by reducing the magnetization transfer (MT) and direct off-resonance irradiation (DORI) effects of the spin tagging pulse and simultaneously keeping the requirements for adiabatic-fast-passage inversion satisfied. In practice, it was shown that this could be done by carefully adjusting the strength of both the radiofrequency (RF) pulse (B_1) and the magnetic field gradient (G_l) for spin tagging. In the next step, the proposed strategy to optimize SNR_{perfu} was experimentally implemented and verified with CBF measurement on normal rat brain. It was also realized along the way that the previous equation for CBF calculation in one-coil AST perfusion imaging (i.e. Eq. [3.30]) underestimates CBF when the commonly used values of B_1 and G_l for spin tagging are altered to improve SNR_{perfu}. Therefore, a general equation (i.e. Eq. [3.27]) for CBF calculation

in one-coil CAST MR perfusion imaging was derived. Increased SNR_{perfu} not only means greater accuracy for CBF measurements but also makes it possible to measure CBF with higher temporal resolution. This was demonstrated on normal rat brain with an acetazolamide stimulation test in which quantitative perfusion images with an in-plane spatial resolution of 0.4×0.4 mm^2 and a slice thickness of 2 mm were acquired with a temporal resolution of 6 minutes. The performance of the SNR-optimized perfusion imaging technique was also evaluated in some other experiments. For example, the effects of anesthetics on CBF in normal rats were investigated and the results either confirmed or added new insights into previous observations. In another experiment, a delayed postischemia hyperemia was found in a rat model of focal ischemia, an observation that few have reported before.

Most existing MR perfusion imaging techniques using CAST are single-slice techniques, and thus are not time efficient in acquiring the data if CBF measurement in more than just one slice is of interest. The last unsolved problem then is how to achieve multiple-slice or three-dimensional acquisition. Some options for multiple-slice and three-dimensional acquisition have been suggested (8,9), but none of which, in my opinion, has showed itself to be a fully satisfactory solution. Further studies are also needed in this direction.

The ultimate goal of research in MR perfusion imaging would be developing and experimentally implementing a technique that can be used to acquire three-dimensional CBF maps with full quantification, high spatial resolution and optimal SNR in an acceptable duration of time. This may seem far away from reality at this stage. However, it is my belief that this goal will be reached someday in a future that may actually not be as far away as it

seems.

In recent years, there has been little doubt that basic research and clinical applications in MR diffusion, perfusion and functional imaging have been thriving. Meanwhile, the progress in *in vivo* MRS has been rather slow in spite of the fact that its value and potential in studying tissue metabolic activities have long been and still are appreciated by many MR researchers. The slow progress in *in vivo* MRS can be attributed to a variety of reasons among which the most significant one, I believe, is that there are still many technical problems remaining to be solved. *In vivo* MRS will have more applications and, particularly, more elaborate applications only after these problems are solved. Trying to recognize and solve all the technical problems for *in vivo* MRS in one Ph.D thesis is unquestionably too ambitious. Therefore, no attempt was made in this thesis to try to cover every detail of every problem one may encounter. Instead, research work was more focused on one particular subject: DQ spectral editing in *in vivo* proton MRS.

Spectral editing is a commonly used technique in *in vivo* proton MRS to suppress water/lipid signals and to eliminate spectral overlap. Among existing spectral editing techniques, DQ coherence transfer, which sometimes is also referred as DQ filtering (DQF), offers a good compromise among detection sensitivity, susceptibility to motion artifacts and efficiency of water/fat suppression, and thus has been considered the most suitable for *in vivo* applications (10). The main theme of part two of the thesis is to develop new DQF techniques and to enhance the performance of existing DQF techniques with the objective of making these techniques more useful for practical applications.

Spectral editing pulse sequences are generally metabolite-specific (11). In other words, spectral editing for different metabolites requires different pulse sequences. Previously, DQF sequences have been developed for selective observation of a number of metabolites including lactate (12,13), γ-aminobutyric acid (GABA) (14,15), citrate (16), glucose (17), N-acetylaspartate (NAA) (18), and glutamate (19). In this thesis, a localized DQF sequence for *in vivo* observation of taurine, an important metabolic product of sulfur amino acid catabolism, was developed and optimized, which may be useful as a tool in investigating the pathophysiology of taurine-related diseases. Since the conventional DQF sequences normally recover spectra of only one metabolite at a time, they are thus inefficient in acquiring the data if more than a single metabolite is of interest. In attempting to enhance the performance of the conventional DQF sequences by recovering signals from more than just one metabolite in a single experiment, two new pulse sequences were developed. The first sequence is a stimulated-echo enhanced selective DQ coherence transfer (STE-SelDQC) sequence which can be used to observe edited lactate signals simultaneously with the signals from other metabolites such as NAA, creatine and choline. The second sequence is a double-editing sequence which in principle can be used to edit for any two metabolites at the same time.

Spatial localization has always been a concern for *in vivo* MR spectroscopists. Although there are many spatial localization techniques currently available, combining these techniques with DQF has been less satisfactory. In this thesis, two-dimensional longitudinal Hadamard encoding was combined with a conventional DQ lactate editing sequence to acquire multiple-voxel localized and lactate edited spectra *in vivo*. The excellent performance

of the combined sequence in both multiple-voxel spatial localization and lactate editing, as demonstrated in rat brain, may indicate its potential for clinical applications.

Unequivocal observation of a metabolite by DQ spectral editing is often at the cost of reduced sensitivity. Generally, only a fraction of the signals from the target metabolite can pass through a DQ editing sequence (10), and the signals passing through the sequence are attenuated further by mechanisms such as transverse relaxation, spin-diffusion, J-modulation, and radiofrequency (RF) pulse imperfections (13). Therefore when DQ spectral editing is used to observe a metabolite with low concentration *in vivo*, it is not only essential for the sequence to be efficient in filtering out major overlapping resonances, but also important for the sequence to have optimal detection sensitivity for the metabolite of interest. The flip angles of the RF pulses in a DQ editing sequence affect the detection sensitivity of the sequence, and it is required that the flip angles of all the RF pulses in a DQ editing pulse are calibrated exactly and do not vary across the sample in order to obtain the optimal detection sensitivity (10). As a result, DQ spectral editing is usually done with volume RF coils because of the highly homogeneous B_1 field generated by these coils, as is also the case in the studies described in this thesis. For *in vivo* MRS, the detection sensitivity of a volume coil is usually lower than that of a surface coil because of the smaller loading factor of the former, and thus it is desirable to be able to use surface coils in DQ spectral editing. However, a surface coil cannot be used directly in a DQ editing experiment because of the highly inhomogeneous B_1 field, and thus the varying flip angle across the sample, that it generates (20). One solution would be to use a volume coil for excitation and a surface coil for reception. However, with the dual-coil configuration, the gain in sensitivity from using a

surface coil would be partially lost because of the different B_1 flux patterns of the two coils (21). Another solution to using surface coils in DQ spectral editing is to use adiabatic RF pulses which generate uniform flip angles despite the inhomogeneous B_1 field, as long as the RF power of the pulses exceeds certain minimum thresholds so as to meet adiabatic conditions (22). With a family of relatively new adiabatic RF pulses such as the B_1-insensitive rotation (BIR-4) pulses and the solvent suppression adiabatic pulses (SSAP) developed by Garwood et al (22), it is possible to construct an adiabatic version of any DQ editing sequence that can be used with surface coils. An adiabatic version of a DQ lactate editing sequence has already been developed (21,23). Using the same strategies, the development of the adiabatic version of all the DQ editing sequences described in this theis would greatly improve the detection sensitivity, and thus the usefulness, of these sequences.

As pointed out in the prologue, because the fundamental principles of MR have already been exploited most thoroughly, coming up with really *new* ideas and developing really *new* pulse sequences is becoming increasingly difficult. In a sense, the acclaimed "new" pulse sequences for *in vivo* MRS developed in this thesis are not really *new*. It may be more appropriate to consider them as *integrated* sequences composed of sequence segments that have been available previously. Although developing *integrated* pulse sequences may seem to be not as exciting or challenging as developing pulse sequences which are originally *new*, it may well be the future of the technical development in *in vivo* MRS. Unlike high resolution MRS performed by chemists, *in vivo* MRS is often troubled by practical problems that are inherently associated with biological samples. Poor spectral resolution, water/fat suppression, spatial localization and outer volume suppression are just some typical examples. Although

some solutions for each individual problem have been found and proven successful over the past years, as is still not adequate since, in practice, all the problems will most likely arise simultaneously instead of appearing individually. A "panacea" therefore is needed. Integrated pulse sequences are formed by incorporating different sequence segments which are designed specifically to address different problems, and thus seem to be a good candidate for the panacea we are all looking for. It may sound simple. The practical implementation of integrated pulse sequences, however, may not be as straightforward as one may think, and as can be seen from the previous chapters of the thesis. Nevertheless, the work described in this thesis along with the efforts made by many others is just a beginning, and more development on this direction is obviously needed.

In a sense, this thesis has turned out in a way that was hardly expected even by myself when I first started my Ph.D program. Initially, I was thinking of doing research projects in which MR imaging and spectroscopy are simply used as tools to investigate the pathophysiology of certain neurological diseases. If I had followed that track, my thesis would certainly have a different look from what it has now and most of what has been described in the previous chapters would also be impossible. It all started when I tried to implement and improve the technique of MR perfusion imaging using CAST. The further I went, the more frequently I found myself amazed by the complexity and at the same time the beauty of *magnetic resonance* itself. I then followed my own interest and curiosity until I finally realized that I had gotten on a road that was totally different from the one I was supposed to be on. I am not sure, even now, whether I chose a harder road to walk on or I was just lucky to find an easier way out of this. It is already too late for me to look back and have that choice all over again.

However, one thing for sure is that I have really enjoyed what I did.

Nonetheless, this thesis is not only just a summary of the relentless work which I did in the past several years, it also represents my very first personal accomplishment in science, if it can be called an accomplishment. There is no need to say that I am proud of it, indeed, just like anyone would do in the same situation. However, no matter how proud I am emotionally, a question remains: Is it a good thesis or not? I am certainly in no position to make that judgement myself. Ultimately, what makes a good thesis a good thesis or a so-so thesis, I believe, is its scientific merits which can only be judged by the objectiveness of science. Sir Isaac Newton once had this famous remark when he tried modestly to summarize his life achievement in science: "*I don't know what I may seem to the world, but, as to myself, I seem to have been only like a boy playing on the sea shore, and diverting myself in now and then finding a smoother pebble or a prettier shell than ordinary whilst the great ocean of truth lay all undiscovered before me.*" Even someone as great as Newton felt overwhelmed when he faced the great ocean of truth. For someone as humble as me, it is absolutely no modesty at all to say that I would be most gratified if what has been described in this thesis could be considered as a tiny grain of sand on the shore of the great ocean of truth which Newton mentioned.

After this paragraph, this thesis will finally come to its end, a point which I devoted twenty consecutive years of my life trying to reach. Ever since I was a little boy who could barely read and write, I have been dreaming that someday I will be in a position where I am right now. Now I am here and what will be the next? I often hear someone use the phrase "a

starting point of pursuing a lifetime scientific career" to describe the completion of ones post-graduate studies, which I can hardly agree to. It always seemed to me that there is a distinct difference between "pursuing a scientific career" and "devoting ones life to science", although I was never able to spell out the difference in words until I red a quote by Michael Faraday not too long ago, and it says: "*I have always felt that there is something degrading in offering rewards for intellectual exertion, and that societies or academies, or even kings and emperors, should mingle in the matter does not remove the degradation.*" I am not sure whether or not everyone in the scientific community agrees with Faraday in his words, but I certainly do. It has always been my belief that the only rewards in pursuing scientific research are the chances for one to see the grand beauty of the truth and the joy and the excitement one may feel along the way in searching for the truth. In this sense, I have never regretted my choice in going down the road of science and never will.

References

1. L. Hernandez, C. A. Branch and J. A. Helpern, *Abstr. Int. Soc. Magn. Reson. Med.*, 1193 (1998).

2. E. G. Walsh, K. Minematsu, J. Leppo and S. C. Moore, Radioactive microsphere validation of a volume localized continuous saturation perfusion measurement, *Magn. Reson. Med.* **31**, 147, (1994).

3. P. R. Allegrin, D. Bochelen, M. Eis, A. Sauter and M. Rudin, *Abstr. Int. Soc. Magn. Reson. Med.*, 377 (1998).

4. M. Hoehn Berlage, K. Kruger, E. Busch and M. Franke, *Abstr. Int. Soc. Magn. Reson. Med.*, 1843 (1999).

5. J. Pekar, P. Jezzard, D. A. Roberts, J. S. Leigh Jr., J. A. Frank and A. C. McLaughlin, Perfusion imaging with compensation for asymmetric magnetization transfer effects, *Magn. Reson. Med.* **35**, 70, (1996).

6. D. C. Alsop and J. A. Detre, Reduced transit-time sensitivity in noninvasive magnetic resonance imaging of human cerebral blood flow, *J. Cereb. Blood Flow Metab.* **16**, 1236, (1996).

7. F. Q. Ye, V. S. Mattay, P. Jezzard, J. A. Frank, D. R. Weinberger and A. C. McLaughlin, Correction for vascular artifacts in cerebral blood flow values measured by using arterial spin tagging techniques, *Magn. Reson. Med.* **37**, 226, (1997).

8. D. C. Alsop and J. A. Detre, Multisection cerebral blood flow MR imaging with continuous arterial spin labeling, *Radiology* **208**, 410, (1998).

9. F. Q. Ye, J. H. Duyn, J. A. Frank, D. R. Weinberger and A. C. McLaughlin, *Abstr. Int. Soc. Magn. Reson. Med.*, 1838 (1999).

10. J. E. van Dijk, A. F. Mehlkopf and W. M. Bovee, Comparison of double and zero quantum NMR editing techniques for in vivo use, *NMR Biomed.* **5**, 75, (1992).

11. P. S. Allen, R. B. Thompson and A. H. Wilman, Metabolite-specific NMR spectroscopy *in vivo*, *NMR Biomed.* **10**, 435, (1997).

12. L. Jouvensal, P. G. Carlier and G. Bloch, Practical implementation of single-voxel double-quantum editing on a whole-body NMR spectrometer: localized monitoring of lactate in the human leg during and after exercise, *Magn. Reson. Med.* **36**, 487, (1996).

13. Q. He, D. C. Shungu, P. C. van Zijl, Z. M. Bhujwalla and J. D. Glickson, Single-scan in vivo lactate editing with complete lipid and water suppression by selective multiple-quantum-coherence transfer (Sel-MQC) with application to tumors, *J. Magn. Reson. B.* **106**, 203, (1995).

14. J. R. Keltner, L. L. Wald, B. D. Frederick and P. F. Renshaw, In vivo detection of GABA in human brain using a localized double-quantum filter technique, *Magn. Reson. Med.* **37**, 366, (1997).

15. J. Shen, D. C. Shungu and D. L. Rothman, In vivo chemical shift imaging of γ-aminobutyric acid in the human brain, *Magn. Reson. Med.* **41**, 35, (1999).

16. A. H. Wilman and P. S. Allen, Double-quantum filtering of citrate for in vivo observation, *J. Magn. Reson. B.* **105**, 58, (1994).

17. J. R. Keltner, L. L. Wald, P. J. Ledden, Y. C. Chen, R. T. Matthews, E. H. Kuestermann, J. R. Baker, B. R. Rosen and B. G. Jenkins, A localized double-quantum filter for the in *vivo* detection of brain glucose, *Magn. Reson. Med.* **39**, 651, (1998).

18. A. H. Wilman and P. S. Allen, Observing N-acetyl aspartate via both its N-acetyl and its strongly coupled aspartate groups in in vivo proton magnetic resonance spectroscopy, *J. Magn. Reson. B.* **113**, 203, (1996).

19. R. B. Thompson and P. S. Allen, A new multiple quantum filter design procedure for use on strongly coupled spin systems found in vivo: its application to glutamate, *Magn. Reson. Med.* **39**, 762, (1998).

20. J. J. Ackerman, T. H. Grove, G. G. Wong, D. G. Gadian and G. K. Radda, Mapping of metabolites in whole animals by ^{31}P NMR using surface coils, *Nature* **283**, 167, (1980).

21. R. A. de Graaf, Y. Lou, M. Terpstra and M. Garwood, Spectral editing with adiabatic pulses, *J. Magn. Reson. B* **109**, 184, (1995).

22. A. Tannús and M. Garwood, Adiabatic pulses, *NMR Biomed.* **10**, 423, (1997).

23. M. Garwood, B. Nease, Y. Ke, R. A. de Graaf and H. Merkle, Simultaneous compensation for B_1 inhomogeneity and resonance offsets by a multiple-quantum NMR sequence using adiabatic pulses, *J. Magn. Reson. A* **112**, 272, (1995).